The Dissertation Committee for Lauren Ashley Lytwak Certifies that this is the approved version of the following dissertation:

Oligothiophenes and Conducting Metallopolymers: Fundamental Studies and Development of Functional Materials

Committee:

Bradley J. Holliday, Supervisor

Richard A. Jones

Simon M. Humphrey

Katherine Willets

John J. Stankus

Oligothiophenes and Conducting Metallopolymers: Fundamental Studies and Development of Functional Materials

by

Lauren Ashley Lytwak, B.S.

Dissertation

Presented to the Faculty of the Graduate School of

The University of Texas at Austin

in Partial Fulfillment

of the Requirements

for the Degree of

Doctor of Philosophy

The University of Texas at Austin

May 2013

Dedication

This work is dedicated to my parents and grandparents for being my biggest fans and never doubting my ability to succeed. Despite being 2,000 miles away, I never once felt alone in this journey.

Acknowledgements

First and foremost, I gratefully acknowledge my advisor, Professor Brad Holliday for his unwaivering support, guidance, and help throughout my graduate career. My success in graduate school and professional growth as a chemist would not be possible without his mentorship. I would like to thank my committee members, Dr. Richard Jones, Dr. Simon Humphrey, Dr. Kallie Willets, and Dr. John Stankus for helpful suggestions and insights that greatly contributed to my dissertation. Additionally, I would like to acknowledge Dr. Keith Stevenson for fruitful conversations regarding electrochemical experiments contained in this work.

In addition, I would like to thank the members of the Holliday group, both past and present, for their support, hospitality, and friendship. I cannot thank them enough for listening to countless practice talks, revising my work, and giving me helpful suggestions regarding my research. Furthermore, I would especially like to thank the Holliday group crystallographers, Michelle Mejía, Julie Wilkerson, and Lauren Mitchell, for the X-ray crystal structures contained in this dissertation.

I also graciously acknowledge the help of Jacob Goran and Stephen Fosdick for their assistance and advice with electrochemical experiments and simulations. Much of the electrochemical work contained within would not be possible without their help. Additionally, I would like to thank the entire Stevenson group for readily allowing me to use their instrumentation and resources.

Oligothiophenes and Conducting Metallopolymers: Fundamental Studies and Development of Functional Materials

Lauren Ashley Lytwak, Ph.D.

The University of Texas at Austin, 2013

Supervisor: Bradley J. Holliday

Diimine rhenium(I) tricarbonyl complexes are known as phosphorescent emitters and electro- and photocatalysts for the reduction of CO_2 to CO. Conducting metallopolymers containing this rhenium(I) moiety should not only retain the photoluminescent and catalytic properties of the complex but also gain the conductivity, processability, and mechanical flexibility typical of π-conjugated polymers. A series of tricarbonyl rhenium(I) diimine-type monomers and metallopolymers have been prepared. Appended to the ligands are thiophene and 3,4-ethylenedioxythiophene (EDOT) groups for electropolymerization of the metal complexes. UV-Vis absorption and emission spectroscopy studies of the monomers indicate that light emission originates from triplet ligand-centered (^{3}LC) $\pi \rightarrow \pi^*$ and triplet metal-to-ligand charge transfer (^{3}MLCT) excited states. Additionally, both the monomers and metallopolymers show electrocatalytic activity towards the reduction of CO_2 to CO. Furthermore, the EDOT-functionalized diimine-type ligand ($EDOT_2$-BPP) also serves as a good sensitizing ligand for luminescent lanthanide emission. A series of lanthanide complexes that utilize *tris*(*β*-diketonates) and $EDOT_2$-BPP ligands have been synthesized and studied using X-ray crystallography and photophysical techniques. Large quantum yields and microsecond lifetimes were found for the Eu^{III} and Sm^{III} complexes. Complexes of Tb^{III} were found to

have weak luminescent emission due to the less-than-optimal energy gap between the sensitizing ligands and the excited state of the Tb^{III} ion.

Oligothiophenes are models for polymeric systems because of solution processability, controlled chain length, and a well-defined structure. We have synthesized a library of alkyl and polyfluoroalkyl-substituted oligothiophenes to study how molecular structure, long-range order, spatial orientation, and varying degree of electronic coupling between molecules influences charge separation in photovoltaics. These oligoalkylthiophenes have been characterized by X-ray diffraction, photophysical methods, electrochemistry, and UV-Vis and EPR spectroscopies. Although the electronic properties of these oligoalkylthiophenes do not vary with alkyl group, aggregates of oligooctylthiophene, made through solution processing, have distinct morphologies with varying amounts of electronic disorder. The extent of electronic disorder within the aggregate is determined by comparing the suppression of the 0-0 vibronic band in the fluorescence spectra to that of the non-aggregated parent molecule. This extent of electronic disorder was correlated with the local contact potential of individual aggregates through Kelvin probe force microscopy (KPFM) measurements.

Table of Contents

List of Tables

List of Figures

List of Schemes

Chapter 1: Rhenium(I)-Containing Metallopolymers

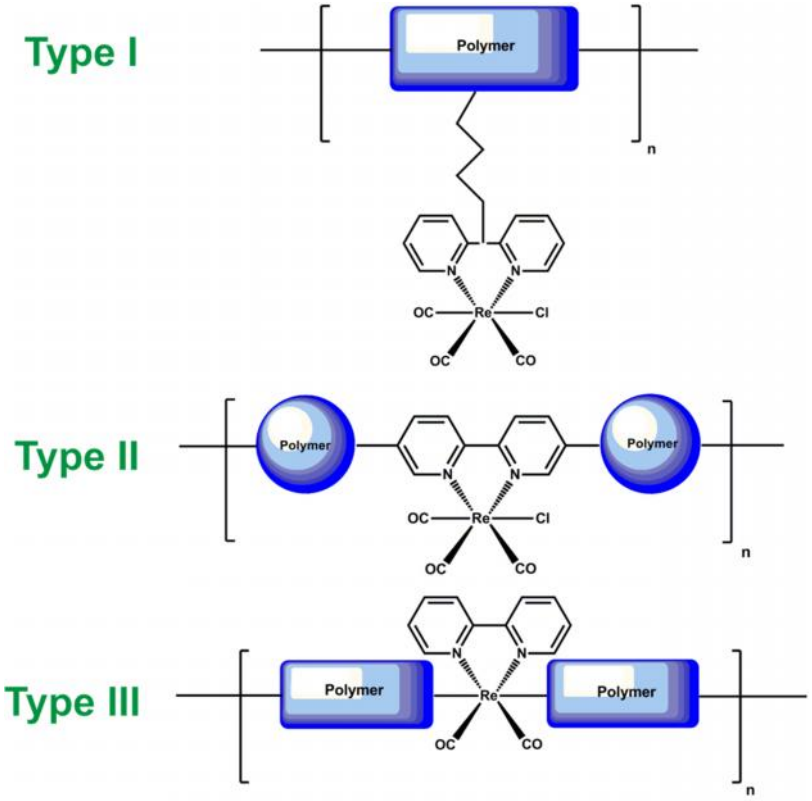

1.1. INTRODUCTION AND SCOPE

Transition metal-containing polymers are materials that incorporate the benefits of both inorganic complexes and organic conjugated polymers. These hybrid materials offer many advantages over conventional inorganic materials such as ease of processing, mechanical strength and flexibility, and low cost of fabrication.[1,2] Additionally, these metallopolymers offer benefits over organic polymer counterparts in that the optical, electronic, and chemical properties of the inorganic metal complexes are retained.[3-9] For these reasons, metal-containing polymers have applications in chemical sensing, catalysis, optics, photovoltaics, and biomedical labeling and imaging.[10-18] These inorganic-organic hybrid polymers are classified into three types according to the position of the metal center in relation to the organic polymeric backbone, as described by Wolf and coworkers.[4] In a Wolf Type I metallopolymer, the metal center is tethered to the organic backbone by a saturated, electrically insulating organic linker. In a Wolf Type II metallopolymer, the metal is covalently coupled to the organic polymeric backbone such that efficient energy transfer can occur between the polymer and the metal center. Lastly, in a Wolf Type III metallopolymer, the metal center plays a structural role in the architecture of the polymer and is directly incorporated within the polymeric backbone, allowing for direct electronic communication between the inorganic and organic components.[4] A schematic representation of the three classes of Wolf Type metallopolymers is shown in Figure 1.1.

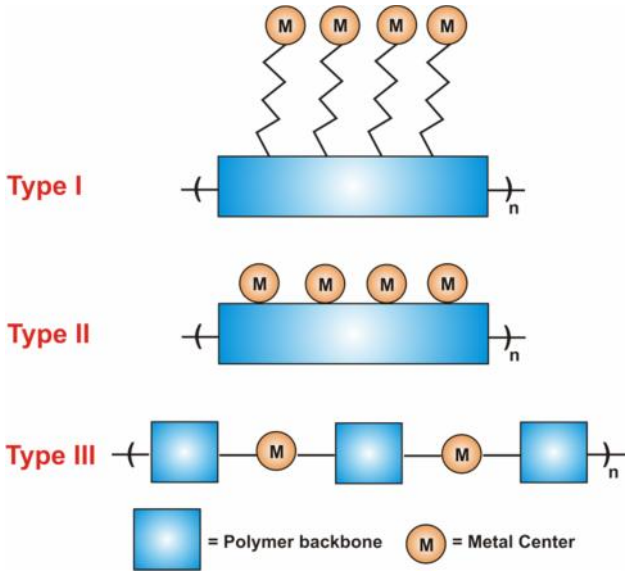

Figure 1.1. Schematic representation of Wolf Type I-III metallopolymers.

Rhenium(I) tricarbonyl diimine complexes, *fac*-(L)Re(CO)$_3$X, where X is a halogen and L is a bidentate diimine-type ligand such as 2,2'-bipyidine (Bipy) and 1,10-phenanthroline (Phen) (Figure 1.2), are well known for intense phosphorescent emission, large photoluminescent quantum yields, and long-lived microsecond lifetimes.[19-26] First discovered by Wrighton and Morse in 1974, this intense visible emission was found to originate from a triplet metal-to-ligand charge transfer (^{3}MLCT) excited state (Figure 1.3).[19] Rhenium(I), like other d^6 metals, experience intense ^{3}MLCT phosphorescent emission due to the heavy atom effect. In the presence of a heavy atom such as Re(I), spin-orbit coupling is enhanced and increased mixing of the excited singlet and triplet states occurs, giving rise to long-lived microsecond excited state lifetimes and large photoluminescent quantum yields.[27-31] In addition to intense visible phosphorescent emission, rhenium(I) tricarbonyl diimine-type complexes also show chemical inertness and redox-active functionality.[32-41] Due to these advantageous properties, *fac*-

$(L)Re(CO)_3X$ complexes have applications as organic light-emitting diodes (OLEDs), biological probes, and photo- and electrocatalysts.[35,36,42-47]

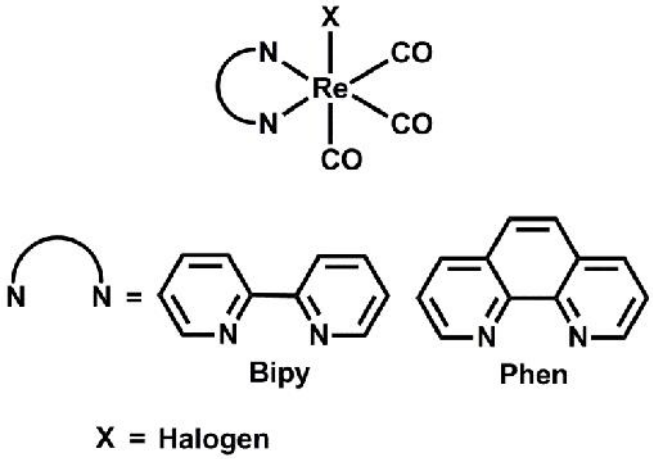

Figure 1.2. Structure of rhenium(I) tricarbonyl diimine-type complexes, *fac*-$(L)Re(CO)_3X$.

Recently, electronic devices have been fabricated from other transition metal complexes. OLED devices of transition metal complexes, such as iridium, osmium, and platinum have been reported.[28-31,48-53] Theoretically, light-emitting devices containing phosphorescent transition metals would have efficiencies 3-4 times greater than devices solely containing fluorescence organic molecules.[42] This increase in internal quantum efficiency is due to the heavy atom effect and the ability of transition metal complexes to harvest both singlet and triplet excitons.[54] Increased mixing of the excited singlet and triplet states allow both singlet and triplet excitons to emit light. The incorporation of transition metal ions into light-emitting devices will potentially allow internal efficiencies to reach 100%.[55]

Additionally, transition metal complexes and metallopolymers have been used as photosensitizers for light harvesting in photovoltaics devices and as efficient charge carriers in electronic devices.[56-58] For example, solution processable Pt(II)-containing

metallopolymers have been used in photovoltaics devices and demonstrate high power conversion efficiencies between 1.1-4.13%.[59-63] Likewise, Ru(II) polypyridyl complexes and polymers have been used in photovoltaic devices due to high intrinsic molar absorptivities and charge carrier mobilities.[64-68] Moreover, materials containing bimetallic Pt-Fe polymers have displayed smaller bandgaps than the parent mononuclear polymers, demonstrating potential application in solar cells.[69,70]

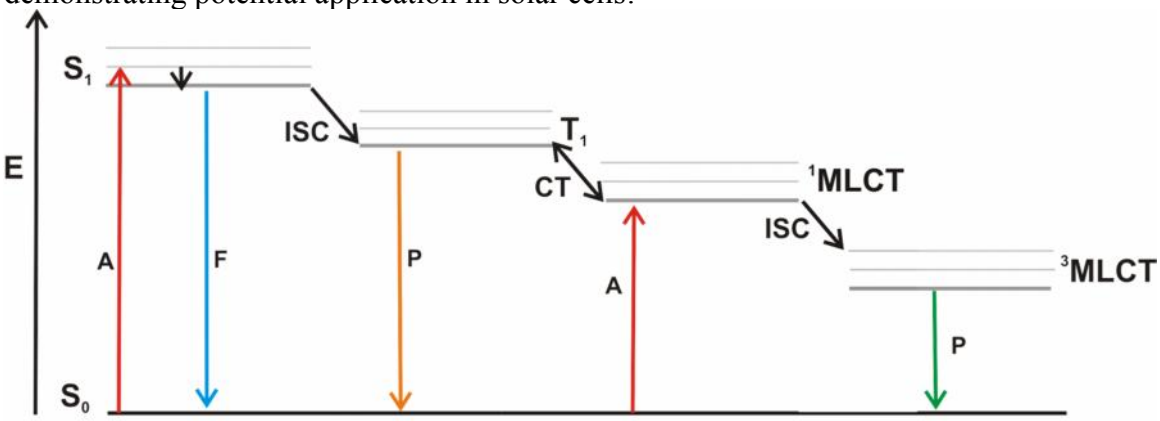

Figure 1.3. Jablonski diagram of absorption and emission pathways in *fac*-(L)Re(CO)$_3$X complexes.

The purpose of this introduction is to provide an overview of rhenium(I)-containing metallopolymers and classify these polymers in accordance with the Wolf Type I-III system. This introduction is by no means a comprehensive compilation of all rhenium(I) metallopolymers but rather, meant to highlight forerunners in this area and identify rhenium(I) polymeric systems with potential applications as functional materials. For reviews focused on other transition metals or lanthanide-containing metallopolymers, the reader is referred to literature published elsewhere.[2-9,71-75]

1.2. RHENIUM(I)-CONTAINING METALLOPOLYMERS

1.2.1. Wolf Type I Metallopolymers

In a Wolf Type I metallopolymer, the metal center acts as a pendant, tethered to the polymeric backbone by a saturated organic linker, such as an alkyl group. Due to the electronically insulating nature of the organic linker, the metal center is generally isolated from the polymeric backbone and often retains the electronic, optical, and chemical properties of the isolated metal complex.[4] In these types of systems, the polymer plays a structural role as a conductive backbone for the pendant metal complex. Generally, Wolf Type I metallopolymers are synthetically easy to make as the metal complex can be complexed to the functionalized polymer backbone post-polymerization.

In 2010, Mak *et al.* reported a low bandgap rhenium(I) complex tethered to a π-conjugated polymer.[76] The π-conjugated polymer backbone, prepared *via* a Suzuki cross-coupling reaction, is functionalized with an *intra*molecular charge transfer dye (ICT) pendant group, 2-phenyl-3-pyridin-2-yl-5,7-di-2-thienylthieno[3,4-b]pyrazine (shown in Figure 1.4). In addition to serving as a bidentate chelate, these ICT groups act as solubilizing, donor-acceptor groups that broaden the absorption of the polymeric backbone. Upon complexation with $ReCl(CO)_5$, the absorption of the metallopolymer broadens into the near-IR region. Additionally, the absorption spectrum of this metallopolymer displays bands in the UV and visible region, corresponding to the $\pi \rightarrow \pi^*$ transition of the polymeric backbone and charge transfer organic linker, respectively. The bandgap for this rhenium(I)-containing polymer system is 1.49–1.82 eV, demonstrating potential application in photovoltaic devices. Bulk-heterojunction solar cells were fabricated with this polymer as the donor material and PCBM as the electron acceptor material on ITO-coated glass. However, low photovoltaic performance was observed due to low absorptivity of the polymer in the visible region and phase

segregation of the donor and acceptor materials. Further work from Mak and coworkers report a low bandgap rhenium(I) metallopolymer in which the metal center is covalently bound to the polymeric backbone in a Wolf Type II fashion (*vide infra*).[77]

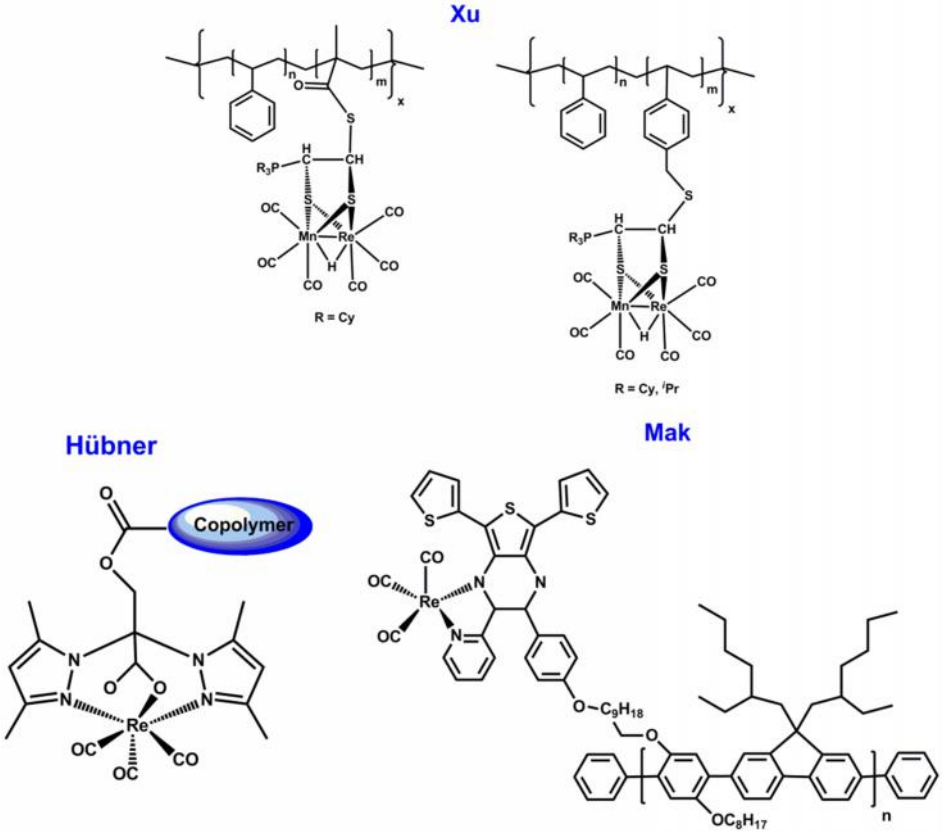

Figure 1.4. Chemical structures of Wolf Type I rhenium-containing metallopolymers.[76,78,79]

Bignozzi *et al.* synthesized methacrylate- and styrene- based homopolymers and copolymers with pyridine-containing side chains for rhenium(I) complexation,[10] as shown in Figure 1.5. In these systems, complexation with $[Re(Phen)(CO)_3(CH_3COCH_3)][ClO_4]$ could successfully occur before or after free radical polymerization. All polymers were found to have low T_g values, good chemical resistance, and the characteristic ^{3}MLCT emission from 534 -574 nm, both in solution

and solid-state films. These rhenium(I)-containing metallopolymers display sensitivity towards luminescent quenching by atmospheric oxygen suggesting that these materials may have applications as oxygen sensors. Moreover, the polymer demonstrating the highest quenching efficiency contained the lowest amount of rhenium(I) complex. Through SEM micrographs, it was found that aggregation occurred in polymers containing free pyridine ligands, thus affecting the optical properties of the metallopolymer.

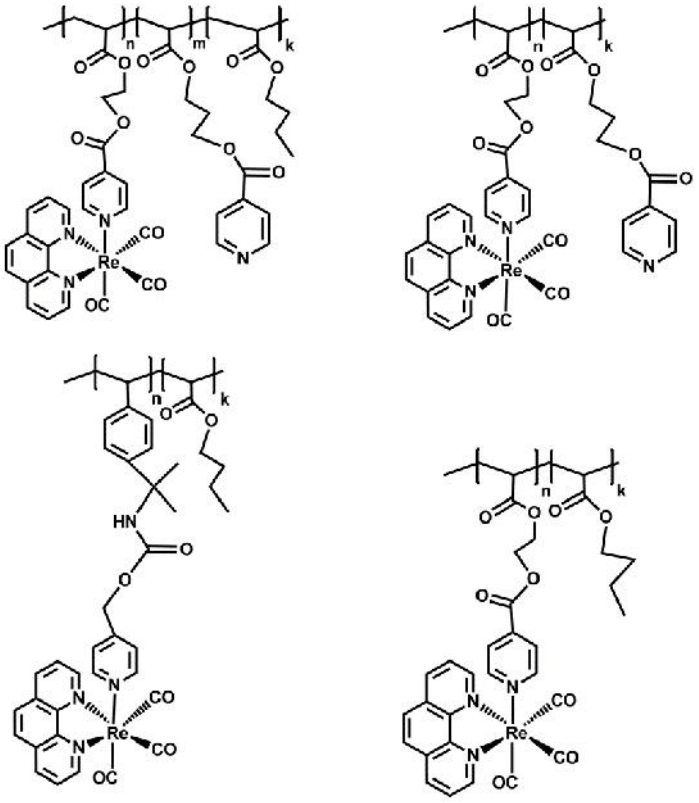

Figure 1.5. Chemical structures of methyacrylate- and styrene-based polymers with $Re(Phen)(CO)_3^+$ units in the side chain.[10]

Additional proof-of-concept examples of rhenium-containing Wolf Type I metallopolymers include work by Hübner *et al.*[78] and Xu and coworkers,[79] as shown in Figure 1.4. A polymerization-active ligand, 2,2-bis(3,5-dimethylpyrazol-1-yl)-3-

methacrylatopropionic acid, a tridentate N-N-O ligand, was successfully copolymerized with methyl methacrylate (MMA). Post-polymerization, the polymer was treated with $[MBr(CO)_5]$ (M = Mn(I), Re(I)) in which binding to the Re(I) metal centered occurred through the N-N-O ligand. Solid-state fixation of the metal complex was confirmed by IR spectroscopy of the polymer. Xu *et al.* report a binuclear Mn-Re carbonyl complex as the pendant group to a styrene-based copolymer backbone. Incorporation of a binuclear metal complex into the side chain of the polymer changed the glass transition temperature as much as 100 ºC from that of polystyrene.

1.2.2. Wolf Type II Metallopolymers

In Wolf Type II metallopolymers, the metal center is covalently bound to the polymeric backbone, such that electronic communication and efficient energy transfer can occur between the metal and the polymer.[4] A majority of the reported rhenium-containing polymers are classified as Wolf Type II metallopolymers. This type of metallopolymer is synthetically easy to make since complexation with the $Re(CO)_3^+$ core can occur before or after polymerization.

In 2011, Ainscough and coworkers reported rhenium(I)-containing Wolf Type II metallopolymers in which a Re(I) metal center is bound to a 3,5-biphenyl-2,2'-bipyridine ligand,[80] as shown in Figure 1.6. This bipyridine-type chelating ligand is appended to a polymeric phosphazene backbone. UV-Vis absorption studies of the resulting polymer displayed a high-energy band at c.a. 300 nm assigned as bipyridyl-based $\pi \rightarrow \pi^*$ transition, and a lower energy absorption band attributed to MLCT transitions. Resonance Raman spectroscopy was used to confirm that the low energy band observed in the UV-Vis was MLCT in nature.

Seminal work in redox-active conducting metallopolymers was reported by Wolf and Wrighton in 1994.[81] As shown in Figure 1.6, 5,5'-(2-thienyl)-2,2'-bithiazole was electropolymerized to form a conducting metallopolymer. Subsequent reaction of the electrode-confined polymer film with $ReCl(CO)_5$ produced the Re(I) metallopolymer. Through FTIR spectroelectrochemistry experiments, Wolf and Wrighton demonstrated that oxidation of the metallopolymer to a conducting state would change the electron density at the metal center. In these experiments the carbonyl stretches of the Re(I) tricarbonyl metallopolymers serve as spectroscopic handles to monitor electron density at the metal center as the polymeric backbone is oxidized. Studies indicated that the carbonyl stretches shifted 4-6 cm^{-1} to higher energy with oxidation of the thienyl-bithiazole polymer backbone, indicating a change in electron density at the Re(I) metal center. Furthermore, the metal moiety remained intact upon oxidation of the polymer, demonstrating the feasibility of these conducting metallopolymers as functional redox-active materials.

Bracco and coworkers synthesized a conjugated pendant polymer in 2009 to study electron transfer processes in biological systems. This polymeric system consists of a poly(4-vinylpyridine) backbone with a pyridine pendant group for chelation to a $Re(CO)_3(tmphen)^+$ (tmphen = 3,4,7,8-tetramethyl-1,10-phenanthroline) chromophore (Figure 1.6).[82] This Re(I) metallopolymer, ReP4VP, was used to study the interconversion of ferricytochrome C, Fe(III)-Cyt c, to ferrocytochrome C, Fe(II)-Cyt c. In a denatured state, Fe(III)-Cyt c forms aggregates which interact with ReP4VP, as confirmed by UV-Vis and TEM spectroscopy. Chemical- or photoinduced reduction causes reductive quenching of the MLCT excited state of the $Re(CO)_3(tmphen)^+$ moiety. Reductive quenching of $Re(CO)_3(tmphen)^+$ in the presence of Fe(III)-Cyt c causes a rapid electron transfer from the Re(I) chromophore to the Fe(III) metal center in the heme

protein to produce Fe(II)-Cyt c. Studying the electron transfer reaction in Fe(III)-Cyt c to Fe(II)-Cyt c is essential in understanding the denatured state of proteins and the role of these denatured states in biological processes such as protein folding and stability.

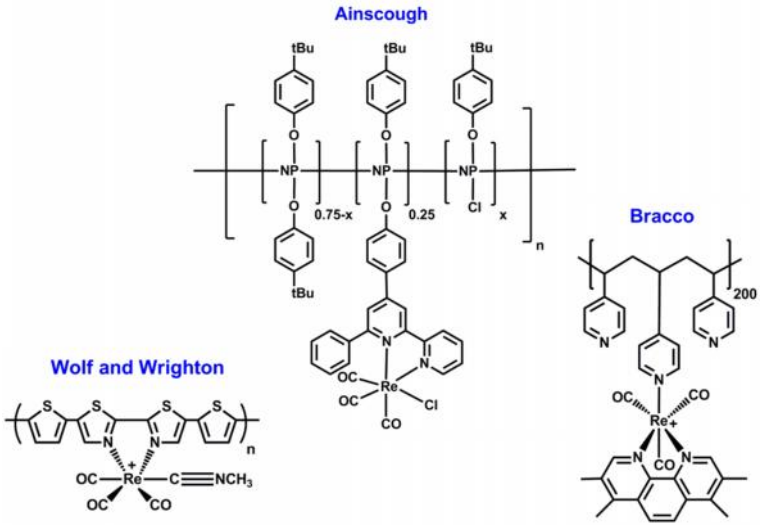

Figure 1.6. Various types of Wolf Type II rhenium-containing metallopolymers.[80-83]

Rhenium complexes embedded in polymeric micelles was reported by Xu *et al.* in 2008.[84] A polystyrene/poly(2-vinylpyridine) diblock copolymer was synthesized in which the $ReCl(Phen)(CO)_3$ complex was attached to the vinylpyridine block by means of a pendant pyridine group, as depicted in Figure 1.7A. The location and morphology of the rhenium complex within the micelle was dictated by solvent. Addition of methanol to a solution of the copolymer-rhenium(I) complex in THF produced micelles in which the $ReCl(Phen)(CO)_3$ complex was embedded within the core of the micelle. The addition of water, at a low pH, to a copolymer-rhenium(I) complex solution formed corona-embedded rhenium complex micelles. In these types of micelles, the rhenium complexes were randomly distributed on the corona of the micelle, forming strawberry-like morphologies. A figure depicting the formation of different types of micelles is shown in Figure 1.7B.

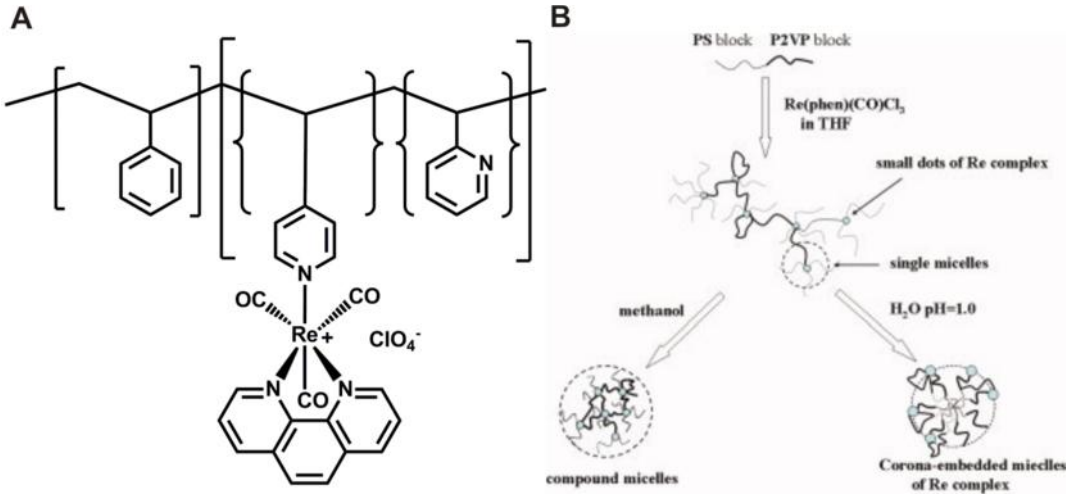

Figure 1.7. (A) Structure of $Re(Phen)(CO)_3^+$ polystyrene/poly-(2-vinylpyridine) copolymer. (B) Solvent preparation pathways to formation of different micelles (From reference 84 by permission of John Wiley and Sons).

A novel polymeric system in which the rhenium(I) metal complex is not bound to the repeating unit of the polymer chain was reported by Lee and coworkers.[85] In this system, the polyfluorene polymeric backbone is end-capped with quinoline or pyridine. The rhenium chromophore, $ReCl(mpy)_2(CO)_3$ (mpy = 4,4'-dimethyl-2,2'-bipyridyl) (M_w = 20,000 g/mol), was coordinated to the qunioline or pyridine end-cap, as shown in Figure 1.8. By end-capping the polymer, the molecular weight can effectively be controlled. IR and photophysical spectra confirm the incorporation of the $Re(mpy)_2(CO)_3^+$ unit within the polymer. Electroluminescence was observed from this Re(I)-polymer system with emission originating from the $\pi \rightarrow \pi^*$ polyfluorene backbone and the ^{3}MLCT state of the $Re(mpy)_2(CO)_3^+$ moieties. However, these polymers display poor thermal stabilities, limiting the application of these systems in electroluminescent devices.

In 2004, Feliz and Ferraudi studied the photophysical and photochemical properties of a rhenium(I) peralkylated vinyl pyridine-based polymer, $\{(vpy\text{-}CH_3^+)_2$-

vpyRe(CO)$_3$(Phen)$^+$}$_{200}$ (Figure 1.8) in which coordination to the Re(Phen)(CO)$_3^+$ occurs through the pendant pyridine group on the π-conjugated backbone.[83] Upon radiation at 350 nm, *intra*strand charge separation occurs within the polymer backbone, unlike the energy migration that occurs in the unsubstituted analogous rhenium(I) metallopolymer, {(vpy)$_2$-vpyRe(CO)$_3$(Phen)$^+$}$_{200}$. The excited states of the vpyRe(CO)$_3$(Phen)$^+$ moiety react with neutral species and anionic electron donors, such as 2,2',2''-nitrilotriethanol, SO_3^{2-}, and I^-, respectively. Feliz and coworkers have demonstrated that the reaction with the anionic electron donors occurs more efficiently in the presence of the MLCT excited states of the rhenium(I)-containing metallopolymer than the parent Re(Phen)(Py)(CO)$_3^+$ complex.

A majority of the Wolf Type II rhenium(I)-containing metallopolymers contain 2,2'-bipyridine and derivatives thereof in the main chain.[80,85-90] Ley and Schanze report a poly(aryleneethynylene) polymer with ReCl(X)(CO)$_3$ (X = 5,5'-diethynyl-2,2'-bipyridine, 4,4'-diethynylbiphenyl, and dialkoxydiiodobenzene) units within the backbone at 10, 25, and 50 mol %,[56,86,90] as shown in Figure 1.8. These rhenium(I)-containing metallopolymers were characterized by NMR, IR, and gel permeation chromatography to confirm the presence of the Re(I) complex within the polymeric backbone. At 77 K, emission at 643 nm is observed and assigned as phosphorescence from the π → π* state of the polymer backbone. Additionally, at 77 K, ^{3}MLCT emission is observed at 690 nm as a broad, structureless emission peak. However, fluorescence from the π → π* exciton state of the polymer at ca. 435 nm is quenched as the mole fraction of Re(I) increases. Schanze and coworkers report analogous rhenium(I)-containing oligomers in which the fluorescence from the π-conjugated backbone is completely quenched by the bound metal complexes, unlike the polymeric systems in which the fluorescence is not efficiently quenched.[87,88,91] In these analogous Re(I)

oligomeric systems, the ^{3}MLCT emission blue shifts to 600 nm, which is expected for a less conjugated system.

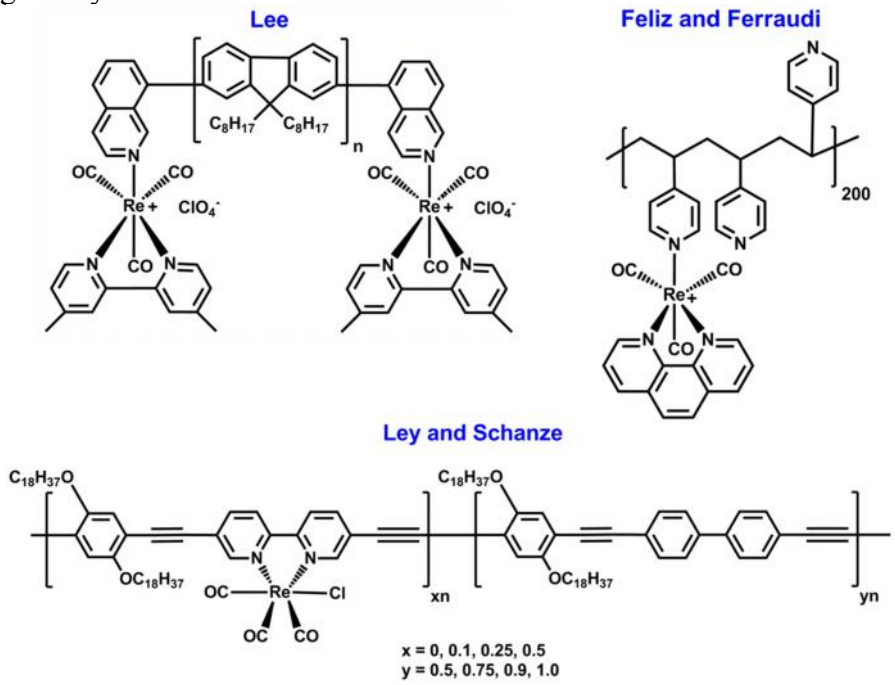

Figure 1.8. Examples of Wolf Type II metallopolymers containing $Re(Bipy)(CO)_3^+$ and $Re(Phen)(CO)_3^+$ moieties.[83,85,90]

In 2004, Tse and coworkers reported a hyperbranched polymer formed by linking two $ReCl(Bipy)(CO)_3$ units with a stilbazole-type ligand.[92] The chemical structure of this Wolf Type II polymer is shown in Figure 1.9. Polymerization is initiated by abstraction of the chloro ligand from the $ReCl(Bipy)(CO)_3$ complex. Subsequent coordination of the stilbazole ligand to the empty coordination site on the Re(I) metal center forms a rhenium bipyridine hyperbranched polymer. Due to the $Re(Bipy)(CO)_3^+$ units within the polymer backbone, self-assembly of polycationic species on a suitably pretreated surface is possible. Atomic force microscopy (AFM) experiments indicate that a monolayer of globular-shaped polymer molecules, on the order of 25-30 nm, self-assembled on the

substrate surface. For this reason, these hyperbranched Re(I)-containing polymers show potential application as building blocks for multilayer ultrathin film devices.

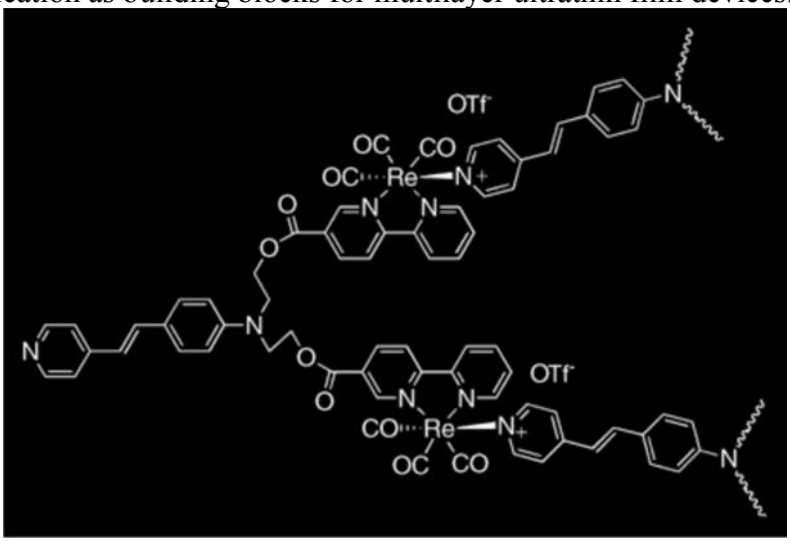

Figure 1.9. Wolf Type II rhenium-containing hyperbranched polymer reported by Tse *et al.* (From reference 92 by permission of John Wiley and Sons).

1.2.3. Wolf Type III Metallopolymers

In a Wolf Type III metallopolymer, the metal center plays a structural role in the architecture of the polymer and is directly in the π-conjugated main chain.[81] Due to incorporation of the metal center within the polymer backbone, direct electronic communication and extremely efficient energy transfer can occur between the metal and the polymer. This section will address classical Wolf Type III systems as well as rhenium(I)-containing coordination polymers and clusters.

In 2008, Yamamoto and coworkers reported the first series of Re(I) linear-shaped oligomers and polymers that can emit in solution at ambient temperatures.[93] Linear-shaped rhenium(I) oligomers and polymers, with bridging bidentate phosphorus ligands, were synthesized by photochemical ligand substitution of $Re(Bipy)(CO)_3^+$ and complexation with bis(diphenylphosphino)acetylene (ac) (Figure 1.10). Oligomers and

polymers containing up to 20 Re(I) units were isolated using size exclusion chromatography (SEC) and characterized by NMR, IR, electrospray ionization Fourier transform mass spectrometry (ESI FTMS), analytical SEC, and elemental analysis. Room temperature solution-state emission was observed for both the oligomers and polymers. In olgiomeric and polymeric systems containing 3 or more Re(I) units, emission at 572 nm was observed and assigned as emission from the ^{3}MLCT excited state of the $Re(Bipy)(CO)_3^+$ moiety. According to analytical SEC and photophysical studies, the linear-shaped rhenium(I) polymers aggregate *intra*molecularly in solutions of acetonitrile.

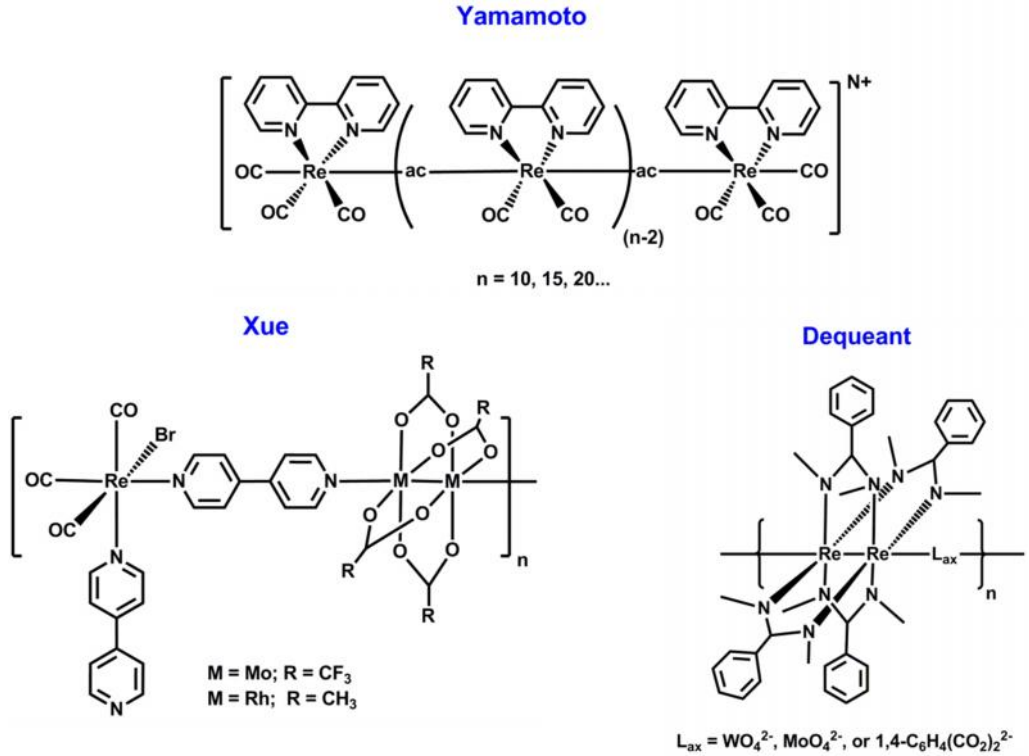

Figure 1.10. Wolf Type III metallopolymers synthesized by Yamamoto,[93] Xue,[94] and Dequeant.[95]

A series of rare earth cations and rhenium (I) cluster anions were prepared and characterized by the Fedorov group in 2008 and 2011.[96,97] As shown in Figures 1.11A and 1.11B, these systems contain tetrahedral and octahedral rhenium(I) cluster cyanides, $[Re_xQ_y(CN)_z]^{4-/3-}$ (x = 4 or 6, y = 4 or 8, z = 6 or 12) (Q = S, Se, Te) that serve as building blocks for the construction of 3-dimensional coordination polymers. These rhenium(I) cyanide clusters were complexed with the aquacations of rare-earth metals, Ln (Ln = La to Yb), to form both 2- and 3-dimensional structures of the general formula $[\{Ln(H_2O)_n\}\{Re_xQ_y(CN)_z\}]\cdot mH_2O$ (n = 3, 4, x = 4 or 6, y = 4 or 8, z = 6 or 12, m = 0, 2, 2.5) (Q = S, Se, Te) with strong covalent Re-CN-Ln interactions. The structures of these coordination polymers were studied and confirmed using single-crystal X-ray diffraction analysis. Magnetic susceptibility studies for Gd- and Er-containing rhenium(I) coordination polymers were studied. Effective magnetic moments of 8.13 μ_B and 10.79 μ_B were found for the Gd and Er coordination polymers, respectively, with weak antiferromagnetic ordering observed at lower temperatures.[96] Likewise, in related studies of rhenium(I)-lanthanide coordination polymers, Jeitschko *et al.* reported the synthesis of a Er_2ReC_2 one-dimensional organometallic $[ReC_2]^{6-}$ polymer embedded in an Er^{3+} ionic matrix.[98]

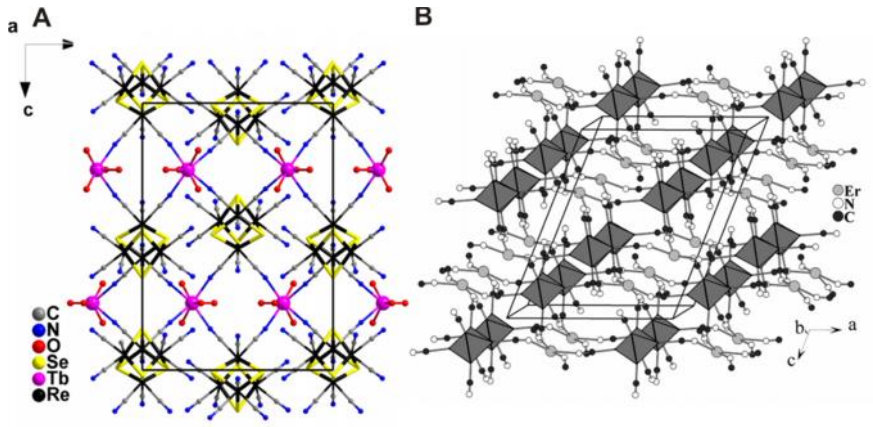

Figure 1.11. (A) Structure of a 3-dimensional rhenium(I) coordination polymer containing Se and Tb (Adapted from reference 97 by permission of Elsevier). (B) Chemical structure of lanthanide(Er1)/rhenium(I)-containing coordination polymer. Polyhedrals are representative of Re_6 clusters. Te, Er2, and O atoms are omitted for clarity (From reference 96 by permission of Elsevier).

Binuclear, mixed metal, linear coordination polymers have been extensively studied and reported.[95,99-120] In particular, Xue *et al.* reported a tetranuclear complex with $Mo_2(O_2CCF_3)_4$ and $Rh_2(O_2CCH_3)_4$ as the building block and [Re(2,2'-Bipy)$(CO)_3$(4,4'-Bipy)]$(CF_3SO_3)_2$ units as the bridging ligand, [(2,2'-Bipy)$(CO)_3$Re(4,4'-Bipy)]$_2$[$M_2(O_2CR)_4$]$(CF_3SO_3)_2$ (M = Mo, R = CF_3; M = Rh, R = CH_3),[94] as shown in Figure 1.10. According to X-ray single crystal analysis of the coordination polymers, strong metal-axial ligand interactions are observed. However, no *intra*molecular electronic communication occurs between the Re(I)-ligands and the central metal-metal unit, due to the less-than-optimal orbital overlap arising from the tilting of the 4,4'-bipyridine ligand. Additionally, Dequeant and Ren reported in 2010 dirhenium(III) coordination polymers, $[Re_2(DMBA)_4(\mu\text{-}O,O'\text{-}X)\cdot 2H_2O]_\infty$ (DMBA = *N,N'*-dimethylbenzamidinate) (X = WO_4^{2-}, MoO_4^{2-}, or $(1,4\text{-}(O_2C)_2C_6H_4)^{2-}$) (Figure 1.10), prepared through slow diffusion of $Re_2(DMBA)_4(NO_3)_2$ solutions in acetonitrile into

aqueous solution of the respective dianion.[95] Previous work by the Ren group in 2005 reported a similar one dimensional $[Re_2(DMBA)_4(\mu\text{-}O,O'\text{-}X)\cdot 2H_2O]_\infty$ (X = WO_4^{2-} or $(1,4\text{-}(O_2C)_2C_6H_4)^{2-}$) polymer displaying near-IR phosphorescence emission.[109]

1.3. APPLICATIONS

1.3.1. Polymer Light-Emitting Diodes (PLEDs)

Light-emitting diodes containing polymeric materials as the active layers (PLEDs) have been intensely studied since the fabrication of the first functioning device utilizing an electroluminescent conducting polymer in 1990.[121] PLEDs containing transition metal complexes, such as rhenium(I), should not only retain the electroluminescence of inorganic materials but also gain the conductivity, thin film processability, and mechanical flexibility typical of conjugated conducting polymers.[1,2] Additionally, incorporation of rhenium(I) ions into the polymeric active layer of light-emitting devices would allow for harvesting of both the singlet and triplet excitons due to the heavy atom effect.[54] Due to the presence of the heavy Re(I) atom, increased mixing of the excited singlet and triplet states is possible. With this singlet-triplet excited state mixing, low efficiencies of current light-emitting devices can be overcome and potentially reach internal efficiencies of 100%.[55]

In 2008, Zhang and coworkers reported a Wolf Type II bipyridine-based aminoalkyl polyfluorene (PFN) copolymer complexed with $ReCl(CO)_5$ post-polymerization, PFN-BpyRe (Figure 1.12).[122] For the fabrication of electronic devices, thin films are often prepared *via* spin-coating. It is crucial that the solvent used for spin-coating the electron injection and transport layers does not dissolve the underlying emissive polymer active layer. Because PFN-BpyRe is soluble in polar solvents such as methanol and DMF and insoluble in common organic solvents traditionally used for spin-

coating emissive active layers, PFN-BpyRe was used as an electron transport and an injection layer in PLEDs. Insertion of a thin layer of PFN-BpyRe polymer between the emissive active layer and cathode resulted in a nearly two-fold increase in the external quantum efficiency of the electroluminescent device.

A PLED utilizing a luminescent rhenium(I) polymer was fabricated by Ng and coworkers in 2001.[123] This Wolf Type II metallopolymer utilized a $ReCl(Phen)(CO)_3$ moiety within a polymeric backbone containing 1,4-divinylbenzene and 2-octoxyl-1,4-divinylbenzene copolymers, as depicted in Figure 1.12. High charge-carrier mobilities were observed for these metallopolymers, indicating potential application as charge transport materials. Single-layer PLED devices of ITO/Re(I) polymer/Al were fabricated and device performance was studied upon application of a DC voltage under a forward bias condition. Devices were found to have an external quantum efficiency of ~0.20 %. Electroluminescent light emission was observed at 570 and c.a. 700 nm, originating from the $\pi \rightarrow \pi^*$ transition of the conjugated main chain and the ^{3}MLCT $d \rightarrow \pi^*$ state of the rhenium(I) complex, respectively. As the rhenium(I) concentration in the metallopolymer was increased, increased quenching of the conjugated main chain emission was observed along with an increase in ^{3}MLCT electroluminescent emission. Additionally, red electrophosphorescent emission has been reported for conjugated bipyridyl fluorine copolymers containing Re(I) tricarbonyl units by Y. Zhang and M. Zhang.[122,124]

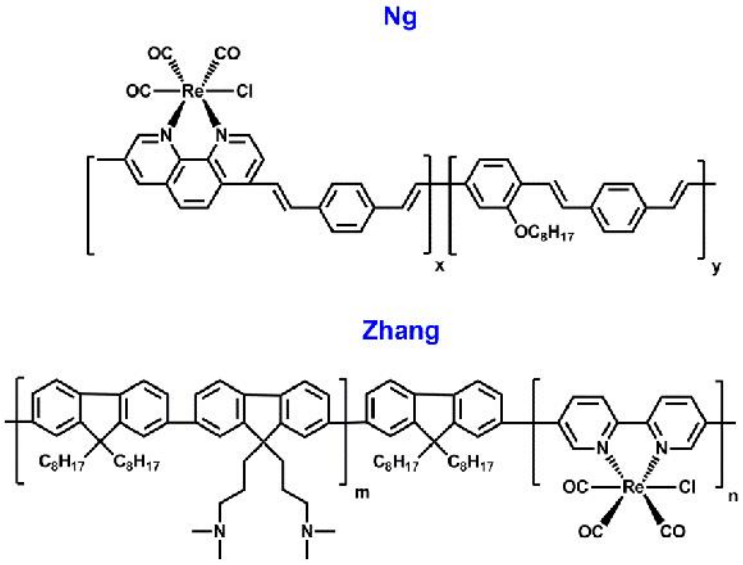

Figure 1.12. Examples of Wolf Type II metallopolymers used in polymer light-emitting diodes (PLEDs).[122,123]

1.3.2. Photovoltaics

Rhenium(I) tricarbonyl complexes incorporating diimine-type ligands have been reported as the active layer in photovoltaic devices due to the absorption profile covering the bulk of the UV-Vis region. Absorption of the $\pi \rightarrow \pi^*$ state of the conjugated polymer backbone at higher energy and metal-to-ligand $d_{Re(I)} \rightarrow \pi^*$ absorption at lower energies lead to broadening and increased coverage of the UV-Vis spectrum. Mak *et al.* desgined a novel low bandgap rhenium(I)-containing polymer for applications in bulk heterojunction photovoltaic devices.[77] This Wolf Type II metallopolymer is comprised of a conjugated copolymer, such as fluorene or cyclopentadithiophene (CPDT), covalently linked with a low bandgap $ReCl(CO)_3$ complex, as shown in Figure 1.13. Incorporation of an *intra*molecular charge transfer unit within the polymeric backbone broadens the absorption band in the UV-Vis spectrum. Complexation with the rhenium(I) complex further broadens the absorption spectrum and reduces the bandgap of the material as much c.a. 0.3 eV. Bulk-heterojunction solar cells were fabricated with the Re(I)-

containing metallopolymer and PCBM and power conversion efficiencies (PCE) were found to range from 0.01-0.03%.

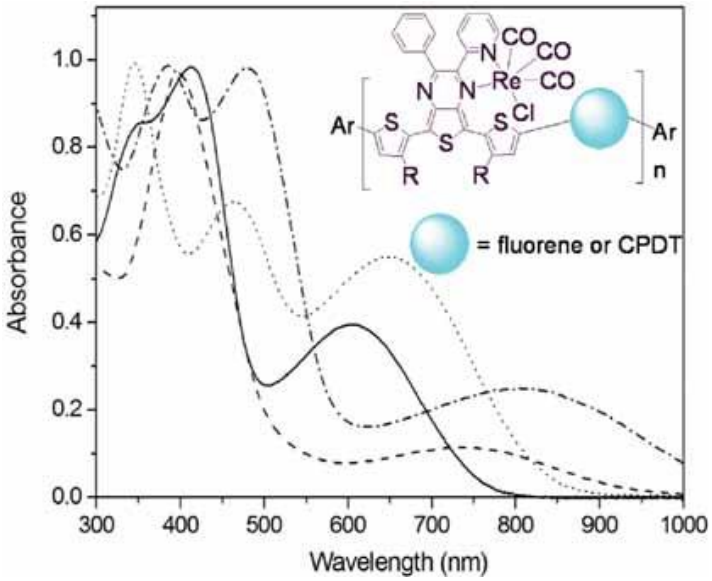

Figure 1.13. Absorbance spectrum and chemical structure of a $ReCl(N\text{-}N)(CO)_3$ metallopolymers containing fluorene or cyclopentadithiophene (CPDT) *intra*molecular charge transfer units: fluorene polymer (solid line), Re-fluorene polymer (dashed line), cyclopentadithiophene polymer (dotted line), and Re-cyclopentadithiophene polymer (dash-dotted line). (From reference 77 by permission of John Wiley and Sons).

Similarly, narrow bandgap Re(I) polymeric systems have been reported by Li, Ho, and Wong in 2011.[69] As shown in Figure 1.14, these heterobimetallic metallopolyyne polymers containing Pt(II) and Re(I) metal centers, bridged by a bithiazole ring, are classified as a Wolf Type II metallopolymer. According to electrochemical experiments and optical spectroscopy, these binuclear metallopolymers have a bandgap as low as 1.85 eV. Incorporation of the $ReCl(CO)_3$ group within the conjugated polymer backbone reduces the bandgap as much 0.25 eV from the parent polymer containing no Re(I) moieties. Current efforts in the Wong lab are focused on constructing solar cell devices of these Re(I)-containing metallopolymers to test the photovoltaic activity.

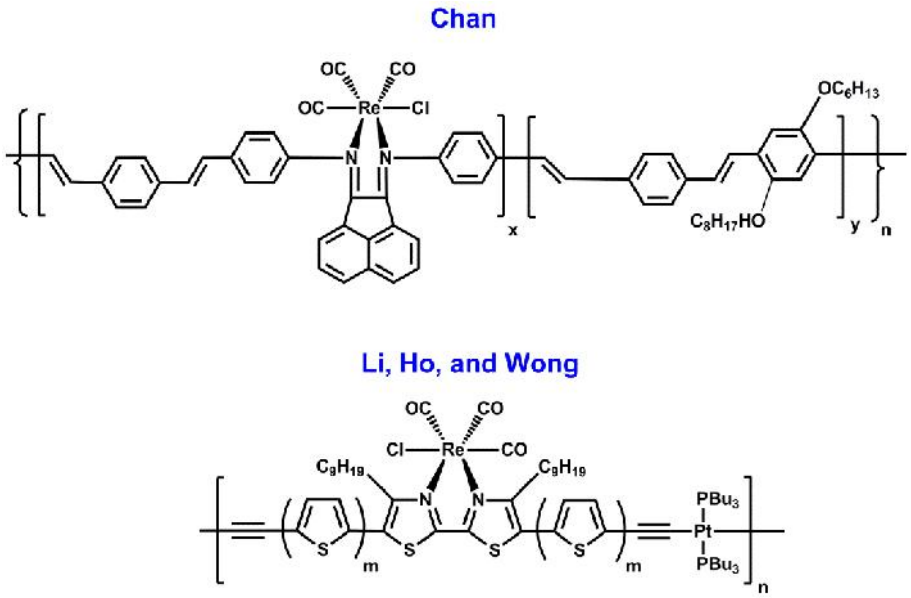

Figure 1.14. Structures of metallopolymers used in photovoltaic devices.[69,125]

A Wolf Type II rhenium(I)-containing metallopolymer was reported by Tse and coworkers as the active layer in photovoltaic devices.[126] Hyperbranched polymers containing a rhenium(I) tricarbonyl bis(stilbazoylimino)acenaphthene complex, with the stilbazoylimino groups serving as dinitrogen bidentate ligands to the rhenium(I) metal center, were prepared and characterized by gel permeation chromatography, laser light scattering, and atomic force microscopy. Polymerization was initiated by removal of the chlorine from the ReCl(stilbazoyliminio)$(CO)_3$ complex *via* $AgSO_3CF_3$. Due to the polycationic nature of these polymers, multilayered films were prepared by layer-by-layer electrostatic self-assembly. From these films, ITO/(polymer/PTEBS)$_{80}$/Al photovoltaic devices were fabricated. Unfortunately, extremely poor power conversion efficiencies, on the order of 10^{-4}%, were observed, likely due to the low fill factors and short circuit currents.

Chan *et al.* reported a *p*-phenylenevinylene polymer containing chlorotricarbonyl bis(phenylimino)acenaphthene rhenium(I) units in the conjugated main chain, as shown

in Figure 1.14.[125] This Wolf Type II metallopolymer shows photosensitizing properties in multilayered photovoltaic devices. The photocurrent response of the rhenium(I)-containing polymer was studied and found to be dependent upon the rhenium(I) content in the polymer, as controlled by the amount of rhenium(I) monomer feed ratio in the polymerization. Solar cell devices were fabricated by layering the Re(I) polymer between PEDOT:PSS and PTCDI, a hole transport polymer and electron transport material, respectively. A power conversion efficiency of 0.06% was measured for devices containing this Re(I) metallopolymer as the photosensitizing active layer. However, an extremely low fill factor of 0.2 was observed and attributed to slow charge transport and high recombination.

1.3.3. Electrocatalysts

Both rhenium(I) tricarbonyl small molecules and metallopolymers serve as efficient electrocatalysts for CO_2 reduction.[36,41,45-47,127-137] Catalytic reduction of CO_2 to CO is an important issue that would both recycle CO_2 and produce a renewable, useable liquid fuel, such as methanol, and thus balance the carbon cycle.[138,139] Carbon monoxide, produced from the reduction of CO_2, can be used to prepare H_2, *via* the water-gas shift reaction. Synthesis gas, CO and H_2, can then be converted to methanol liquid fuel through the Fischer-Tropsch process.[140] Electrocatalytic activity towards CO_2 reduction is identified in a cyclic voltammogram (CV) by an increase in reductive current upon moving from an atmosphere of N_2 to a CO_2-saturated environment. Additionally, electrocatalytic activity is identified by an anodic potential shift of the reduction wave and a loss of reversibility in the electrochemical wave under a CO_2-saturated environment due to the reaction between CO_2 and the electrocatalyst.[141] Electrode-confined metal-containing polymers offer advantages over traditional small molecule electrocatalysts

such as easier recovery of reduction products from the catalyst, stabilization of the catalyst, increased catalytic reactivity due to the elimination of normal solution deactivation pathways, and use of smaller quantities of catalyst for efficient CO_2 reduction.[41,136]

Seminal work by Cabrera *et al.* in 1986 reported an electropolymerizable $ReCl(vbipy)(CO)_3$ (vbipy = 4-vinyl-4'-methyl-2,2'-bipyridine) (Figure 1.15) monomer onto metallic electrodes, such as Pt, and surface-modified semiconductor electrodes, such as single crystal p-Si and polycrystalline thin films of p-WSe_2.[135] Electrocatalytic and photocatalytic reduction of the Re(I) metallopolymer on the Pt electrode gives large turnovers of ~600 upon illumination and under a CO_2-rich atmosphere. Gas chromatographic (GC) analysis of the reduction product indicates a near quantitative yield of CO with current efficiencies greater than 95%. Electrocatalytic reduction of CO with $ReCl(vbipy)(CO)_3$ on a surface modified p-WSe_2 semiconductor electrode gives a lower turnover number of 450. However, electrocatalytic reduction on this p-WSe_2 electrode selectively produces CO, as confirmed by GC analysis.

Two reports of electrocatalytic reduction of CO_2 with rhenium(I) tricarbonyl metallopolymers have been reported by O'Toole and coworkers.[41,130] In 1985, O'Toole electropolymerized a $ReCl(vbipy)(CO)_3$ complex (vbipy = 4-vinyl-4'-methyl-2,2'-bipyridine), depicted in Figure 1.15, onto a Pt disc electrode.[41] This electrode-confined metallopolymer films showed 20-30 times more turnovers per site than the corresponding $ReCl(Bpy)(CO)_3$ monomer. Additionally, the metallopolymer films selectively reduce CO_2 to CO with no CO_3^{2-} present, unlike the $ReCl(Bpy)(CO)_3$ monomer which forms equal amounts of CO and CO_3^{2-}.[47] In 1989, O'Toole reported a more detailed electrocatalytic study of the aforementioned $ReX(vbipy)(CO)_3^n$ ($X = Cl^-$, n = 0 or X = CH_3CN, n = 1) electrode-confined metallopolymer. In a more comprehensive analysis of

the reduction products, CO was confirmed to be the major reduction product. Furthermore, formation of oxalate was detected and speculated to occur through a bimolecular carbon-carbon coupling pathway.[130] Electrochemical kinetic studies indicate that that the rate determining step in CO_2 reduction occurs in the chemical reaction between the reduced Re(I) tricarbonyl complex and CO_2. However, as the thickness of the electrode-confined film increases, electron transport to the catalytic sites of the polymer becomes the rate determining step.[130]

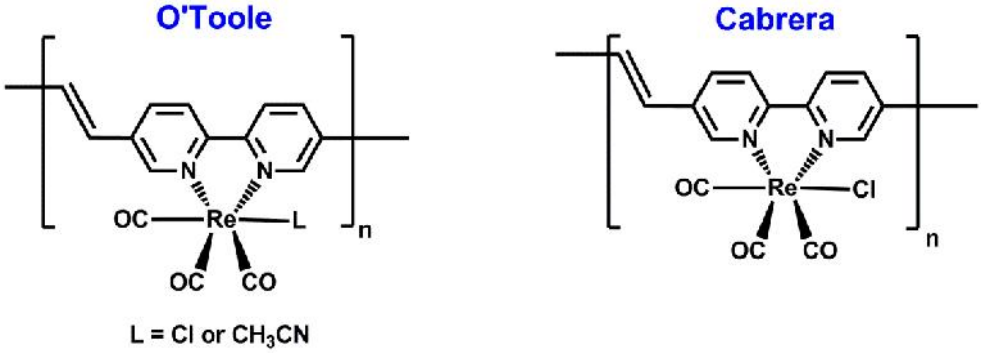

Figure 1.15. Vinylbipyridine rhenium-containing metallopolymers synthesized by O'Toole[41,130] and Cabrera[135] for electrocatalytic reduction of CO_2.

Cosnier and coworkers designed and synthesized a chlorotricarbonyl rhenium(I) complex with a pyyrole-substituted 2,2'-bipyridine ligand, as shown in Figure 1.16.[137] In this study, 1, 2, or 4 pyrrole groups were appended to the bipyridine ligand, serving as the moiety for electrochemical polymerization. Electrode-confined films comprised of monomers containing 1 pyrrole group are nearly as stable as monomers containing 2 pyrrole groups. Metallopolymers with lower reduction potentials were found to be more stable but show no electrocatalytic activity towards CO_2 reduction. For the metallopolymer films showing electrocatalytic activity, current efficiencies ranged from 69-98.5% with essentially equimolar concentrations of CO and CO_3^{2-} produced from the

reduction of CO_2. Additionally, Cosnier *et al.* correlated the maximum catalytic efficiency with an optimum film thickness.[137]

Cheung and coworkers, in 2009, reported $ReCl(CO)_3(\kappa^2$-*N,N*-PPP), a chlorotricarbonyl rhenium(I) complex with a 2,2'-dipyridylamine ligand functionalized with a pendant pyrrole group (*N*-(3-*N,N'*-bis(2-pyridyl)propylamino)pyrrole, PPP) at the amine nitrogen bridge between the two pyridines of the ligand (Figure 1.16).[136] Electrochemical polymerization of the pyyrole group produced electrode-confined films of $ReCl(CO)_3(\kappa^2$-*N,N*-PPP) that showed electrocatalytic activity towards the reduction of CO_2. FTIR spectroelectrochemical studies suggest CO absorption, as made evident by an increase in the carbonyl stretch at 2138 cm^{-1}. No stretches for other reduction products, such as formate, were detected, indicating that this rhenium(I)-containing metallopolymer selectively electroreduces CO_2 to CO.

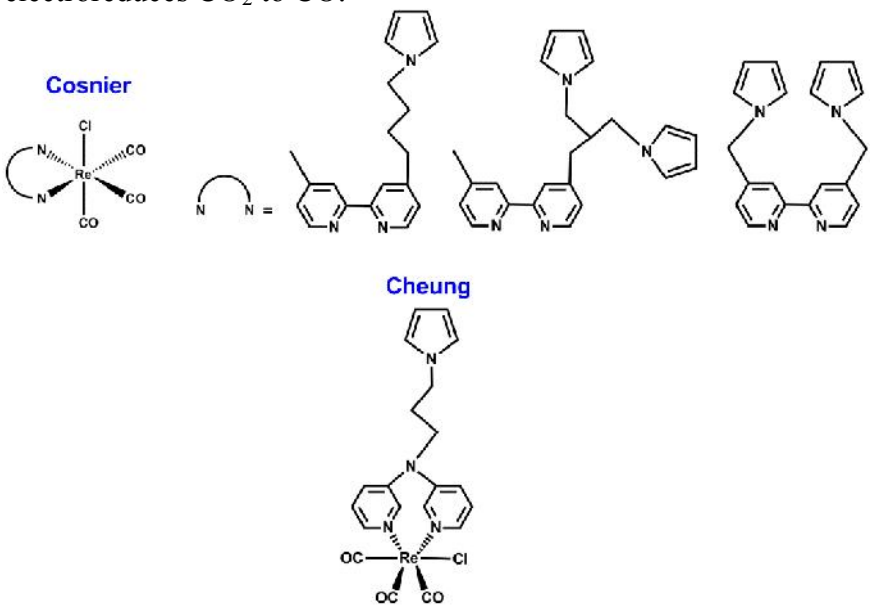

Figure 1.16. Electropolymerizable pyyrole-functionalized $ReCl(Bipy)(CO)_3$ metallopolymers showing electrocatalytic activity towards CO_2 reduction.[136,137]

Current efforts in our group are focused on the development of rhenium(I)-containing metallopolymer films utilizing bidentate diimine-type ligands such as 2,2'-bipyridine (Bipy), 1,10-phenanthroline (Phen), and a tridentate 2,6-bis(pyrazolyl)pyridine (BPP) that behaves as a bidentate chelate. A series of facial tricarbonyl rhenium(I) diimine-type monomers and corresponding Wolf Type II metallopolymers are depicted in Figure 1.17A. Appended to the ligands are 3,4-ethylenedioxythiophenes (EDOTs), a thiophene derivative, for electropolymerization of the metal complexes. Electrocatalytic CO_2 reduction by these electrode-confined metallopolymer films was observed, as displayed in Figure 1.17B. An increase in the reductive current was observed going from an atmosphere of N_2 to a CO_2-rich environment, indicative of CO_2 reduction (Figure 1.17B).

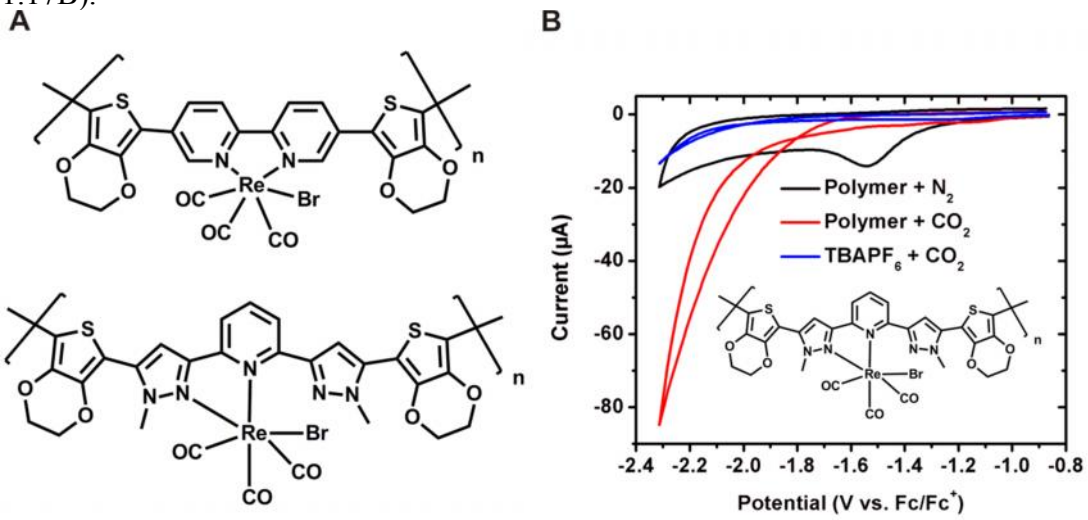

Figure 1.17. (A) Wolf Type II metallopolymers for electrocatalytic reduction of CO_2. (B) Cyclic voltammogram of poly-ReBr(EDOT$_2$-BPP)(CO)$_3$ polymer under N_2- and CO_2-rich atmospheres.

1.3.4. Radiopharmaceuticals

Saatchi and Häfeli designed and synthesized polylactic acid "polymers with a grip" for binding of $[Re(CO)_3]^+$ moieties with potential application in radiolabeling and

radiotherapy of cancer.[142] The $[Re(CO)_3]^+$ moiety is remarkably stable and kinetically inert and thus, useful for radiopharmaceuticals in cancer patients. Moreover, polylactic acid is one of three FDA approved biodegradable polymers. Therefore, a $[Re(CO)_3]^+$-containing polylactic acid polymer shows potential application as a biodegradable polymers for imaging and treatment of tumors. In this Wolf Type I metallopolymer, $_L$-lactide is functionalized with a hydroxyl group, for initiation of ring-opening polymerization, and a trinitrogen-donor, tridentate bis(pycolylamine) group for complexation with a rhenium(I) tricarbonyl moiety (Figure 1.18). The resulting metallopolymer was characterized by GPC and MALDI-TOF mass spectrometery. A break in symmetry of the polylactic acid backbone upon complexation with $[Re(CO)_3]^+$ was confirmed by NMR. Additionally, confirmation of the rhenium(I) metal center in the polymeric backbone was confirmed by shifts in the carbonyl stretching frequency, as determined by infrared spectroscopy, and a shift in polymer mass *via* MALDI-TOF.

Kunz and coworkers designed and synthesized a $Re(CO)_3^+$-labeled copolymer for uses in radiopharmaceuticals, as displayed in Figure 1.18.[143] In this system, a copolymer of *N*-(2-hydroxypropyl)methacrylamide (HPMA), namely HPMA-*co*-bis(2-pyridylmethyl)-4-vinyl-benzylamine was chosen due to water solubility, biocompatibility, and non-immunogenicity. The copolymer was complexed with $[N(n\text{-}Bu)_4]_2[Re(CO)_3Br_3]$ at the bis(2-pyridylmethyl)amine group and subsequently studied *via* IR spectroscopy to confirm that the $Re(CO)_3^+$ group was tethered to the copolymer. This $Re(CO)_3^+$-labeled copolymer was found to have optimal molecular weights for effective permeability and passive accumulation in solid tumors. Furthermore, IR spectroscopy confirmed that the $Re(CO)_3^+$ labels were not lost in aqueous media after a Soxhlet extraction.

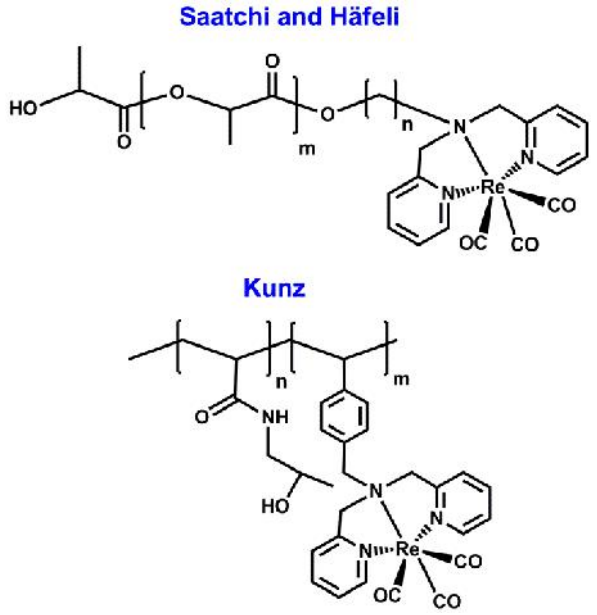

Figure 1.18. Chemical structures of rhenium(I)-containing metallopolymers used in radiopharmaceuticals, as reported by Saatchi and Häfeli[142] and Kunz.[143]

1.4. SUMMARY AND OUTLOOK

We have highlighted and reviewed the area of rhenium-containing metallopolymers and classified each polymer according to the Wolf Type I, II, and III system. Much of these polymeric systems contain rhenium(I) metal centers bound to three carbonyls and a dinitrogen donor ligand such as 2,2'-bipyridine, 1,10-phenanthroline, and derivatives thereof. Polymers containing an organometallic rhenium(I) moiety offer advantages over polymers comprised of solely organic compounds such as increased harvesting of singlet and triplet excitons for increased quantum efficiencies and potential for catalytic activity. Chemical incorporation of the rhenium(I) metal center directly within the polymer is favored over materials in which the rhenium complex is simply blended with the polymer matrix. Incorporation of rhenium in the polymer allows for direct electronic communication and energy transfer between the metal and the polymeric backbone. This direct incorporation of the metal

precludes any phase segregation or aggregation of the rhenium(I) metal center that is generally observed in doped polymeric systems. Current efforts are focused on developing low bandgap rhenium(I)-containing metallopolymers for photovoltaic devices. Additionally, rhenium metallopolymers that can electrocatalytically reduce carbon dioxide with increased efficiencies and high turnover frequencies are currently being developed.

Chapter 2: Small Molecules and Conducting Metallopolymers of Rhenium(I) Tricarbonyl Diimine-Type Complexes for Luminescent and Electrocatalytic Applications

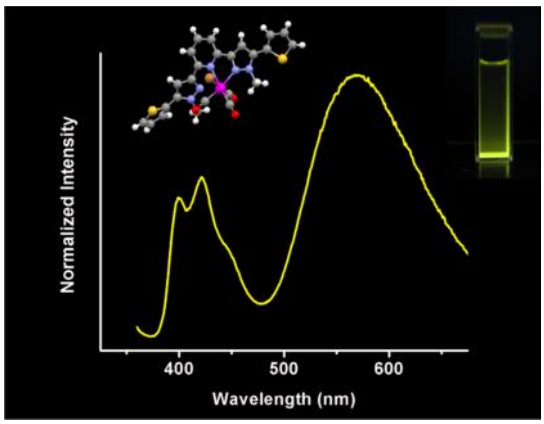

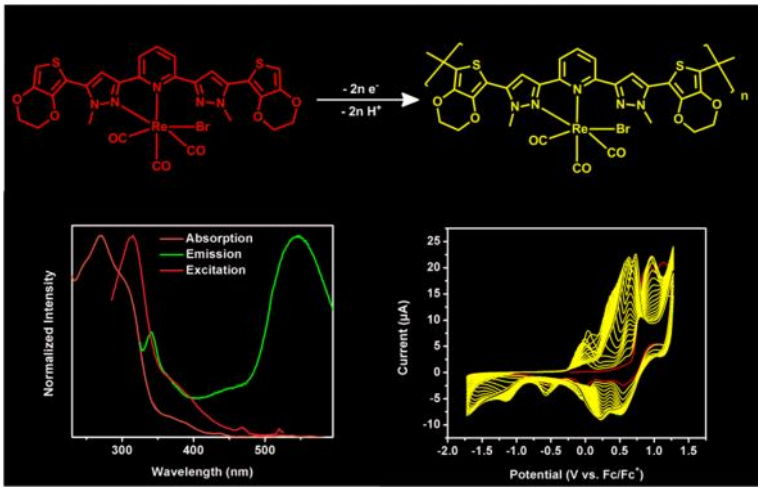

2.1. INTRODUCTION

Rhenium diimine complexes have distinct and interesting photophysical properties. In particular, *fac*-ReX(L)$(CO)_3$, where L is a bidentate diimine ligand and X is a halogen, are good phosphorescent materials due to emission from the triplet metal-to-ligand charge transfer (^{3}MLCT) excited state.[19-22,24-26,43,144,145] In general, rhenium(I), like other d^6 metals, produce intense phosphorescent emission because of the heavy atom effect. The heavy atom effect facilitates sufficient mixing of excited singlet and triplet states, giving rise to relatively long-lived microsecond excited state lifetimes and large quantum yields of emission.[42,146-148] Tricarbonyl diimine rhenium(I) complexes are advantageous not only due to efficient phosphorescent emission and microsecond excited state lifetimes, but also because of chemical inertness and the ability to undergo redox chemistry.[124,149,150]

Because of intense visible region emission, ReX(L)$(CO)_3$-type complexes have various applications. For example, rhenium(I) diimine complexes show promise in organic light-emitting diodes (OLEDs). OLED devices of other transition metal complexes, such as iridium, platinum, and osmium, have been reported.[28-31] Phosphorescent rhenium(I) complexes are also chemically inert and thus, have found uses as biological probes.[32-34] Additionally, these complexes are used as photocatalysts and moieties for luminescent and redox-active supramolecular systems.[35-40,151]

Tricarbonyl rhenium(I) diimine complexes can electrocatalytically reduce CO_2 to CO upon applied voltage.[46,47,127-129,135,151] Catalytic reduction of CO_2 to CO is an important two-fold challenge that would both recycle CO_2, a greenhouse gas, and produce a renewable and useable fuel, thus balancing the carbon cycle.[138,139] Formation of CO from the reduction of CO_2 can be used to prepare H_2 (synthesis gas), *via* the water-gas shift reaction. Through the Fischer-Tropsch process, liquid fuels can then be

synthesized from CO and H_2.[140] Current efforts are focused on designing electrocatalysts that can catalyze the reduction of CO_2 to CO with high efficiency and selectivity at low overpotentials ($V_{applied}$- E^0(products/substrates). Electrocatalytic activity can be identified in a cyclic voltammogram (CV) by an anodic potential shift and large increase in the reductive current of the electrocatalyst. Additionally, the reversibility of the redox couple of the electrocatalyst is lost due to the reaction between CO_2 and the electrocatalyst.[141]

Electrocatalytic reduction of CO_2 to CO by a rhenium(I) diimine-type complex was first reported by Lehn *et al.* in 1984 with a $ReCl(CO)_3$(bipy) complex (bipy = 2,2'-bipyridine).[36] A series of derivatives of this parent complex, in particular compounds with functionalized bipyridine ligands such as $ReCl(CO)_3$(bipy-*t*Bu), $ReCl(CO)_3$(bipy-COOH), and $ReCl(CO)_3$(bipy-OMe), were studied for electrocatalytic reactivity by Kubiak and coworkers in 2010.[46] The mechanism of CO_2 reduction is believed to occur through a one- or two-electron process with some studies suggesting that these one- and two-electron processes happen simultaneously.[45,46,127,130] Initially, the $ReCl(CO)_3$(bipy) complex undergoes a one electron reversible reduction, with electron density mostly centered on the bipyridine ligand.[127-134] In a one-electron catalytic pathway, loss of a chlorine forms a coordinatively unsaturated complex, $[Re(CO)_3(bipy)]^{\cdot}$. Coordination of CO_2 to the unsaturated rhenium metal center is quickly followed by reduction of the bound CO_2 to CO in an additional one-electron process. In a two-electron pathway, a one-electron reduction of Re(I) to Re(0) occurs after sequential loss of the chlorine ligand to form the anionic complex, $[Re(CO)_3(bipy)]^{-}$. Carbon dioxide then binds to the anionic five-coordinate rhenium complex. In another one-electron reduction and in the presence of an oxide ion acceptor, CO is formed.[47,127,130] Conversely, the mechanism suggested by Lehn and coworkers propose a loss of CO to form $[ReCl(bipy)(CO)_2]^{\cdot-}$ after the initial one-electron reduction of the neutral complex.[45]

Luminescent rhenium(I) tricarbonyl moieties have been incorporated into polymeric systems for the development of light-emitting materials for solid-state lighting applications.[122,124] Polymer light-emitting diodes (PLEDs) have been a forerunner in solid-state lighting technology since the fabrication of the first functioning device utilizing a conducting polymer as the electroluminescent material in 1990.[121] These polymer based materials offer many advantages over conventional inorganic electroluminescent materials such as ease of processing, mechanical strength and flexibility, and low cost of fabrication.[1,2] Previously, PLEDs have been fabricated by doping a phosphorescent metal complex into a polymer. However, devices of these metal complex-doped polymers often have low efficiencies and inefficient stability due to phase separation and poor energy transfer from polymer to dopant.[8,152] These problems can be remedied by incorporating the metal center directly into the polymer backbone. This covalent coupling of the metal and the polymer backbone promotes efficient energy transfer from the polymer to the metal center.

We have prepared a series of facial tricarbonyl rhenium(I) diimine-type monomers and corresponding metallopolymers, as shown in Scheme 2.1. The dinitrogen donor ligands are 2,2'-bipyridine (Bipy) and 1,10-phenanthroline (Phen) or a trinitrogen 2,6-bis(pyrazolyl)pyridine (**BPP**) ligand that behaves as a bidentate chelate. Appended to the ligands are thiophene (Th) or 3,4-ethylenedioxythiophene (EDOT), a thiophene derivative, for electropolymerization of the metal. In these types of metallopolymeric systems, the metal is covalently coupled to the polymer backbone allowing for direct communication between the metal center and organic polymer. Ethylenedioxythiophene (EDOT)-functionalized 2,2'-bipyridine (**$EDOT_2$-Bipy**)[153], 1,10-phenanthroline (**$EDOT_2$-Phen**)[154], 2,6-bis(pyrazolyl)pyridine (**$EDOT_2$-BPP**), and thiophene-functionalized 2,6-bis(pyrazolyl)pyridine (**Th_2-BPP**) ligands were complexed with tricarbonyl rhenium(I)

moieties to form $ReBr(Th_2\text{-}BPP)(CO)_3$ (**1**), $Re(t\text{-}BuNC)(Th_2\text{-}BPP)(CO)_3$ (**2**), $ReBr(EDOT_2\text{-}BPP)(CO)_3$ (**3**), $ReBr(BPP)(CO)_3$ (**4**), $ReBr(EDOT_2\text{-}Bipy)(CO)_3$ (**5**), and $ReBr(EDOT_2\text{-}Phen)(CO)_3$ (**6**). To thoroughly study our $ReBr(Th_2\text{-}BPP)(CO)_3$ and $ReBr(EDOT_2\text{-}BPP)(CO)_3$ systems, model ligand and complex systems, **BPP** and $ReBr(BPP)(CO)_3$ (**3**), were synthesized and studied. The EDOT group of monomers **3**, **5**, and **6** can readily be electropolymerized to form **poly-3**, **poly-5**, and **poly-6**. In addition to ease of electropolymerization, functionalization of the aforementioned ligands with thiophene and EDOT enhance the photophysical properties of the ligand and corresponding rhenium(I) metal complexes. Incorporation of thiophene or EDOT into the diimine-type ligand extends the conjugation of the system and lowers the triplet excited state energy level of the ligand. Additionally, spin-orbit coupling from the heavy sulfur atoms of the thiophenes increases the population of the triplet excited state, thereby enhancing the phosphorescent quantum yield. In fact, work by de Bettencourt Días *et al.* demonstrated that functionalization of isophthalic acid with thiophene lowered the triplet state energy by 5000 cm^{-1}, on average.[155] In addition to exhibiting luminescence, these monomers and corresponding metallopolymers show electrocatalytical activity towards the reduction of CO_2.

Scheme 2.1. Series of electropolymerizable tricarbonyl rhenium(I) diimine-type complexes

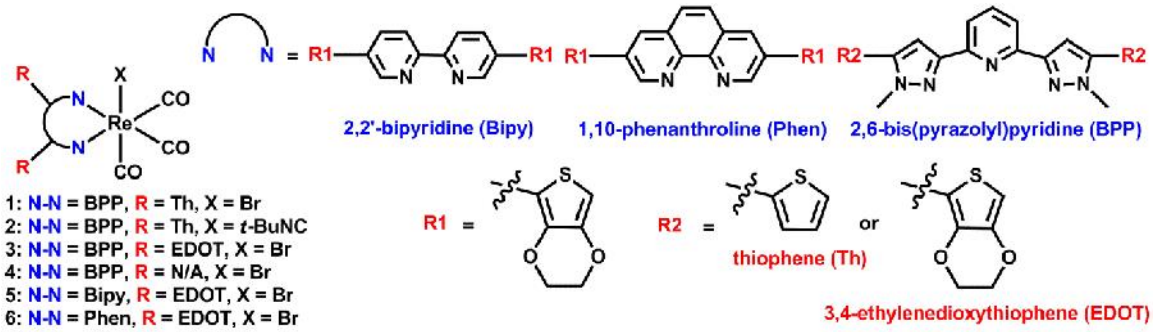

2.2. EXPERIMENTAL

2.2.1. Instrumentation

2.2.1.1. General Methods

Air- and moisture-sensitive reactions were carried out in flame-dried glassware using standard Schlenk techniques under an inert nitrogen atmosphere. All chemicals were purchased from commercial sources and used as received. Dry solvents were dried using an Innovative Technology, Pure Solv solvent purifier with a double purifying column. ^{1}H NMR (400 MHz) and ^{13}C {^{1}H} NMR (100 MHz) spectra were obtained on a Varian (400 MHz) spectrometer and were referenced to residual solvent peaks. All peak positions are given in ppm and coupling constants are reported in Hz. Low-resolution and high-resolution mass spectrometry was carried out by a Thermo Finngan TSQ 700 and Waters Autospec Ultima, respectively. Melting points were recorded with an OptiMelt Automated Melting Point System with digital image processing technology from Stanford Research System (SRS, Sunnyvale, CA). Elemental analysis was performed by QTI, Whitehouse, NJ (www.qtionline.com). X-ray photoelectron spectroscopy (XPS) was carried out on a PHI 5700 XPS system equipped with dual Mg X-ray source and

monochromatic Al X-ray source complete with depth profile and angle-resolved capabilities.

2.2.1.2. Crystal Structure Determination

The single–crystal diffraction data were collected on a AFC12 diffractometer with a Saturn 724+ CCD, a Nonius Kappa CCD diffractometer, or a Rigaku SCX-Mini diffractometer with a Mercury CCD using a graphite monochromator with MoKα radiation (λ = 0.71073 Å). Absorption corrections were applied using multi-scan technique using either Abscor[156] for the Rigaku data or Scalepack[157] for the Nonius data. Data reduction were performed using the Rigaku Americas Corporation's Crystal Clear version 1.40.[158] The structures were solved by direct methods and refined anisotropically using full-matrix least-squares methods with the SHELX 97 program package.[159] The coordinates of the non-hydrogen atoms were refined anisotropically, while hydrogen atoms were included in the calculation isotropically but not refined. Neutral atom scattering factors and values used to calculate the linear absorption coefficient are from the International Tables for X-ray Crystallography (1992).[160] Crystal data collection and structure refinement details are given in Tables 2.4, 2.10, 2.14, 2.6, 2.8, 2.12, 2.16, and 2.18 for **Th_2-BPP**, **$EDOT_2$-BPP**, **BPP**, **1**, **2**, **3**, **4**, and **5**, respectively (Supplemental Data). Selected bond lengths and angles for **Th_2-BPP**, **$EDOT_2$-BPP**, **BPP**, **1**, **2**, **3**, **4**, and **5** are given in Tables 2.5, 2.11, 2.15, 2.7, 2.9, 2.13, 2.17, and 2.19, respectively (Supplemental Data).

2.2.1.3. Electrochemistry

Electrochemical syntheses and studies were performed in a dry-box under an atmosphere of nitrogen using a GPES system from Eco. Chemie B. V. All the electrochemical experiments were carried out in a three-electrode cell with a $Ag/AgNO_3$

reference electrode (silver wire dipped in a 0.01 M silver nitrate solution with 0.1 M [(*n*-Bu)$_4$N]$^+$[PF$_6$]$^-$ in CH$_3$CN), a Pt working electrode, and a Pt wire coil counter electrode. Potentials were relative to this 0.01 M Ag/AgNO$_3$ reference electrode. Ferrocene was used as an external reference to calibrate the reference electrode before and after experiments were performed and that value was used to correct the measured potentials. All electrochemistry and electropolymerizations were performed in dichloromethane (DCM) or acetonitrile (ACN) solutions using 0.1 M [(*n*-Bu)$_4$N]$^+$[PF$_6$]$^-$ (TBAPF$_6$) as the supporting electrolyte. The TBAPF$_6$ was purified by recrystallization three times from hot ethanol before being dried for 3 days at 100-150 °C under active vacuum prior to use. Polymer films were prepared on Delta Technologies ITO-coated glass for spectroscopic measurement and on stainless steel for XPS. Electrosyntheses of the polymer films were performed from monomer solutions by continuous cycling between -1.5 and 1.5 V (vs. Fc/Fc$^+$) at a scan rate of 100 mV/s. The films obtained were then washed with copious amounts of fresh DCM before further experiments.

Electrocatalysis experiments were conducted in a three-electrode cell with a Ag/AgNO$_3$ reference electrode, a glassy carbon working electrode (3 mm in diameter from BASi), and a Pt wire coil counter electrode. All electrocatalytic experiments were performed in a dry-box with 0.1 M TBAPF$_6$ in dry ACN as the supporting electrolyte. All electrocatalysis experiments with CO$_2$ were performed at gas saturation (~ 0.25 M)[161,162] in ACN by purging solutions with CO$_2$ for 3 minutes before CVs were taken. Electrocatalytic studies were performed by cycling three times between ~-2.3 V and -0.6 V (vs. Fc/Fc$^+$) at a scan rate of 100 mV/s. Re(I) complex solution concentrations ranged from 0.1 mM to 0.6 mM but were most often limited by the solubility of the monomer in ACN. Studies to determine the electrocatalytic activity of Re(I) metallopolymers were performed on glassy carbon electrode-confined films.

Rotating disk experiments were performed by a Metrohm Autolab RDE-2 electrode rotator with a Teflon-shrouded glassy carbon rotating disk electrode (3 mm in diameter from Metrohm), a Pt wire counter electrode, and a $Ag/AgNO_3$ reference electrode. Experiments were performed in a rotating disk electrochemical cell with 25 mL of 0.1 mM to 0.6 mM solutions of the Re(I) complex in 0.1 M $TBAPF_6$ in dry ACN. CVs were taken in triplicate from 200-2000 rpm rotation rates at potentials from ~ -2.3 V to -0.6 V (vs. Fc/Fc^+) at a scan rate of 100 mV/s. The concentration of each solution was confirmed by UV-Vis spectroscopy using Beer's Law and the molar absorptivity of the Re(I) complex in 0.1 M $TBAPF_6$ in ACN. Levich-Koutecky plots were constructed by tabulating the absolute peak currents of the two reduction peaks observed for every rotation rate. A good linear plot of inverse current *versus* the negative square root of the rotation rate for each reduction peak indicates usable data for the calculation of the diffusion coefficient, *D*. Data points from the plots were then inserted into the Levich-Koutecky equation, equation (1), to calculate the diffusion coefficient for the neutral and singly reduced species, respectively.[163]

$$i_L = (0.620)nFAD^{2/3}\omega^{1/2}v^{-1/6}C \quad (1)$$

In the Levich-Koutecky equation, i_L is the Levich current from the rotating disk experiment, n is the number of electrons (1 for the first reduction, 2 for the second reduction), F is Faraday's constant, A is the electrode area (determined using a known concentration of ferrocene), ω is the rotation rate in rad s^{-1}, v is the kinematic viscosity of the solution (0.00442 cm^2 s^{-1} for 0.1 M $TBAPF_6$ in ACN[164]), and C is the concentration of the Re(I) complex in solution (obtained from UV-Vis spectroscopy and the molar absorptivity). The second order rate constant, k, for CO_2 reduction was calculated using the diffusion coefficient and additional information, according to equation (2).

$$i_c = nFA[\text{cat}](Dk[\text{Q}]^y)^{1/2} \quad (2)$$

In eqn 2, i_c is the catalytic current observed in the CV, n is the number of electrons (2 for the reduction of CO_2 to CO), F is Faraday's constant, A is the electrode area (determined using a known concentration of ferrocene), [cat] is the concentration of the Re(I) complex in solution (obtained from UV-Vis spectroscopy and the molar absorptivity), D is the diffusion coefficient of the singly reduced active catalytic species, k is the rate constant (the variable of interest), Q is the concentration of the CO_2 substrate (0.25 M, the gas saturation of CO_2 in ACN[161,162]), and y is the order of the CO_2 substrate in this reaction (1 in this case).

2.2.1.4. Spectroscopy

All spectroscopic data were obtained in methylene chloride solutions unless otherwise noted. Infrared spectra were recorded using a Nicolet IR 200 FTIR spectrophotometer. Absorption spectra were recorded on a Varian Cary 6000i UV-VIS-NIR spectrophotometer with Starna Quartz fluorometer cells with a pathlength of 10 mm. Luminescence measurements were recorded on a Photon Technology International QM 4 spectrophotometer equipped with a 6-inch diameter K Sphere-B integrating sphere for quantum yield measurements. Quantum yield was calculated by dividing the area under the emission peak of the complex by the difference between the area under the excitation peak of the sample from that of a blank solution ($A_{em,\ sample}$ / ($A_{ex,\ blank}$ - $A_{ex,\ sample}$), where A = area under peak).[165] Measurements at 77 K were recorded using an optical liquid nitrogen Dewar sample holder. Low-temperature samples were made in 2-methyltetrahydrofuran in quartz 4 mm outer diameter EPR tubes. Ligand triplet state energies were calculated by using the wavelength corresponding to the onset of ligand phosphorescence and converting to cm^{-1}. Ligand phosphorescent data and lifetimes were acquired from airfree samples made in deoxygenated freeze-pump thawed (four cycles)

2-methyltetrahydrofuran in quartz 4 mm outer diameter EPR tubes. Radiative and non-radiative rate constants (k_r and k_{nr}) were calculated using equations (3) and (4), respectively.[148]

$$k_r = \Phi_{em} / \tau \quad (3)$$

$$k_{nr} = (1- \Phi_{em}) / \tau \quad (4)$$

2.2.1.5. Computational Methods

The molecular geometry of **1** was optimized at the DFT level of theory using the B3LYP hybrid functional[166] with the Gaussian 03 and GaussView 4.1 programs.[167] The basis set employed was the SDD basis set utilizing the default parameters included in this program.[168] The geometric parameters of the optimized geometry determined by this method closely matched those determined by single-crystal X-ray diffraction. The NMR shielding tensors were then calculated in a series of single-point energy calculations using the optimized structure as a starting point and systematically varying the torsion angle between the central pyridine ring and the unbound pyrazole ring leaving all other geometric parameters unchanged. The torsion angle was varied between -180° and 180° performing a calculation at 20° intervals. The relative chemical shifts were determined by calibrating the calculated NMR shielding tensors to the value determined for TMS which was calculated using the same computational method.[169]

2.2.2. Synthesis

The bis(pyrazolyl)pyridine, **BPP**, ligand was synthesized according to a literature procedure.[170] Starting material 2-acetyl-3,4-ethylenedioxythiophene was prepared according to a literature method.[171] The rhenium precursor $[NEt_4]_2[ReBr_3(CO)_3]$ was prepared according to the reported procedure.[172] The 4,4'-bis(3,4-ethylenedioxythiophene)-2,2'-bipyridine ligand, **$EDOT_2$-Bipy**, was prepared according

to a literature procedure described by Zhu *et al*.[153] The 3,8-bis(3,4-ethylenedioxythiophene)-1,10-phenanthroline ligand, **EDOT$_2$-Phen**, was prepared according to a procedure described by Chen and coworkers.[154] 2-*n*-hexyl-3,4-ethylenedioxythiophene and 2-tributylstannyl-5-*n*-hexyl-3,4-ethylenedioxythiophene were synthesized according to a previously described method by Turbiez and coworkers.[173] Model compounds, ReBr(Bipy)(CO)$_3$ and ReBr(Phen)(CO)$_3$, were prepared by literature procedures described by Vitali and Calderazzo and Si *et al.*, respectively, and were used for comparative studies.[174,175]

2.2.2.1. Synthesis of Ligands and Precursors

2,6-bis(1'-(thiophen-2-yl)-1',3'-dioxopropyl)pyridine. Prepared with slight modification to a literature procedure described by Fenton *et al*.[176] Under an inert atmosphere of argon, sodium ethoxide was prepared *in situ* upon addition of ethanol (15 mL) to NaH (0.672 g, 26.6 mmol). To the freshly prepared sodium ethoxide, 2-acetylthiophene (3.31 mL, 30.7 mmol) in dry toluene was added, followed quickly by dimethyl pyridine-2,6-dicarboxylate (2.000 g, 10.2 mmol). The solution was stirred for 16 hours at room temperature. After stirring at 60 ºC for 4 hours, the solution was filtered and washed with diethyl ether. The yellow solid was then added to a vigorously stirred solution of acetic acid and water. Product was recovered from the aqueous solution by addition of methylene chloride. The resulting solution was then washed with three 75 mL portions of a 6% sodium bicarbonate solution and deionized water and dried over anhydrous magnesium sulfate. Upon recrystallization in methylene chloride and hexanes, a yellow feathery solid was recovered (1.580 g, 40%). The purity and composition of the target compound was confirmed by comparison of the ^{1}H and ^{13}C $\{^{1}H\}$ NMR spectroscopy data to literature values.[176]

2,6-bis[1*H*-5-(thiophen-2-yl)-pyrazol-3-yl]pyridine (Th_2-H_2BPP). A mixture of 2,6-bis(1'-(thiophen-2-yl)-1',3'-dioxopropyl)pyridine (0.400 g, 1.0 mmol), hydrazine monohydrate (80%, 1.10 mL, 17.7 mmol) and a few drops of concentrated HCl in methanol were refluxed for 36 hours. After reducing the solution to approximately 5 mL, water was added to precipitate a tan solid. The product was isolated from the solution by filtration and dried *in vacuo* to yield a tan powder (0.310 g, 80%). mp: decomp. at 285 ºC; ^{1}H NMR (DMSO-d_6): δ 13.54 (s, 2H), 8.00 (s, 1H) 7.83 (s, 2H), 7.47 (s, 4H), 7.39 (s, 2H), 7.14 (s, 2H); The compound was not soluble enough in any common organic solvent for ^{13}C {^{1}H} NMR analysis; UV-Vis (CH_3OH, nm): λ_{max} 274 (ε, 3.75 x 10^4 M^{-1} cm^{-1}); HRMS (CI+) calcd. for $C_{19}H_{13}N_5S_2$: 375.0612. Found 375.0612.

2,6-bis[1-methyl-5-(thiophen-2-yl)-pyrazol-3-yl]pyridine (Th_2-BPP). Under an inert atmosphere of argon, NaH (0.020 g, 1.0 mmol) and dry THF (20 mL) were combined to create a suspension. Upon addition of Th_2-H_2BPP (0.150 g, 0.4 mmol), a white precipitate formed. The resulting solution was stirred under argon at room temperature for 2 hours and treated with methyl iodide (0.06 mL, 0.9 mmol). After stirring overnight, H_2O was added to produce a cloudy white solution. The product was extracted with chloroform and solvent was removed to yield a pale yellow solid (0.130 g, 81%). mp: 236-240 ºC; ^{1}H NMR ($CDCl_3$): δ 7.88 (m, 2H), 7.75 (dd, J = 6.9, 8.5, 1H), 7.41 (dd, J = 0.9, 4.9, 2H), 7.23 (dd, J = 1.2, 3.6, 2H), 7.15 (s, 2H), 7.13 (dd, J = 3.6, 5.1, 2H), 4.05 (s, 6H); ^{13}C {^{1}H} NMR: δ 151.6, 150.9, 138.0, 137.1, 131.3, 127.6, 127.0, 126.6, 118.5, 105.8, 38.2; UV-Vis (CH_2Cl_2, nm): λ_{max} 249 (ε, 5.56 x 10^4 M^{-1} cm^{-1}); HRMS (CI+) calcd. for $C_{21}H_{17}N_5S_2$: 403.0925. Found 403.0932; Anal. calcd. for $C_{21}H_{17}N_5S_2$: C, 62.51; H, 4.25; N, 17.36. Found: C, 62.17; H, 4.16; N, 17.17.

2,6-bis(1'-(3,4-ethylenedioxythien-2-yl)-1',3'-dioxopropyl)pyridine. Prepared according to a procedure described by Lytwak *et al.*[177] except 2-acetyl-3,4-ethylenedioxythiophene was used in place of 2-acetylthiophene. Product recovered as a yellow solid (39%). mp: 206-210 °C; ^{1}H NMR ($CDCl_3$): Spectrum is complicated by the presence of several tautomers in solution, δ 15.99 (br, 8H), 15.81 (br, 8H), 8.32 (d, *J* = 7.6, 8H), 8.12 (dd, *J* = 2.4, 8.0, 8H), 7.98 (q, *J* = 8.0, 10H), 7.51 (s, 14H), 7.59 (s, 1H), 7.47 (s, 14H), 6.78 (s, 12H), 6.72 (s, 2H), 6.71 (s, 2H), 4.84 (s, 2H), 4.46 (m, 2H), 4.42 (m, 2H), 4.29 (m, 2H), 4.25 (m, 2H); The compound was not soluble enough in any common organic solvent for ^{13}C {^{1}H} NMR analysis; UV-Vis (CH_2Cl_2, nm): λ_{max} 359 (ε, 3.85 x 10^4 M^{-1} cm^{-1}); HRMS (CI+) calcd. for $C_{23}H_{17}NO_8S_2$: 499.0396. Found 499.0390; Anal. calcd. for $C_{23}H_{17}NO_8S_2 \cdot H_2O$: C, 53.38; H, 3.70; N, 2.71. Found: C, 53.52; H, 3.24; N, 3.27.

2,6-bis[1*H*-5-(3,4-ethylenedioxythien-2-yl)-pyrazol-3-yl]pyridine ($EDOT_2$-H_2BPP). Prepared according to a procedure described for Th_2-H_2BPP by Lytwak *et al.*[177] Product recovered as a tan powder (71%). mp: decomp. at 255 ºC; ^{1}H NMR (DMSO-d_6): δ 13.48 (s, 2H), 7.95 (t, *J* = 8.0, 1H), 7.82 (d, *J* = 8.0, 2H), 7.21 (s, 2H), 6.52 (s, 2H), 4.31 (dd, *J* = 3.6, 33.8, 8H); The compound was not soluble enough in any common organic solvent for ^{13}C {^{1}H} NMR analysis; UV-Vis (CH_2Cl_2, nm): λ_{max} 286 (ε, 1.62 x 10^4 M^{-1} cm^{-1}); HRMS (CI+) calcd. for $C_{23}H_{17}N_5O_4S_2$: 491.0722. Found 491.0728; Anal. calcd. for $C_{23}H_{17}N_5O_4S_2 \cdot H_2O$: C, 56.20; H, 3.49; N, 14.25. Found: C, 54.57; H, 3.65; N, 13.35.

2,6-bis[1-methyl-5-(3,4-ethylenedioxythien-2-yl)pyrazol-3-yl]pyridine ($EDOT_2$-BPP). Prepared according to a procedure described for the preparation of **Th_2-BPP** by Lytwak *et al.*[177] Product recovered as a pale yellow solid (87%). mp: 241–243 °C; ^{1}H NMR ($CDCl_3$): δ 7.84 (d, *J* = 7.5, 2H), 7.71 (t, *J* = 7.8, 1H), 7.11 (s, 2H), 6.44 (s, 2H), 4.25 (m, 8H), 3.97 (s, 6H); ^{13}C {^{1}H} NMR: δ 151.7, 151.1, 141.5, 139.1, 136.9,

135.6, 118.3, 106.4, 105.3, 100.3, 64.8, 64.4, 38.2; UV-Vis (CH_2Cl_2, nm): λ_{max} 266 (ε, 4.76 x 10^4 M^{-1} cm^{-1}); HRMS (CI+) calcd. for $C_{25}H_{21}N_5O_4S_2$: 520.1113. Found 520.1105; Anal. calcd. for $C_{25}H_{21}N_5O_4S_2$: C, 57.79; H, 4.07; N, 13.48. Found: C, 57.62; H, 3.45; N, 12.80.

5,5'-bis(2-*n*-hexyl-3,4-ethylenedioxythiophene)-2,2'-bipryidine ((EDOT-Hexyl)$_2$-Bipy). Prepared according to an analogous procedure described by Zhu *et al.*[153] (52%). mp: 170.0 °C; ^{1}H NMR ($CDCl_3$): δ 8.96 (dd, *J* = 0.8, 2.4, 2H), 8.32 (dd, *J* = 0.8, 8.4, 2H), 8.02 (dd, *J* = 2.4, 8.4, 2H), 4.30 (m, 4H), 4.25 (m, 4H), 2.66 (t, *J* = 8.0, 4H), 1.62 (m, 4H), 1.31 (m, 12H), 0.88 (t, *J* = 6.4, 6H); ^{13}C {^{1}H} NMR: δ 145.8, 139.5, 138.1, 132.9, 129.5, 120.5, 118.7, 115.3, 109.6, 64.9, 64.3, 31.5, 30.3, 28.8, 25.9, 22.6, 14.1; UV-Vis (CH_2Cl_2, nm): λ_{max} 375 (ε, 9.00 x 10^4 M^{-1} cm^{-1}); HRMS (CI+) calcd. for $C_{34}H_{40}N_2O_4S_2$: 605.2508. Found 605.2491 $(MH)^+$; Anal. calcd. for $C_{34}H_{40}N_2O_4S_2$: C, 67.52; H, 6.67; N, 4.63. Found: C, 67.17; H, 6.50; N, 4.32.

3,8-bis(2-*n*-hexyl-3,4-ethylenedioxythiophene)-1,10-phenanthroline ((EDOT-Hexyl)$_2$-Phen). Prepared according to an analogous procedure described by Zhu *et. al.*[153] (2.2%). mp: decomp. at 194 °C; ^{1}H NMR ($CDCl_3$): δ 9.39 (d, *J* = 1.6, 2H), 8.42 (d, *J* = 2.4, 2H), 7.72 (s, 2H), 4.30 (m, 4H), 4.36 (m, 4H), 4.28 (m, 4H), 2.69 (t, *J* = 7.6, 4H), 1.65 (m, 4H), 1.31 (m, 12H), 0.88 (t, *J* = 6.4, 6H); The compound was not soluble enough in any common organic solvent for ^{13}C {^{1}H} NMR analysis; UV-Vis (CH_2Cl_2, nm): λ_{max} 399 (ε, 3.61 x 10^4 M^{-1} cm^{-1}); HRMS (MALDI) calcd. for $[C_{36}H_{41}N_2O_4S_2]^+$: 629.2502. Found 629.2504; Anal. calcd. for $C_{36}H_{40}N_2O_4S_2 \cdot CH_2Cl_2$: C, 62.26; H, 5.93; N, 3.92. Found: C, 62.11; H, 5.40; N, 5.10.

2,6-bis[1-methyl-5-(2-*n*-hexyl-3,4-ethylenedioxythien-2-yl)pyrazol-3-yl]pyridine ((EDOT-Hexyl)$_2$-BPP). Under an inert atmosphere of nitrogen, a solution of **EDOT$_2$-BPP** (0.780 g, 1.5 mmol) in 150 mL of dry THF was cooled to -78 ºC and *n*-

butyllithium (1.98 mL of a 1.6 M solution in hexanes) was added dropwise. After stirring at -78 ºC for 1 hour, 1-bromohexane (0.63 mL, 4.5 mmol) was added. The resulting maroon-colored solution was allowed to warm to room temperature and was stirred overnight. Upon removal of the solvent, the brown-yellow residue was dissolved in methylene chloride and washed with three 100 mL portions of saturated NH_4Cl and deionized water and dried over anhydrous $MgSO_4$. Solvent was removed to yield the crude product as a brown oil. The crude product was purified by column chromatography on silica gel using ethyl acetate as eluent to yield pure ligand as a brown oily solid (0.810 g, 78%). mp: 128 °C; ^{1}H NMR ($CDCl_3$): δ 7.82 (d, *J* = 0.8, 2H), 7.70 (t, *J* = 8.0, 1H), 7.07 (s, 2H), 4.24 (m, 8H), 3.97 (s, 6H), 2.66 (t, *J* = 7.6, 4H), 1.62 (m, 4H), 1.30 (m, 12H). 0.88 (t, *J* = 6.0, 6H); ^{13}C {^{1}H} NMR: δ 151.8, 151.0, 138.9, 137.2, 136.8, 135.9, 119.5, 118.2, 106.0, 100.8, 64.9, 64.4, 38.2, 31.5, 30.3, 28.8, 25.8, 22.6, 14.1; UV-Vis (CH_2Cl_2, nm): λ_{max} 272 (ε, 4.18 x 10^4 M^{-1} cm^{-1}); HRMS (CI+) calcd. for $C_{37}H_{45}N_5O_4S_2$: 688.2991. Found 688.2984; Anal. calcd. for $C_{37}H_{45}N_5O_4S_2$: C, 64.60; H, 6.59; N, 10.18. Found: C, 64.19; H, 6.03; N, 9.58.

2.2.2.2. Synthesis of Complexes

Synthesis of *fac*-ReBr(Th$_2$-BPP)(CO)$_3$ (1). Ligand, **Th$_2$-BPP**, (0.055 g, 0.14 mmol) in methanol (25 mL) was added to a stirred solution of $[NEt_4]_2[ReBr_3(CO)_3]$[172] (0.10 g, 0.14 mmol) in methanol (20 mL). The solution was refluxed for 5 hours to yield a cloudy yellow-green solution. Solvent was removed to yield a green solid (0.052 g, 50%). mp: decomp. at 267 ºC; ^{1}H NMR ($CDCl_3$): δ 7.97 (t, *J* = 7.8, 1H), 7.85 (dd, *J* = 1.8, 7.8, 1H), 7.64 (dd, *J* = 1.2, 7.8, 1H), 7.56 (dd, *J* = 1.2, 4.8, 1H), 7.44 (dd, *J* = 1.2, 4.8, 1H), 7.31 (dd, *J* = 1.2, 3.3, 1H), 7.26 (d, *J* = 3.0, 1H), 7.21 (dd, *J* = 3.6, 5.4, 1H), 7.14 (dd, *J* = 3.6, 5.4, 1H), 6.95 (s, 1H), 6.93 (s, 1H), 4.22 (s, 3H), 4.07

(s, 3H); The compound was not soluble enough in any common organic solvent for ^{13}C $\{^1H\}$ NMR analysis; UV-Vis (CH_2Cl_2, nm): λ_{max} 245 (ε, 2.12 x 10^4 M^{-1} cm^{-1}); IR (cm^{-1}): ν_{CO}, 2014 (s), 1908 (s), 1867 (s); HRMS (ESI) calcd. for $[C_{24}H_{17}N_5O_3S_2Re]^+$ ($[M\text{-}Br]^+$): 674.0329. Found 674.0325; Anal. calcd. for $C_{24}H_{17}BrN_5O_3ReS_2$: C, 38.25; H, 2.27; N, 9.29. Found: C, 38.02; H, 2.69; N, 8.88.

Synthesis of *fac*-Re(*t*-BuNC)(Th$_2$-BPP)(CO)$_3$ (2). In an airfree glovebox, **1** (0.100 g, 0.13 mmol) was dissolved in dry methylene chloride and reacted with $Ag(SO_3CF_3)$ (0.040 g, 0.13 mmol) for 1 hour at room temperature. The AgBr salt was filtered off and the resulting filtrate was reacted with (*t*-butyl)isocyanide (15 μL, 0.13 mmol) in the dark at room temperature for 4 days. The solvent was removed and the crude product was recrystallized out of methylene chloride and hexanes to yield a yellow solid as pure product (0.036 g, 30%). mp: decomp. at 156 ºC; ^1H NMR ($CDCl_3$): δ 8.57 (dd, *J* = 1.5, 8.0, 1H), 8.30 (t, *J* = 8.0, 1H), 7.75 (dd, *J* = 1.5, 7.7, 1H), 7.59 (dd, *J* = 1.0, 5.5, 1H), 7.57 (s, 1H), 7.56 (dd, *J* = 1.0, 3.8, 1H), 7.18 (dd, *J* = 5.0, 5.5, 1H), 6.69 (s, 1H), 4.21 (s, 3H), 4.08 (s, 3H), 1.28 (s, 9H); The compound was not soluble enough in any common organic solvent for ^{13}C $\{^1H\}$ NMR analysis; UV-Vis (CH_2Cl_2, nm): λ_{max} 253; IR (cm^{-1}): ν_{CO}, 2030 (s), 1949 (s), 1920 (s); ν_{CN}, 2095 (s); HRMS (ESI) calcd. for $[C_{29}H_{26}N_6O_3S_2Re]^+$ ($[M\text{-}Br]^+$): 757.10598. Found 757.10622.

***fac*-ReBr(EDOT$_2$-BPP)(CO)$_3$ (3).** Prepared according to a procedure described for the preparation of ReBr(Th$_2$-BPP)(CO)$_3$ by Lytwak *et al*.[177] Product was purified by column chromatography on alumina using ethyl acetate as eluent to remove a mixture of ligand and complex. Afterwards, eluent was switched to methylene chloride to yield pure complex as a green solid (0.053 g, 16%). mp: decomp. at 258 °C; ^1H NMR ($CDCl_3$): δ 7.92 (t, *J* = 8.0, 1H), 7.81 (dd, *J* = 1.6, 7.8, 1H), 7.61 (dd, *J* = 1.6, 7.8, 1H), 6.97 (s, 1H), 6.89 (s, 1H), 6.57 (s, 1H), 6.47 (s, 1H), 4.26 (m, 8H), 4.17 (s, 3H), 4.05 (s, 3H); The

compound was not soluble enough in any common organic solvent for ^{13}C $\{^1H\}$ NMR analysis; UV-Vis (CH_2Cl_2, nm): λ_{max} 271 (ε, 5.33 x 10^4 M^{-1} cm^{-1}); IR (cm^{-1}): ν_{co}, 2006 (s), 1896 (s), 1879 (w); HRMS (CI+) calcd. for $C_{28}H_{21}BrN_5O_7ReS_2$: 868.9623. Found 868.9620; Anal. calcd. for $C_{28}H_{21}BrN_5O_7ReS_2$: C, 38.67; H, 2.43; N, 8.05. Found: C, 38.31; H, 2.28; N, 7.73.

***fac*-ReBr(BPP)(CO)$_3$ (4).** Prepared according to a procedure described by Lytwak *et al*.[177] Product was purified by washing with methanol and filtering product to recover a green solid (57%). mp: decomp. at 244 °C; ^1H NMR ($CDCl_3$): δ 7.92 (t, *J* = 8.0, 1H), 7.81 (dd, *J* = 1.4, 7.8, 1H), 7.58 (dd, *J* = 1.6, 2.8, 1H), 7.55 (d, *J* = 1.2, 1H), 7.49 (d, *J* = 2.4, 1H), 6.82 (d, *J* = 2.8, 1H), 6.76 (d, *J* = 2.4, 1H), 4.19 (s, 3H), 4.02 (s, 3H); The compound was not soluble enough in any common organic solvent for ^{13}C $\{^1H\}$ NMR analysis; UV-Vis (CH_2Cl_2, nm): λ_{max} 240 (ε, 2.64 x 10^4 M^{-1} cm^{-1}); IR (cm^{-1}): ν_{co}, 2014 (s), 1912 (s), 1891 (s); HRMS (ESI+) calcd. for $[C_{16}H_{13}N_5O_3Re]^+$ ($[M\text{-}Br]^+$): 510.05708. Found 510.05706; Anal. calcd. for $C_{16}H_{13}BrN_5O_3Re$: C, 32.60; H, 2.22; N, 11.88. Found: C, 32.65; H, 1.50; N, 11.47.

***fac*-ReBr(EDOT$_2$-Bipy)(CO)$_3$ (5).** Prepared according to an analagous procedure described by Smieja *et al*.[46] Product recovered as an orange solid (56%). mp: decomp. at 314 °C; ^1H NMR (CD_2Cl_2): δ 9.55 (s, 2H), 8.15 (dd, *J* = 2.0, 8.6, 2H), 8.07 (d, *J* = 8.8, 2H), 6.56 (s, 2H), 4.45 (m, 4H), 4.31 (m, 4H); The compound was not soluble enough in any common organic solvent for ^{13}C $\{^1H\}$ NMR analysis; UV-Vis (CH_2Cl_2, nm): λ_{max} 423 (ε, 4.57 x 10^4 M^{-1} cm^{-1}); IR (cm^{-1}): ν_{co}, 2018 (s), 1936 (s), 1900 (s); HRMS (CI+) calcd. for $C_{26}H_{19}BrN_2O_7ReS_2$: 785.9140. Found 785.9118; Anal. calcd. for $C_{26}H_{19}BrN_2O_7ReS_2$: C, 38.17; H, 2.05; N, 3.56. Found: C, 38.90; H, 2.21; N, 3.50.

***fac*-ReBr(EDOT$_2$-Phen)(CO)$_3$ (6).** Prepared according to an analagous procedure described by Sacksteder *et al*.[178] Product was purified by recrystallization from

methylene chloride and hexanes to yield an orange solid (43%). mp: decomp. at 307 °C; ^{1}H NMR ($CDCl_3$): δ 9.88 (d, *J* = 2.0, 2H), 8.48 (d, *J* = 2.0, 2H), 7.88 (s, 2H), 6.54 (s, 2H), 4.47 (m, 4H), 4.33 (m, 4H); The compound was not soluble enough in any common organic solvent for ^{13}C {^{1}H} NMR analysis; UV-Vis (DMSO, nm): λ_{max} 420 (ε, 2.03 x 10^4 M^{-1} cm^{-1}); IR (cm^{-1}): ν_{co}, 2022 (s), 1920 (s), 1867 (s); HRMS (CI+) calcd. for $C_{27}H_{16}BrN_2O_7ReS_2$: 809.9092. Found 809.9122; Anal. calcd. for $C_{27}H_{16}BrN_2O_7ReS_2$: C, 40.00; H, 1.99; N, 3.46. Found: C, 39.45; H, 1.94; N, 3.61.

***fac*-ReBr[(EDOT-Hexyl)$_2$-BPP](CO)$_3$ (7).** Prepared according to an analagous procedure described by Smieja *et al*.[46] Product recovered as an orange solid (86%). mp: decomp. at 215 °C; ^{1}H NMR ($CDCl_3$): δ 8.00 (t, *J* = 8.0, 1H), 7.87 (dd, *J* = 1.2, 8.0, 1H), 7.63 (dd, *J* = 1.2, 7.8, 1H), 6.95 (s, 1H), 6.87 (s, 1H), 4.29 (m, 8H), 4.16 (s, 1H), 4.04 (s, 1H), 2.71 (m, 4H), 1.67 (m, 4H), 1.32 (m, 12H), 0.91 (m, 6H); The compound was not soluble enough in any common organic solvent for ^{13}C {^{1}H} NMR analysis; UV-Vis (CH_2Cl_2, nm): λ_{max} 306 (ε, 3.64 x 10^4 M^{-1} cm^{-1}); IR (cm^{-1}): ν_{co}, 2022 (s), 1919 (s), 1879 (s); HRMS (ESI+) calcd. for $[C_{40}H_{45}N_5O_7ReS_2]^+$ ($[M\text{-}Br]^+$): 958.23111; Found 958.23113. Anal. calcd. for $C_{40}H_{45}BrN_5O_7ReS_2$: C, 46.28; H, 4.37; N, 6.75. Found: C, 46.12; H, 4.17; N, 6.38.

***fac*-ReBr[(EDOT-Hexyl)$_2$-Bipy](CO)$_3$ (8).** Prepared according to an analagous procedure described by Smieja *et al*.[46] Product recovered as an orange solid (64%). mp: decomp. at 241 °C; ^{1}H NMR ($CDCl_3$): δ 9.50 (dd, *J* = 0.8, 2.0, 2H), 7.93 (dd, *J* = 2.0, 8.6, 2H), 7.90 (dd, *J* = 0.8, 8.8, 2H), 4.38 (m, 4H), 4.27 (m, 4H), 2.68 (t, *J* = 8.0, 4H), 1.63 (m, 4H), 1.30 (m, 12H), 0.88 (t, *J* = 7.2, 6H); The compound was not soluble enough in any common organic solvent for ^{13}C {^{1}H} NMR analysis; UV-Vis (CH_2Cl_2, nm): λ_{max} 437 (ε, 5.55 x 10^4 M^{-1} cm^{-1}); IR (cm^{-1}): ν_{co}, 2018 (s), 1920 (s), 1904 (s); HRMS (CI+)

calcd. for $[C_{37}H_{40}N_2O_7ReS_2]^+$ $([M\text{-}Br])^+$: 875.1835. Found 875.1819; Anal. calcd. for $C_{37}H_{40}BrN_2O_7ReS_2$: C, 46.54; H, 4.22; N, 2.93. Found: C, 46.31; H, 4.12; N, 2.94.

***fac*-ReBr[(EDOT-Hexyl)$_2$-Phen](CO)$_3$ (9).** Prepared according to an analagous procedure described by Sacksteder *et al*.[178] Product recovered as an orange solid (75%). mp: decomp. at 254 °C; ^{1}H NMR ($CDCl_3$): δ 9.79 (d, J = 2.0, 2H), 8.36 (d, J = 2.4, 2H), 7.77 (s, 2H), 4.32 (m, 4H), 4.30 (m, 4H), 2.71 (t, J = 7.6, 4H), 1.66 (m, 4H), 1.33 (m, 12H), 0.90 (m, 6H); The compound was not soluble enough in any common organic solvent for ^{13}C {^{1}H} NMR analysis; UV-Vis (CH_2Cl_2, nm): λ_{max} 435 (ε, 3.50 x 10^4 M^{-1} cm^{-1}); IR (cm^{-1}): ν_{co}, 2018 (s), 1932 (s), 1875 (s); HRMS (CI+) calcd. for $C_{39}H_{40}N_2O_7BrReS_2$: 978.1018. Found 978.1017; Anal. calcd. for $C_{39}H_{40}BrN_2O_7ReS_2$: C, 47.85; H, 4.12; N, 2.86. Found: C, 46.69; H, 3.82; N, 2.76.

Gd(tta)$_3$(BPP) (10). Prepared according to an analogous procedure described by Stanley and coworkers[179] (97%). mp: decomp. at 204 °C; UV-Vis (CH_2Cl_2, nm): λ_{max} 324 (ε, 4.80 x 10^4 M^{-1} cm^{-1}); HRMS (CI+) calcd. for $[C_{29}H_{21}N_5O_4S_2F_6Gd]^+$ ($[Gd(tta)_2(EDOT_2\text{-}Bipy)]^+$): 839.0180. Found 839.0176; Anal. calcd. for $C_{37}H_{25}N_5O_6S_3F_9Gd\cdot H_2O$: C, 41.92; H, 2.38; N, 6.61. Found: C, 41.58; H, 2.22; N, 6.17.

Gd(tta)$_3$(EDOT$_2$-BPP) (11). Prepared according to an analogous procedure described by Stanley and coworkers[179] (99%). mp: 181 °C; UV-Vis (CH_2Cl_2, nm): λ_{max} 270 (ε, 6.39 x 10^4 M^{-1} cm^{-1}); HRMS (CI+) calcd. for $[C_{41}H_{29}N_5O_8S_4F_6Gd]^+$ ($[Gd(tta)_2(EDOT_2\text{-}BPP)]^+$): 1119.0044. Found 1119.0060; Anal. calcd. for $C_{49}H_{33}N_5O_{10}S_5F_9Gd\cdot H_2O$: C, 43.19; H, 2.48; N, 5.22. Found: C, 43.54; H, 2.34; N, 5.05.

2.3. Results and Discussion

2.3.1. Synthesis

2.3.1.1. Synthesis of Ligands

The synthesis of the thiophene and 3,4-ethylenedioxythiophene (EDOT)-functionalized bis(pyrazolyl)pyridine ligands is outlined in Scheme 2.2. The **Th_2-BPP** and **$EDOT_2$-BPP** ligands were synthesized by modification of literature procedures.[176] In summary, the *trans*-esterification of acetylthiophene or 2-acetyl-3,4-EDOT and dimethyl pyridine-2,6-dicarboxylate formed a tetraketone synthetic intermediate (Scheme 2.2, top right). Treatment of the tetraketone with hydrazine hydrate in a condensation reaction produced the protonated pyrazolyl pyridine species (H_2BPP-Th_2 and H_2BPP-$EDOT_2$). The desired ligand was then formed by alkylation of the pyrazoles with sodium hydride and methyl iodide. The bis(pyrazolyl) pyridine model ligand, **BPP**, was synthesized according to a literature procedure by Zhao and coworkers.[170] A 2,2'-bipyridine (Bipy) ligand functionalized with electropolymerizable EDOT groups, **$EDOT_2$-Bipy**, was synthesized according to a literature procedure.[153] Likewise, an electropolymerizable EDOT-functionalized 1,10-phenanthroline (Phen) ligand, **$EDOT_2$-Phen**, was prepared according to a literature procedure.[154] To address solubility issues associated with the aforementioned diimine-type ligands, a hexyl-substituted EDOT group was appended to the 2,6-bis(pyrazol-3-yl)pyridine, 2,2-bipyridine, and 1,10-phenanthroline ligands to form **(EDOT-Hexyl)$_2$-BPP**, **(EDOT-Hexyl)$_2$-Bipy**, and **(EDOT-Hexyl)$_2$-Phen**. The **(EDOT-Hexyl)$_2$-Bipy**, and **(EDOT-Hexyl)$_2$-Phen** ligands were prepared in the same manner as the less soluble **$EDOT_2$-Bipy** and **$EDOT_2$-Phen** ligands by means of a Stille coupling between 2-tributylstannyl-5-*n*-hexyl-3,4-ethylenedioxythiophene[173] and the appropriate

dibromo diimine precursor. The **(EDOT-Hexyl)$_2$-BPP** ligand was synthesized by lithiation of **EDOT$_2$-BPP** with *n*-BuLi and subsequent quenching with 1-bromohexane.

Scheme 2.2. Synthesis of **Th$_2$-BPP** and **EDOT$_2$-BPP** ligands

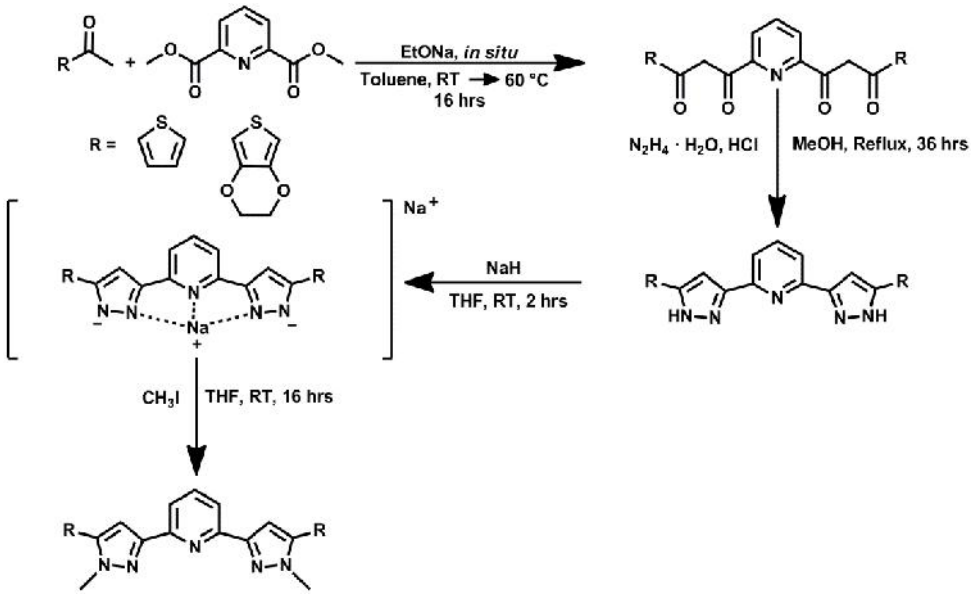

2.3.1.2. Synthesis of Rhenium(I) Complexes

ReBr(**Th$_2$-BPP**)(CO)$_3$ (**1**), ReBr(**EDOT$_2$-BPP**)(CO)$_3$ (**3**), and ReBr(**BPP**)(CO)$_3$ (**4**) were prepared by refluxing **Th$_2$-BPP**, **EDOT$_2$-BPP**, or **BPP** with $[NEt_4]_2[ReBr_3(CO)_3]$ for 5 hours in methanol, as shown in Scheme 2.3. Complexes **1**, **3**, and **4** have three bound carbonyls, as indicated by the three IR peaks in the carbonyl stretching region: **1**: 2014 cm^{-1}, 1907 cm^{-1}, and 1867 cm^{-1}; **3**: 2006 cm^{-1}, 1896 cm^{-1}, and 1879 cm^{-1}; **4**: 2014 cm^{-1}, 1912 cm^{-1}, and 1891 cm^{-1}. Complex **2** was prepared by halide abstraction of ReBr(**Th$_2$-BPP**)(CO)$_3$ with Ag(SO_3CF_3) and subsequent reaction with (*t*-butyl)isocyanide in the dark for 4 days (Scheme 2.3). Monomers **5-6** were synthesized by refluxing $ReBr(CO)_5$ with the appropriate ligand for a few hours, as shown in Scheme 2.4. The more soluble rhenium(I) tricarbonyl analogues, ReBr[**(EDOT-Hexyl)$_2$-**

BPP](CO)$_3$ (**7**), ReBr[**(EDOT-Hexyl)$_2$-Bipy**](CO)$_3$ (**8**), and ReBr[**(EDOT-Hexyl)$_2$-Phen**](CO)$_3$ (**9**), were prepared according to the same procedures for the non-solubilized complexes **3**, **5**, and **6**, as depicted in Schemes 2.3 and 2.4, respectively. Additionally, **5-9** have three IR peaks in the carbonyl stretching region, as predicted by group theory analysis of a metal complex containing three facially-bound carbonyls.[180] Proposed structures for **1-9** were confirmed by ^{1}H NMR spectroscopy, high-resolution mass spectrometry, combustion analysis, and single crystal X-ray diffraction (*vide infra*).

Scheme 2.3. Synthesis of complexes **1-4** and **7**

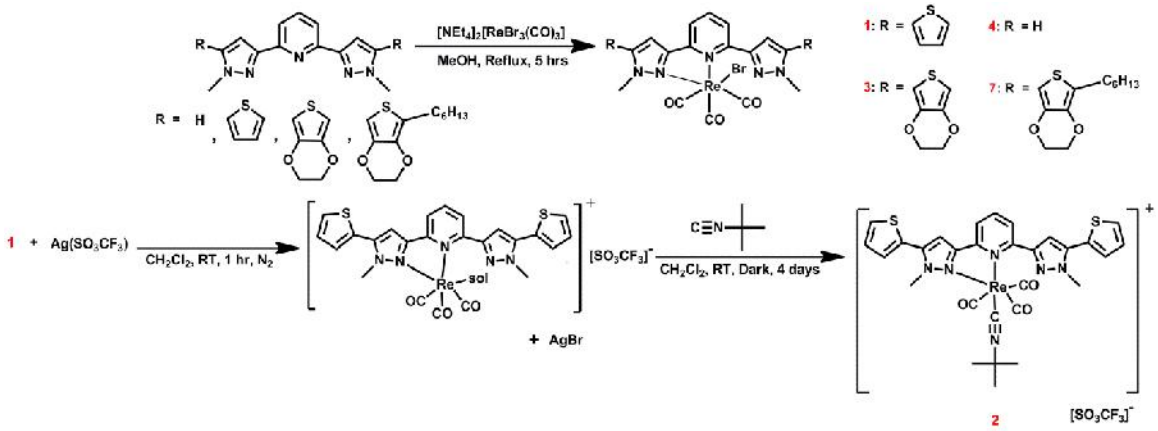

Scheme 2.4. Synthesis of complexes **5-6** and **8-9**

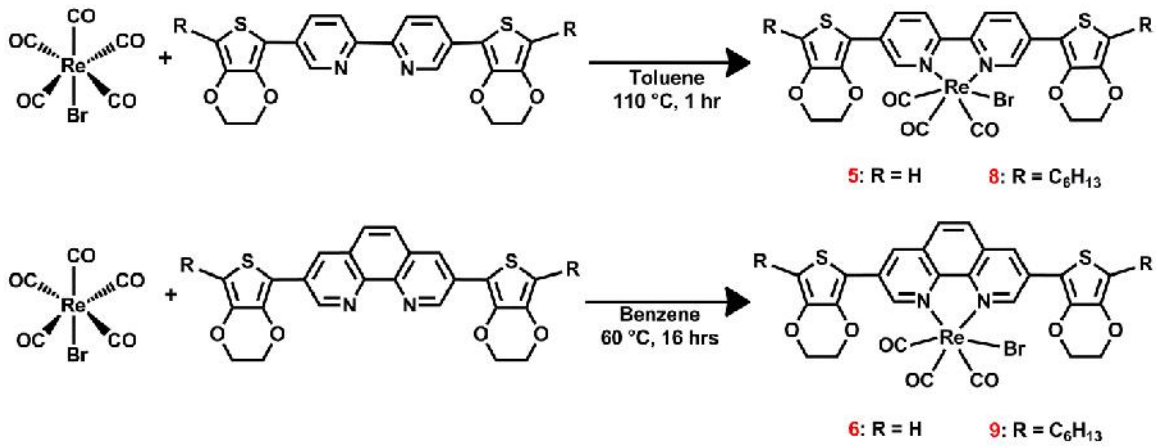

2.3.2. Structure Determination

2.3.2.1. X-Ray Crystal Structures of Ligands and Rhenium(I) Complexes

X-Ray quality crystals of **Th_2-BPP** were obtained by slow diffusion of hexanes into a saturated dichloromethane solution. Figure 2.1A shows the asymmetric unit containing one molecule of **Th_2-BPP** while Figure 2.1B shows the close packing of two molecules in the unit cell. Selected bond lengths and angles for **Th_2-BPP** are shown in Table 2.5 (Supplemental Data). The pyrazole rings are in a nearly coplanar arrangement with the central pyridine ring with the nitrogens of the pyrazoles (N7/N13, Figure 2.1A) in a *s-trans* configuration. As shown in the single molecule crystal structure in Figure 2.1A, the thiophene rings (containing S1aa and S1ae) are twisted slightly from the plane of the pyrazole rings, as indicated by dihedral angles of 0.63º and 6.29°, respectively. However, in the close packing unit cell (Figure 2.1B), the thiophene rings of the second ligand molecule are twisted 13.39° and 7.19° with respect to the pyrazole rings. This is consistent with the work of You *et al.* wherein the authors report dihedral angles of 5.3° and 3.5° for a phenyl-substituted BPP ligand.[181] Interestingly, Thiel and coworkers report a much more twisted solid state geometry when electron deficient aromatic rings are appended. This group observed dihedral angles of 66.2° and 61.3° for nitroarylated BPP derivatives.[182] The angle between the two ligand molecules in the close packing unit cell is 87.43°. The remaining structural features (e.g., bond lengths and angles) closely agree with that of analogous BPP structures.[183]

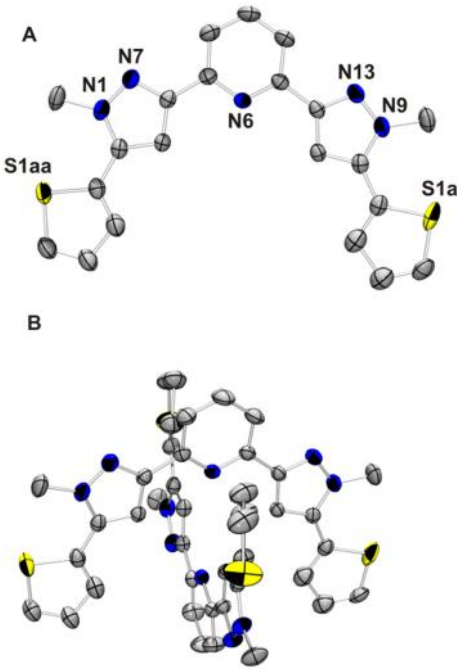

Figure 2.1. (A) ORTEP diagram of a single molecule of **Th_2-BPP**, showing the labeling scheme of selected atoms. Thermal ellipsoids are shown at the 50% probability level. Hydrogen atoms have been omitted for clarity. (B) Close packing of two molecules in the unit cell.

Crystals suitable for single-crystal X-ray diffraction analysis were grown by slow diffusion of hexanes into a saturated solution of **1** in dichloromethane. As shown in Figure 2.2, the three carbonyl ligands are arranged in a facial fashion about the rhenium metal center, thus causing the nearly planar **Th_2-BPP** to bind in a bidentate mode with one pyrazolyl ring twisted (47º) out of plane. Similar dihedral angles have been reported for rhenium complexes in which terdentate ligands behave as bidentate chelates. Hor *et al.* report a dihedral angle of 42.3° for the unbound pyridine of a $ReBr(terpy)(CO)_3$ complex.[184] In contrast, Jones and Heard report a chloro tricarbonyl rhenium complex containing a bis(oxazole)pyridine ligand in which the unbound oxazole ring is twisted 76.2° out of planarity.[185] The rhenium(I) metal center is in a distorted octahedral

environment, as made evident by C(3)-Re-N(4) and Br-Re-N(3) bond angles of 101.7º and 82.6º, respectively. The average Re-C and Re-N bond distances, 1.912 Å and 2.199 Å, respectively, agree closely to those bond distances found in similar structures.[40,146,184,186] Additional bond lengths and angles of **1** are shown in Table 2.7 (Supplemental Data).

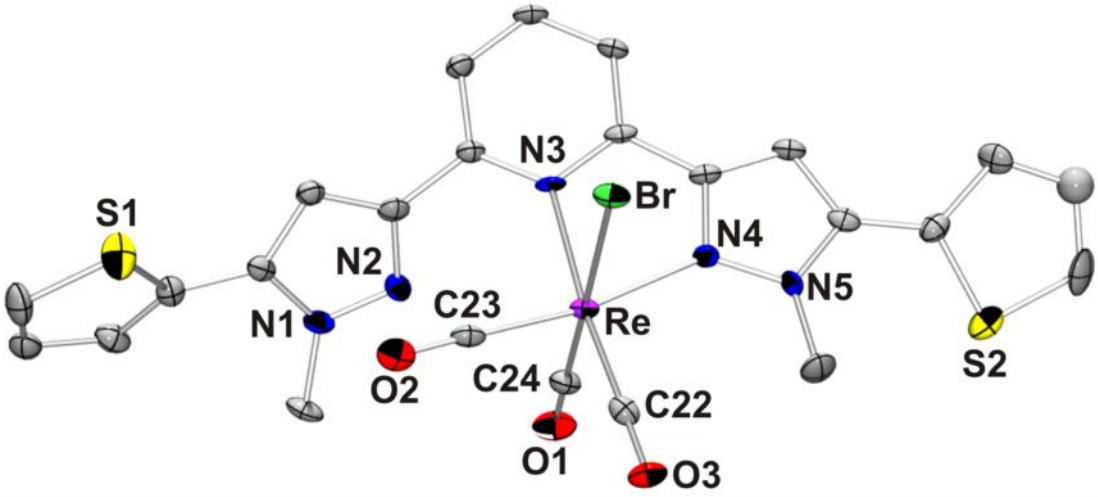

Figure 2.2. ORTEP diagram of **1**, showing the labeling scheme of selected atoms. Thermal ellipsoids are drawn at the 50% probability level. Hydrogen atoms have been omitted for clarity.

Single crystals suitable for X-ray diffraction were grown from the recrystallization of **2** in methylene chloride and hexanes. The solid-state structure, shown in Figure 2.3, shows that the three bound carbonyls are arranged in a facial orientation about the rhenium(I) metal center. As in complex **1**, the tridentate trinitrogen donor ligand, **Th_2-BPP**, is bound in a bidentate fashion, with the unbound pyrazolyl ring (containing N5 and N6) twisted 44º out of plane. The rhenium(I) metal center is in a distorted octahedral environment, as made evident by the bond angles of 73.8º, 101.5º, and 77.7º for N(2-1)-Re(1-1)-N(4-1), C(4-1)-Re(1-1)-C(1-1), N(2-1)-Re(1-1)-C(2-1),

respectively, that vary greatly from the expected 90º. The average bond lengths of 2.011 Å and 2.1425 Å for Re-C and Re-N, respectively, agree closely with our previously reported *fac*-ReBr(Th$_2$-BPP)(CO)$_3$ complex.[177] Additional bond lengths and angles are listed in Table 2.9 (Supplemental Data).

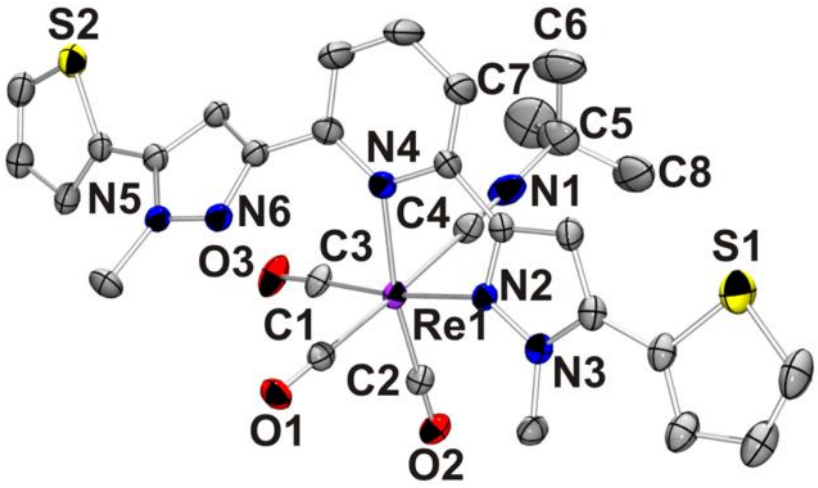

Figure 2.3. ORTEP diagram of **2**, showing the labeling scheme of selected atoms. Thermal ellipsoids are drawn at the 50% probability level. Hydrogen atoms, solvent molecules, and counter ions have been omitted for clarity.

The solid-state structure of **EDOT$_2$-BPP**, as determined by single crystal X-ray diffraction, is shown in Figure 2.4. Selected bond lengths and angles are summarized in Table 2.11 (Supplemental Data). As observed in the **Th$_2$-BPP** structure, the nitrogens of the pyrazoles (N2/N4, Figure 2.4) are in a *s-trans* configuration with the central pyridine ring. However, unlike the coplanar BPP moiety in the **Th$_2$-BPP** ligand, the pyrazoles of the **EDOT$_2$-BPP** ligand are twisted from the central pyridine ring. The pyrazolyl ring containing N1 and N2 is twisted 11.10º from the pyridine ring while the pyrazolyl ring containing N4 and N5 experiences a greater dihedral angle of 16.46º. Additionally, the appended EDOTs are much more severely twisted in the **EDOT$_2$-BPP** ligand with dihedral angles of 47.15º and 33.80º for EDOT rings containing S1 and S2, respectively.

This varies greatly from the dihedral angle observed between the thiophenes and the BPP backbone in the **Th_2-BPP** ligand (0.63º and 6.29º).[177]

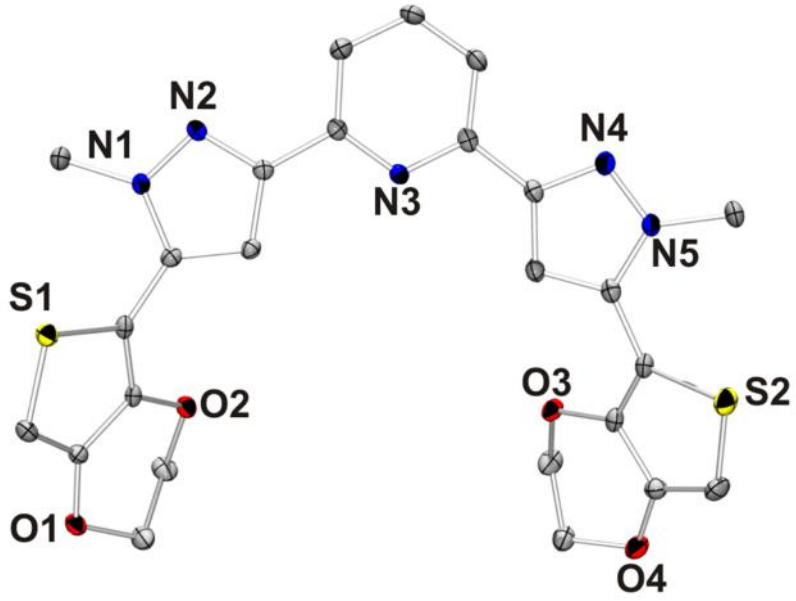

Figure 2.4. ORTEP diagram of **$EDOT_2$-BPP**, showing the labeling scheme of selected atoms. Thermal ellipsoids are drawn at the 50% probability level. Hydrogen atoms have been omitted for clarity.

Crystals suitable for single-crystal X-ray diffraction analysis were grown by slow diffusion of hexanes into a saturated solution of **3** in dichloromethane. Figure 2.5 shows the ORTEP diagram of monomer **3,** while selected bond lengths and angles are summarized in Table 2.13 in the Supplemental Data. The three carbonyls of **3** are in a facial orientation about the rhenium metal center, forcing the **$EDOT_2$-BPP** ligand to bind in a planar bidentate mode with one pyrazole unbound and twisted 66.1° out of plane. The rhenium metal center is in a distorted octahedral environment as made evident by bond angles of 74.2° and 99.5° for N(3)-Re(1)-N(4) and C(27)-Re(1)-N(4), respectively. In fact, the N(3)-Re(1)-N(4) angle is much less than 90° (74°) due to the required bite distance of the bidentate BPP ligand. This reduced bite angle of diimine-type ligands is

also observed in related $[Re(bipy)(CO)_3]^+$ (bipy = 2,2'-bipyridine) systems.[40,42,184,186] Complex **3** has average bond lengths of 2.201 Å and 1.943 Å for Re-N and Re-C, respectively. These bond lengths and angles agree closely with that of analogous $ReX(diimine)(CO)_3$-type complexes.[40,42,184,186]

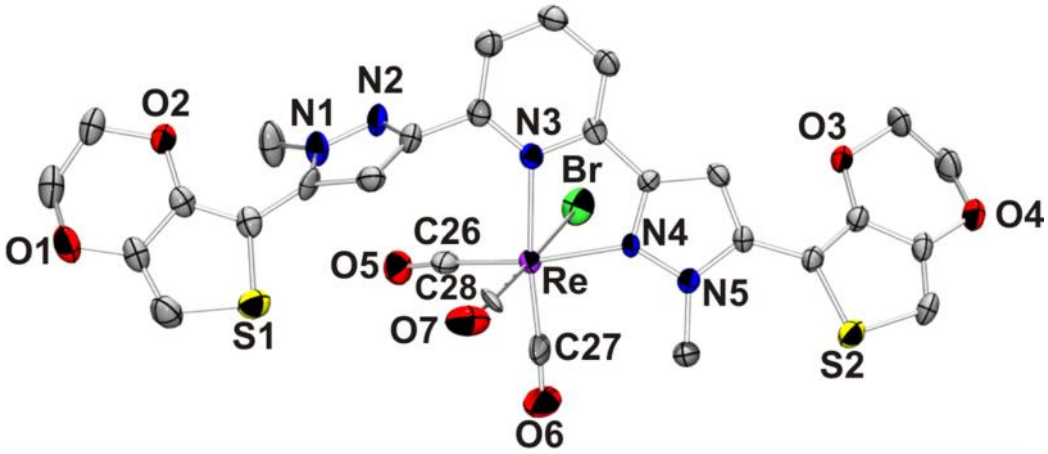

Figure 2.5. ORTEP diagram of **3**, showing the labeling scheme of selected atoms. Thermal ellipsoids are drawn at the 50% probability level. Hydrogen atoms have been omitted for clarity.

Crystals suitable for X-ray diffraction were grown by slow evaporation of a solution of **BPP** in dichloromethane and hexanes. Figure 2.6 shows the symmetric unit containing one molecule of the **BPP** ligand in which the nitrogens of the pyrazole rings are in a *s-trans* configuration with respect to the nitrogen of the central pyridine ring. Additionally, the pyrazole rings are completely coplanar with the central pyridine ring. Selected bond lengths and angles for the **BPP** ligand are shown in Table 2.15 (Supplemental Data). All bond lengths and angles closely agree with that of similar functionalized BPP ligands.[177,181,182]

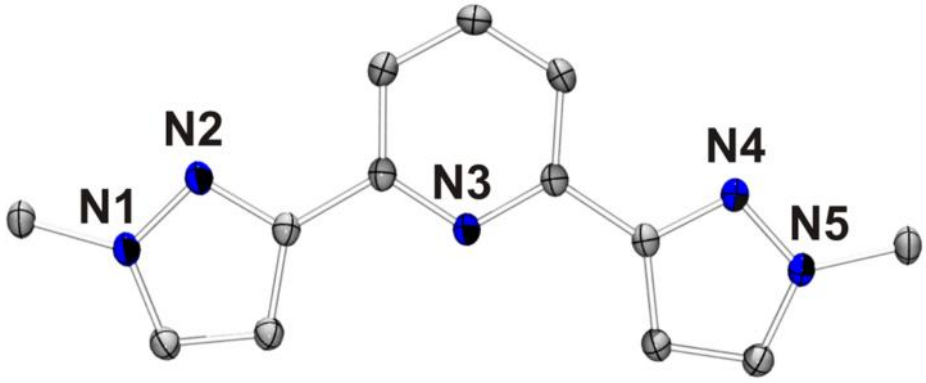

Figure 2.6. ORTEP diagram of **BPP**, showing the labeling scheme of selected atoms. Thermal ellipsoids are drawn at the 50% probability level. Hydrogen atoms have been omitted for clarity.

X-Ray quality crystals of **4** were obtained by slow diffusion of hexanes into a saturated dichloromethane solution. As shown in Figure 2.7, **4** is in a distorted octahedral environment with the three bound carbonyls arranged in a facial orientation. This distorted octahedral environment around the rhenium(I) metal center is supported by bond angles that vary greatly from 90° and 180°: 73.3° for N(2)-Re(1)-N(3) and 174.9° for Br(1)-Re(1)-C(14). In **4**, the trinitrogen donor **BPP** ligand binds to rhenium in a bidentate mode, leaving one pyrazole unbound. According to single-crystal X-ray diffraction analysis, the unbound pyrazole ring is twisted 41° out of plane from the BPP backbone. This twisting of the unbound pyrazole has been observed in other rhenium tricarbonyl BPP complexes, such as complexes **1**, **2**, and **3**.[177] In a thiophene-functionalized rhenium(I) tricarbonyl complex (**1**), a similar dihedral angle of 47° was reported for the unbound pyrazole ligand.[177] However, in a rhenium(I) BPP complex appended with EDOT groups (**3**), the unbound pyrazole is twisted 66° out of plane. This large twist in the unbound pyrazole ring is attributed to the steric bulk of the EDOT groups. Bond lengths of 1.918 Å and 2.225 Å for Re-C_{avg} and Re-N_{avg}, respectively, are

typical for that of BPP-rhenium(I) complexes and agree closely with that of similar ReX(diimine)$(CO)_3$-type complexes.[40,42,184,186] Selected bond lengths and angles are reported in Table 2.17 (Supplemental Data).

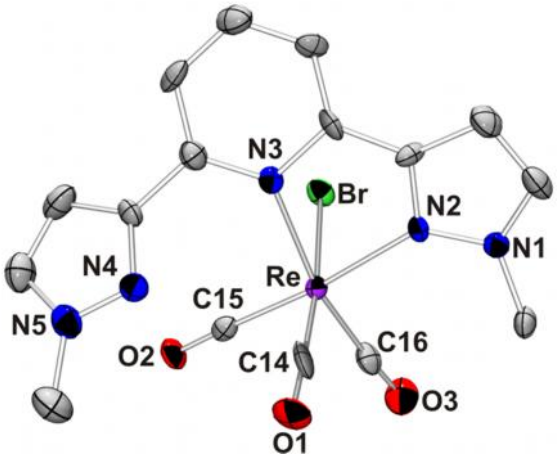

Figure 2.7. ORTEP diagram of **4**, showing the labeling scheme of selected atoms. Thermal ellipsoids are drawn at the 50% probability level. Hydrogen atoms have been omitted for clarity.

X-ray quality crystals were grown by slow diffusion of hexanes into a concentrated solution of **5** in methylene chloride. The solid-state structure confirms that three carbonyls are bound in a facial arrangement and the bipy ligand is planar upon coordination to rhenium (Figure 2.8). The rhenium(I) metal center is in a distorted octahedral environment as made by evident by bond angles of 74.9° and 99.0° for N(1)-Re(1)-N(2) and C(24)-Re(1)-N(2), respectively. Notably, there is virtually no torsion angle between the appended EDOTs and the bipy backbone; the EDOT moieties are nearly coplanar with the bipy backbone. Bond lengths and angles are similar to an analogous $ReCl(^tBu_2bipy)(CO)_3$ structure reported by Yam *et al*.[40] Additional bond lengths and angles for **5** are shown in Figure 2.19 (Supplemental Data).

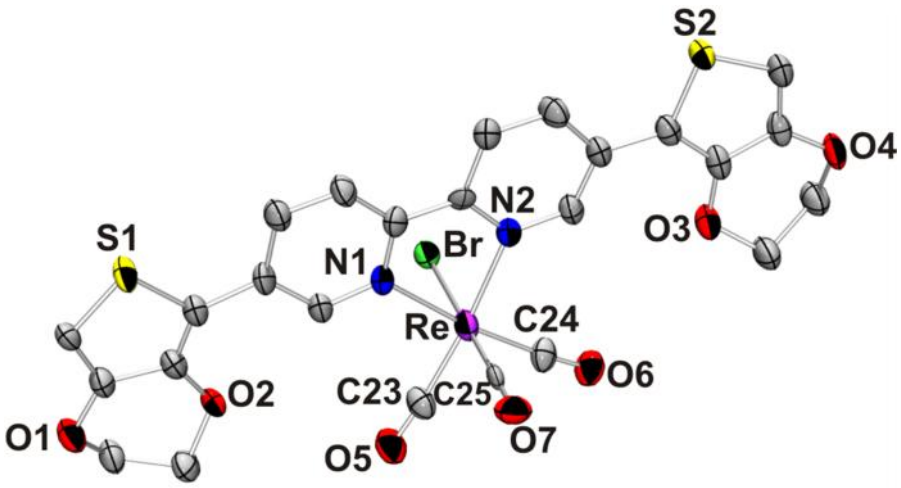

Figure 2.8. ORTEP diagram of **5**, showing the labeling scheme of selected atoms. Thermal ellipsoids are drawn at the 50% probability level. Hydrogen atoms have been omitted for clarity.

2.3.2.2. NMR Studies

To further elucidate the solution structure of complex **1**, detailed ^{1}H NMR experiments were performed. The COSY 2-D NMR of complex **1**, shown in Figure 2.9, confirms a break in symmetry of the ligand upon complexation with rhenium that results from coordination to only two of the three nitrogens of the ligand. The ability to record a spectrum with sharp resonances present for each proton in the molecule indicates that the movement of the rhenium metal center within the binding pocket of the ligand (i.e., exchange of the free and bound pyrazolyl ligands, or tick-tock exchange[185,187-189]) is absent or slow on the NMR timescale. The COSY ^{1}H NMR data shown in Figure 2.9 also confirms that the solution structure of **1** is the same as the solid-state structure, determined by X-ray crystallography, shown in Figure 2.2. Peak density off the diagonal of the 2-D NMR spectrum show protons that are strongly coupled. For example, a correlation is observed between the central proton of the pyridine (G) and the F and F' protons on either side of it. Observed chemical shifts unperturbed relative to that of the

free ligand are assigned as signals from protons of the unbound side of the ligand (Figure 2.9).

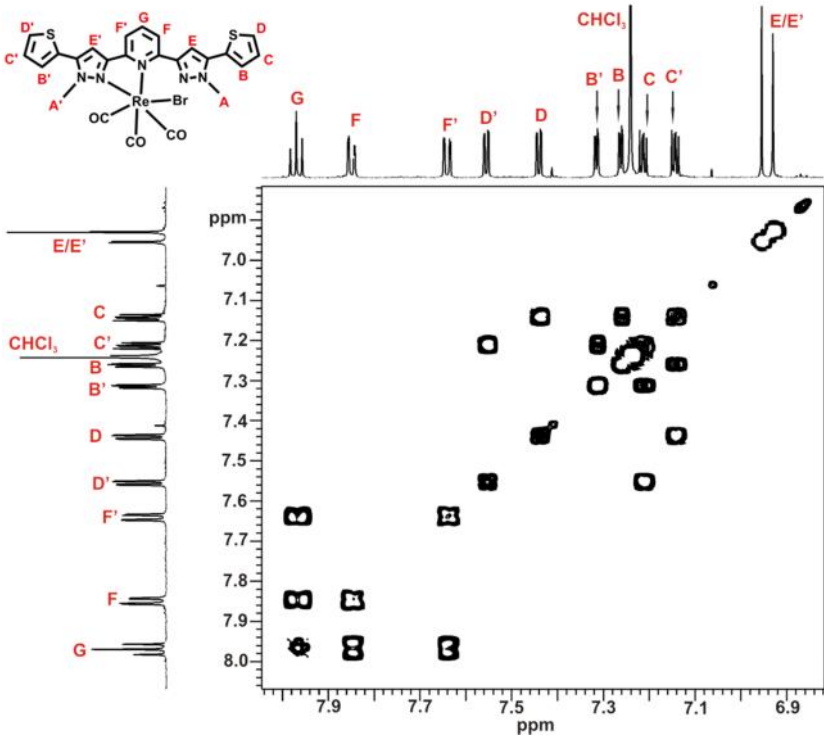

Figure 2.9. Aromatic expansions of the COSY 2-D ^{1}H NMR of **1** in $CDCl_3$ at room temperature.

Variable temperature NMR experiments of **1** were performed in 1,1,2,2-tetrachloroethane-d_2, $(CDCl_2)_2$, from 300 to 400 K. At high temperatures, no coalescence of equivalent protons on the bound and unbound sides of the ligand was observed (e.g., F/F' or E/E'), indicating that no tick-tock movement of the ligand about the rhenium metal center is present within this temperature range (Figure 2.10). The one notable change in the ^{1}H NMR spectrum with temperature is the E proton on the unbound side of the ligand shifts to lower field with increasing temperature while the E' proton on the bound side of the ligand experiences no change in chemical shift (Figure 2.11A). The

observed change in chemical shift of the E proton is attributed to a change in the dihedral angle between the central pyridine ring and pyrazole ring of the unbound side of the ligand at elevated temperatures. Figure 2.12 depicts the chemical shift of the E and E' protons as a function of the dihedral angle between the pyridine and unbound pyrazole, as determined by Gaussian nuclear magnetic resonance shielding tensor calculations. Dihedral angles similar to that displayed in the X-ray crystal structure (~47°) were of particular interest (Figure 2.11B). As shown in Figure 2.11B, the chemical shift of E' remains fairly constant as the dihedral angle is varied. However, the chemical shift of E changes as this proton is initially deshielded by through-space interactions with the proton on the adjacent pyridine ring (F, Figure 2.9) as the dihedral angle approaches 0º. Proton E is then further deshielded by through-space interactions with the ancillary ligands on the metal center, particularly the nearest carbonyl group, as the dihedral angle becomes increasingly negative. This incremental deshielding of E is a function of the dihedral angle as the E proton rotates towards the neighboring carbonyl (Figure 2.11). The relative difference between chemical shifts E and E', as determined by Figure 2.11B, were compared to the difference in chemical shifts of E and E' in the experimental spectra (Figure 2.11A) to assign a dihedral angle present in the equilibrium geometry of the time-averaged signal at each particular temperature. For example, this correlation between the theoretical and experimental data indicates that the dihedral angle of **1** is 49.6° at room temperature which is in agreement with the solid-state geometry determined by X-ray diffraction (47° dihedral angle). As the temperature is increased, the unbound side of the ligand is given enough energy to twist, as exemplified by a dihedral angle of 28.6° at 400 K. The decrease in dihedral angle, and corresponding approach towards planarity of the three nitrogen atoms in the ligand, observed in **1** with increasing temperature, is consistent with the lack of tick-tock movement in **1** which is observed for

similar complexes.[185,187-189] Moreover, it is this molecular twisting motion which precludes the exchange of the metal center between the two equivalent positions by introducing an additional activation energy to the exchange which is associated with planarizing the ligand.

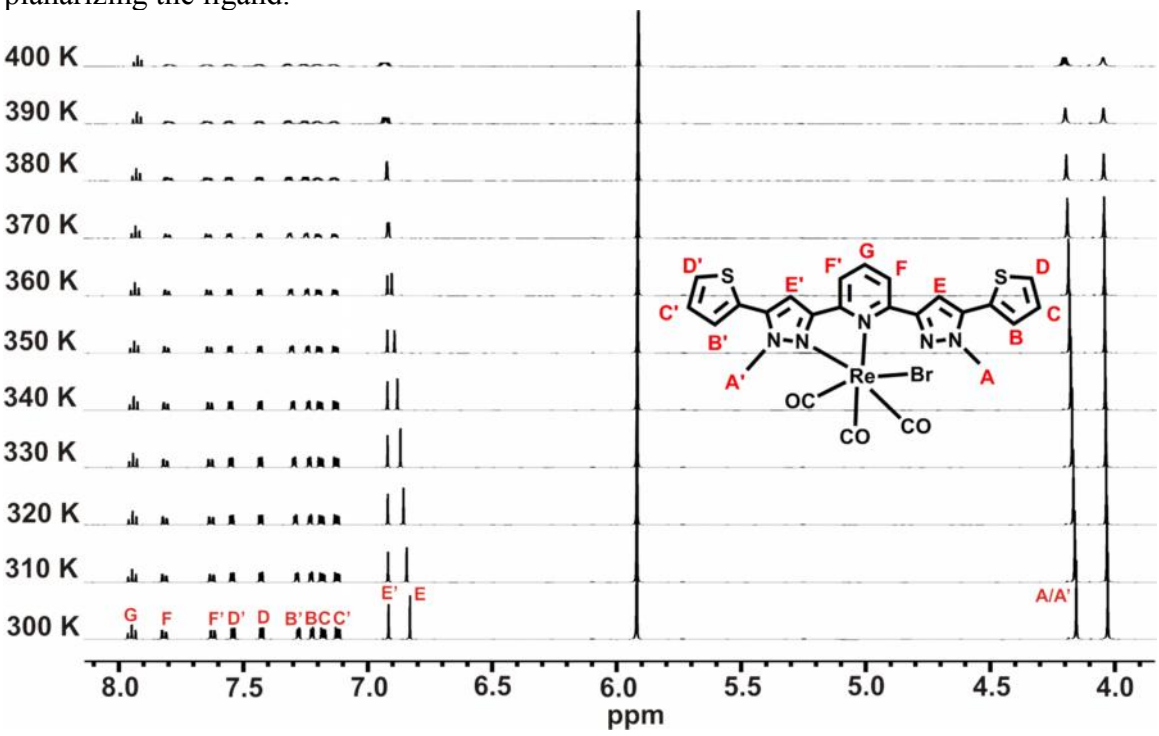

Figure 2.10. Full variable temperature ^{1}H NMR spectra of **1** in $(CDCl_2)_2$.

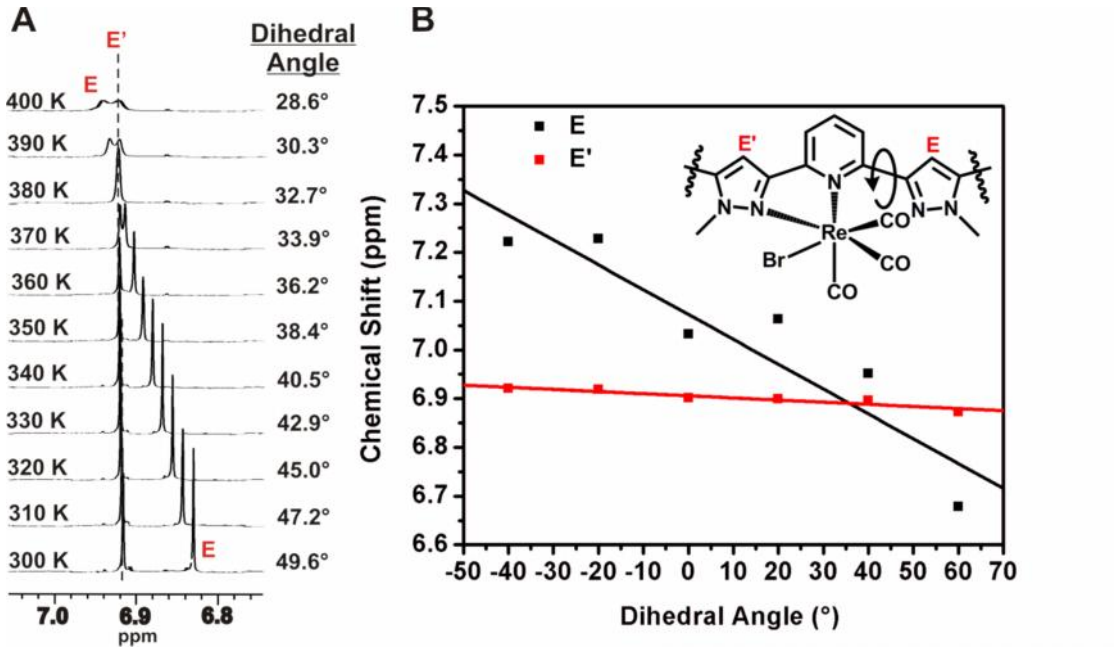

Figure 2.11. (A) Variable temperature ^{1}H NMR of **1** showing the E and E' protons in $(CDCl_2)_2$, with corresponding dihedral angle. (B) Chemical shift *versus* dihedral angle plot of **1**, as determined by Gaussian NMR shielding tensor calculations.

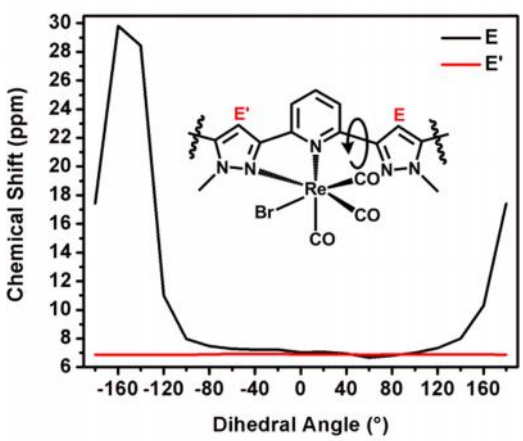

Figure 2.12. Full plot of chemical shift *versus* dihedral angle of **1**, as determined by Gaussian NMR shielding tensor calculations.

2.3.3. Electrochemistry of Rhenium(I) Complexes

2.3.3.1. Electrochemistry of 3

Monomer **3** was electropolymerized to form **poly-3** (Scheme 2.5) on ITO-coated glass for photophysical studies and stainless steel for X-ray photoelectron spectroscopy (XPS) analysis. Figure 2.13A shows the cyclic voltammogram (CV) of **3** and growth of a polymer film in a window of +1.3 to -1.7 V (vs. Fc/Fc^{+}). As shown in Figure 2.13, irreversible oxidation of monomer **3** occurs at 1.02 V (vs. Fc/Fc^{+}) on the first scan (shown as red trace, Figure 2.13A). As the number of scans is increased, the peak corresponding to monomer oxidation steadily becomes more positive. In sequential scans, the electrode-confined polymer undergoes oxidation and reduction (blue trace, Figure 2.13A), corresponding to an $E_{1/2}$ = -0.36 V. The inset of Figure 2.13A shows a linear relationship between the oxidizing current and the number of scans during polymerization, indicating uniform polymer growth up to 20 scans. For the reductive current, a linear relationship is only observed up to 6 scans due to polymer reduction that occurs over multiple peaks. Shown in Figure 2.13B is the scan rate dependence study of the electrode-confined film of **poly-3** in a monomer-free electrolyte solution. The inset for Figure 2.13B displays a linear relationship between the current of **poly-3** and the electrochemical scan rate, up to 500 mV/s. This linear relationship indicates that the electrode-confined film is an electroactive polymer that is not limited by the ionic flux of counter ions.

Scheme 2.5. Electrochemical polymerization of monomer **3**

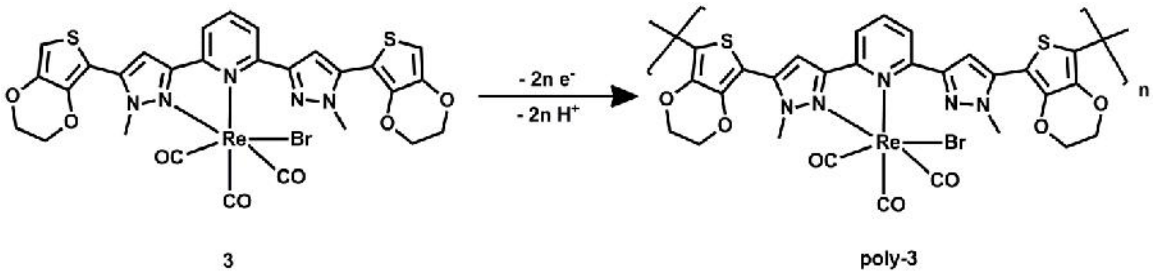

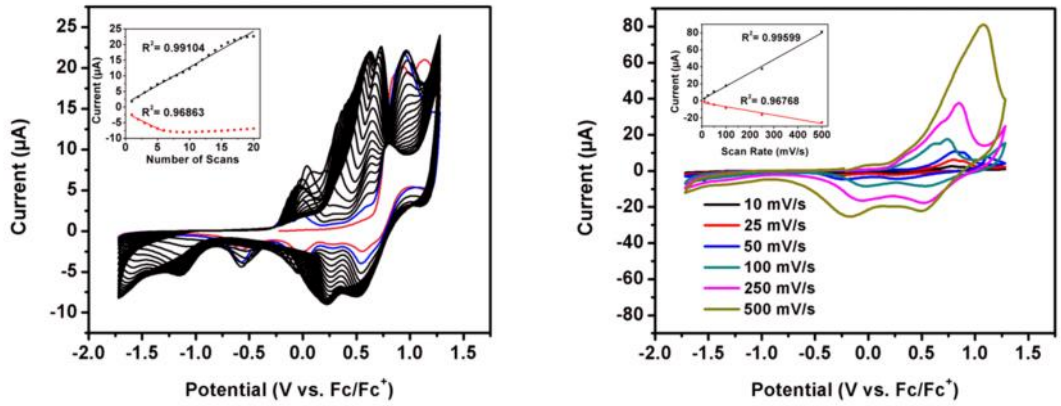

Figure 2.13. (A) Cyclic voltammogram of **3**. Inset: plot of current *versus* number of scans. (B) Scan rate dependence study of **poly-3**. Inset: plot of current *versus* scan rate.

2.3.3.2. Electrochemistry of 5

Monomer **5** was electropolymerized to form the corresponding metallopolymer, **poly-5**, as depicted in Scheme 2.6. Cyclic voltammetry (CV) experiments of **5** were carried out in CH_2Cl_2 solutions of 0.1 M $TBAPF_6$ at a scan rate of 100 mV/s. The CV in Figure 2.14A shows electrochemical growth of **poly-5** as an electrode-confined polymer film. On the first scan, irreversible oxidation of EDOT occurs at +1.1 V (vs. Fc/Fc^+) and upon sequential scans, EDOT oxidation moves to more positive oxidation potentials. After scan 1, a peak attributed to polymer oxidation at +0.30 V (vs. Fc/Fc^+) appears and becomes increasingly more positive as the number of scans is increased. Polymer

reduction occurs between -0.15 and -1.8 V (vs. Fc/Fc^+), with most of the polymer reduction centered at ~-1.5 V (vs. Fc/Fc^+). Quasi-reversible metal oxidation of Re(I) to Re(II) occurs at +1.05 V (vs. Fc/Fc^+) with metal-centered reductive processes occurring at +0.95 V, +0.45 V, and -1.6 V (vs. Fc/Fc^+). This assignment of rhenium(I)-centered oxidation at +1.05 V is supported by literature of previously reported Re(I)-bipy complexes.[42,145,190,191] Additionally, rhenium(I) oxidation and reduction assignments are confirmed by comparing the CV of **poly-5** to that of $ReBr(Bipy)(CO)_3$ (Figure 2.15). Separate electrochemical experiments were conducted on 2,2'-bipyridine in CH_2Cl_2 solutions and no redox processes were observed in this solvent window (+1.2 to -1.8 V, vs. Fc/Fc^+). The inset of Figure 2.14A shows a linear relationship between the oxidative and reduction current and the number of scans, indicating that uniform polymer growth occurs up to 10 electrochemical scans. Shown in Figure 2.14B is the scan rate dependence study of **poly-5** as an electrode-confined film. The relationship between the current and the scan rate could not be determined as it was difficult to assign polymer oxidation and reduction of the electrode-confined film in this CV.

Scheme 2.6. Electrochemical polymerization of monomer **5**

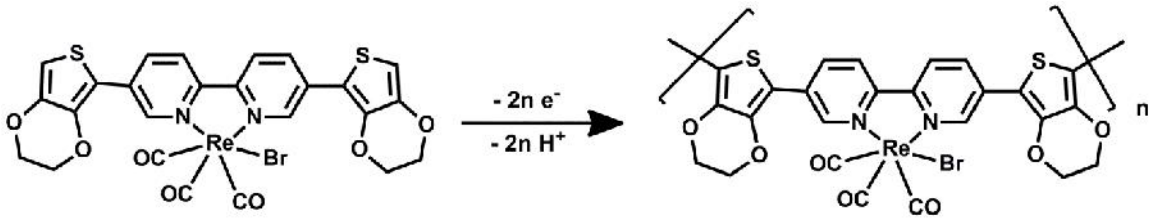

5 poly-5

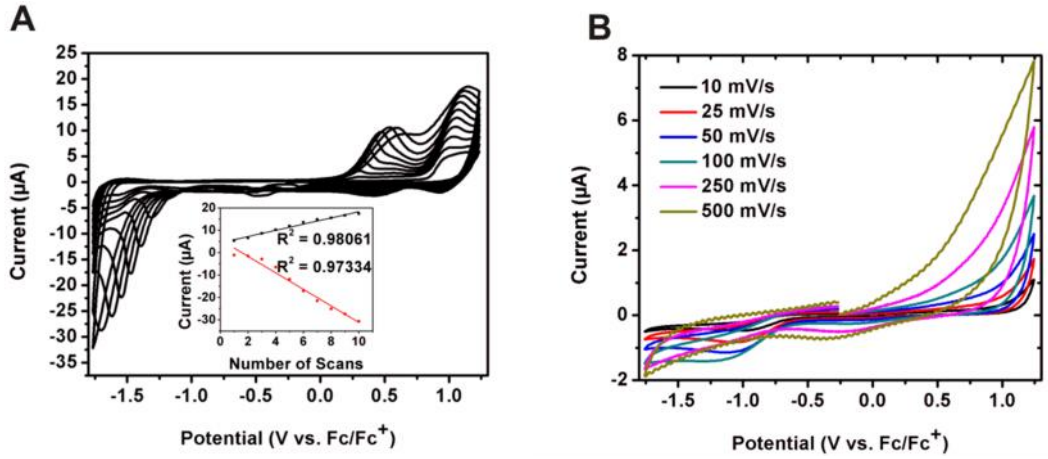

Figure 2.14. (A) Cyclic voltammogram of **5**. Inset: plot of current *versus* number of scans. (B) Scan rate dependence study of **poly-5**.

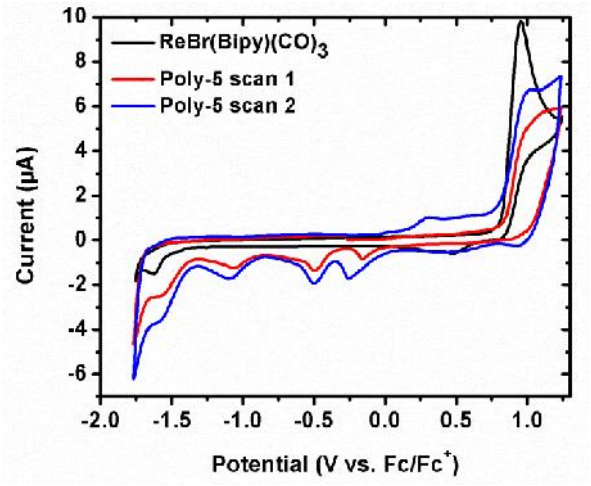

Figure 2.15. Cyclic voltammogram of $ReBr(Bipy)(CO)_3$ and **poly-5** in 0.1 M $TBAPF_6$ in CH_2Cl_2.

2.3.3.3. Electrochemistry of 6

Films of **poly-6** were made by electropolymerization of **6** (Scheme 2.7) in CH_2Cl_2 solutions of 0.1 M $TBAPF_6$ at a scan rate of 100 mV/s (Figure 2.16). Cyclic voltammetry of **6** in a window of -1.75 V to +1.25 V (vs. Fc/Fc^+) shows electrochemical growth of **poly-6** as an electrode-confined film, as depicted in Figure 2.16A. Oxidation of EDOT occurs right before the solvent window (~1.25 V, vs. Fc/Fc^+) and steadily becomes more

positive as the number of electrochemical cycles is increased. As an electroactive polymer film is made, peaks centered at -0.25 V and +0.75 V (vs. Fc/Fc^+) appear, indicative of polymer oxidation. Likewise, peaks attributed to polymer-based reduction occur between -1.25 V and 0 V (vs. Fc/Fc^+). Also observed in the CV of **poly-6** is a quasi-reversible to irreversible metal-based Re(I) to Re(II) oxidation wave at +1.0 V (vs. Fc/Fc^+), which is in close agreement with the redox behavior of similar Re(I) dimine complexes.[42,190,191] This assignment was made by comparing the CV of **poly-6** to the CVs of 1,10-phenanthroline and $ReBr(Phen)(CO)_3$ (Figure 2.17). The inset of Figure 2.16A shows a plot of current versus the number of electrochemical scans. As indicated in the inset, a linear relationship exists between both the oxidative and reductive currents and the number of scans, indicating that polymer growth is uniform up to 8 electrochemical scans. Shown in Figure 2.16B is the scan rate dependence of an electrode-confined film of **poly-6** in pure electrolyte solution. The inset of Figure 2.16B shows that the peak current of **poly-6** varies linearly with the rate of the electrochemical scan up to 500 mV/s. This linear relationship between current and scan rate indicates that **poly-6** is an electroactive polymer that is not limited by the ionic flux of counter ions in solution.

Scheme 2.7. Electrochemical polymerization of monomer **6**

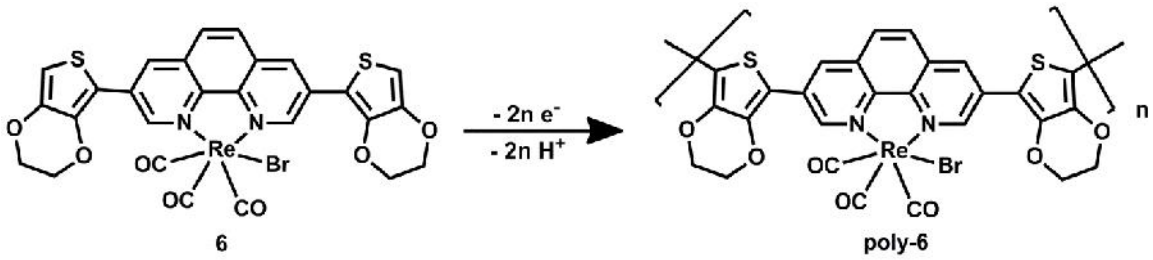

6 poly-6

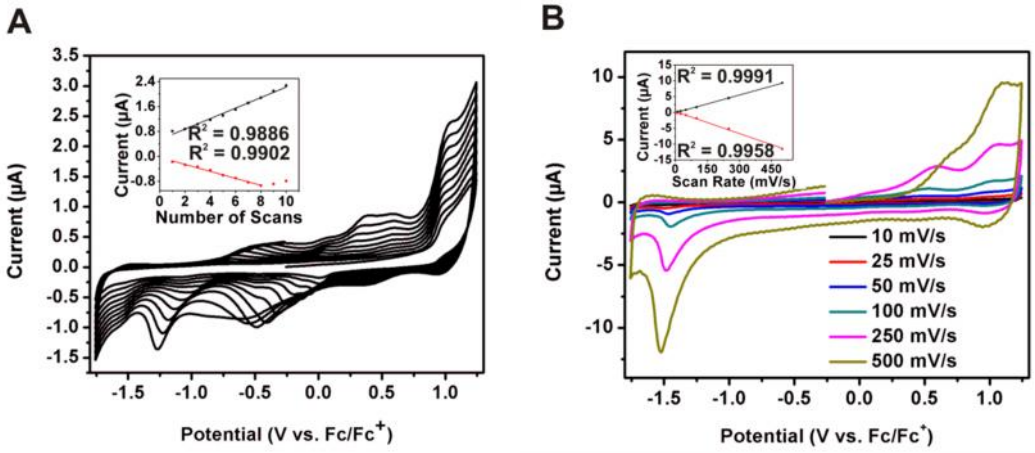

Figure 2.16. (A) Cyclic voltammogram of **6**. Inset: plot of current *versus* number of scans. (B) Scan rate dependence study of **poly-6**. Inset: plot of current *versus* scan rate.

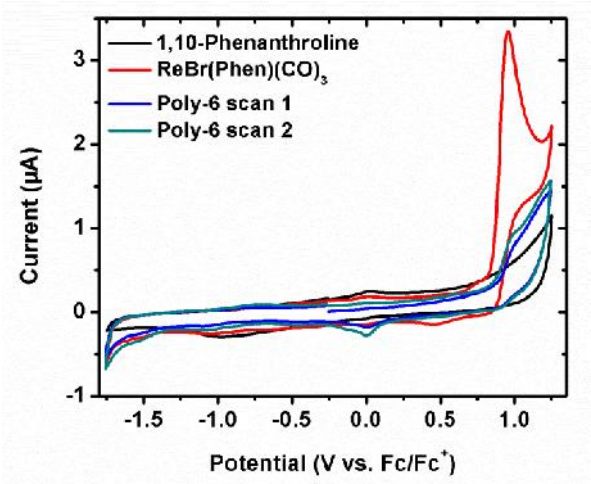

Figure 2.17. Cyclic voltammogram of 1,10-phenanthroline, $ReBr(Phen)(CO)_3$, and **poly-6** in 0.1 M $TBAPF_6$ in CH_2Cl_2.

2.3.4. Characterization of Rhenium(I) Metallopolymers

X-Ray photoelectron spectroscopy (XPS) was used to determine the elemental composition of films of **poly-3**, **poly-5,** and **poly-6** on ITO-coated glass, as shown in Figures 2.18, 2.19, and 2.20, respectively. The data plots for **poly-3** films are shown in Figure 2.18. Re $4f_{7/2}$ and Re $4f_{5/2}$ peaks are observed at 41.05 eV and 43.55 eV,

respectively, for **poly-3**. These binding energies agree closely to the expected Re $4f_{7/2}$ and Re $4f_{5/2}$ values of 41.4 eV and 43.7 eV, respectively, for Re(I) bound to Br.[192] A Re:S atomic ratio of 1:2.08 was found for films of **poly-3**, as determined by quantitative XPS analysis. This experimental atomic ratio agrees closely with that of the proposed film structure, 1:2. Additionally, three IR peaks in the carbonyl stretching region were observed for **poly-3**: 2030 cm^{-1}, 1912 cm^{-1}, 1826 cm^{-1} (spectrum not shown). This agrees with the IR spectrum predicted by group theory analysis for an asymmetrical tricarbonyl complex.[180] The corresponding XPS data plots for **poly-5** and **poly-6** are shown in Figure 2.19 and Figure 2.20, respectively. For **poly-5**, Re $4f_{7/2}$ and Re $4f_{5/2}$ peaks are observed at 40.75 eV and 43.15 eV, respectively. Films of **poly-6** also show peaks at 40.75 eV and 43.55 eV, corresponding to Re $4f_{7/2}$ and Re $4f_{5/2}$, respectively. These ionization energies agree with the expected values for Re(I) bound to Br.[192] The S $2p$ peaks for **poly-5** and **poly-6** are at 163.25 eV and 164.05 eV, respectively. Quantitative XPS analysis indicate that films of **poly-5** have a rhenium(I):sulfur atomic ratio of 1:2.44 while films of **poly-6** were found to have a atomic ratio of 1:1.93. These experimental Re(I):sulfur atomic ratios are close that of the proposed film structure (1:2) for both **poly-5** and **poly-6**.

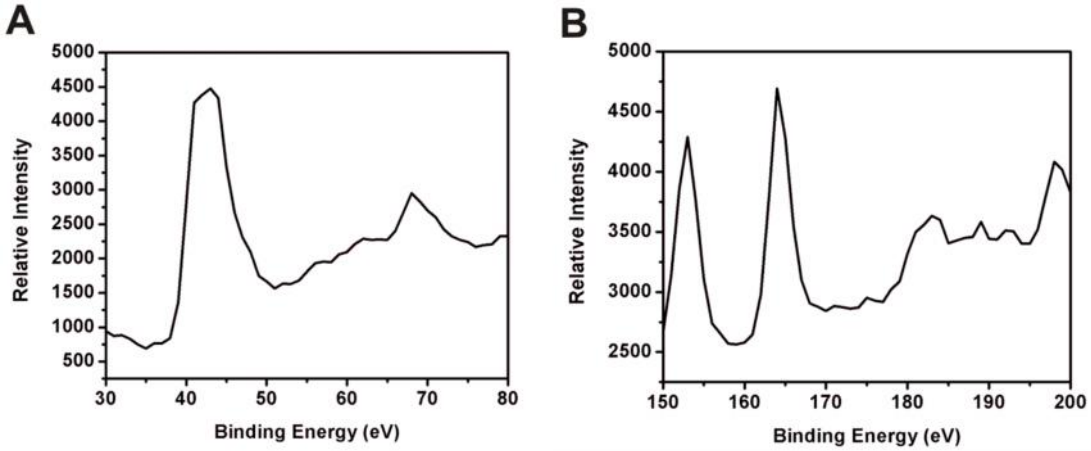

Figure 2.18. XPS data plots for **poly-3**. (A) Re $4f$. (B) S $2p$.

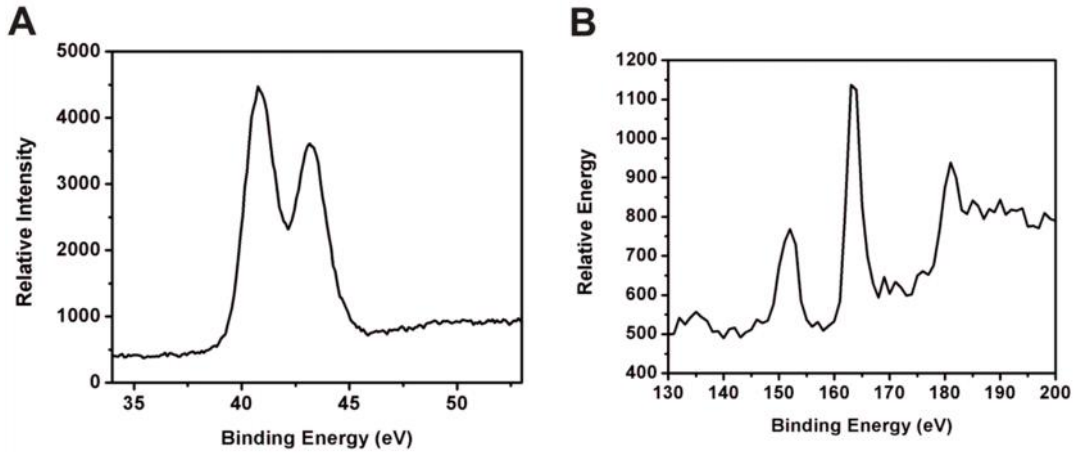

Figure 2.19. XPS data plots for **poly-5**. (A) Re 4*f* . (B) S 2*p*.

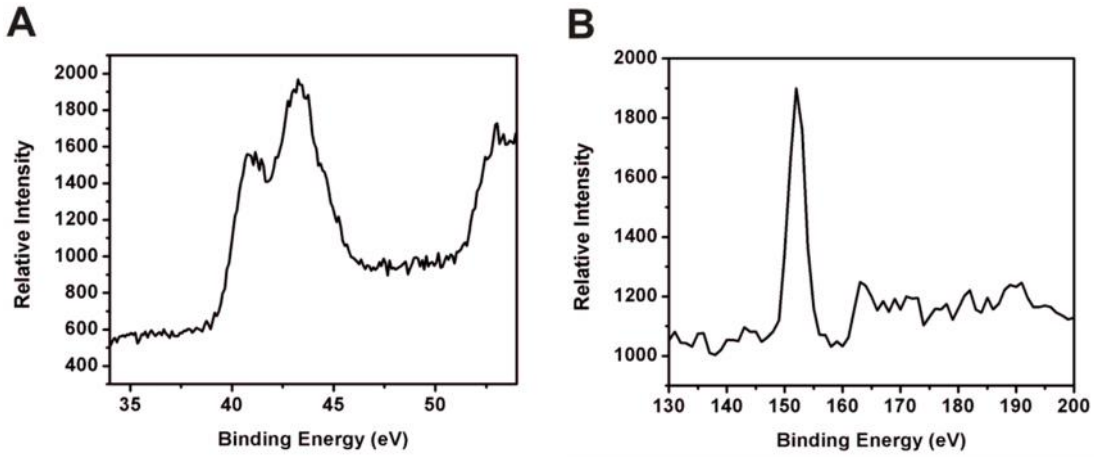

Figure 2.20. XPS data plots for **poly-6**. (A) Re 4*f* . (B) S 2*p*.

2.3.5. Photophysical Studies of Ligands and Rhenium(I) Complexes

2.3.5.1. Spectroscopy of Th_2-BPP

The photophysical properties of **Th_2-BPP** are summarized in Table 2.1. In solution, the absorption spectrum (Figure 2.21A) shows an intense absorption band at 251 nm ($\varepsilon = 5.63 \times 10^4$ M^{-1} cm^{-1}) with lower-energy shoulders at 270 nm and 305 nm. The room temperature emission spectrum, when excited at 250 nm, displays a maximum at 341 nm. This emission peak can be attributed to ligand fluorescence ($\Phi_{fl} = 2.6\%$) due to

determination of a relatively short excited state lifetime (τ = 1.31 ±0.01 ns). Upon cooling to 77 K in 2-methyltetrahydrofuran (2-MeTHF), ligand phosphorescence is observed, centered at 420 nm (Table 2.1). A large Stokes shift from ligand absorption and long-lived excited-state lifetime (τ = 37 ±3 μs) confirm that the emission is phosphorescence.

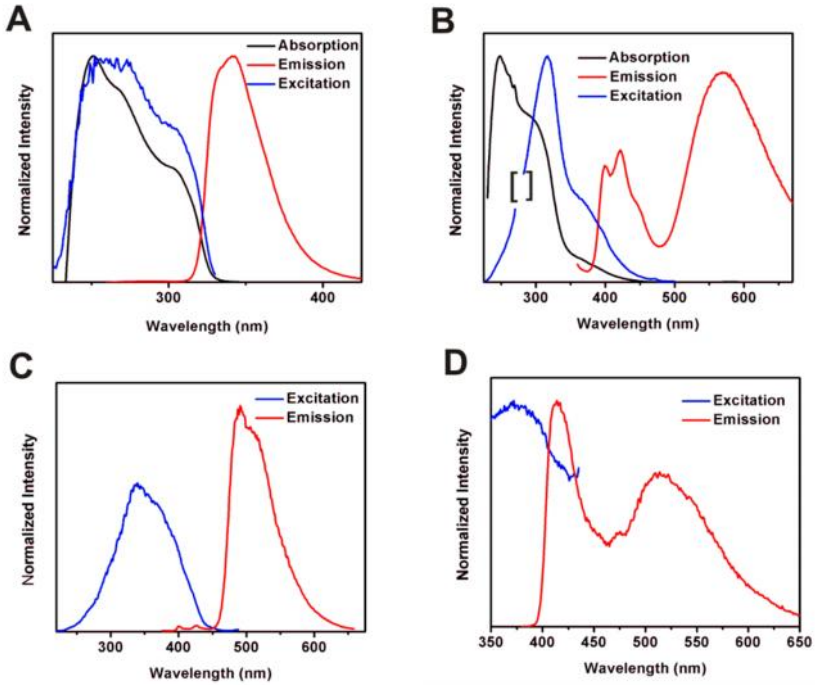

Figure 2.21. (A) Absorption, emission, and excitation spectra of **Th_2-BPP** at room temperature in CH_2Cl_2. (B) Absorption, emission, and excitation spectra of **1** at room temperature in CH_2Cl_2. Brackets in excitation profile indicate an omitted peak due to half of the monitored emission wavelength. (C) Emission and excitation of **1** at 77 K in 2-MeTHF. (D) Emission and excitation of **1** at room temperature in the solid state.

2.3.5.2. Spectroscopy of 1

The solution and solid-state photophysical properties of **1** were studied and are summarized in Table 2.1. As shown in Figure 2.21B, **1** displays a similar absorption profile to that of **Th_2-BPP** with the notable differences being a red shift of the ligand peak at 305 nm to 317 nm and a broad low energy band from ~350-425 nm. The latter is

indicative of a metal-to-ligand charge transfer (MLCT) d → π* transition.[42,44,146-148,191,193] The room temperature emission spectrum (Figure 2.21B) shows a set of peaks from 380-470 nm and an intense broad peak at 550 nm. The peaks from 380-470 nm (λ_{max} = 420 nm) correspond to ligand phosphorescence emission (τ = 10 ±1 μs). The ligand triplet excited state energy level, when bound to rhenium, is measured as 25,000 cm^{-1}, which is unchanged relative to that of the free ligand. Based on previous luminescence studies of rhenium(I) diimine tricarbonyl complexes, the intense emission band at 550 nm is assigned as ^{3}MLCT phosphorescence emission (Φ_{ph} = 2.2%).[19-26,32,42-44,144,145,178,191,193] Monitoring changes in emission intensity of **1** at 550 nm while varying excitation wavelength produces an excitation profile that displays two overlapping components (Figure 2.21B). A matching excitation profile is also obtained when monitoring the emission peaks at 420 nm, corresponding to ligand phosphorescence. This suggests a mixed excited state for **1** with both ^{3}LC (ligand centered) and ^{3}MLCT character. The heavily mixed excited state of **1** is also supported by variable wavelength excitation experiments to rule out non-selective excitation. Utilizing a λ_{ex} of up to 390 nm, which is the experimental limit to allow the observation of the high energy emission peak, consistently displays both ^{3}LC and ^{3}MLCT emission peaks. The two components observed in the excitation profile of **1** are assigned to π → π* absorption by the bound ligand centered at 310 nm and ^{1}MLCT absorption centered at 375 nm. This interpretation is strongly supported by considering the phosphorescence excitation spectrum of the free ligand at 77 K which is similar in position and profile to the higher energy component observed in the excitation profile of **1**. Schanze and coworkers report similar findings in which excitation of a tricarbonyl rhenium(I) diimine analogue populates both MLCT and IL excited states.[194]

Upon cooling to 77 K, the major emission band remains broad and structureless but experiences a significant blue shift (Figure 2.21C). This blue shift upon cooling further confirms that the emissive state is ^{3}MLCT in nature. The ligand phosphorescent peaks at 380-470 nm are still present at 77 K (τ = 9.7 ±0.6 μs) but are much less intense than at room temperature indicating that upon cooling, the emission is dominated by the ^{3}MLCT character of the mixed excited state. Additionally, the lack of any observed shift in the position of the peaks at 380-470 nm with cooling further supports the assignment of these peaks as a LC $^3(\pi \rightarrow \pi^*)$ transition. Solid-state luminescence experiments were conducted on drop cast films of **1**. The ^{3}MLCT band is blue shifted in the solid-state emission spectrum and there is a decrease in the absolute quantum yield from 2.2% to 0.6% (Figure 2.21D). The ^{3}LC peak (τ = 8.5 ±0.9 μs) loses vibronic structure in the solid-state but does not exhibit a shift in position.

2.3.5.3. Spectroscopy of 2

The photophysical properties of **2** were studied and are depicted in Figure 2.22 and summarized in Table 2.1. As shown in Figure 2.22A, the absorption profile displays a maximum at 253 nm with a shoulder at 307 nm, typical of $\pi \rightarrow \pi^*$ transitions within diimine-type ligands.[19,20,22,23,39,40,148,195-197] Upon selective excitation at 300 nm, an emission profile with peaks centered at 380 nm and 544 nm is observed, as shown in Figure 2.22A. The high energy emission at 380 nm is attributed to ligand fluorescence. The ~40 nm shift from free ligand fluorescence (λ_{em} = 341 nm, Figure 2.21A) to ligand fluorescence observed in the complex (λ_{em} = 380 nm) is attributed to planarization of the **Th_2-BPP** upon complexation with Re(I). The lower energy, broad, structureless emission at 544 nm is assigned as ^{3}MLCT phosphorescence (Φ_{ph} = 1.8 ±0.2%), in accordance with analogous rhenium(I) tricarbonyl complexes.[19-26,32,42,43,145] Monitoring this ^{3}MLCT

emission at 544 nm gives a lifetime of 8.0 ±0.5 μs, which matches closely to that of our previously prepared **ReBr(Th$_2$-BPP)(CO)$_3$** complex, **1** (τ = 9 ±1 μs).[177] Upon substitution of the Br with (*t*-Bu)NC, color-tuning, or a change in the ^{3}MLCT emission, is expected. However, only a 14 nm bathochromic shift in the ^{3}MLCT emission peak from the parent compound, **1**, to the (*t*-Bu)NC-Re(I) complex, **2** is observed. This lack of significant shifting suggests that color-tuning does not occur upon replacement of the ancillary ligand in this class of ReX(**Th$_2$-BPP**)(CO)$_3$ complexes. Upon cooling to 77 K, the emission maximum shifts to 510 nm and has an increase in vibronic structure and thus, an increase in LC π → π* character (Figure 2.2B). Monitoring this emission at 77 K, gives a two component lifetime of 530 ±10 μs and 150 ±7 μs, suggesting that the emission is dominated by highly structured LC π → π* phosphorescence with underlying broad, structureless, ^{3}MLCT emission.

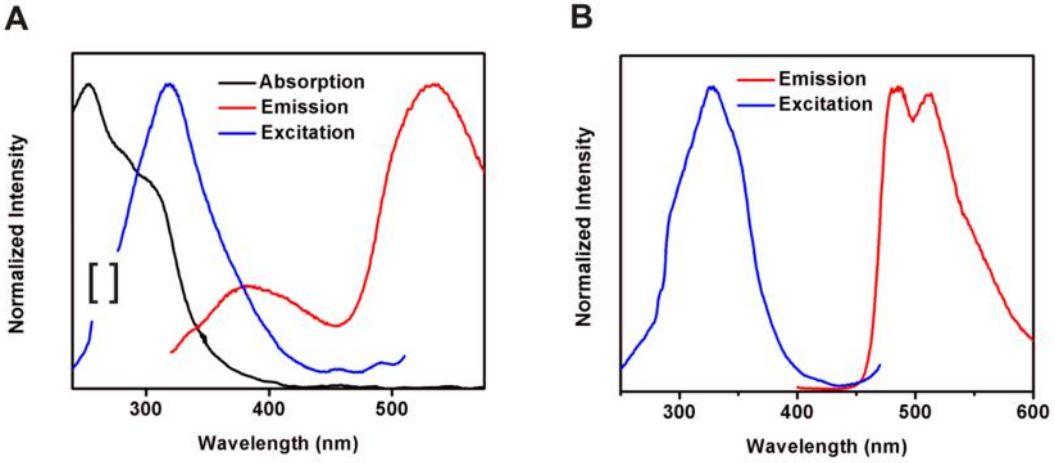

Figure 2.22. (A) Absorption, emission, and excitation spectra of **2** at room temperature in CH_2Cl_2. Brackets in excitation profile indicate an omitted peak due to half of the monitored emission wavelength. (B) Emission and excitation spectra of **2** at 77 K in 2-MeTHF.

2.3.5.4. Spectroscopy of EDOT$_2$-BPP

The photophysical properties of **EDOT$_2$-BPP** were studied and are represented in Figure 2.23 and reported in Table 2.1. The absorption spectrum in Figure 2.23A shows an intense peak at 267 nm (ε = 4.76 x 10^4 M^{-1} cm^{-1}) and a shoulder at 310 nm. When exciting at 310 nm, the room temperature emission spectrum displays a maximum at 343 nm, assigned as ligand fluorescence (Φ_{fl} = 2.6 ±0.4%) due to the small Stokes shift (~75 nm) from absorption and very small nanosecond lifetime (τ = 0.36 ±0.09 ns). Additionally, a broad, low energy shoulder is observed in the emission profile at ~450 nm. To further study this shoulder, the emission profile was monitored in solvents with a wide variety of dielectric constants (Figure 2.23B). In a very nonpolar solvent, such as toluene (k = 2.38), the shoulder at 450 nm is not present. In more polar solvents, like acetonitrile and DMSO (k = 37.5 and 46.7, respectively), the band slightly shifts to 400 nm, indicative of a charge transfer band. This low energy charge transfer band is speculated to arise from the movement of charge from the EDOT to the BPP moiety of the ligand.

Upon cooling to 77 K, both ligand fluorescence and phosphorescence is observed (Figure 2.23A). When exciting at 320 nm, fluorescence is observed at 337 nm with a less intense, low energy band present at 519 nm. This peak at 519 nm is assigned as ligand phosphorescence due to a long-lived excited-state microsecond lifetime (τ = 34 ±4 μs) and large Stokes shift from absorption (~250 nm). Additionally, the emission peak of **EDOT$_2$-BPP** at 519 nm matches closely to the emission peak observed at 77 K for **EDOT$_2$-BPP** bound to gadolinium, Gd(tta)$_3$(**EDOT$_2$-BPP**) (λ_{em} = 490 nm, Figure 2.24). Figure 2.24 further confirms that this emission event at 519 nm is phosphorescent in nature. Complexation with a heavy atom, such as gadolinium, facilitates mixing of the triplet and singlet states and produces pure ligand-based phosphorescent emission. Based

on the ligand phosphorescence observed in Figure 2.23A, the triplet excited state energy of the unbound ligand is 21,700 cm^{-1}.

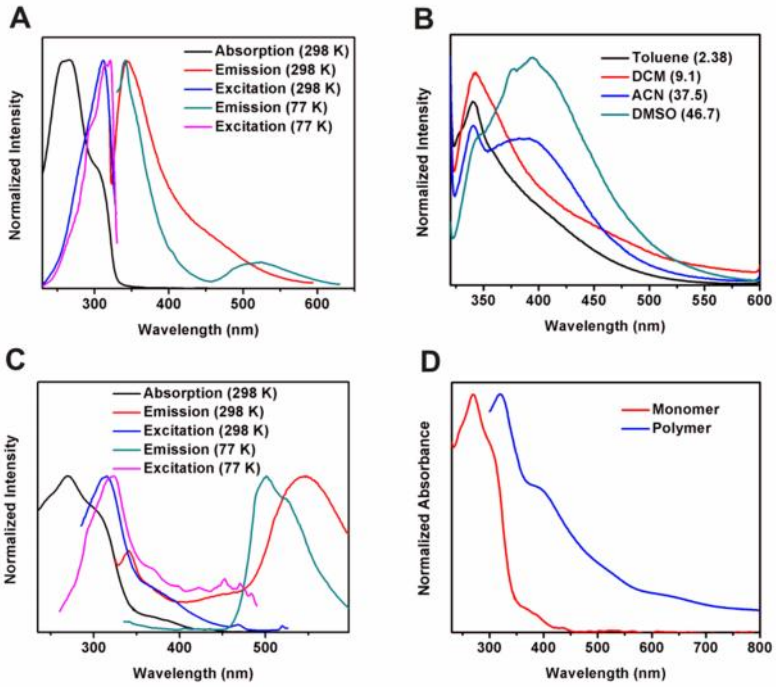

Figure 2.23. (A) Absorption, emission, and excitation spectra of **$EDOT_2$-BPP** in CH_2Cl_2 (298 K) and 2-MeTHF (77 K). (B) Emission spectra of solvent dependence study of **$EDOT_2$-BPP** at room temperature with dielectric constants of solvents. (C) Absorption, emission, and excitation spectra of **3** in CH_2Cl_2 (298 K) and 2-MeTHF (77 K). (D) Absorption spectra of **3** in CH_2Cl_2 and **poly-3** on ITO-coated glass at room temperature.

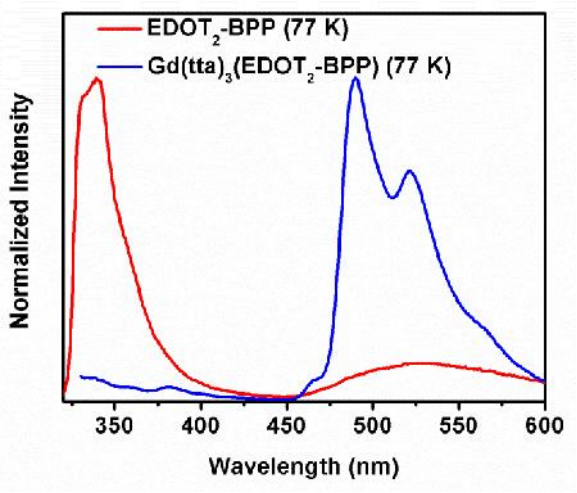

Figure 2.24. Emission spectra of **$EDOT_2$-BPP** and $Gd(tta)_3$(**$EDOT_2$-BPP**) in 2-MeTHF at 77 K.

2.3.5.5. Spectroscopy of 3 and poly-3

Photophysical studies were conducted on **3** and are shown in Figure 2.23C and summarized in Table 2.1. The absorption profile is similar to that of **$EDOT_2$-BPP** except for the appearance of a broad, low energy band from 350-405 nm (λ_{max} = 375 nm). The maximum at 270 nm ($\varepsilon = 5.33 \times 10^4$ M^{-1} cm^{-1}) and shoulder at 310 nm are attributed to *intra*ligand $\pi \rightarrow \pi^*$ transitions while the lower energy band centered at 375 nm is assigned as a metal-to-ligand charge transfer (MLCT) $d \rightarrow \pi^*$ transition, as confirmed by assignments made in analogous structures.[22,42,145,178] Also present in the spectrum is a very weak absorption band ($\varepsilon = 1.10 \times 10^3$ M^{-1} cm^{-1}) from 420-450 nm, indicative of spin-forbidden ^{3}MLCT absorption. When exciting at 315 nm, the room temperature emission spectrum shows residual ligand fluorescence and an intense broad peak at 543 nm (τ = 5 ±1 μs), assigned as ^{3}MLCT phosphorescent emission (Φ_{ph} = 1.0 ±0.3%), in accordance with previously reported rhenium(I) diimine tricarbonyl complexes.[19,22,145-148,178] Notably, some underlying ligand phosphorescence from 410-475 nm is observed in the room temperature emission spectrum. Based on this phosphorescence, the ligand

triplet excited state energy, when bound to rhenium, is 24,400 cm^{-1}. This triplet state energy is higher than that of the free ligand (21,700 cm^{-1}) and is likely caused by twisting of the ligand upon complexation with rhenium.

At 77 K and upon select excitation at 324 nm, the major low energy emission band blue shifts to 501 nm, confirming that this emission is ^{3}MLCT in nature (Figure 2.23C). Also upon cooling, the ligand fluorescence and phosphorescence is much less intense, indicating that at 77 K, the emission is dominated by ^{3}MLCT emission. Monitoring emission at 501 nm gives a lifetime comprised of two components: 46.7 ±0.5 μs and 8.90 ±0.05 μs. This two component lifetime is attributed to ^{3}MLCT emission with some underlying ligand phosphorescence.

Shown in Figure 2.23D is the UV-Vis absorption spectrum of **poly-3** on ITO-coated glass. Broad bands are observed in the absorption profile due to the extended conjugated system of **poly-3**. Extended conjugation also causes the UV-Vis spectrum of **poly-3** to be red-shifted relative to that of the monomer. Upon excitation at 319 nm, however, no observable emission was detected from the polymer film.

2.3.5.6. Spectroscopy of BPP

The solution-state photophysical properties of the **BPP** model ligand are represented in Figures 2.25A and B and summarized in Table 2.1. The absorption spectrum of the **BPP** ligand shows maximum absorption at 249 nm ($\varepsilon = 2.64 \times 10^4$ M^{-1} cm^{-1}) with less intense shoulders at 300 and 350 nm, characteristic of $\pi \rightarrow \pi^*$ transitions.[170] Upon excitation at 306 nm, an emission peak at 336 nm ($\Phi_{fl} = 2.5 \pm 0.4$ %) appears. This emission peak is attributed to ligand fluorescence due to the small Stokes shift from ligand absorption to emission (~85 nm) and small nanosecond lifetime (τ = 1.657 ±0.007 ns), characteristic of fluorescent emission. Additionally, excitation at 361

nm gives an emission peak centered at 402 nm. Emission at 402 nm is assigned as ligand phosphorescence due to a long-lived excited-state lifetime of 6.3 ±0.6 μs and large Stokes shift from ligand absorption (~150 nm). Because excitation at 361 nm produces ligand phosphorescent emission, the absorption band at 350 nm in the UV-Vis spectrum can be assigned as ligand-centered triplet absorption. Upon cooling to 77 K in 2-MeTHF, much more vibronic structure is visible in the fluorescence and phosphorescence emission peaks at 334 nm and 443 (τ = 12 ±2 μs), respectively (Figure 2.25B).

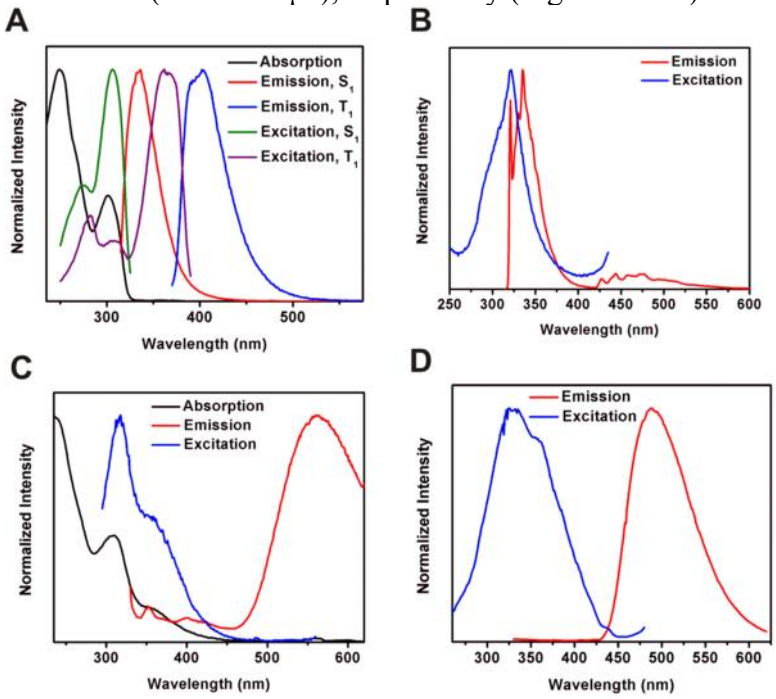

Figure 2.25. (A) Absorption, emission, and excitation spectra of **BPP** at room temperature in CH_2Cl_2. (B) Emission and excitation spectra of **BPP** at 77 K in 2-MeTHF. (C) Absorption, emission, and excitation spectra of **4** at room temperature in CH_2Cl_2. (D) Emission and excitation spectra of **4** at 77 K in 2-MeTHF.

2.3.5.7. Spectroscopy of 4

The photophysical properties of **4** are depicted in Figures 2.25C and D and compiled in Table 2.1. The absorption profile of **4** (Figure 2.25C) is similar to the

absorption of the free **BPP** ligand with peaks at 240 nm, 310 nm, and 360 nm. The peaks at 240 nm (ε = 2.64 x 10^4 M^{-1} cm^{-1}) and 310 nm (ε = 1.26 x 10^4 M^{-1} cm^{-1}) are characteristic of $\pi \rightarrow \pi^*$ *intra*ligand transitions. The broad, low energy band at 360 nm is attributed to both ligand-based singlet to triplet absorption and singlet metal-to-ligand d $\rightarrow \pi^*$ absorption. The room temperature emission spectrum, when excited at 318 nm, shows an intense, broad peak at 560 nm (Φ_{ph} = 3.3 ±0.3 %) with less intense, higher energy emission peaks at 350 nm and 400 nm. The intense peak at 560 nm is assigned as ^{3}MLCT phosphorescent emission (τ = 8 ±1 μs) based on previous luminescent studies of similar rhenium tricarbonyl diimine-type complexes.[22,40,145-148,178] The less intense, higher energy peaks at 350 nm and 400 nm are attributed to residual ligand fluorescence and phosphorescence, respectively. Upon cooling to 77 K, the major emission band blue shifts to 500 nm (τ = 8.7 ±0.4 μs), confirming that this peak is ^{3}MLCT in character, as shown in Figure 2.25D. The ligand fluorescence and phosphorescence peaks at 350 nm and 400 nm are no longer present upon cooling, indicating that ^{3}MLCT emission is the dominant emission pathway at 77 K.

2.3.5.8. Spectroscopy of EDOT$_2$-Bipy

The solution-state photophysical properties of the **EDOT$_2$-Bipy** ligand are represented in Figures 2.26A and 2.26B and are summarized in Table 2.1. The UV-Vis spectrum shows an absorption maximum at 367 nm (ε = 5.87 x 10^4 M^{-1} cm^{-1}) with shoulders at 300 nm and 420 nm, indicative of $\pi \rightarrow \pi^*$ *intra*ligand transitions typically found in 2,2'-bipyridine and derivatives thereof.[19,20,22,23,39,40,195-197] As shown in Figure 2.26A, excitation at 368 nm gives fluorescent emission at 426 nm (Φ_{fl} = 10 ±4 %), as confirmed by the small Stokes shift from absorption (~60 nm) and small nanosecond lifetime (τ = 0.869 ±0.003 ns). Cooling to 77 K, as shown in Figure 2.26B gives an

emission peak at 430 nm that contains much more vibronic structure than the room temperature emission spectrum.

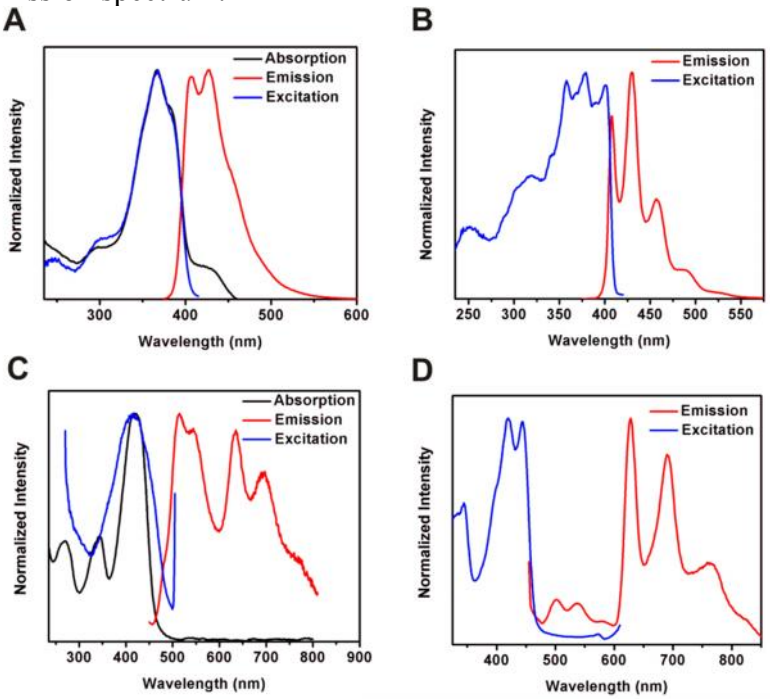

Figure 2.26. (A) Absorption, emission, and excitation spectra of **EDOT$_2$-Bipy** at room temperature in CH_2Cl_2. (B) Emission and excitation spectra of **EDOT$_2$-Bipy** at 77 K in 2-MeTHF. (C) Absorption, emission, and excitation spectra of **5** at room temperature in CH_2Cl_2. (D) Emission and excitation spectra of **5** at 77 K in 2-MeTHF.

2.3.5.9. Spectroscopy of 5 and poly-5

The room temperature solution-state photophysical spectra of **5** are shown in Figure 2.26C and summarized in Table 2.1. An absorption maximum in the UV-Vis spectrum is observed at 418 nm ($\varepsilon = 4.57 \times 10^4$ M^{-1} cm^{-1}) with less intense higher-energy transitions at 270 nm and 343 nm. Like the absorption spectrum of the free ligand, these transitions are attributed to $\pi \rightarrow \pi^*$ absorptions of the bipyridine moiety.[19,20,22,23,26,39,40,196,197] Upon excitation at 417 nm, two major emission profiles centered at 511 nm and 634 nm are observed. The emission at 511 nm is assigned as

EDOT$_2$-Bipy ligand fluorescence in the complex. The 85 nm shift from free ligand emission (λ_{em} = 426 nm, Figure 2.26A) is due to planarization of the **EDOT$_2$-Bipy** ligand upon complexation with rhenium. The emission at 634 nm (Φ_{ph} = 2 ±1 %) is attributed to **EDOT$_2$-Bipy** ligand phosphorescence in the complex. This emission is confirmed as ligand phosphorescence due to the long-lived microsecond lifetime (τ = 6 ±2 μs) and lack of shift upon cooling to 77 K (λ_{em} = 628 nm, Figure 2.26D). Upon cooling to 77 K, an increase in vibronic structure of the ligand phosphorescence peaks at 628 nm is observed (Figure 2.26D). Notably, the peaks assigned as ligand fluorescence at 511 nm are much less intense at 77 K. Monitoring emission at 628 nm gives a lifetime comprised of two components: 55 ±7 μs and 20.7 ±0.6 μs. This two component lifetime is attributed to ligand phosphorescence and underlying ^{3}MLCT emission. The second lifetime component (20.7 ±0.6 μs) is believed to be ^{3}MLCT in nature as most ^{3}MLCT emission bands lie between 550-650 nm for analogous tricarbonyl bipyridine rhenium(I) complexes.[19,20,22,23,39,40,145,196,197] Furthermore, in the polymeric system **poly-5**, no observable absorption or emission was detected from the films.

2.3.5.10. Spectroscopy of 6 and poly-6

The solution-state room temperature photophysical properties of **EDOT$_2$-Phen** have been studied and reported elsewhere.[154] As shown in Figure 2.27A, the UV-Vis spectrum of **6** displays an absorption maximum at 414 nm (ε = 2.03 x 10^4 M^{-1} cm^{-1}) with less intense, higher-energy shoulders at 261 nm and 297 nm. The absorption bands at 261 nm, 297 nm, and 414 nm are assigned as *intra*ligand $\pi \rightarrow \pi^*$ transitions, in accordance with analogous rhenium(I) phenanthroline complexes.[42,44,178,193] Selective excitation at 414 nm produces emission centered at 526 nm (Φ_{fl} = 8 ±2 %) that is assigned as **EDOT$_2$-Phen** ligand fluorescence (τ = 0.836 ±0.001 ns). Fluorescence of the ligand in the

complex (λ_{em} = 526 nm) is shifted from that of the free ligand (λ_{em} = 415 nm)[154] due to planarization of the phenanthroline ligand upon complexation with rhenium. At 77 K, a highly structured emission profile at 605 nm is observed and attributed to ligand-centered phosphorescence, as shown in Figure 2.27B. Lifetime determination of this emission peak at 605 nm gives a two component lifetime of 126.8 ±0.9 μs and 47 ±6 μs. Like complex **5**, this two component lifetime suggests underlying ^{3}MLCT emission beneath the emission dominated by ligand-centered phosphorescence.

Shown in Figure 2.27C is the UV-Vis absorption spectrum of **poly-6** on ITO-coated glass. As depicted in Figure 2.27C, **poly-6** is red-shifted from the absorption profile of a CH_2Cl_2 solution of monomer **6**. Notably, a much broader absorption peak is observed in **poly-6** than in **6** due to the extended conjugated system of the polymer. Upon selective excitation at 415 nm, no observable emission was detected from **poly-6**.

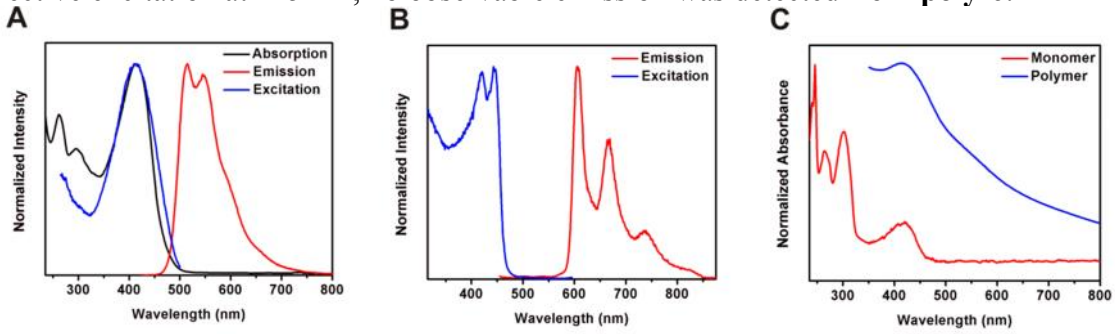

Figure 2.27. (A) Absorption, emission, and excitation spectra of **6** at room temperature in CH_2Cl_2. (B) Emission and excitation spectra of **6** at 77 K in 2-MeTHF. (C) Absorption spectra of **6** in CH_2Cl_2 and **poly-6** on ITO-coated glass at room temperature.

Table 2.1. Photophysical properties of ligands and rhenium(I) complexes

Compound	Solvent	λ_{Abs} (nm)	λ_{Ex} (nm)	λ_{Em} (nm)	Φ_{Em} (%)	τ_0 (μs)
Th_2-BPP	CH_2Cl_2	251	260	341	2.6 ±0.6	1.31 ±0.01 (ns)
	2-MeTHF	c	323[a] 334[b]	342[a] 420[b]	c	37 ±3[b]
1	CH_2Cl_2	248	317	550	2.2 ±0.6	9 ±1
	2-MeTHF	c	339	491	c	70 ±1
	Solid	c	372	514	0.6 ±0.3	10 ±1
2	CH_2Cl_2	253	310	544	1.8 ±0.2	8.0 ±0.5
	2-MeTHF	c	323	525	c	530 ±10[b] 150 ±7
$EDOT_2$-BPP	CH_2Cl_2	267	310	343	2.6 ±0.4	0.36 ±0.09 (ns)
	2-MeTHF	c	320	337[a] 519[b]	c	34 ±4[b]
3	CH_2Cl_2	270	315	543	1.0 ±0.3	5 ±1
	2-MeTHF	c	324	501	c	46.7 ±0.5 8.90 ±0.05[b]
BPP	CH_2Cl_2	249	306[a]	366[a]	2.5 ±0.4[a]	1.657 ±0.007 (ns)[a]
			361[b]	402[b]	c	6.3 ±0.6[b]
	2-MeTHF	c	319	334[a] 443[b]	c	12 ±2[b]
4	CH_2Cl_2	240	318	560	3.3 ±0.3	8 ±1
	2-MeTHF	c	317	500	c	8.7 ±0.4
$EDOT_2$-Bipy	CH_2Cl_2	367	368	426	10 ±4	0.869 ±0.003 (ns)[a]
	2-MeTHF	c	400	430	c	860 ±3[a]
5	CH_2Cl_2	420	417	511[a] 634[b]	2 ±1[b]	6 ±2
	2-MeTHF	c	420	628[b]	c	55 ±7[b] 20.7 ±0.6
6	CH_2Cl_2	414	413	515	8 ± 2	0.836 ±0.001 (ns)
	2-MeTHF	c	443	605	c	126.8 ±0.9[b] 47 ±6

a: Ligand fluorescence data
b: Ligand phosphorescence data
c: Not measured or calculated
*Measurements in CH_2Cl_2 and 2-MeTHF were at 298 K and 77 K, respectively.

2.3.6. Electrocatalytic Studies of Rhenium(I) Complexes and Metallopolymers

2.3.6.1. Electrocatalytic Studies of Rhenium(I) Complexes

Electrochemical studies of the *fac*-ReBr(N-N)$(CO)_3$ monomers under nitrogen all display a one electron quasi-reversible reduction wave and a one electron irreversible wave at more negative potentials. The quasi-reversible reduction wave is attributed to the diimine ligand-based reduction while the more cathodic irreversible wave is due to metal-based reduction.[47] In CO_2-saturated acetonitrile solutions, an increase in the current of the metal-based reduction wave is observed, signifying electrocatalytic reduction of CO_2. This increase in the peak current of the second reduction wave under a CO_2-rich atmosphere is observed for ReBr(Bipy)$(CO)_3$, ReBr(Phen)$(CO)_3$, and monomers **4**, **7**, and **8**, as depicted in Figures 2.28-2.32. Notably, in these electrocatalytic CVs, significant reductive current is observed in the scan of $TBAPF_6$ electrolyte in acetonitrile under CO_2. The large reductive current present in the blank is attributed to solvent degradation due to acidification of the solvent. Small amounts of water in the acetonitrile react with CO_2 to form carbonic acid, thus degrading the solvent and collapsing the electrochemical window. In some cases, the scan of $TBAPF_6$ in CO_2 has a much larger peak current than that of the monomer under nitrogen. This is attributed to the low concentration of monomer in solution (typically 0.1 mM to 0.6 mM), arising from the low solubility of these *fac*-ReBr(N-N)$(CO)_3$ complexes, despite functionalization with solubilizing hexyl groups. Differences in the CVs, from monomer to monomer, are observed in the second reduction wave under CO_2-saturated conditions. Furthermore, a tabulation of the first and second reduction potentials of ReBr(Bipy)$(CO)_3$, ReBr(Phen)$(CO)_3$, and monomers **4**, **7**, and **7** are displayed in Table 2.2.

Table 2.2. Reduction potentials for ReBr(N-N)$(CO)_3$ complexes

Complex	1st reduction potential[a] (V vs. Fc/Fc^+)	2nd reduction potential[b] (V vs. Fc/Fc^+)
ReBr(Bipy)$(CO)_3$	-1.746	-2.114
ReBr(Phen)$(CO)_3$	-1.703	-2.041
ReBr(BPP)$(CO)_3$ (**4**)	-1.965	-2.187
ReBr[(EDOT-Hexyl)$_2$-BPP]$(CO)_3$ (**7**)	-1.963	-2.154
ReBr[(EDOT-Hexyl)$_2$-Bipy]$(CO)_3$ (**8**)	-1.623	-1.865
ReBr[(EDOT-Hexyl)$_2$-Phen]$(CO)_3$ (**9**)	[c]	[c]

[a] Potential is for the $E_{1/2}$ of the quasi-reversible wave.
[b] Potential is the peak maximum for the cathodic wave.
[c] No Faradaic current was observed for ReBr[(EDOT-Hexyl)$_2$-Phen]$(CO)_3$ (**9**) in the potential range of this experiment (-0.6 V to -2.3 V, vs. Fc/Fc^+).

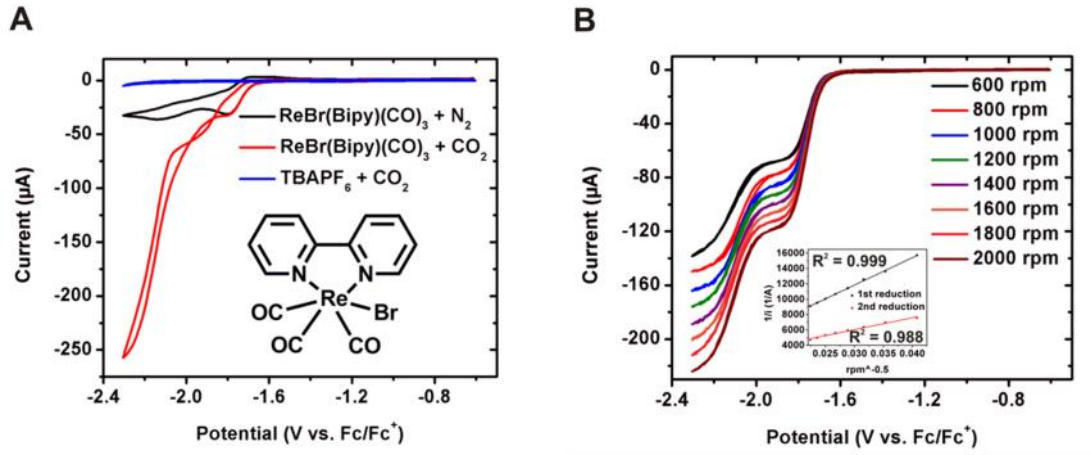

Figure 2.28. (A) Cyclic voltammogram of ReBr(Bipy)$(CO)_3$ under both nitrogen and CO_2 and electrolyte (0.1 M $TBAPF_6$ in acetonitrile) under CO_2. (B) Cyclic voltammogram of the rotating disk experiment of ReBr(Bipy)$(CO)_3$ in 0.1 M $TBAPF_6$ in acetonitrile. Inset: Levich-Koutecky plot for the data from 600-2000 rpm.

The classical rhenium(I) diimine complex, ReBr(Bipy)$(CO)_3$, the bromo analogue of Lehn's catalyst, exhibits a 6.7-fold increase in the current of the second reductive wave going from a nitrogen-rich atmosphere to a CO_2-rich atmosphere at 100 mV/s, as shown in Figure 2.28A. Additionally, the bromo derivative has a lower reduction potential (-

2.114 vs. Fc/Fc^+) than the chloride-containing Lehn's catalyst (-2.278 V vs. Fc/Fc^+).[46] Another extensively studied rhenium(I) diimine tricarbonyl complex, $ReBr(Phen)(CO)_3$, shows electrocatalytic activity towards the reduction of CO_2, as depicted in Figure 2.29A. Under CO_2, a 1.4-fold increase in the peak current is observed at -2.041 V (vs. Fc/Fc^+) at a scan rate of 100 mV/s. As shown in Figure 2.30A, **4** undergoes current enhancement under a CO_2-rich atmosphere, as well. Exchanging a saturated solution of nitrogen for that of CO_2 produces a 1.8-fold increase in the reductive current at -2.187 V (vs. Fc/Fc^+).

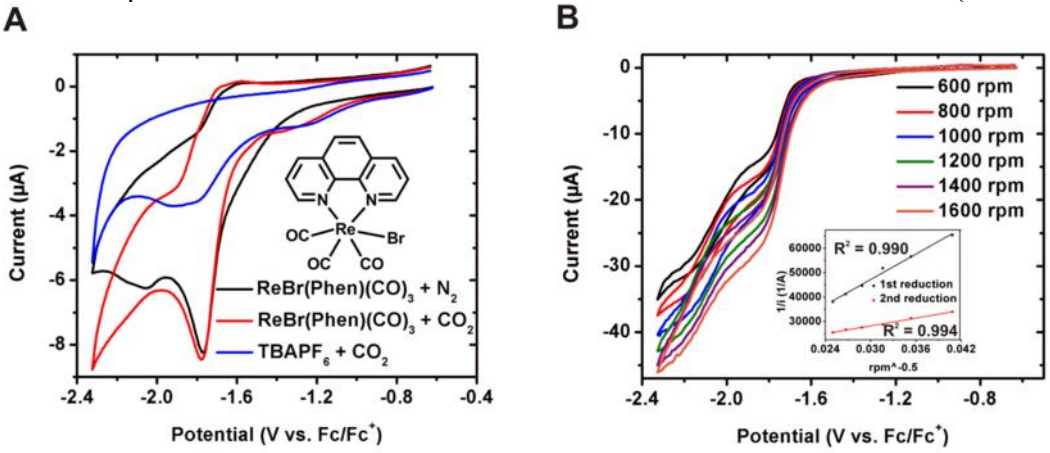

Figure 2.29. (A) Cyclic voltammogram of $ReBr(Phen)(CO)_3$ under both nitrogen and CO_2 and electrolyte (0.1 M $TBAPF_6$ in acetonitrile) under CO_2. (B) Cyclic voltammogram of the rotating disk experiment of $ReBr(Phen)(CO)_3$ in 0.1 M $TBAPF_6$ in acetonitrile. Inset: Levich-Koutecky plot for the data from 600-1600 rpm.

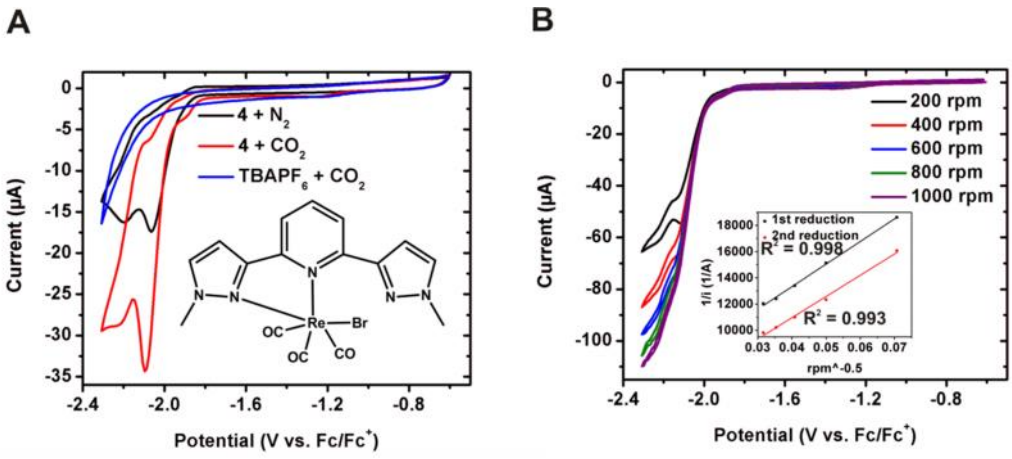

Figure 2.30. (A) Cyclic voltammogram of **4** under both nitrogen and CO_2 and electrolyte (0.1 M $TBAPF_6$ in acetonitrile) under CO_2. (B) Cyclic voltammogram of the rotating disk experiment of **4** in 0.1 M $TBAPF_6$ in acetonitrile. Inset: Levich-Koutecky plot for the data from 200-1000 rpm.

Complex **7**, the EDOT-Hexyl derivative of complex **4**, has a lower reduction potential for the second reduction (-2.154 V vs. Fc/Fc^+) than the model compound (-2.187 V vs. Fc/Fc^+), as shown in Table 2.2. As shown in Figure 2.31A, **7** displays a 1.7-fold increase in both the first and second reductive peaks between the monomer under nitrogen and the monomer under a CO_2-rich atmosphere. A similar increase (1.8-fold increase) in the reductive current going from nitrogen to CO_2 is observed with **4**, the analogous model complex without appended EDOT-Hexyl groups. Similarly, the EDOT-Hexyl-functionalized rhenium(I) bipyridine complex, **8**, has a lower reduction potential at -1.865 V (vs. Fc/Fc^+) than the unfunctionalized model complex, $ReBr(Bipy)(CO)_3$ (-2.114 V vs. Fc/Fc^+) due to the presence of electron withdrawing EDOT groups. In CO_2-saturated acetonitrile, five times more current is observed for the second reduction wave of **8** at a scan rate of 100 mV/s (Figure 2.32A). Despite observing electrocatalytic CO_2 reduction with $ReBr(Phen)(CO)_3$, the $(EDOT\text{-}Hexyl)_2$-Phen derivative, **9**, shows no Faradaic current in the potential range of this experiment (-0.6 V to -2.3 V, vs. Fc/Fc^+).

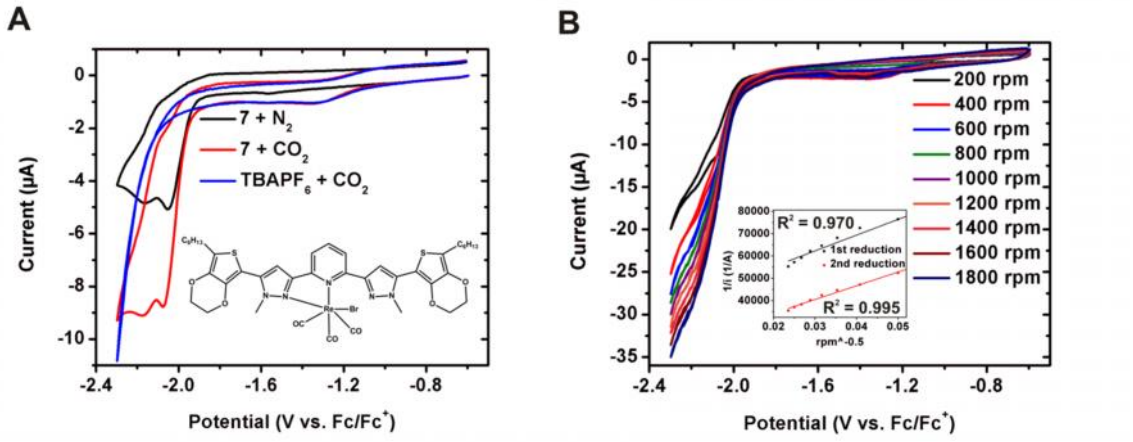

Figure 2.31. (A) Cyclic voltammogram of **7** under both nitrogen and CO_2 and electrolyte (0.1 M $TBAPF_6$ in acetonitrile) under CO_2. (B) Cyclic voltammogram of the rotating disk experiment of **7** in 0.1 M $TBAPF_6$ in acetonitrile. Inset: Levich-Koutecky plot for the data from 200-1800 rpm.

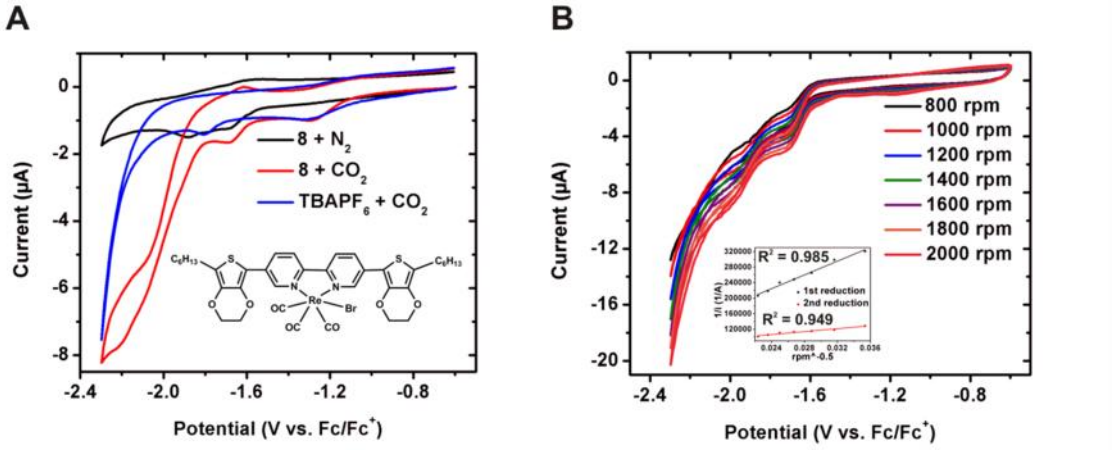

Figure 2.32. (A) Cyclic voltammogram of **8** under both nitrogen and CO_2 and electrolyte (0.1 M $TBAPF_6$ in acetonitrile) under CO_2. (B) Cyclic voltammogram of the rotating disk experiment of **8** in 0.1 M $TBAPF_6$ in acetonitrile. Inset: Levich-Koutecky plot for the data from 800-2000 rpm.

Rotating disk experiments were performed on $ReBr(Bipy)(CO)_3$, $ReBr(Phen)(CO)_3$, and complexes **4**, **7**, and **8** to determine the diffusion coefficient, *D*, of the neutral and singly reduced species, corresponding to the first and second reduction waves, respectively. Using data from the rotating disk experiments, Levich-Koutecky

plots were constructed. Plots with good linear fits ($R > 0.9$) for the first and second reductions indicated usable data for the calculation of *D* (see Experimental Section for details of calculation of *D*). Figure 2.28B is a representative example of the CVs obtained during a rotating disk experiment at rotation rates ranging from 600 rpm to 2000 rpm. Shown in the inset of Figure 2.28B are the Levich-Koutecky plots of the first and second reductions of $ReBr(Bipy)(CO)_3$. CVs from the rotating disk experiments and corresponding Levich-Koutecky plots for $ReBr(Phen)(CO)_3$, **4**, **7**, and **8** are shown in Figures 2.29B, 2.30B, 2.31B, and 2.32B, respectively. Table 2.3 compiles the diffusion coefficients of the neutral and singly reduced species for rhenium(I) complexes demonstrating electrocatalytic activity. These calculated diffusion coefficients are reasonable when compared to those found for similar rhenium(I) and other transition metal bipyridine complexes in the literature.[46,198] Second order rate constants for CO_2 reduction, *k*, were calculated for each complex using the diffusion coefficient and additional data from the electrocatalysis experiment (see Experimental Section for details of calculation of *k*). The rate constant calculated for $ReBr(Bipy)(CO)_3$, 60.59 M^{-1} s^{-1}, closely agrees with the *k* found for Lehn's catalyst by Smieja and Kubiak (50 M^{-1} s^{-1}). The second order rate constants calculated for each of the electrocatalytic *fac*-$ReBr(N-N)(CO)_3$ complexes in this study are shown in Table 2.3. The *k* for **8** (23.88 M^{-1} s^{-1}) is slower than that of the unfunctionalized $ReBr(Bipy)(CO)_3$ complex (60.59 M^{-1} s^{-1}), suggesting that electron donating groups, rather than electron withdrawing substituents like EDOT, should be appended to the bipyridine backbone to increase the rate of CO_2 reduction, as proposed by Kubiak and coworkers.[46] Conversely, the rate constant of the EDOT-Hexyl-functionalized rhenium(I) BPP complex, **7** (3.38 M^{-1} s^{-1}), is 1.5 times faster than the $ReBr(BPP)(CO)_3$ complex (**4**) (2.15 M^{-1} s^{-1}) that contains no functionalization of

the BPP ligand. This suggests that the electron richness of the trinitrogen BPP ligand is much different than that of the dinitrogen bipyridine ligand.

Table 2.3. Diffusion coefficients and rate constants for $ReBr(N\text{-}N)(CO)_3$ complexes

Complex	*D* (neutral) (x 10^{-5}, cm^2/s)	*D* (singly reduced) (x 10^{-5}, cm^2/s)	*k* (M^{-1} s^{-1})
$ReBr(Bipy)(CO)_3$	1.80 ±0.06	1.7 ±0.1	60.59
$ReBr(Phen)(CO)_3$	1.23 ±0.05	1.0 ±0.1	1.37
$ReBr(BPP)(CO)_3$ (**4**)	12 ±3	6 ±1	2.15
$ReBr[(EDOT\text{-}Hexyl)_2\text{-}BPP](CO)_3$ (**7**)	3 ±1	2.0 ±0.6	3.38
$ReBr[(EDOT\text{-}Hexyl)_2\text{-}Bipy](CO)_3$ (**8**)	1.28 ±0.04	1.5 ±0.2	23.88
$ReBr[(EDOT\text{-}Hexyl)_2\text{-}Phen](CO)_3$ (**9**)	[a]	[a]	[a]

[a] No Faradaic current was observed for $ReBr[(EDOT\text{-}Hexyl)_2\text{-}Phen](CO)_3$ (**9**) in the potential range of this experiment (-0.6 V to -2.3 V, vs. Fc/Fc^+).

2.3.6.2. Electrocatalytic Studies of Rhenium(I) Metallopolymers

Electrocatalytic reduction of CO_2 has also been observed with electrode-confined films of **poly-3** and **poly-5** in CO_2-saturated solutions of acetonitrile. These polymeric electrocatalytic systems offer advantages over traditional homogeneous catalysts such as $ReBr(Bipy)(CO)_3$, $ReBr(Phen)(CO)_3$, **4**, **7**, and **8**. Polymeric electrode-confined electrocatalysts often require smaller amounts of catalyst for efficient conversion of the substrate and allow for reduction products to be easily separated from the catalyst. Additionally, increased catalytic reactivity is observed with electrode-confined electrocatalysts due to stabilization of the catalyst and the absence of normal solvation pathways that lead to deactivation of the catalyst. The CVs of electrocatalytic polymeric systems are much simpler than those of the monomer counterparts, as illustrated in Figure 2.33. Under nitrogen, the electrode-confined polymer films only have one irreversible reduction peak present in the CV. Under a CO_2-rich atmosphere, **poly-3** and **poly-5** show an enhancement in the reductive current along with a cathodic shift outside the window of the electrochemical experiment (Figure 2.33). Notably, no electrocatalytic activity was

detected for **poly-6.** Little or no current enhancement was observed for the reductive peak of **poly-6** under an atmosphere of CO_2. For **poly-3**, an irreversible reduction peak at -1.518 V (vs. Fc/Fc^+) is observed in the absence of CO_2, as shown in Figure 2.33A. In CO_2-saturated acetonitrile, a 6-fold enhancement of the cathodic current is observed at a scan rate of 100 mV/s for **poly-3**. As depicted in Figure 2.33B, **poly-5** has an irreversible reduction peak at -1.760 V (vs. Fc/Fc^+). A 1.2-fold increase in the current of this reduction peak is observed upon moving from a nitrogen-rich atmosphere to a CO_2-rich atmosphere. Polymer films of **poly-3** and **poly-5** have larger reduction currents than the monomeric EDOT-Hexyl-substituted systems (**7** and **8**, respectively), demonstrating the feasibility of these polymers as the next generation of electrocatalyts for the reduction of CO_2.

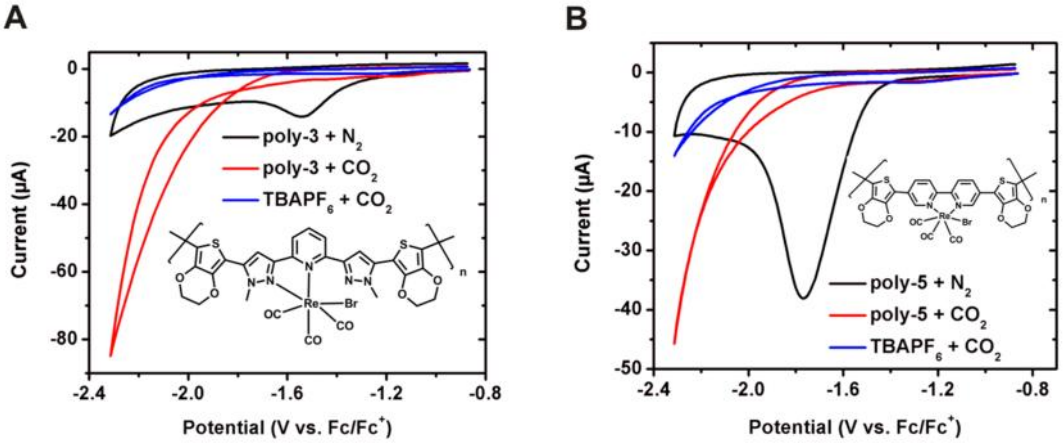

Figure 2.33. (A) Cyclic voltammogram of **poly-3** under both nitrogen and CO_2 and electrolyte (0.1 M $TBAPF_6$ in acetonitrile) under CO_2. (B) Cyclic voltammogram of **poly-5** under both nitrogen and CO_2 and electrolyte (0.1 M $TBAPF_6$ in acetonitrile) under CO_2.

2.4. CONCLUSIONS

In summary, we have reported a series of novel tricarbonyl rhenium(I) diimine monomers, *fac*-$ReBr(N\text{-}N)(CO)_3$, functionalized with thiophene or EDOT groups that

can be easily electropolymerized into electrode-confined conducting metallopolymers. These metallopolymers show uniform film growth and good ionic porosity as electrode-confined films, demonstrating that these metallopolymeric systems are promising candidates for electroactive materials. The rhenium(I) diimine monomers were characterized by single crystal X-ray diffraction and photophysical methods. All of the *fac*-ReBr(N-N)$(CO)_3$ monomers display visible photoluminescence in solution *via intra*ligand fluorescence and phosphorescence and ^{3}MLCT phosphorescence. Additionally, both the monomers and electrode-confined metallopolymers show electrocatalytic activity towards the reduction of CO_2. Future efforts will be focused on determining the mechanism of CO_2 reduction by these small molecules and metallopolymers through infrared spectroelectrochemistry (FTIR-SEC).

2.5. SUPPLEMENTAL DATA: CRYSTALLOGRAPHIC DATA

Table 2.4. Crystal data and structure refinement for **Th_2-BPP**

Formula	$C_{21}\ H_{17}\ N_5\ S_2$
FW	403.52
T (K)	223(2)
Crystal system	Triclinic
Space group	[illegible]
a (Å)	10.045(2)
b (Å)	10.104(2)
c (Å)	20.422(4)
α (deg)	100.221(8)
β (deg)	101.683(9)
γ (deg)	91.634(8)
V ($Å^3$)	1993.1(7)
Z	4
ρ (g/cm^3)	1.345
μ (mm^{-1})	0.284
F(000)	840
θ (deg)	2.99 to 27.50
Index ranges	$-13 \le h \le 12$
	$-12 \le k \le 13$
	$-26 \le l \le 26$
Absorption correction	Multi-scan
Max. and min. transmission	0.9172 and 0.8326
GOF on F^2	1.056
$R1$, w$R2$ [$I > 2\sigma(I)$]	0.0731, 0.1668
$R1$, w$R2$ (all data)	0.0966, 0.1781
Largest diff. peak and hole ($e.Å^{-3}$)	0.509 and -0.551

Table 2.5. Selected bond lengths (Å) and angles (°) for **Th_2-BPP**

Bond distances (Å)			
S(1A)-C(1A)	1.725(3)	N(9)-N(13)	1.356(3)
S(1A)-C(4A)	1.702(6)	S(1AC)-C(1AC)	1.685(4)
C(1A)-C(2A)	1.355(7)	S(1AC)-C(4AC)	1.680(6)
C(1A)-C(24)	1.459(4)	C(1AC)-C(2AC)	1.390(1)
C(2A)-C(3A)	1.450(1)	C(1AC)-C(31C)	1.452(3)
C(3A)-C(4A)	1.340(1)	C(2AC)-C(3AC)	1.460(1)
S(1AA)-C(1AA)	1.718(3)	C(3AC)-C(4AC)	1.330(1)
S(1AA)-C(4AA)	1.763(6)	S(1AF)-C(1AF)	1.711(4)
C(1AA)-C(2AA)	1.318(6)	S(1AF)-C(4AF)	1.726(6)
C(1AA)-C(24A)	1.459(4)	C(1AF)-C(2AF)	1.339(8)
C(2AA)-C(3AA)	1.409(9)	C(1AF)-C(31)	1.462(5)
C(3AA)-C(4AA)	1.364(9)	C(2AF)-C(3AF)	1.420(1)
N(1)-C(52)	1.466(4)	C(3AF)-C(4AF)	1.339(9)
N(1)-N(7)	1.357(7)	N(12)-C(43)	1.460(4)
N(9)-C(3)	1.458(4)	N(12)-N(2)	1.359(4)
N(14)-C(40)	1.459(4)	N(14)-N(11)	1.357(3)
Bond angles (°)			
C(19)-C(30)-C(26)	128.2(2)	S(1A)-C(1A)-C(24)	118.1(2)
C(23)-C(27)-C(33)	127.1(2)	C(2A)-C(1A)-C(24)	131.5(4)
N(6)-C(23)-C(27)	114.9(2)	S(1AA)-C(1AA)-C(24A)	123.6(2)
N(7)-N(1)-C(52)	118.1(2)	C(2AA)-C1(AA)-C(24A)	123.7(3)
N(13)-N(9)-C(3)	118.5(2)		

Table 2.6. Crystal data and structure refinement for **1**

Formula	$C_{24}\ H_{17}\ Br\ N_5\ O_3\ Re\ S_2$
FW	753.66
T (K)	100(2)
Crystal system	Monoclinic
Space group	$P2_1/n$
a (Å)	14.664(2)
b (Å)	9.8970(10)
c (Å)	17.330(2)
α (deg)	90.000
β (deg)	102.493(2)
γ (deg)	90.000
V (Å^3)	2455.5(5)
Z	4
ρ (g/cm^3)	2.039
μ (mm^{-1})	6.784
F(000)	1448
θ (deg)	4.60 to 27.50
Index ranges	$-19 \le h \le 19$
	$-12 \le k \le 12$
	$-22 \le l \le 22$
Absorption correction	Semi-empirical from equivalents
Max. and min. transmission	1.000 and 0.385
GOF on F^2	1.843
$R1$, w$R2$ [I > 2σ (I)]	0.0603, 0.1840
$R1$, w$R2$ (all data)	0.0654, 0.1896
Largest diff. peak and hole (e.Å^{-3})	3.192 and -2.645

Table 2.7. Selected bond lengths (Å) and angles (°) for **1**

Bond distances (Å)			
Re(1)-C(23)	1.895(6)	Re(1)-N(4)	2.135(5)
Re(1)-C(22)	1.902(6)	Re(1)-N(3)	2.259(4)
Re(1)-C(24)	1.917(6)	Re(1)-Br(1)	2.6222(6)
Re(1)-N(4)	2.135(5)		
Bond angles (°)			
C(23)-Re(1)-C(22)	86.2(2)	C(23)-Re(1)-Br(1)	90.38(17)
C(23)-Re(1)-C(24)	90.8(3)	C(22)-Re(1)-Br(1)	93.20(16)
C(22)-Re(1)-C(24)	89.8(2)	C(24)-Re(1)-Br(1)	176.81(19)
C(23)-Re(1)-N(4)	170.6(2)	N(4)-Re(1)-Br(1)	83.62(13)
C(22)-Re(1)-N(4)	101.3(2)	N(3)-Re(1)-Br(1)	82.87(11)
C(24)-Re(1)-N(4)	94.9(2)	C(8)-N(3)-Re(1)	127.8(4)
C(23)-Re(1)-N(3)	98.0(2)	C(12)-N(3)-Re(1)	113.7(4)
C(22)-Re(1)-N(3)	174.3(2)	C(13)-N(4)-N(5)	105.5(5)
C(24)-Re(1)-N(3)	94.0(2)	C(13)-N(4)-Re(1)	118.0(4)
N(4)-Re(1)-N(3)	74.14(18)	N(5)-N(4)-Re(1)	136.3(4)

Table 2.8. Crystal data and structure refinement for **2**

Formula	$C_{30.41}\ H_{26.82}\ Cl_{0.82}\ F_3\ N_6\ O_6\ Re\ S_3$
FW	940.68
T (K)	100(2)
Crystal system	Triclinic
Space group	[illegible]
a (Å)	12.470(5)
b (Å)	16.754(5)
c (Å)	18.372(5)
α (deg)	95.650(5)
β (deg)	104.302(5)
γ (deg)	99.748(5)
V (Å^3)	3625.9
Z	4
ρ (g/cm^3)	1.723
μ (mm^{-1})	3.650
F(000)	1853
θ (deg)	1.16 to 27.48
Index ranges	$-13 \le h \le 16$
	$-21 \le k \le 21$
	$-23 \le l \le 23$
Absorption correction	Multi-scan
GOF on F^2	1.151
*R*1, w*R*2 [I > 2σ (I)]	0.0557, 0.1362
*R*1, w*R*2 (all data)	0.0698, 0.1423
Largest diff. peak and hole (e.Å^{-3})	3.034 and -2.177

Table 2.9. Selected bond lengths (Å) and angles (°) for **2**

Bond distances (Å)			
Re(1-1)-N(2-1)	2.181(6)	Re(1-1)-C(3-1)	1.926(8)
Re(1-1)-N(4-1)	2.104(8)	Re(1-1)-C(4-1)	2.243(6)
Re(1-1)-C(1-1)	1.967(7)	C(4-1)-N(1-1)	1.144(10)
Re(1-1)-C(2-1)	1.906(7)		
Bond angles (°)			
N(2-1)-Re(1-1)-N(4-1)	73.8(2)	C(4-1)-Re(1-1)-C(2-1)	91.8(3)
N(2-1)-Re(1-1)-C(4-1)	85.7(3)	N(4-1)-Re(1-1)-C(3-1)	99.6(3)
N(2-1)-Re(1-1)-C(2-1)	101.5(3)	N(4-1)-Re(1-1)-C(1-1)	97.4(3)
N(2-1)-Re(1-1)-C(1-1)	94.7(3)	N(4-1)-Re(1-1)-C(2-1)	171.1(3)
N(2-1)-Re(1-1)-C(3-1)	173.1(3)	C(3-1)-Re(1-1)-C(1-1)	88.0(3)
C(4-1)-Re(1-1)-N(4-1)	80.5(3)	C(3-1)-Re(1-1)-C(2-1)	84.8(3)
C(4-1)-Re(1-1)-C(3-1)	91.3(3)	C(1-1)-Re(1-1)-C(2-1)	90.4(3)
C(4-1)-Re(1-1)-C(1-1)	77.7(3)		

Table 2.10. Crystal data and structure refinement for **$EDOT_2$-BPP**

Formula	$C_{25}\,H_{21}\,N_5\,O_4\,S_2$
FW	519.59
T (K)	293(2)
Crystal system	Monoclinic
Space group	$P2_1/c$
a (Å)	10.800(5)
b (Å)	11.180(5)
c (Å)	19.204(5)
α (deg)	90.000(5)
β (deg)	96.410(5)
γ (deg)	90.000(5)
V (Å^3)	2304.27
Z	4
ρ (g/cm^3)	1.498
μ (mm^{-1})	0.276
F(000)	1080
Crystal size (mm)	.21 x .29 x .30
θ (deg)	3.01 to 27.48
Index ranges	$-14 \le h \le 12$
	$-14 \le k \le 14$
	$-24 \le l \le 24$
Absorption correction	Multi-scan
Max. and min. transmission	1.000 and 0.637
GOF on F^2	2.162
$R1$, w$R2$ [I > 2σ (I)]	0.0421, 0.1045
$R1$, w$R2$ (all data)	0.0498, 0.1054
Largest diff. peak and hole (e.Å^{-3})	0.691 and -0.688

Table 2.11. Selected bond lengths (Å) and angles (°) for **$EDOT_2$-BPP**

Bond distances (Å)			
N(1)-N(2)	1.350(2)	O(1)-C(4)	1.371(2)
N(1)-C(7)	1.456(2)	O(2)-C(1)	1.452(2)
N(2)-C(10)	1.336(2)	O(2)-C(5)	1.369(2)
N(3)-C(11)	1.346(2)	O(3)-C(21)	1.364(2)
N(3)-C(15)	1.349(2)	O(3)-C(25)	1.447(3)
N(4)-N(5)	1.345(2)	O(4)-C(22)	1.374(2)
N(4)-C(16)	1.347(2)	O(4)-C(24)	1.439(2)
N(5)-C(19)	1.461(2)	S(1)-C(3)	1.719(2)
C(6)-C(8)	1.459(2)	S(1)-C(6)	1.738(2)
C(18)-C(20)	1.458(3)	S(2)-C(20)	1.738(2)
O(1)-C(2)	1.437(2)	S(2)-C(23)	1.727(2)
Bond angles (°)			
N(3)-C(11)-C(10)	115.99(15)	C(15)-C(16)-N(4)	119.96(12)
N(3)-C(15)-C(16)	115.82(15)	C(19)-N(5)-N(4)	118.48(14)
C(11)-C(10)-N(2)	120.31(15)	N(5)-C(18)-C(20)	125.05(16)
N(1)-C(8)-C(6)	124.08(16)	S(1)-C(6)-C(8)	122.84(14)
C(7)-N(1)-N(2)	117.82(14)	S(2)-C(20)-C(18)	124.83(14)

Table 2.12. Crystal data and structure refinement for **3**

Formula	C_{28} H_{21} Br Re N_5 O_7 S_2
FW	869.73
T (K)	233(2)
Crystal system	Monoclinic
Space group	$P2_1/n$
a (Å)	9.469(5)
b (Å)	22.642(5)
c (Å)	14.257(5)
α (deg)	90.00(5)
β (deg)	106.87(5)
γ (deg)	90.00(5)
V ($Å^3$)	2925(2)
Z	4
ρ (g/cm^3)	1.975
μ (mm^{-1})	5.72
F(000)	1688
crystal size (mm)	0.21 × 0.11 × 0.07
θ (deg)	3.0 to 27.50
Index ranges	$-12 \le h \le 12$
	$-29 \le k \le 29$
	$-18 \le l \le 18$
Absorption correction	Multi-scan
Max. and min. transmission	1.000 and 0.739
GOF on F^2	1.126
$R1$, w$R2$ [$I > 2\sigma(I)$]	0.0485, 0.0947
$R1$, w$R2$ (all data)	0.0723, 0.0882
Largest diff. peak and hole ($e.Å^{-3}$)	1.18 and -1.36

Table 2.13. Selected bond lengths (Å) and angles (º) for **3**

Bond distances (Å)			
Re(1)-C(26)	1.933(7)	Re(1)-Br(1)	2.6276(9)
Re(1)-C(27)	1.899(8)	Re(1)-N(3)	2.222(5)
Re(1)-C(28)	1.998(9)	Re(1)-N(4)	2.179(5)
Bond angles (°)			
N(3)-Re(1)-Br(1)	82.09(12)	C(26)-Re(1)-C(27)	85.8(3)
N(3)-Re(1)-N(4)	74.22(18)	C(26)-Re(1)-C(28)	92.6(3)
C(27)-Re(1)-N(4)	99.5(2)	C(28)-Re(1)-Br(1)	176.85(19)
C(28)-Re(1)-N(3)	94.8(2)	C(28)-Re(1)-N(4)	95.6(2)
N(4)-Re(1)-Br(1)	83.33(13)	C(28)-Re(1)-C(27)	88.5(3)
C(26)-Re(1)-N(3)	100.0(2)	C(27)-Re(1)-N(3)	173.2(2)
C(26)-Re(1)-Br(1)	88.2(2)	C(27)-Re(1)-Br(1)	94.6(2)
C(26)-Re(1)-N(4)	170.3(2)		

Table 2.14. Crystal data and structure refinement for **BPP**

Formula	$C_{13}\,H_{13}\,N_5$
FW	239.28
T (K)	100(2)
Crystal system	Monoclinic
Space group	$P2_1/c$
a (Å)	10.2593(4)
b (Å)	21.3727(8)
c (Å)	13.4582(12)
α (deg)	90.000
β (deg)	124.909(5)
γ (deg)	90.000
V (Å^3)	2420.0(3)
Z	8
ρ (g/cm^3)	1.314
μ (mm^{-1})	0.085
F(000)	1008
Crystal size (mm)	.357 x .275 x .151
θ (deg)	3.04 to 27.49
Index ranges	$-13 \le h \le 13$
	$-27 \le k \le 27$
	$-17 \le l \le 17$
Absorption correction	Multi-scan
Max. and min. transmission	1.000 and 0.910
GOF on F^2	1.046
$R1$, w$R2$ [I > 2σ (I)]	0.0414, 0.1091
$R1$, w$R2$ (all data)	0.0467, 0.1129
Largest diff. peak and hole (e.Å^{-3})	0.364 and -0.331

Table 2.15. Selected bond lengths (Å) and angles (º) for **BPP**

Bond distances (Å)			
N(1)-C(1)	1.455(2)	C(2)-C(3)	1.376(3)
N(1)-C(2)	1.351(2)	C(3)-C(4)	1.403(2)
N(1)-N(2)	1.3446(13)	C(4)-C(5)	1.471(2)
N(2)-C(4)	1.3432(14)	C(5)-C(6)	1.394(2)
N(3)-C(5)	1.3465(14)	C(6)-C(7)	1.380(3)
N(3)-C(9)	1.3462(14)	C(7)-C(8)	1.381(2)
N(4)-N(5)	1.3465(13)	C(8)-C(9)	1.393(2)
N(4)-C(10)	1.3414(15)	C(9)-C(10)	1.42(2)
N(5)-C(12)	1.348(2)	C(10)-C(11)	1.407(2)
N(5)-C(13)	1.455(2)	C(11)-C(12)	1.379(2)
Bond angles (°)			
N(3)-C(5)-C(4)	116.78(10)	C(1)-N(1)-N(2)	119.40(10)
N(3)-C(9)-C(10)	116.93(10)	C(13)-N(5)-N(4)	118.86(10)
C(4)-N(2)-N(1)	104.71(10)	C(1)-N(1)-C(2)	128.09(10)
C(10)-N(4)-N(5)	104.72(9)	C(13)-N(5)-C(12)	128.51(10)

Table 2.16. Crystal data and structure refinement for **4**

Formula	C_{16} H_{13} Br N_5 O_3 Re
FW	589.42
T (K)	153(2)
Crystal system	Monoclinic
Space group	$P2_1/n$
a (Å)	14.667(5)
b (Å)	8.336(5)
c (Å)	15.692(5)
α (deg)	90.000
β (deg)	110.945(5)
γ (deg)	90.000
V (Å^3)	1791.8(14)
Z	4
ρ (g/cm^3)	2.185
μ (mm^{-1})	9.038
F(000)	1112
Crystal size (mm)	.266 x .093 x .037
θ (deg)	3.27 to 25.00
Index ranges	$-17 \leq h \leq 17$
	$-9 \leq k \leq 9$
	$-18 \leq l \leq 18$
Absorption correction	Multi-scan
Max. and min. transmission	1.000 and 0.442
GOF on F^2	1.643
$R1$, w$R2$ [I > 2σ (I)]	0.0706, 0.1096
$R1$, w$R2$ (all data)	0.0879, 0.1128
Largest diff. peak and hole (e.Å^{-3})	2.842 and -4.570

Table 2.17. Selected bond lengths (Å) and angles (°) for **4**

Bond distances (Å)			
Re(1)-C(14)	1.91(2)	Re(1)-Br(1)	2.642(2)
Re(1)-C(15)	1.93(1)	Re(1)-N(2)	2.17(1)
Re(1)-C(16)	1.91(1)	Re(1)-N(3)	2.276(9)
Bond angles (°)			
N(3)-Re(1)-C(15)	101.7(5)	Br(1)-Re(1)-N(3)	81.0(3)
N(3)-Re(1)-C(16)	167.5(5)	N(2)-Re(1)-C(15)	174.4(5)
C(15)-Re(1)-C(16)	87.0(6)	N(2)-Re(1)-Br(1)	87.4(3)
C(15)-Re(1)-C(14)	87.6(7)	C(15)-Re(1)-Br(1)	89.3(4)
C(14)-Re(1)-C(16)	93.6(7)	C(16)-Re(1)-Br(1)	90.2(5)
C(14)-Re(1)-Br(1)	174.9(5)	N(2)-Re(1)-C(14)	95.4(6)
N(3)-Re(1)-N(2)	73.3(4)	N(2)-Re(1)-C(16)	97.5(6)
C(15)-Re(1)-N(3)	101.7(5)	N(3)-Re(1)-C(14)	95.7(6)

Table 2.18. Crystal data and structure refinement for **5**

Formula	C_{25} H_{16} Br N_2 O_7 Re S_2
FW	786.63
T (K)	100(2)
Crystal system	Triclinic
Space group	[illegible]
a (Å)	10.231(9)
b (Å)	10.814(8)
c (Å)	13.518(6)
α (deg)	111.625(7)
β (deg)	104.510(8)
γ (deg)	97.921(9)
V (Å^3)	1301.2(16)
Z	2
ρ (g/cm^3)	2.008
μ (mm^{-1})	6.414
F(000)	756
Crystal size (mm)	0.200 × 0.200 × 0.200
θ (deg)	1.71 to 24.99
Index ranges	$-12 \le h \le 12$
	$-12 \le k \le 12$
	$-16 \le l \le 12$
Absorption correction	Multi-scan
Max. and min. transmission	1.000 and 0.6861
GOF on F^2	1.158
*R*1, w*R*2 [I > 2σ (I)]	0.1120, 0.2883
*R*1, w*R*2 (all data)	0.1444, 0.3376
Largest diff. peak and hole (e.Å^{-3})	3.949 and -3.237

Table 2.19. Selected bond lengths (Å) and angles (º) for **5**

Bond distances (Å)			
Re(1)-C(23)	1.950(20)	Re(1)-Br(1)	2.619(2)
Re(1)-C(24)	1.950(20)	Re(1)-N(1)	2.200(10)
Re(1)-C(25)	1.950(20)	Re(1)-N(2)	2.210(10)
Bond angles (°)			
N(1)-Re(1)-Br(1)	86.6(4)	N(1)-Re(1)-C(25)	90.5(7)
N(2)-Re(1)-Br(1)	87.8(4)	N(2)-Re(1)-C(23)	174.0(6)
C(23)-Re(1)-Br(1)	92.0(6)	N(2)-Re(1)-C(24)	99.0(7)
C(24)-Re(1)-Br(1)	91.9(5)	N(2)-Re(1)-C(25)	89.8(7)
C(25)-Re(1)-Br(1)	176.6(6)	C(23)-Re(1)-C(24)	87.0(8)
N(1)-Re(1)-N(2)	74.9(5)	C(23)-Re(1)-C(25)	90.2(8)
N(1)-Re(1)-C(23)	99.1(7)	C(24)-Re(1)-C(25)	90.8(8)
N(1)-Re(1)-C(24)	173.7(6)		

Chapter 3: Electronic Properties of Alkylated and Polyfluoroalkylated Oligothiophenes as Models for Buried Electronic Interfaces in Photovoltaic Devices

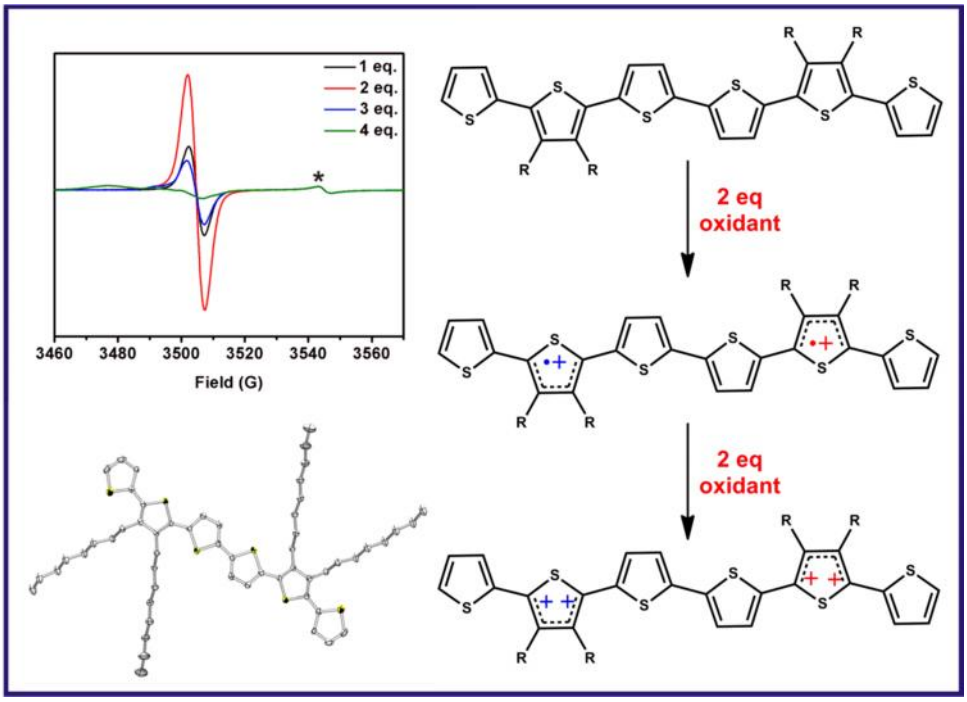

3.1. INTRODUCTION

Conjugated polymers, such as polyacetylene, polypyrrole, and polythiophene, are inherently insulating due to the large (> 1.5 eV) bandgap or difference between the conduction and valence bands. However, in 1977, McDiarmid *et al.* discovered that polyacetylene became conductive, ~10^3 S·cm^{-1}, upon doping.[199] For this reason, the conjugated conducting polymer polythiophene and the solution-processable polyalkylthiophene (PAT), have found applications in photovoltaics, polymer light-emitting diodes (PLEDs), chemical sensors, and memory devices.[6,200-202] Although PATs are inherently insulating, electrical conductivity can be achieved by removing an electron from the valence band and creating a polaron (radical cation). When a conjugated polymer is oxidized, a polaron is formed and discrete electronic states form in the bandgap due to the lowering and raising of the conduction and valence bands, respectively. Upon further ionization, the second electron can be removed from the polaron or from another orbital in the chain. If the electron is removed from the polaron, a bipolaron (or dication) is formed. However, if the electron is removed from another orbital, two polarons are formed. The distortion energy for a bipolaron is greater than that for two polarons and thus, the electronic states in a bipolaron are farther away from the valence and conduction bands than those formed when a second polaron is created. This difference in distortion energy is attributed to the increase in lattice relaxation around a dication than around a monocation. Additionally, the ionization energy to form a bipolaron is much less than that of two polarons, indicating that the formation of a bipolaron is favored.[199] Upon further oxidation, more bipolaron states form in the bandgap and begin to overlap to form bipolaron bands. These bipolaron bands then begin to broaden until the upper and lower bipolaron bands merge with the conduction and valence bands. At this point, the bandgap is significantly decreased and the conductivity

of the conjugated polymer begins to mimic that of a metal.[203] Additionally, the high electrical conductivity and stability of PATs is attributed to the formation of π stacks between the planar PAT backbones.[201]

Traditionally, PATs have been prepared electrochemically, by polymerization with $FeCl_3$, or through halo-Grignard Kumada cross-coupling reactions to yield high molecular weight, solution-processable polymers.[201,204,205] The Kumada cross-coupling and $FeCl_3$ synthetic routes, however, produce irregular PATs with little control over the regioregularity of the products. Head-to-tail (HT) regioregularity is desired to achieve good electrical conductivity. PATs with head-to-tail coupling can easily achieve low energy conformations with high degrees of conjugation. Irregular couplings in PATs, such as head-to-head (HH) and tail-to-tail (TT), force the thiophenes to twist due to the steric demands associated with the orientation of the alkyl chains. This, in turn, leads to an increase in the bandgap, thus lowering the conductivity of the material.[201] Upon doping with iodide, irregular PATs have conductivities of 0.1-10 $S \cdot cm^{-1}$ while regioregular PATs have conductivities of 100-1000 $S \cdot cm^{-1}$.[200] To target regioregularity, three synthetic routes, utilizing a nickel catalyst, are used: the McCullough, the Rieke, or Grignard Metathesis (GRIM) methods.[200,201]

Despite high electrical conductivity and the potential to function as the active layer in a variety of electronic devices, PATs possess a multitude of flaws making structure-property relationships difficult to establish. Mislinkages, varying polymer chain lengths, lack of crystallinity, and other defects limit the understanding of the structure of a polymer, making structure-property relationships difficult to establish.[201,206] In particular, it is crucial to know the backbone conformation and packing in order to understand the electronic properties of the polymer for application purposes.[206,207] Oligothiophenes, on the other hand, serve as good models for polymers because the

regiochemistry can be controlled. In addition to regioregularity, chain and conjugation length of the oligothiophene are also well defined allowing 'real' structure-property correlations to be made.[201] This structure-property information of the oligothiophene can then be extrapolated to an infinite chain length of the corresponding polymer.[207] Additionally, oligothiophenes are highly crystalline materials in which the exact structure of the oligomer can be determined through single crystal X-ray diffraction. PATs, on the other hand, often lack uniform crystallinity in bulk polymeric samples and single crystals cannot be grown to determine the molecular structure. Oligothiophenes have enhanced solubility, purity, and processability over polythiophene counterparts making these oligomers attractive materials for electronic devices. Even after extensive purification steps, PATs often contain impurities from Fe and Ni polymerization catalysts. Because of these advantageous properties, oligothiophenes have been used as the active layers in field-effect transistors and light-emitting diodes.[208-213] Interestingly, α-sexithiophene demonstrated better performance than polythiophene in field-effect transistor applications.[208,214,215]

Current organic photovoltaic technology utilizes regioregular-poly(3-hexylthiophene), RR-P3HT, as the electron-donating layer. To study how parameters such as the crystallinity, electronic coupling, and molecular morphology of P3HT influence charge separation at donor/acceptor interfaces, 3,3'''',4',4''''-tetraalkylsexithiophene, 6Th, is used as the oligomeric model for the polymeric RR-P3HT. Using 6Th as a model for RR-P3HT makes it easier to study structure-property correlations in relation to photovoltaic performance. Substitution at the 3,4 position of 6Th eliminates any synthetic complications associated with preparing regioregular 3-substituted oligo- or polythiophenes. Furthermore, 6Th is soluble in a wide variety of organic solvents so extremely pure, solution-processable oligomers can be produced.

Additionally, single crystals of 6Th, suitable for X-ray diffraction, can be grown for structural investigations. The convergent, efficient synthesis of 6Th allows a library of oligothiophenes, in which the alkyl group is varied, to be easily made (*vide infra*).

Herein, we report the design, synthesis, and electronic properties of a library of sexithiophenes with varying R groups in the 3,3'''' and 4',4'''' positions. The R group is systematically varied from a short ethyl chain (**1**) to a long decyl chain (**5**), as listed in Scheme 3.1. Additionally, a 6Th with an appended trifluorohexyl group (**6**) was synthesized to study the polarity effects that a fluorinated R group may have on the electronic properties of the oligothiophene. This library of sexithiophenes will be used to study how parameters such as packing and molecular morphology, crystallinity, and electronic coupling influence charge separation at electronic interfaces in organic photovoltaic devices. In this study, we inspect how the appended R group of a series of sexithiophenes affects crystallinity and the electronic properties which ultimately dictate photovoltaic performance.

Scheme 3.1. Synthesis of a library of sexithiophene molecules, **1**-**6**

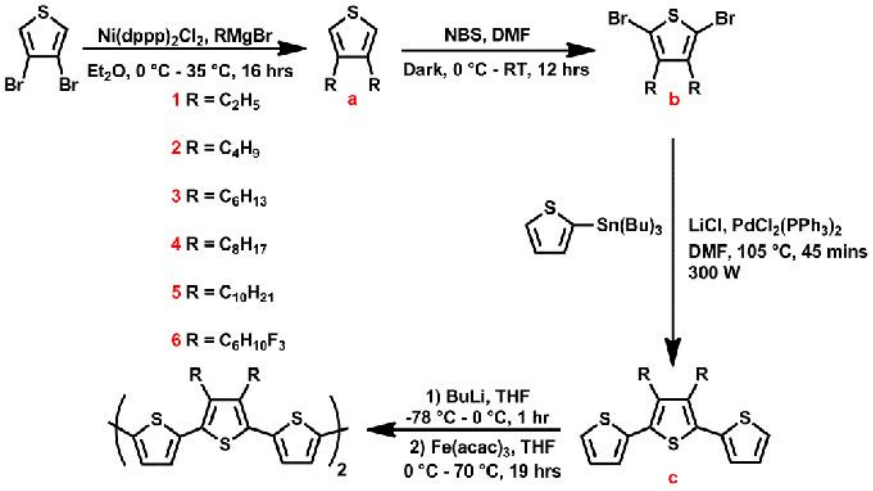

3.2.EXPERIMENTAL

3.2.1. Instrumentation

3.2.1.1. General Methods

Air- and moisture-sensitive reactions were carried out in flame-dried glassware using standard Schlenk techniques under an inert nitrogen atmosphere. All chemicals and DMF were purchased from commercial sources and used as received. All other solvents were dried using an Innovative Technology, Pure Solv solvent purifier with a double purifying column. For chemical oxidations and reductions, tris(4-bromophenyl)ammoniumyl hexachloroantimonate ($[(BrC_6H_4)_3N]^{+\cdot}[SbCl_6]^-$) and decamethyl ferrocene ([FeCp*$_2$]), respectively, were used without further purification. In methylene chloride, $[(BrC_6H_4)_3N]^{+\cdot}[SbCl_6]^-$ has a formal potential of +0.70 V (vs. Fc/Fc^+) in CH_2Cl_2 and [FeCp*$_2$] has a formal potential of -0.59 V (vs. Fc/Fc^+) in CH_2Cl_2.[216] ^1H NMR (400 MHz) and $^{13}C\{^1H\}$ NMR (100 MHz) spectra were obtained on a Varian (400 MHz) spectrometer and were referenced to residual solvent peaks. NMR peaks are reported in ppm and coupling constants are reported in Hz. Elemental analyses were performed by QTI, Whitehouse, NJ (www.qtionline.com). Low-resolution and high-resolution mass spectrometery was carried out by a Thermo Finngan TSQ 700 and Waters Autospec Ultima, respectively. The microwave assisted reaction was performed in a CEM Discover reactor. Melting points were recorded with an OptiMelt Automated Melting Point System with digital image processing technology from Stanford Research System (SRS, Sunnyvale, CA).

3.2.1.2. Crystal Structure Determination

The single–crystal diffraction data were collected on a Rigaku AFC12 diffractometer with a Saturn 724+ CCD, a Rigaku SCX-Mini diffractometer with a

Mercury CCD, or a Nonius Kappa CCD diffractometer using a graphite monochromator with MoKα radiation (λ = 0.71070 Å). Absorption corrections were applied using the multi-scan technique using either Abscor[156] for the Rigaku data or Scalepack[157] for the Nonius data. Data reduction were performed using the Rigaku Americas Corporation's Crystal Clear version 1.40.[158] The structures were solved by direct methods and refined anisotropically using full-matrix least-squares methods with the SHELX 97 program package.[159] The coordinates of the non-hydrogen atoms were refined anisotropically, while hydrogen atoms were included in the calculation isotropically but not refined. Neutral atom scattering factors and values used to calculate the linear absorption coefficient are from the International Tables for X-ray Crystallography (1992).[160] Tables 3.6, 3.9, 3.11, 3.13, and 3.15 list the crystal data and structure refinement for **1**, **3**, **4**, **5**, and **6**, respectively (Supplemental Data). Selected bond lengths and angles for **1**, **2**, **3**, **4**, **5**, and **6** are given in Tables 3.7, 3.8, 3.10, 3.12, 3.14, and 3.16, respectively (Supplemental Data).

3.2.1.3. Electrochemistry

Electrochemical studies were performed with a GPES system from Eco. Chemie B. V. The electrolyte used was 0.1 M tetrabutylammonium hexafluorophosphate [(*n*-Bu)$_4$N]$^+$[PF$_6$]$^-$ (TBAPF$_6$) which was purified through recrystallization three times from hot ethanol then dried for 3 days under active vacuum at 100-150 ˚C. Electrochemical experiments were carried out in a three-electrode cell with a Ag/AgNO$_3$ reference electrode, a Pt button working electrode (area determined by a standard solution of ferrocene), and a Pt wire counter electrode. To calibrate the reference electrode, ferrocene was used as an external reference to which potentials were corrected. Differential pulse voltammetry (DPV) was performed in CH_2Cl_2 with 0.1 M TBAPF$_6$ supporting electrolyte

with a step potential of 0.00195 V, modulation amplitude of 0.1005 V, an interval time of 0.10 s, and a modulation time of 0.05 s. DPV potentials were also corrected to ferrocene. Electrochemical simulations of CVs were performed using DigiElch software. Currents plotted in Figure 3.13B were calculated using the Randles-Sevcik equation, equation (1)[217]

$$i_p = (2.69 \times 10^5) n^{3/2} A D^{1/2} v^{1/2} c \quad (1)$$

In eqn (1), i_p is the variable of interest, n is the number of electrons (1 or 2, in this case), A is the area of the macroelectrode (0.032 cm^2), D is the diffusion coefficient (3.3 x 10^{-6} cm^2/s, determined for **4** using chronoamperometric studies), v is the scan rate (0.01 V/s-0.5 V/s), and c is the concentration of **4** in 0.1 M $TBAPF_6$ in 1,2-dichloroethane (DCE) (9.20 x 10^{-7} mol/cm^3).

Chronoamperometry experiments were performed with a CH Instruments electrochemical workstation (CHI 700, Austin, TX) in a Faraday cage with a three-electrode cell consisting of a Pt ultramicroelectrode (UME) (10 μm in diameter from BASi), a Pt wire counter electrode, and a $Ag/AgNO_3$ reference electrode. The UME was cleaned by cycling between -0.2 V to +1.4 V (vs. Ag/AgCl) at a scan rate of 100 mV/s for 20 segments in degassed 0.1 M H_2SO_4. Prior to each experiment, the diffusion coefficient (D, 2.24 x 10^{-5} cm^2/s for Fc in 0.1 M $TBAPF_6$ in acetonitrile at 298.15 K[218]) and number of electrons (n, 1 for Fc) were determined for ferrocene (1-3 mM solution in acetonitrile) to ensure sound electrochemical practices. The area of the UME was determined with a standard solution of ferrocene (1-3 mM solution in acetonitrile) before each experiment. Chronoamperometry measurements were made in ~1 mM solutions of 6Th in 0.1 M $TBAPF_6$ in distilled DCE by stepping from +0.3 V to + 1.1 V (vs. $Ag/AgNO_3$) with a sample interval of 0.001 s and a pulse width of 5-20 s. Plots of $i(t)/i_{ss}$ vs. $t^{-1/2}$ were constructed and linear regression was used to calculate the slope and

intercept of the plot. The intercept in each case was very close to one. The diffusion coefficient (D) was calculated using the slope of the linear plot and the radius of the UME (r_0) according to equation (2)[163,219]

$$D = 4r_0^2/(\text{slope})^2\pi^3 \quad (2)$$

The number of electrons, n, was calculated using equation (3)[220]

$$i_{ss} = 4nFDc^*r_0 \quad (3)$$

In eqn (2), i_{ss} is the current from the steady state voltammogram, F is Faraday's constant, D is the calculated diffusion coefficient, c^* is the concentration of analyte, and r_0 is the radius of the UME (determined from a standard solution of ferrocene).

3.2.1.4. Spectroscopy

All spectroscopic data were obtained in CH_2Cl_2 solutions unless otherwise noted. Absorption spectra were recorded on a Varian Cary 6000i UV-VIS-NIR spectrophotometer with Starna Quartz fluorometer cells with a pathlength of 10 mm. Luminescence measurements were recorded on a Photon Technology International QM 4 spectrophotometer equipped with a 6-inch diameter K Sphere-B integrating sphere for quantum yield measurements. The quantum yield was calculated by dividing the area under the emission peak of the complex by the difference between the area under the excitation peak of the sample from that of a blank solution ($A_{em,\ sample}$ / ($A_{ex,\ blank}$ - $A_{ex,\ sample}$), where A = area under peak).[165] Measurements at 77 K were recorded using an optical liquid nitrogen Dewar sample holder. Low-temperature samples were made in 2-methyltetrahydrofuran (2-MeTHF) in quartz 4 mm outer diameter EPR tubes.

3.2.1.5. Electron Paramagnetic Resonance Spectroscopy

EPR spectra were recorded on a Bruker EMX Plus spectrometer at 298 K and at 2.000 mW. All samples were made from fresh solutions in CH_2Cl_2 and prepared

immediately prior to analysis. An aluminum internal reference marker (Bruker Biospin ER4119HS-2100 marker accessory, g-factor = 1.9800 ±0.0006), positioned at 0 mm for maximum signal, was used in each experiment.

3.2.2. Synthesis

3.2.2.1. Synthesis of Oligothiophenes

3,4-diethylthiophene (1a). Prepared according to an analogous procedure described for the synthesis of 3,4-dioctylthiophene (*vide infra*) (1.305 g, 15%). ^{1}H NMR ($CDCl_3$): δ 6.94 (s, 2H), 2.56 (m, 4H), 1.29 (t, *J* = 7.6, 6H); $^{13}C\{^{1}H\}$ NMR (100 MHz, $CDCl_3$): δ 143.3, 119.4, 21.8, 13.6; HRMS (CI+): calcd. for $C_8H_{12}S$: 141.0738. Found 141.0737.

2,5-dibromo-3,4-diethylthiophene (1b). Prepared with slight modification to a literature procedure described by Würthner *et al*.[221] In 50 mL of DMF, **1a** (1.305 g, 9,3 mmol) was dissolved and cooled to 0 ºC under the absence of light. NBS (3.532 g, 19.8 mmol) was dissolved in 75 mL of DMF and added to the reaction mixture dropwise for 1 hour. Once added, the reaction was stirred for 20 minutes at 0 ºC and then warmed to room temperature overnight. The reaction mixture was washed with water and hexanes to give a yellow oil. (2.456 g, 89%). The purity and composition of the target compound was confirmed by comparison of the ^{1}H NMR spectroscopy data to literature values.[221]

3',4'-diethyl-2,2':5',2"-terthiophene (1c). Prepared according to an analogous procedure described for the synthesis of 3',4'-dioctyl-2,2':5'2''-terthiophene (*vide infra*) (74%). ^{1}H NMR ($CDCl_3$): δ 7.30 (dd, *J* = 1.2, 5.4, 2H), 7.15 (dd, *J* = 1.2, 3.4, 2H), 7.06 (dd, *J* = 3.4, 4.8, 2H), 2.76 (m, 4H), 1.23 (t, *J* = 8.0, 6H); $^{13}C\{^{1}H\}$ NMR (100 MHz, $CDCl_3$): δ 141.1, 136.0, 129.8, 127.4, 125.8, 125.3, 21.0, 15.3; HRMS (CI+): calcd. for $C_{16}H_{16}S_3$: 304.0492. Found 305.0490.

3',3'''',4',4''''-tetraethyl-2,2':5',2'':5",2''':5''',2'''':5'''',2''''':sexithiophene (1). Prepared to an analogous procedure described for the synthesis of 3',3'''',4',4''''-tetraoctyl-2,2':5',2'':5",2''':5''',2'''':5'''',2''''':-sexithiophene (*vide infra*) (53%). mp: 168.0 °C; ^{1}H NMR ($CDCl_3$): δ 7.30 (dd, *J* = 1.0, 5.0, 2H), 7.14 (dd, *J* = 1.0, 3.8, 2H), 7.13 (d, *J* = 3.6, 2H), 7.06 (d, *J* = 3.6, 2H), 7.05 (d, *J* = 4.0, 2H), 2.77 (m, 8H), 1.23 (m, 12H); ^{13}C {^{1}H} NMR: δ 141.3, 127.4, 126.4, 125.9, 125.4, 123.9, 21.1 (d, *J* = 14.2), 15.3; UV-Vis (CH_2Cl_2, nm): λ_{max} 412 (ε, 3.78 x 10^4 M^{-1} cm^{-1}); HRMS (CI+) calcd. for $C_{32}H_{30}S_6$: 606.0672. Found 606.0673; Anal. calcd. for $C_{32}H_{30}S_6$: C, 63.32; H, 4.98; N, 0.00. Found: C, 63.30; H, 4.74; N, < 0.05.

3,4-dibutylthiophene (2a). Prepared according to a procedure described by Guo *et al*.[222] (86%). The purity and composition of the target compound was confirmed by comparison of the ^{1}H NMR spectroscopy data to literature values.[222]

2,5-dibromo-3,4-dibutylthiophene (2b). Prepared with slight modification to a literature procedure described by Araki *et al*.[223] In 50 mL of DMF, **2a** (1.389 g, 7.1 mmol) was dissolved and cooled to 0 ºC under the absence of light. NBS (2.682 g, 15 mmol) was dissolved in 75 mL of DMF and added to the reaction mixture dropwise for 1 hour. Once added, the reaction was stirred for 20 minutes at 0 ºC and then warmed to room temperature overnight. The reaction mixture was washed with water and hexanes to give a yellow oil. (1.972 g, 79%). The purity and composition of the target compound was confirmed by comparison of mass spectrometry and ^{1}H NMR and ^{13}C {^{1}H} spectroscopy data to literature values.[223]

3',4'-dibutyl-2,2':5',2"-terthiophene (2c). Prepared with slight modification to a literature procedure described by Araki *et al*.[223] To an 80 mL microwave vessel, **2b** (1.972 g, 5.6 mmol), LiCl (1.206 g, 28 mmol), 2-(tributylstannyl)thiophene (4.950 g, 16 mmol), $PdCl_2(PPh_3)_2$ (210 mg, 0.30 mmol), and 30 mL of DMF were added. The reaction

was run in a microwave reactor for 45 minutes at 300 W and at 105 ºC. The reaction mixture was washed with hexanes and water (3 x 100 mL), dried with Na_2SO_4, and dried *in vacuo*. Product was purified by vacuum distillation to yield a green oil (1.059 g, 53 %). The purity and composition of the target compound was confirmed by comparison of mass spectrometry and ^1H NMR and ^{13}C $\{^1H\}$ spectroscopy data to literature values.[223]

3',3'''',4',4''''-tetrabutyl-2,2':5',2'':5'',2''':5''',2'''':5'''',2'''''-sexithiophene (2). Prepared according to a literature procedure described by Pappenfus *et al*.[224] (53 %). The purity and composition of the target compound was confirmed by comparison of mass spectrometry and ^1H NMR spectroscopy data to literature values.[224]

3,4-dihexylthiophene (3a). Prepared according to a procedure described by Li *et al*.[225] (98%). The purity and composition of the target compound was confirmed by comparison of ^1H NMR and ^{13}C $\{^1H\}$ spectroscopy data to literature values.[225]

2,5-dibromo-3,4-dihexylthiophene (3b). Prepared with slight modification to a literature procedure described by Li *et al*.[225] In 50 mL of DMF, **3a** (2.758 g, 11 mmol) was dissolved and cooled to 0 ºC under the absence of light. NBS (4.155 g, 23 mmol) was dissolved in 75 mL of DMF and added to the reaction mixture dropwise for 1 hour. Once added, the reaction was stirred for 20 minutes at 0 ºC and then warmed to room temperature overnight. The reaction mixture was washed with water and hexanes to give a yellow oil. (4.097 g, 83%). The purity and composition of the target compound was confirmed by comparison of the ^1H NMR spectroscopy data to literature values.[225]

3',4'-dihexyl-2,2':5',2"-terthiophene (3c). Prepared with slight modification to a literature procedure described by Diaz-Quijada *et al*.[226] To an 80 mL microwave vessel, **3b** (4.097 g, 10 mmol), LiCl (2.124 g, 50 mmol), 2-(tributylstannyl)thiophene (10.427 g, 10 mmol), $PdCl_2(PPh_3)_2$ (378 mg, 0.54 mmol), and 30 mL of DMF were added. The reaction was run in a microwave reactor for 45 minutes at 300 W and at 105 ºC. The

reaction mixture was washed with hexanes and water (3 x 100 mL), dried with Na_2SO_4, and dried *in vacuo*. Product was purified by vacuum distillation to yield a green oil (2.875 g, 69%). The purity and composition of the target compound was confirmed by comparison of the ^{1}H NMR spectroscopy data to literature values.[226]

3',3'''',4',4''''-tetrahexyl-2,2':5',2'':5'',2''':5''',2'''':5'''',2''''':5''''',2''''''-sexithophene (3). Prepared with slight modification to a literature procedure described by Delabouglise *et al*. Under argon, **3c** (2.840 g, 6.8 mmol) was dissolved in dry THF and cooled to -78 ºC. *n*-BuLi (1.6 M in hexanes, 4.260 mL, 6.8 mmol) was added dropwise and stirred for 1 hour and then allowed to warm to 0 ºC. Once warmed to 0 ºC, the reaction was cannula transferred to a solution of $Fe(acac)_3$ (2.409 g, 6.8 mmol) in THF. The reaction was refluxed for 19 hours and allowed to cool to room temperature. The red precipitate was removed from the reaction by vacuum filtration. The product was purified by column chromatography on silica gel using pure hexanes as eluent to give an orange powder (0.999 g, 35%). mp: 82.8 °C; ^{1}H NMR ($CDCl_3$): δ 7.32 (dd, J = 1.2, 4.8, 2H), 7.14 (dd, J = 1.2, 3.6, 2H), 7.13 (d, J = 3.60, 2H), 7.07 (dd, J = 3.6, 5.4, 2H), 7.05 (d, J = 3.6, 2H), 2.70 (m, 8H), 1.58 (m, 8H), 1.44 (m, 8H), 1.32 (m, 16H), 0.90 (m, 12H); ^{13}C {^{1}H} NMR: δ 140.3, 136.7, 136.1, 135.2, 130.0, 129.6, 127.4, 126.3, 125.9, 125.4, 123.8, 31.5, 30.7 (d, J = 6.7), 29.6, 28.2 (d, J = 12.7), 22.6, 14.1 (d, J = 2.3); UV-Vis (CH_2Cl_2, nm): λ_{max} 412 (ε, 3.47 x 10^4 M^{-1} cm^{-1}); HRMS (CI+) calcd. for $C_{48}H_{62}S_6$: 830.3176. Found 830.3171; Anal. calcd. for $C_{48}H_{62}S_6$: C, 69.34; H, 7.52; N, 0.00. Found: C, 69.68; H, 6.90; N, 0.28.

3,4-dioctylthiophene (4a). Under an inert atmosphere of argon, 3,4-dibromothiophene (20.150 g, 83.3 mmol) and $Ni(dppp)_2Cl_2$ (0.315 g, 0.6 mmol) were added to a round bottom flask and dissolved in dry ether. The reaction mixture was cooled to 0 ºC and octyl magnesium bromide (2.0 M in diethyl ether, 100 mL, 200 mmol)

was added dropwise over 2 hours. The reaction was stirred at 0 ºC for an additional 30 minutes and then allowed to warm to room temperature for 1 hour. The reaction was then heated to 40 ºC and stirred for 16 hours. Once cooled to room temperature, the reaction was placed in an ice bath and 50 mL of water with 10 drops of concentrated HCl was added. The reaction mixture was vacuum filtered and the filtrate was then washed with ether and water (3 x 50 mL). The organic phase was dried with magnesium sulfate and reduced *in vacuo*. Purification by vacuum distillation at 165 °C yielded a yellow oil (24.468 g, 95%). ^{1}H NMR ($CDCl_3$): δ 6.93 (s, 2H), 2.56 (t, *J* = 7.8, 4H), 1.68 (m, 4H), 1.38 (m, 20H), 0.95 (m, 6H); $^{13}C\{^{1}H\}$ NMR (100 MHz, $CDCl_3$): δ 142.0, 119.8, 31.9, 29.7, 29.5, 29.3, 28.8, 22.7, 14.1; HRMS (CI+): calcd. for $C_{20}H_{36}S$: 309.2616. Found 309.2618.

2,5-dibromo-3,4-dioctylthiophene (4b). In 50 mL of DMF, **4a** (5.001 g, 16.2 mmol) was dissolved and cooled to 0 ºC under the absence of light. NBS (5.693 g, 32 mmol) was dissolved in 75 mL of DMF and added to the reaction mixture dropwise for 1 hour. Once added, the reaction was stirred for 20 minutes at 0 ºC and then warmed to room temperature overnight. The reaction mixture was washed with water and hexanes (3 x 100 mL) to give a yellow oil (6.749 g, 89%). ^{1}H NMR **(**CD_2Cl_2): δ 2.66 (t, *J* = 7.8, 4H), 1.62 (m, 4H), 1.42 (m, 20H), 1.03 (t, *J* = 6.2, 6H); $^{13}C\{^{1}H\}$ NMR (100 MHz, CD_2Cl_2): δ 142.1, 108.5, 32.7, 30.3, 30.09, 30.02, 29.6, 23.5, 14.7; HRMS (CI+) calcd. for $C_{20}H_{34}SBr_2$: 466.0727. Found 466.0739.

3',4'-dioctyl-2,2':5',2"-terthiophene (4c). To an 80 mL microwave vessel, **4b** (5.000 g, 10.72 mmol), LiCl (2.270 g, 53.5 mmol), 2-(tributylstannyl)thiophene (9.800 g, 26.3 mmol), $PdCl_2(PPh_3)_2$ (400 mg, 0.57 mmol), and 30 mL of DMF were added. The reaction was run in a microwave reactor for 45 minutes at 300 W and at 105 ºC. The reaction mixture was washed with hexanes and water (3 x 100 mL), dried with Na_2SO_4,

and dried *in vacuo*. Product was purified by vacuum distillation to yield a green oil (4.980 g, 98 %). ^{1}H NMR **(**CD_2Cl_2): δ 7.37 (dd, *J* = 1.2, 5.4, 2H), 7.24 (dd, *J* = 1.2, 3.6, 2H), 7.13 (dd, *J* = 3.6, 5.1, 2H), 2.82 (t, *J* = 8.1, 4H), 1.75-1.63 (m, 4H), 1.58-1.36 (m, 20H), 1.02 (t, *J* = 6.9, 6H); ^{13}C{^{1}H} NMR (100 MHz, CD_2Cl_2): δ 140.7, 136.7, 130.3, 127.9, 126.3, 125.8, 32.5, 31.3, 30.5, 29.9, 28.7, 23.3, 14.6; HRMS (CI+) calcd. for $C_{28}H_{40}S_3$: 472.2292. Found 472.2290.

3',3'''',4',4''''-tetraoctyl-2,2':5',2'':5'',2''':5''',2'''':5'''',2''''':5''''',2''''''-sexithiophene (4). Under argon, **4c** (180 mg, 0.38 mmol) was dissolved in dry THF and cooled to -78 ºC. *n*-BuLi (1.6 M in hexanes, 0.24 mL, 0.38 mmol) was added dropwise and stirred for 1 hour and then allowed to warm to 0 ºC. Once warmed to 0 ºC, the reaction mixture was cannula transferred to a solution of $Fe(acac)_3$ (0.1340 g, 0.38 mmol) in THF. The reaction was refluxed for 19 hours and allowed to cool to room temperature. The $Fe(acac)_3$ red precipitate was removed from the reaction by vacuum filtration. The product was purified by column chromatography on silica gel using pure hexanes as eluent to give an orange powder (0.0870 g, 49%). mp: 67-69 ˚C; ^{1}H NMR **(**CD_2Cl_2): δ 7.27 (dd, *J* = 1.2, 5.1, 2H), 7.08 (dd, *J* = 1.2, 3.6, 4H), 7.00 (m, 4H), 2.67 (t, *J* = 7.8, 8H), 1.50 (m, 8H), 1.22 (m, 40H), 0.81 (m, 12H); ^{13}C{^{1}H} NMR (100 MHz, CD_2Cl_2): δ 140.2, 136.6, 136.1, 135.2, 130.0, 129.6. 127.3, 126.2, 125.8, 125.3, 123.7, 31.9, 30.7, 29.9, 29.3, 28.1, 22.7, 14.1; UV-Vis (CH_2Cl_2, nm): λ_{max} 408 (ε, 4.98 x 10^4 M^{-1} cm^{-1}); HRMS (CI+) calcd. for $C_{56}H_{78}S_6$: 942.4398. Found 942.4400; Anal. calcd. for $C_{56}H_{78}S_6$: C, 71.23; H, 8.58. Found: C, 71.28; H, 8.33.

3,4-didecylthiophene (5a). Prepared according to an analogous procedure for the preparation of 3,4-dioctylthiophene. Product recovered as a brown oil (84%). ^{1}H NMR ($CDCl_3$): δ 6.90 (s, 2H), 2.52 (t, *J* = 8.0, 4H), 1.64 (m, 4H), 1.30 (m, 28H), 0.91 (m, 6H);

$^{13}C\{^{1}H\}$ NMR (100 MHz, $CDCl_3$): δ 142.0, 119.8, 31.9, 29.7, 29.6, 29.4, 28.8, 22.7, 14.1; HRMS (CI+) calcd. for $C_{24}H_{44}S$: 365.3242. Found 365.3232.

2,5-dibromo-3,4-didecylthiophene (5b). Prepared with slight modification to a literature procedure described by Liu *et al*.[227] In 100 mL of a 1:1 acetic acid: chloroform mixture, **5a** (1.363 g, 3.7 mmol) was dissolved under the absence of light. NBS (1.456 g, 8.2 mmol) was dissolved in 75 mL of 1:1 acetic acid:chloroform, and added to the reaction mixture dropwise for 1 hour. Once added, the reaction was stirred for 4 hours at 70 ºC. The reaction mixture was poured over ice water and extracted with methylene chloride. The organic layer was washed with three 150 mL portions of 10% sodium bicarbonate and deionized water. Product recovered as a red-brown oil (1.806 g, 93%). The purity and composition of the target compound was confirmed by comparison of the ^{1}H NMR spectroscopy data to literature values.[227]

3',4'-didecyl-2,2':5',2"-terthiophene (5c). Prepared according to a procedure described by Ie *et al*.[228] The purity and composition of the target compound was confirmed by comparison of mass spectrometry and ^{1}H NMR and ^{13}C $\{^{1}H\}$ spectroscopy data to literature values.[228]

3',3'''',4',4''''-tetradecyl-2,2':5',2'':5",2''':5''',2'''':5'''',2''''':5''''',2'''''-sexithiophene (5). Prepared according to an analogous procedure for the synthesis of 3',3'''',4',4''''-tetraoctyl-2,2':5',2'':5",2''':5''',2'''':5'''',2''''':5''''',2'''''-sexithiophene. Product recovered an oily orange solid (10%). mp: 54 °C; ^{1}H NMR ($CDCl_3$): δ 7.30 (dd, J = 1.2, 5.6, 2H), 7.12 (dd, J = 1.2, 3.6, 2H), 7.11 (d, J = 3.6, 2H), 7.05 (dd, J = 3.6, 5.20, 2H), 7.03 (d, J = 3.6, 2H), 2.69 (m, 8H), 1.53 (m, 24H), 1.25 (m, 40H), 0.86 (m, 12H); ^{13}C $\{^{1}H\}$ NMR: δ 140.3, 136.7, 136.1, 135.2, 130.0, 129.6, 128.1, 127.4, 126.3, 125.9, 125.4, 123.8, 31.9, 30.7, 29.9, 29.6, 29.3 (d, J = 6.0), 28.1, 22.7, 14.1; UV-Vis (CH_2Cl_2, nm): λ_{max} 412 (ε, 4.01 x 10^4 M^{-1} cm^{-1}); HRMS (CI+) calcd. for $C_{64}H_{94}S_6$: 1054.5680. Found 1054.5675;

Anal. calcd. for $C_{64}H_{94}S_6$: C, 72.80; H, 8.97; N, 0.00. Found: C, 72.51; H, 8.81; N, < 0.05.

3,4-bis(6,6,6-trifluorohexyl) thiophene (6a). Prepared according to an analogous procedure for the preparation of 3,4-dioctylthiophene. Product recovered as a clear, pale yellow oil (65%). ^{1}H NMR ($CDCl_3$): δ 6.91 (s, 2H), 2.54 (t, *J* = 7.60, 4H), 2.09 (m, 4H), 1.65 (m, 8H), 1.48 (m, 4H); ^{13}C {^{1}H} NMR: δ 141.3, 127.2 (q, *J* = 276.0), 120.3, 33.6 (q, *J* = 28.5), 29.2, 28.5, 28.4, 21.8 (d, *J* = 3.0); HRMS (CI+) calcd. for $C_{16}H_{22}F_6S$: 361.1425. Found 361.1428.

2,5-dibromo-3,4-bis(6,6,6-trifluorohexyl)thiophene (6b). Prepared according to an analogous procedure for the synthesis of 2,5-dibromo-3,4-dioctylthiophene. Product recovered as an orange oil (94%). ^{1}H NMR ($CDCl_3$): δ 2.48 (t, J = 7.60, 4H), 2.03 (m, 4H), 1.54 (m, 4H), 1.42 (m, 8H); ^{13}C {^{1}H} NMR: δ 140.6, 127.0 (q, *J* = 276.1), 108.2, 33.5 (q, *J* = 28.5), 29.0, 28.4, 28.3, 21.5 (d, *J* = 3.0); HRMS (CI+) calcd. for $C_{16}H_{20}Br_2F_6S$: 516.9635. Found 516.9632.

2,5-bis(2'-thienyl)-3,4-bis(6,6,6-trifluorohexyl)thiophene (6c). Prepared according to a procedure for the preparation of 3',4'-dioctyl-2,2':5',2"-terthiophene. Product recovered as a yellow oil (84%). ^{1}H NMR ($CDCl_3$): δ 7.32 (dd, *J* = 1.2, 5.4, 2H), 7.12 (dd, *J* = 1.2, 3.6, 2H) 7.06 (dd, *J* = 3.6, 5.2, 2H), 2.71 (t, *J* = 8.4, 4H), 2.05 (m, 4H), 1.58 (m, 8H), 1.47 (m, 4H); ^{13}C {^{1}H} NMR: δ 139.2, 135.8, 130.2, 127.4, 126.1, 125.5, 33.6 (q, *J* = 28.3), 30.3, 28.7, 27.7, 21.6 (d, *J* = 3.0); HRMS (CI+) calcd. for $C_{24}H_{26}F_6S_3$: 525.1179. Found 525.1169.

3',3'''',4',4''''-tetra(6,6,6-trifluorohexyl)-2,2':5',2'':5'',2''':5''',2'''':5'''',2''''':-sexithophene (6). Prepared according to an analogous procedure for the synthesis of 3',3'''',4',4''''-tetraoctyl-2,2':5',2'':5",2''':5''',2'''':5'''',2''''':-sexithiophene. Product recovered as an oily red-

orange solid (19%). mp: 118.2 °C; ^{1}H NMR ($CDCl_3$): δ 7.32 (dd, *J* = 1.2, 5.6, 2H), 7.12 (d, *J* = 3.6, 4H), 7.06 (dd, *J* = 3.6, 5.2, 2H), 7.03 (d, *J* = 4.0, 2H), 2.71 (m, 8H), 2.06 (m, 8H), 1.53 (m, 24H); ^{13}C {^{1}H} NMR: δ 139.4, 136.8, 135.7, 135.0, 130.5, 130.0, 128.5, 127.5, 126.7, 126.2, 125.7, 124.0, 33.7, 33.4, 30.3, 28.7, 27.8 (d, *J* = 3.02), 27.8 (d, *J* = 12.77), 21.6; UV-Vis (CH_2Cl_2, nm): λ_{max} 409 (ε, 3.95 x 10^4 M^{-1} cm^{-1}); HRMS (CI+) calcd. for $C_{48}H_{50}F_{12}S_6$: 1046.2045. Found 1046.2062; Anal. calcd. for $C_{48}H_{50}F_{12}S_6$: C, 55.05; H, 4.81; N, 0.00. Found: C, 55.51; H, 4.06; N, 0.09.

3.2.2.2. Formation of Oligothiophene Aggregates

Aggregates were made by making a 1.5 mM solution of **4** in THF or hexanes and quickly injecting 100 μL of this solution into 10 mL of ethanol, nanopure water, or methanol. Upon injection, the solution was stirred at 1200 rpm for 7 minutes. As molecules of **4** were forced out of solution, aggregates of **4** were then formed.

3.3. RESULTS AND DISCUSSION

3.3.1. Synthesis

3.3.1.1.Synthesis of Oligothiophenes

A library of sexithiophene molecules, with R groups of varying length and polarity, **1-6**, were prepared through a convergent and efficient synthesis route outlined in Scheme 3.1. Molecule **a**, 3,4-dialkylthiophene, was synthesized by a halo-Grignard Kumada cross-coupling reaction of 3,4-dibromothiophene and the appropriate alkyl magnesium bromide Grignard reagent. Bromination of **a** with *N*-bromosuccinimide (NBS), in the absence of light, produced 2,5-dibromo-3,4-dialkylthiophene, **b**. Molecule **b** then undergoes a Stille coupling with 2-(tributylstannyl)thiophene, in the presence of a palladium catalyst, to yield 3',4'-dialkyl-2,2':5',2"-terthiophene, **c**. Two terthiophene molecules are then coupled together with an iron catalyst to produce the target molecule,

3’,3’’’’,4’,4’’’’-tetraalkyl-2,2’:5’,2’’:5”,2’’’:5’’’,2’’’’:5’’’’,2’’’’’-sexithiophene, molecules **1-6**.

3.3.1.2. Preparation of Aggregates of Oligothiophenes

Aggregates of molecule **4** were made by simply crashing the oligothiophene out of a solvent/cosolvent mixture. A 1.5 mM solution of **4** was prepared in a “good” solvent, a solvent that the oligothiophene was soluble in (THF or hexanes). While vigorously stirring, 100 μL of the 1.5 mM solution of **4** was quickly injected into a “bad” solvent, a solvent that the oligothiophene was partially or not soluble in but still miscible with the “good” solvent (ethanol, water, or methanol). Due to the insolubility of **4** in the “bad” solvent, particles or aggregates were forced out of the “good” solvent, thus forming a colloidal suspension of oligothiophene aggregates.

3.3.2. X-Ray Crystal Structure of Oligothiophenes

Crystals suitable for single-crystal X-ray diffraction analysis were grown by the slow evaporation of hexanes. Single crystal structures were determined for molecules **1** and **3-6**. The single crystal of butyl sexithiophene, **2**, was previously reported by Liao and coworkers.[206] Shown in Table 3.1 are the torsion angles of the terminal thiophenes in each sexithiophene molecule. The torsion angle of the terminal thiophenes gradually increase as the length of R is increased, from butyl to decyl sexithiophene (**2-5**). However, the ethyl-substituted sexithiophene (**1**) deviates from this trend; the terminal thiophenes of ethyl sexithiophene are severely twisted with a torsion angle of 78.3°. The drastic contrast in the torsion angles of the terminal thiophenes between the ethyl- (78.3°) and decyl-substituted (38.7°) sexithiophene molecules is apparent in Figures 3.1A and 3.4A. The packing diagrams of butyl- to trifluorohexyl-substituted sexithiophenes (Figures 3.2B to 3.5B) all show ordered packing in the unit cell with pi-stacking

occurring between two or three molecules. Likewise, in **2-6**, the sexithiophene molecules are in a pseudo-herringbone and staggered arrangement due to the appended alkyl chains. The ethyl-substituted sexithiophene, **1**, however, shows no pi-stacking or ordered packing in the unit cell. This lack of order is likely due to the large torsion angle (78.3°) observed in the single crystal structure. Shown in Table 3.2 are the average bond distances and angles for **1-6**. Noteably, the terminal C(1)-C(2) double bond (1.34 ±0.02 Å) is shorter than the other bond lengths. Additionally, a shorter bond length is observed in the terminal S-C bond (S(1)-C(1), 1.70 ±0.04 Å) than for the rest of the S-C bonds in the sexithiophene molecule. The greatest deviation in the bond angles is observed for the S(2)-C(5)-C(4) angle (117 ±4°), corresponding to the dihedral angle between the terminal thiophene, Th(1), and second thiophene, Th(2). The large deviation in this bond angle is expected as the terminal torsion angle varies greatly for the entire series **1-6**, as previously exemplified in Table 3.1. All other bond lengths and angles reported in Table 3.2 agree closely to those reported for unsubstituted α-sexithiophene.[229] Bond lengths and angles for **1-6** are compiled in Tables 3.7, 3.8, 3.10, 3.12, 3.14, and 3.16 (Supplemental Data).

Table 3.1. Torsion angles of the terminal thiophenes in R-substituted sexithiophenes, **1-6**

R =	Torsion Angle Th(1)-Th(2) (°)
Ethyl (**1**)	78.3
Butyl (**2**)	19.0
Hexyl (**3**)	18.7
Octyl (**4**)	25.2
Decyl (**5**)	38.7
Trifluorohexyl (**6**)	26.3

Table 3.2. Average bond distances (Å) and bond angles (º) for R-substituted sexithiophenes, **1-6**

Bond distances (Å)			
C(1)-C(2)	1.34 ±0.02	C(11)-C(12)	1.37 ±0.01
C(2)-C(3)	1.44 ±0.05	C(6)-C(13)	1.51 ±0.01
C(3)-C(4)	1.40 ±0.04	C(7)-C(14)	1.50 ±0.01
C(4)-C(5)	1.46 ±0.01	S(1)-C(1)	1.70 ±0.04
C(5)-C(6)	1.40 ±0.04	S(1)-C(4)	1.74 ±0.02
C(6)-C(7)	1.434 ±0.009	S(2)-C(5)	1.734 ±0.007
C(7)-C(8)	1.38 ±0.01	S(2)-C(8)	1.735 ±0.004
C(8)-C(9)	1.46 ±0.01	S(3)-C(9)	1.735 ±0.002
C(9)-C(10)	1.39 ±0.04	S(3)-C(12)	1.732 ±0.002
C(10)-C(11)	1.415 ±0.008		
Bond angles (º)			
C(1)-S(1)-C(4)	91. 9 ±0.7	S(2)-C(5)-C(4)	117 ±4
C(5)-S(2)-C(8)	92.5 ±0.4	S(2)-C(8)-C(9)	117.2 ±0.5
C(9)-S(3)-C(12)	92.7 ±0.2	S(3)-C(9)-C(8)	123 ±1
S(1)-C(4)-C(5)	122 ±2		

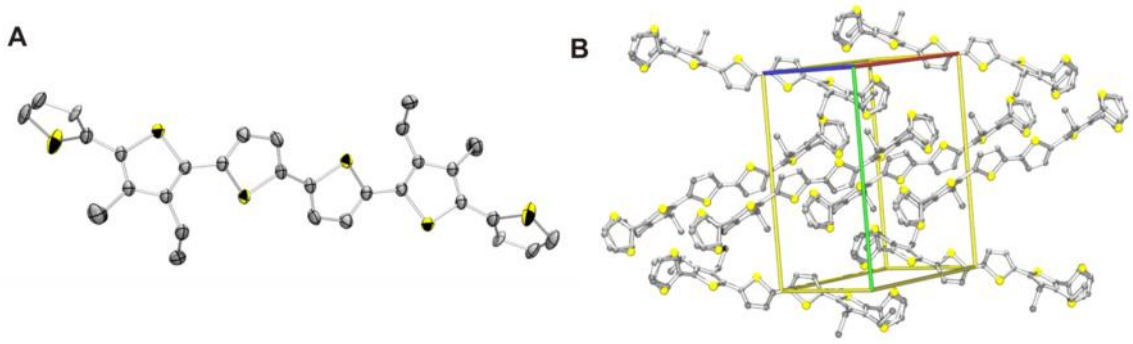

Figure 3.1. (A) ORTEP diagram of a single molecule of **1** with thermal ellipsoids drawn at the 50% probability level. Hydrogen atoms have been omitted for clarity. (B) Packing diagram of **1** in the unit cell.

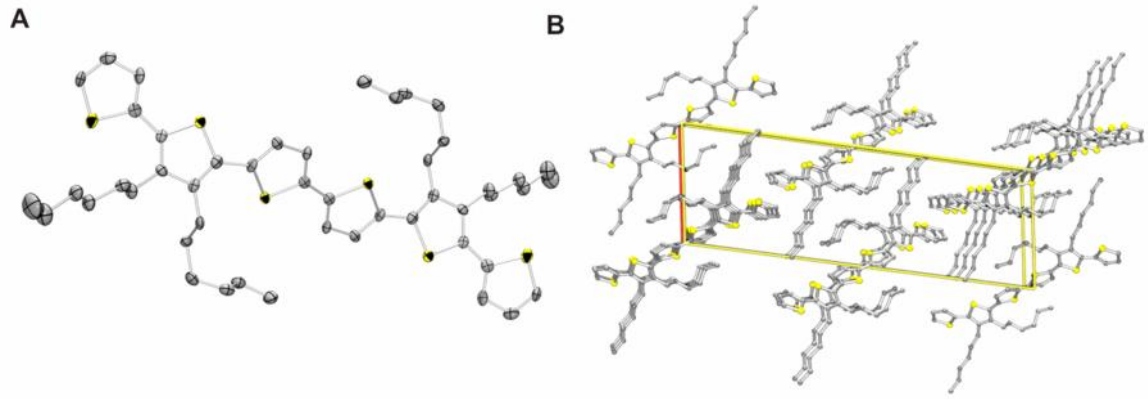

Figure 3.2. (A) ORTEP diagram of a single molecule of **3** with thermal ellipsoids drawn at the 50% probability level. Hydrogen atoms have been omitted for clarity. (B) Packing diagram of **3** in the unit cell.

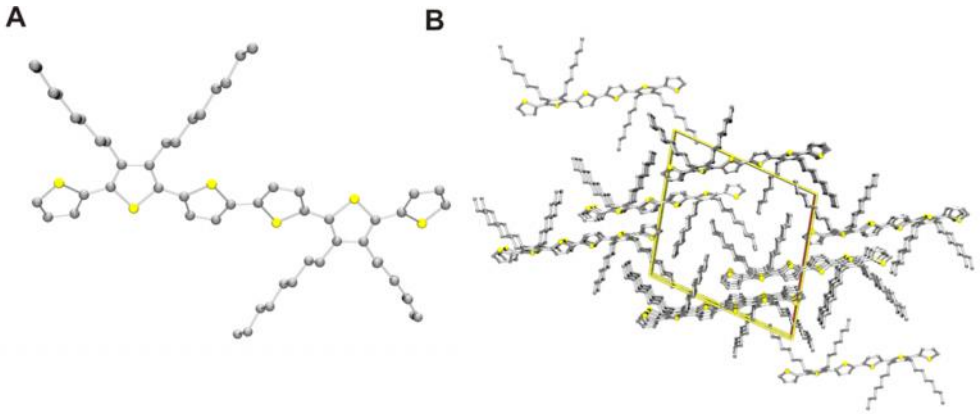

Figure 3.3. (A) ORTEP diagram of a single molecule of **4** with thermal ellipsoids drawn at the 50% probability level. Hydrogen atoms have been omitted for clarity. (B) Packing diagram of **4** in the unit cell.

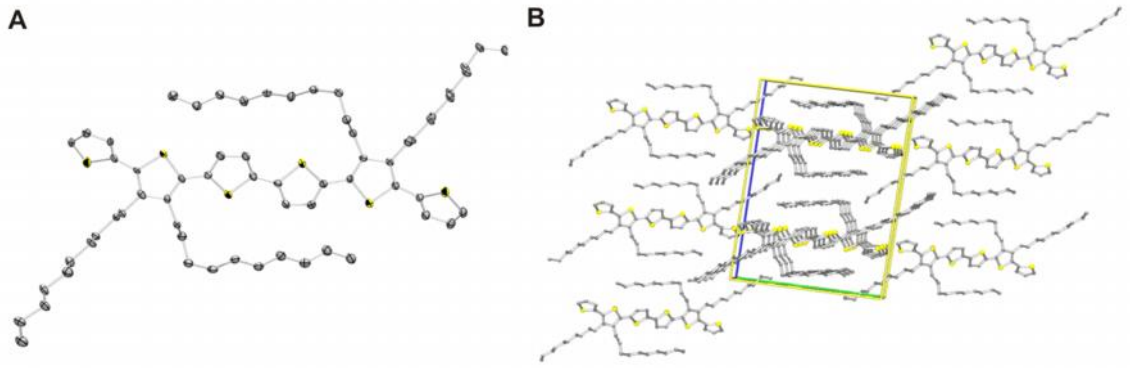

Figure 3.4. (A) ORTEP diagram of a single molecule of **5** with thermal ellipsoids drawn at the 50% probability level. Hydrogen atoms have been omitted for clarity. (B) Packing diagram of **5** in the unit cell.

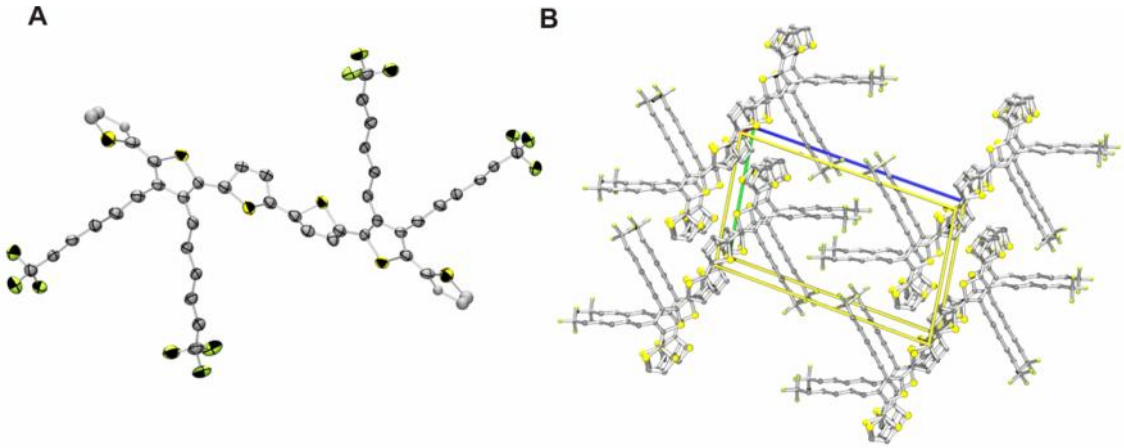

Figure 3.5. (A) ORTEP diagram of a single molecule of **6** with thermal ellipsoids drawn at the 50% probability level. Hydrogen atoms have been omitted for clarity. (B) Packing diagram of **6** in the unit cell.

3.3.3. Spectroscopy of Oligothiophenes

The photophysical properties of molecules **1-6** were studied and are summarized in Table 3.3. Figure 3.6 shows the absorption, emission, and excitation spectra of hexyl-substituted sexithiophene at room temperature and 77 K. Since all absorption, emission, and excitation profiles are very similar for the entire series of sexithiophenes, Figure 3.6 is a representative example of the photophysical spectra of **1-6**. The solution-state

absorption spectra of these sexithiophenes have maxima at 412 nm, which is typical of $\pi \rightarrow \pi^*$ absorptions. Upon selective excitation at 411 nm, an emission maximum is observed at 512 nm. This emission at 512 nm is assigned as fluorescence emission due to the very short nanosecond lifetime (~1 ns) and small Stokes shift from absorption (100 nm). Molecules **1-6** have moderate fluorescent quantum yields of ~30-40%. Colditz *et al.* report a lifetime and fluorescent quantum yield of 1.04 ±0.10 ns and 34 ±7%, respectively, for unsubstituted α-sexithiophene.[230] This agrees reasonably well with the lifetimes and quantum yields determined for **1-6**. Upon cooling to 77 K, the emission spectrum does not experience a large shift (λ_{em} = 503 nm) however, an increase in vibronic structure is observed. This increase in vibronic structure at 77 K is often attributed to the deactivation of non-radiative pathways at cold temperatures. Notably, the excitation profile red shifts (λ_{ex} = 449 nm) at 77 K due to planarization of the sexithiophene backbone in rigid media.

Table 3.3. Photophysical data for R-substituted sexithiophenes, **1-6**

Compound	Temp. (K)	ε (x 10^4) (M^{-1} cm^{-1})	λ_{Abs} (nm)	λ_{Ex} (nm)	λ_{Em} (nm)	Φ_{Em} (%)	τ_0 (ns)
1	298	3.78	412	416	512	40 ±10	0.837 ±0.008
	77	a	a	448	501	a	a
2	298	4.01	412	411	515	37 ±5	0.867 ±0.003
	77	a	a	494	544	a	a
3	298	3.47	412	412	512	40 ±10	1.038 ±0.004
	77	a	a	449	503	a	a
4	298	4.98	408	410	505	64 ±6	0.841 ±0.002
	77	a	a	455	500	a	a
5	298	4.01	412	415	513	25 ±2	0.882 ±0.004
	77	a	a	461	505	a	a
6	298	3.95	409	408	514	36 ±2	0.808 ±0.004
	77	a	a	454	500	a	a

a: Not measured
*Solvents used at 298 K and 77 K were CH_2Cl_2 and 2-MeTHF, respectively

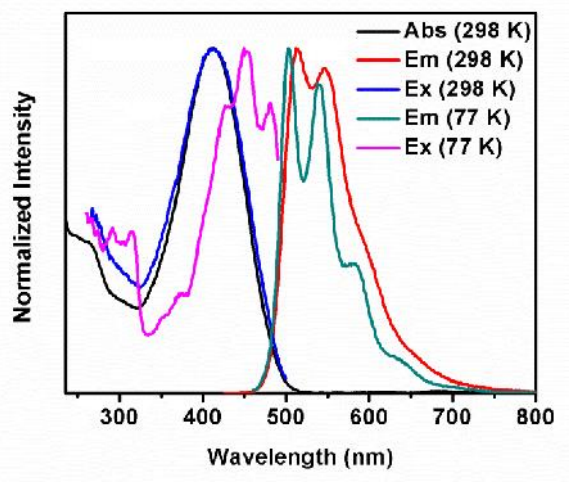

Figure 3.6. Absorption, emission, and excitation spectra of **3** in CH_2Cl_2 (298 K) and 2-MeTHF (77 K).

3.3.4. Electronic Properties of Oligothiophenes

3.3.4.1. Oxidative Doping Electron Paramagnetic Resonance (EPR) Spectroscopy

EPR experiments were performed on **1-6** upon step-wise oxidation with the chemical oxidant, $[(BrC_6H_4)_3N][SbCl_6]$, in the presence of an internal standard. Shown in Figure 3.7 is the EPR spectrum of the step-wise oxidation of butyl-substituted sexithiophene, **2**. Figure 3.7 also serves as a representative example of the EPR spectra observed for **1-6**. Titration with one equivalent of chemical oxidant gives an EPR signal with a g value of 2.007 (typical for that of an organic radical) corresponding to the formation of a cationic polaron species. Upon the addition of two equivalents of oxidant, an increase in EPR signal is observed as a second polaron is formed. After the addition of a third equivalent of oxidant, the EPR signal slightly decreases as a bipolaron and polaron are now present in solution. Finally, with the addition of four equivalents of chemical oxidant, the EPR signal completely disappears with the formation of two bipolarons, a spinless, EPR silent species. Any residual signal observed with four equivalents of oxidants is attributed to excess chemical oxidant in solution. Figure 3.8 shows the

compiled EPR data for the series of sexithiophenes, **1-6**. For each sexithiophene, the same trend is observed: an increase in EPR signal from one to two equivalents of oxidant and the steady, gradual decrease of signal from three to four equivalents of oxidant.

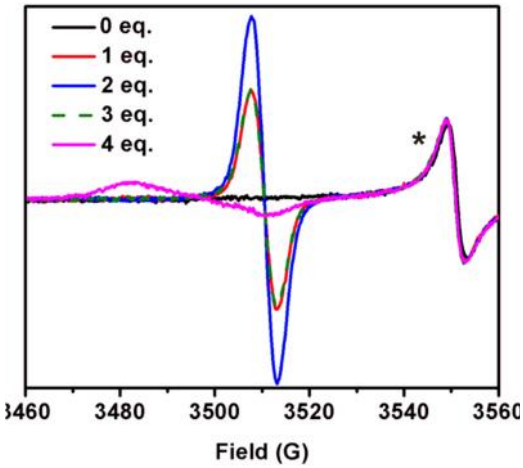

Figure 3.7. EPR spectrum of **2** upon step-wise oxidation with $[(BrC_6H_4)_3N][SbCl_6]$ in CH_2Cl_2. Asterisk denotes an internal reference with a g of 1.9800 ±0.0006 with 3 G line width.

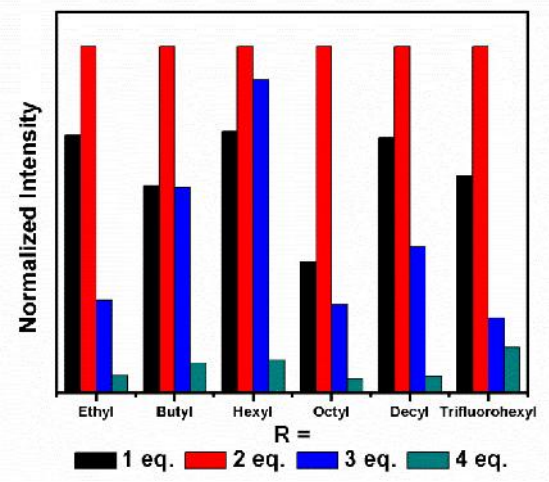

Figure 3.8. Compiled EPR data for sexithiophenes **1-6** upon step-wise oxidation with $[(BrC_6H_4)_3N][SbCl_6]$ in CH_2Cl_2.

3.3.4.2. Oxidative Doping UV-Vis Spectroelectrochemistry

To confirm the results of the EPR doping study, oxidative doping experiments were done on **1-6** and monitored by UV-Vis spectroscopy. Molecules **1-6** were chemically oxidized by titration with $[(BrC_6H_4)_3N][SbCl_6]$ in CH_2Cl_2. Table 3.4 compiles the UV-Vis absorption maximum for each of the oxidized states of **1-6**. Figure 3.9 shows the UV-Vis spectrum of octyl-substituted sexithiophene, **4**, upon titration with the chemical oxidant, $[(BrC_6H_4)_3N][SbCl_6]$. All the other sexithiophenes in the series show the same general trend upon step-wise oxidation and same relative absorption maxima at each of the oxidized states thus, Figure 3.9 is shown as a representative example of **1-6**. As shown in Figure 3.9, the typical $\pi \rightarrow \pi^*$ transition at 411 nm is observed in the neutral state spectrum of **4**. Upon addition of one equivalent of oxidant, the peak at 411 nm decreases and peaks at 770 nm and 1458 nm appear, corresponding to the formation of a polaron on the sexithiophene backbone. With the addition of two equivalents of oxidant, a bipolaron is expected to form. Bipolaron formation is signified by the disappearance of the polaron bands and the appearance of a bipolaron band in the UV-Vis spectrum. However, this expected trend does not occur; the absorption peaks at 770 nm and 1458 nm intensify upon the addition of the second equivalent of oxidant, indicative of the formation of a second polaron on the oligothiophene backbone. This formation of two localized polarons on the sexithiophene backbone is depicted in Scheme 3.2. Upon the addition of a third equivalent of oxidant, the polaron peaks at 770 nm and 1458 nm begin to disappear while a new maximum at 977 nm, attributed to bipolaron formation, appears in the UV-Vis spectrum. Lastly, with the addition of a fourth equivalent of oxidant, the bipolaron band at 977 nm continues to grow while the polaron bands at 770 nm and 1458 nm continue to decrease, corresponding to the formation of two bipolarons, as shown in Scheme 3.2.

Table 3.4. λ_{max} of UV-Vis spectrum of R-substituted sexithiophenes, **1-6** upon oxidative doping

R =	Neutral (λ_{max}, nm)	+1 (λ_{max}, nm)	+2 (λ_{max}, nm)	+3 (λ_{max}, nm)	+4 (λ_{max}, nm)
Ethyl (**1**)	411	770, 1458	770, 1458	977	977
Butyl (**2**)	408	772, 1470	772, 1470	980	980
Hexyl (**3**)	411	773, 1468	773, 1468	980	980
Octyl (**4**)	411	774, 1480	774, 1480	979	979
Decyl (**5**)	413	775, 1475	775, 1475	981	981
Trifluorohexyl (**6**)	402	768, 1472	768, 1472	975	975

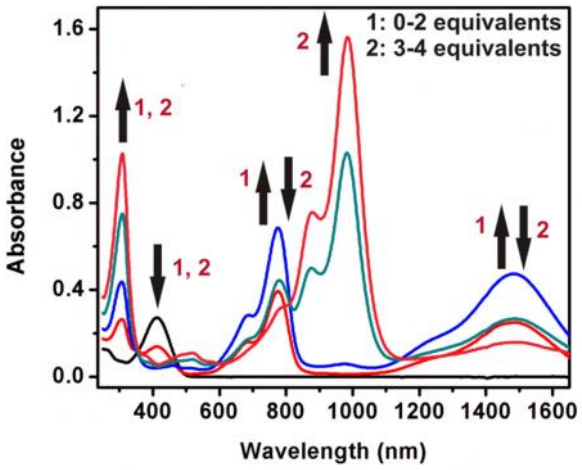

Figure 3.9. UV-Vis absorption spectrum of **4** upon step-wise oxidation with $[(BrC_6H_4)_3N][SbCl_6]$ in CH_2Cl_2.

After chemical oxidation, the oxidized species of **4** was subsequently chemically reduced with decamethyl ferrocene, $[FeCp^*_2]$ (Figure 3.10). With the addition of one equivalent of reductant, the UV-Vis spectrum looks similar to the spectrum for one equivalent of oxidant and the formation of a polaron, as the peaks at 785 nm and 1494 nm increase in intensity. However, with the addition of a second equivalent of reductant, the polaron peaks at 785 nm and 1494 nm decrease. The decrease in absorbance of these polaron peaks usually indicates formation of a bipolaron. However, the typical bipolaron band at 992 nm does not appear with two equivalents of reductant. Upon the addition of

the third and fourth equivalents of reductant, the UV-Vis spectrum is virtually identical to the spectrum of the neutral species. Notably, the peak at 311 nm is attributed to the product of the reaction between the reductant and oxidant, as shown in Figure 3.11. At this time, it is unclear as to why the chemical reduction of the oxidized species of **4** does not follow the reverse mechanism of oxidation.

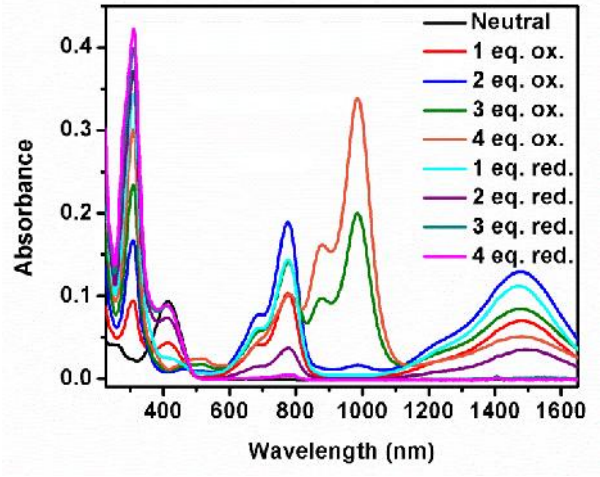

Figure 3.10. UV-Vis absorption spectrum of **4** in DCE upon step-wise oxidation with $[(BrC_6H_4)_3N][SbCl_6]$ and reduction with $[FeCp^*_2]$.

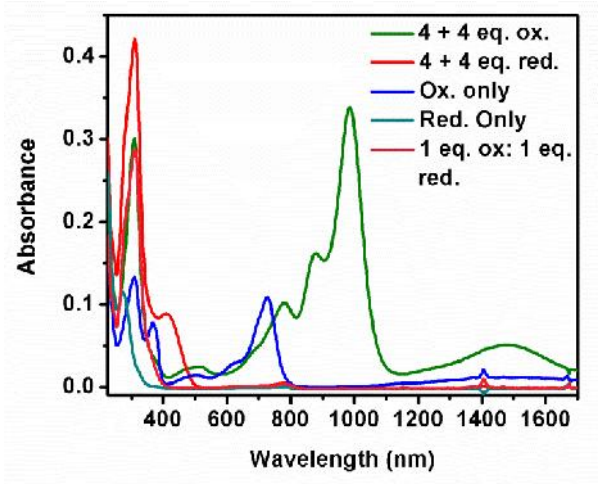

Figure 3.11. UV-Vis absorption spectrum of oxidant $[(BrC_6H_4)_3N][SbCl_6]$ and reductant $[FeCp^*_2]$ in DCE.

Scheme 3.2. Proposed oxidation scheme of R-substituted sexithiophenes **1-6** upon chemical oxidation with $[(BrC_6H_4)_3N][SbCl_6]$

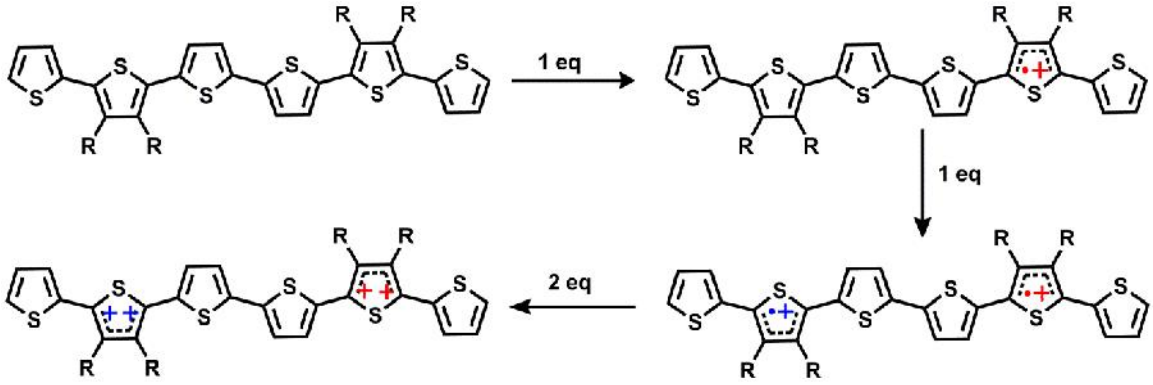

3.3.4.3. Electrochemistry

The electrochemistry of molecules **1-6** was studied in 0.1 M $TBAPF_6$ solutions in methylene chloride at a scan rate of 100 mV/s. Shown in Figures 3.12A and 3.12B are the cyclic voltammogram (CV) and differential pulse voltammogram (DPV), respectively, of octyl-substituted sexithiophene, **4**. Figure 3.12A is shown as a representative CV of the entire series, **1-6**. As depicted in Figure 3.12A, two reversible redox couples occur at 0.31 V and 0.46 V (vs. Fc/Fc^+). Table 3.5 lists the $E_{1/2}$ values for each of the R-substituted sexithiophenes in the series. All sexithiophenes, with the exception of trifluorohexyl-substituted sexithiophene, have $E_{1/2}$ values around ~0.35 V and ~0.55 V (vs. Fc/Fc^+). However, the fluoroalkylated sexithiophene in the series, **6**, only has one reversible redox couple with an $E_{1/2}$ value (0.45 V, vs. Fc/Fc^+) that is the average of the two $E_{1/2}$ values observed in the alkyl-substituted sexithiophenes. The differential pulse voltammogram, shown in Figure 3.12B, does not resolve the waves in the CV but does indicate that the number of electrons associated with each wave is the same.

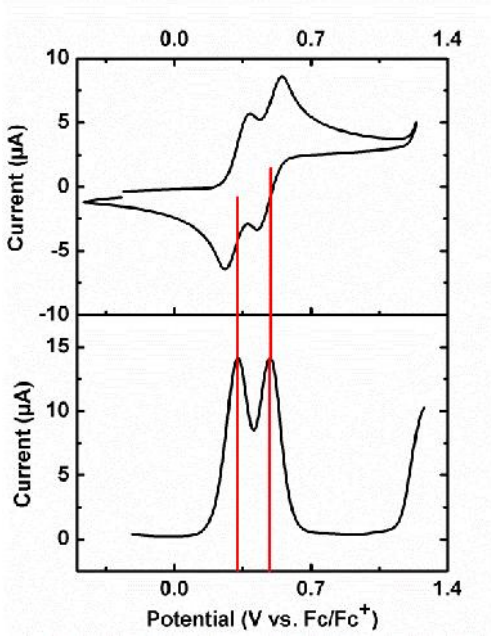

Figure 3.12. (A) Cyclic voltammogram of **4** in 0.1 M $TBAPF_6$ in CH_2Cl_2 at a scan rate of 100 mV/s. (B) Differential pulse voltammogram of **4** in 0.1 M $TBAPF_6$ in CH_2Cl_2.

Table 3.5. $E_{1/2}$ potentials (*versus* Fc/Fc^+) for R-substituted sexithiophenes, **1-6**

R =	$E_{1/2}$ (V)	$E_{1/2}$ (V)
Ethyl (**1**)	0.35	0.55
Butyl (**2**)	0.34	0.58
Hexyl (**3**)	0.34	0.52
Octyl (**4**)	0.31	0.46
Decyl (**5**)	0.36	0.50
Trifluorohexyl (**6**)	0.45	---

Shown in Figure 3.13A is the scan rate dependence study of **4** performed in 0.1 M $TBAPF_6$ in DCE with a Pt button macroelectrode. A linear dependence is observed between the current and the scan rate, indicating that good diffusion of the molecule to the electrode surface occurs (Figure 3.14). The peak current from the first oxidation wave in Figure 3.13A was plotted as a function of the square root of the scan rate ($v^{1/2}$) and is shown in Figure 3.13B as the black dots. Additionally, the current was calculated using

the Randles-Sevcik equation (see Experimental section for details of calculations) when n is 1 electron or 2 electrons. The calculated current, for n = 1 and n = 2, was plotted as a function of the square root of the scan rate and is depicted in Figure 3.13B as red circles and blue triangles, respectively. In Figure 3.13B, the experimental data is closer to the plot for n = 1, indicating that the number of electrons associated with the first and each redox wave in the CV is one. Additionally, analysis of the peak-to-peak separation (ΔE_p) in Figure 3.13A further supports that n is 1 for each redox wave in the CV of **4**. The peak-to-peak separation for both the first and second redox event is 70.5 mV. According to the equation ΔE_p = 56.5 mV/n, n, in this case, must equal one.[217]

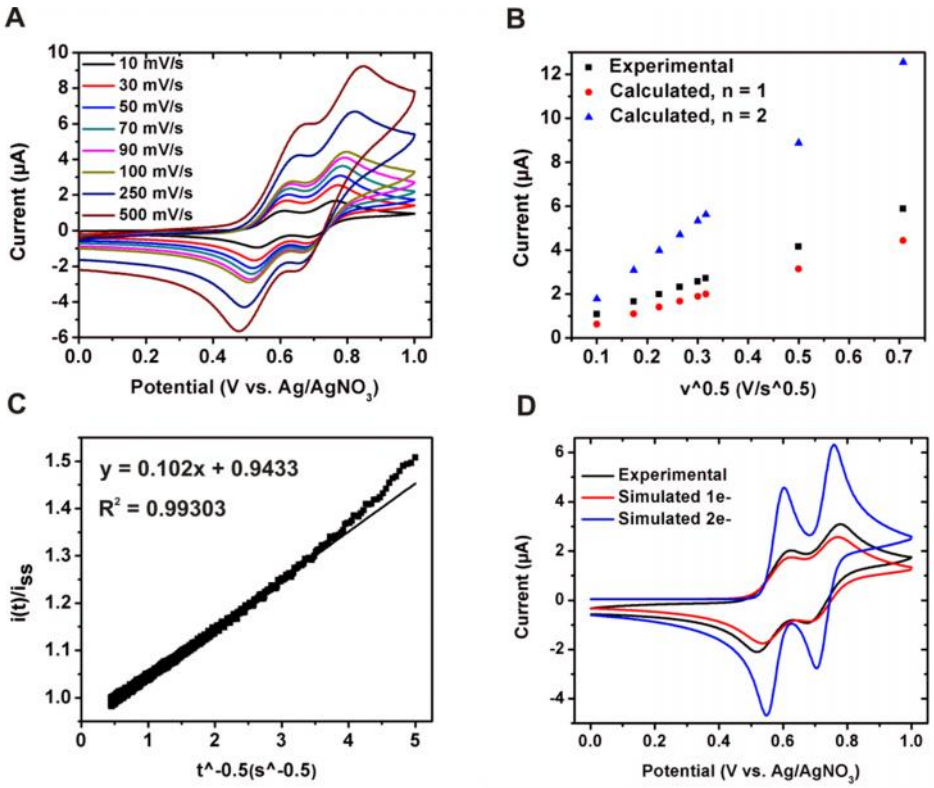

Figure 3.13. (A) Scan rate dependence study of **4** in 0.1 M $TBAPF_6$ in DCE. (B) Experimental current *versus* $v^{1/2}$ of **4** in 0.1 M $TBAPF_6$ in DCE and calculated current *versus* $v^{1/2}$ when $n = 1$ and $n = 2$. (C) Plot of the experimental ratio of $i(t)/i_{ss}$ *versus* $t^{-1/2}$ of **4** in 0.1 M $TBAPF_6$ in DCE with a 10 µm diameter Pt UME. (D) Simulation of **4** in 0.1 M $TBAPF_6$ in DCE at 50 mV/s when $n = 1$ and $n = 2$ for each redox wave.

Chronoamperometry experiments were performed on **4** by stepping the potential from +0.3 V to +1.1 V (vs. $Ag/AgNO_3$) and thus, stepping both the first and second oxidations. Figure 3.13C show the linear plot of $i(t)/i_{ss}$ *versus* $t^{-1/2}$ for the experimental data and an intercept that is very close to one.[220] Upon stepping both oxidations, the average diffusion coefficient was calculated to be 3.3 ±0.3 x 10^{-6} cm^2/s (see Experimental section for details of calculation). Shown in Figure 3.15 is the steady state voltammogram of **4** at a 10 µm diameter UME. Using i_{ss} from the steady state voltammogram (i_{ss} = 1.606 x 10^{-9} A), n was found to be 2.1 ±0.2 electrons. Based on the results of the

chronoamperometry experiments, a total of two electrons are transferred in the first and second oxidations. Since the differential pulse voltammogram indicates that the same number of electrons are associated with each oxidation wave (Figure 3.12B), each redox wave in the CV of **4** represents a one electron transfer process. Additionally, electrochemical simulations, using experimentally determined values, predict two one-electron redox processes, as shown in Figure 3.13D. Although the simulation parameters are not optimized, the simulated CV of two one-electron redox processes is closer to the experimental CV than the CV predicted for two two-electron redox processes.

There is a discrepancy between the number of electrons predicted by electrochemical and spectroscopic methods for each redox wave in the CV of **4**. Electrochemical studies, such as chronoamperometry, simulations, peak-to-peak current separation, and scan rate dependence analysis, calculate that the number of electrons associated with each redox process is one. However, spectroscopic methods, such as UV-Vis and EPR doping studies, predict a net four electron transfer meaning that each redox process in the CV of **4** is attributed to two electrons. The oxidizing agent, $[(BrC_6H_4)_3N][SbCl_6]$, has a formal potential of +0.7 V in methylene chloride (vs. Fc/Fc^+). As demonstrated by UV-Vis and EPR doping studies, this oxidant produces a four electron oxidation. In the CV of **4** in methylene chloride (Figure 3.12A), both redox waves occur before +0.7 V (vs. Fc/Fc^+), suggesting that a net four electron oxidation also occurs in the electrochemical CV. Since the differential pulse voltammogram for each oxidation wave are of equal height (Figure 3.12B), each redox wave has two electrons associated with it. Conversely, chronoamperometric studies, electrochemical simulations, and scan rate dependence analysis suggest that $n = 1$ for each redox wave. At this time, it is unclear as to why this discrepancy in the predicted number of electrons occurs between the electrochemical and spectroscopic data.

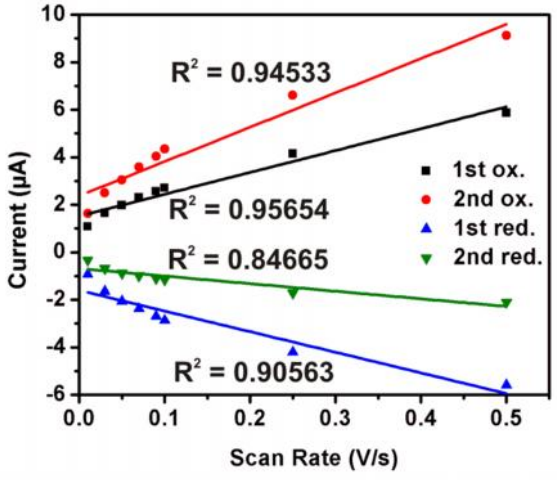

Figure 3.14. Current *versus* scan rate of **4** in 0.1 M $TBAPF_6$ in DCE with a Pt working macroelectrode, Pt counter electrode, and $Ag/AgNO_3$ reference electrode.

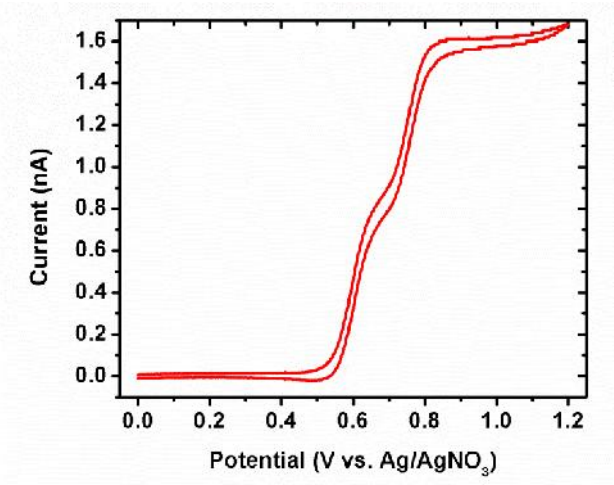

Figure 3.15. Steady state voltammogram of **4** in 0.1 M $TBAPF_6$ in DCE with a 10 μm diameter Pt UME, Pt counter electrode, and $Ag/AgNO_3$ reference electrode.

3.3.4.4. Spectroscopy and Kelvin Probe Force Microscopy (KPFM) of Oligothiophene Aggregates

The spectroscopy and electronic properties of aggregates of **4** were studied through collaborative efforts.[231] Aggregates of **4**, formed through solution processing, were found to have distinct and reproducible morphologies dependent upon the solvents used in aggregate formation. For example, the THF/methanol ('good'/'bad') solvent

combination produced aggregates of rectangular shape while the THF/H_2O solvent combination produced both discoid and ellipse morphologies. In addition to having different morphological shapes, aggregates prepared through different solution processing preparations gave different fluorescence spectra. An ensemble average emission spectrum was obtained from drop cast films of aggregates of **4** made from a particular solvent combination. A compiled fluorescence spectrum of each set of aggregates and a solution of **4** in THF is shown in Figure 3.16. As depicted in Figure 3.16, the difference in each spectrum occurs in the intensity of the highest energy 0-0 vibronic band. Spano and coworkers reported the suppression of the 0-0 vibronic band in the emission spectrum of weakly coupled H-aggregates and related the intensity of the 0-0 band with the extent of electronic disorder within the aggregate.[232,233] Suppression of the 0-0 vibronic band in the fluorescence spectra of the aggregates, relative to the vibronic structure of a solution of **4** in THF, indicates that the extent of electronic disorder can be varied through different solution processing preparations. Additionally, the intensity of the 0-0 vibronic band was found to correlate with the amount of electronic disorder within the aggregate; the greater the intensity of the 0-0 transition, the greater the electronic disorder within the aggregate.[231]

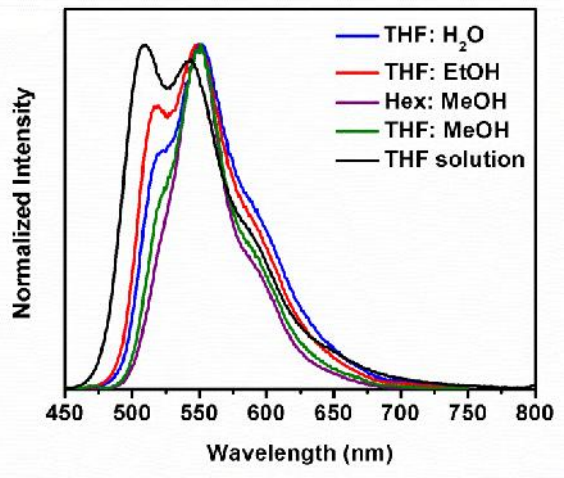

Figure 3.16. Emission spectra of drop cast films of aggregates of **4**, prepared from different solution processing preparations, and a solution of **4** in THF at room temperature.

To study the molecular order of each morphological shape, polarized confocal microscopy was done on aggregates of **4** prepared by THF/methanol and THF/H_2O solution processing preparations. The fluorescence images collected from horizontal and vertical polarizations (as defined by the lab plane) are shown in the top images in Figures 3.17A and 3.17B. The fluorescence dichroism (bottom left, Figures 3.17A and 3.17B) was calculated by determining the difference between the horizontal and vertical polarization images and dividing by the sum of these two images. Fluorescence dichroism values can range from -1 to 1; values of -1 or 1 indicate that the transition dipole moments for the sample are extremely well aligned; a fluorescence dichroism value of 0 indicates that the sample is isotropic and not geometrically aligned. A fluorescence dichroism value of 0.81 was obtained for aggregates prepared by a THF/methanol solvent combination. Likewise, fluorescence dichroism values of 0.72 and 0.80 were obtained for the THF/H_2O ellipse and discoid aggregates, respectively.[231] These fluorescence dichroism values are very similar and close to a value of 1,

suggesting that all the aggregates, regardless of the solution processing preparation, are highly aligned. Since all the aggregates are geometrically aligned, differences in the emission spectrum must be attributed to other factors.

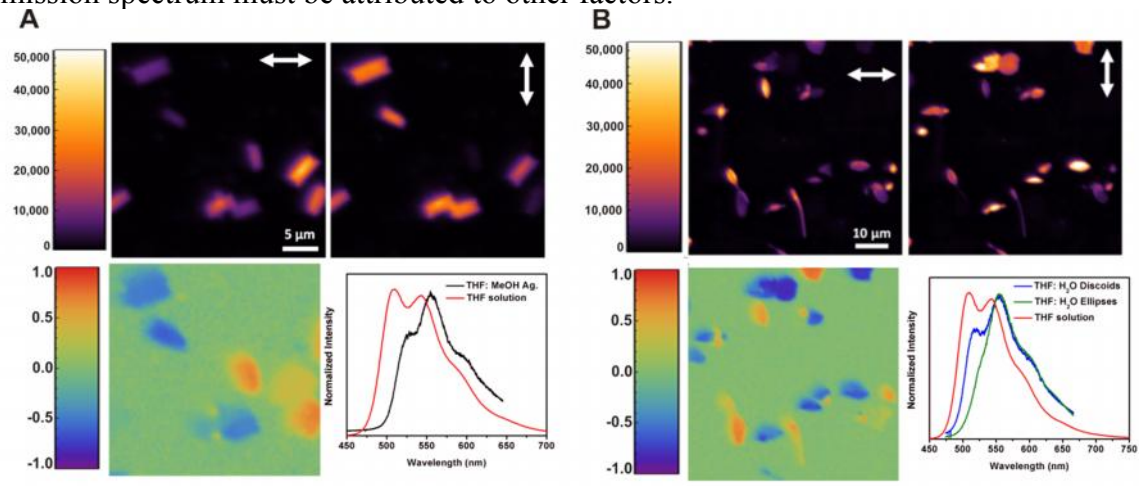

Figure 3.17. (A) Horizontally (top left) and vertically (top right) polarized fluorescence images (as defined in terms of the lab plane) from polarized scanning confocal microscopy of THF/methanol aggregates of **4**. Fluorescence dichroism image (bottom left) calculated from the horizontally and vertically polarized fluorescence images. Emission spectra (bottom right) of drop cast films of aggregates of **4**, prepared from THF/methanol, and a solution of **4** in THF at room temperature. (B) Horizontally (top left) and vertically (top right) polarized fluorescence images (as defined in terms of the lab plane) from polarized scanning confocal microscopy of THF/H_2O aggregates of **4**. Fluorescence dichroism image (bottom left) calculated from the horizontally and vertically polarized fluorescence images. Emission spectra (bottom right) of drop cast films of aggregates of **4**, prepared from THF/H_2O, and a solution of **4** in THF at room temperature.

The electronic properties of the aggregates were studied by determining the local contact potential (LCP) difference using Kelvin probe force microscopy (KPFM). The LCP value, calculated by the difference between the scanning probe tip and the surface, correlates to the differences in intermolecular charge distribution between the aggregates. Shown in Figure 3.18A is a topographic atomic force microscopy (AFM) image showing

structural features of the aggregates formed by the THF/H_2O solution processing preparation. Additionally, a representative LCP image is shown in Figure 3.18B. The LCP was found to be 70 ±30 mV between the ellipse and discoid aggregates. This 70 mV difference in the LCP from ellipse to discoid particles suggests that the highest occupied molecular orbital (HOMO) level may shift as much as 70 mV due to changes in the molecular packing, electronic disorder, and aggregation of the material. Moreover, the LCP of the rectangular aggregates, formed from a THF/methanol solvent combination, was found to be ~23 ±14 mV higher than the discoid aggregates and ~50 ±30 mV lower than the ellipse particles. This difference in LCP values, and consequently HOMO levels, with small changes in aggregation and molecular packing, imply that changes may occur in the HOMO level of polymer film materials from completely amorphous to highly crystalline regions. Differences in the effective position of the HOMO level throughout a film of varying crystallinity may affect charge separation efficiency at the donor-acceptor interface and thus, affect the efficiency of the photovoltaic device.[231]

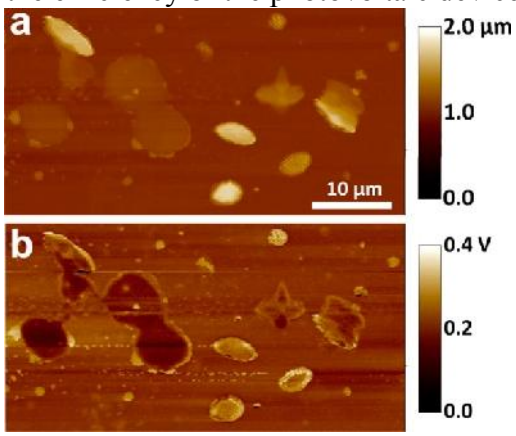

Figure 3.18. (A) Topography and (B) Local contact potential images of ellipse and discoid aggregates of **4**, prepared from a THF/H_2O solution processing preparation, on a glass substrate. Images were linearly flattened for lucidity. Data analysis was performed on the unaltered images.[231]

3.4. CONCLUSIONS

In conclusion, we have reported the convergent synthesis and characterization of a library of extremely pure, highly symmetric, and solution-processable oligoalkylthiophenes, 3',3'''',4',4''''-tetraalkyl-2,2':5',2'':5'',2''':5''',2'''':5'''',2''''':-sexithiophene, in which the alkyl group is systemically changed from a short ethyl chain to a long decyl chain. UV-Vis absorption and EPR studies suggest that upon step-wise chemical oxidation, sexithiophene first forms two polarons and then two bipolarons through a net four electron oxidation. Conversely, electrochemical studies calculate that two one-electron processes occur in the oxidation of sexithiophene. Upon variation of the alkyl group, no difference in the electronic properties of the oligoalkylthiophenes was observed. However, aggregates of oligooctylthiophene were found to have varying morphologies and amounts of electronic disorder that were tunable through solution processing preparations. The extent of molecular aggregation and electronic disorder within the aggregates was determined by comparing the suppression of the 0-0 vibronic band in the fluorescence spectra to the vibronic structure of the non-aggregated parent molecule. Additionally, a high degree of molecular alignment was observed for these aggregates, as determined by fluorescence dichroism. The extent of electronic disorder within the aggregate was correlated with the local contact potential through Kelvin probe force microscopy (KPFM) measurements. Local contact potential (LC), a measure of differences in intermolecular charge distribution, was found to vary as much as 70 mV between aggregates. This variation in local contact potential from particles of varying aggregation suggest that the effective position of the HOMO level may change with small variations in molecular packing and aggregation. Changes in the HOMO level of a material, arising from variations in crystallinity of a bulk polymer sample, may affect the charge separation and thus, efficiency of a photovoltaic device. Future efforts are focused

on determination of the local contact potential, through KPFM measurements, of the oligoalkylthiophenes with a C_{60}-type acceptor molecule under dark and illuminated conditions.

3.5. SUPPLEMENTAL DATA: CRYSTALLOGRAPHIC DATA

Table 3.6. Crystal data and structure refinement for **1**

Formula	C_{32} H_{30} S_6
FW	606.92
T (K)	223(2)
Crystal system	Monoclinic
Space group	$P2_1/c$
a (Å)	11.548(5)
b (Å)	16.028(5)
c (Å)	8.228(5)
α (deg)	90.000(5)
β (deg)	105.173(5)
γ (deg)	90.000(5)
V ($Å^3$)	1469.8(12)
Z	2
ρ (g/cm^3)	1.371
μ (mm^{-1})	0.487
F(000)	636
Crystal size (mm)	0.48 × 0.24 × 0.10
θ (deg)	3.00 to 27.50
Index ranges	$-14 \le h \le 14$
	$-20 \le k \le 20$
	$-10 \le l \le 10$
Absorption correction	Multi-scan
Max. and min. transmission	1.000 and 0.786
GOF on F^2	1.085
$R1$, w$R2$ [$I > 2\sigma(I)$]	0.0472, 0.1093
$R1$, w$R2$ (all data)	0.0580, 0.1149
Largest diff. peak and hole ($e.Å^{-3}$)	0.58 and -0.40

Table 3.7. Selected bond lengths (Å) and angles (º) for **1**

Bond distances (Å)			
C(1)-C(2)	1.371(3)	C(11)-C(12)	1.373(3)
C(2)-C(3)	1.434(4)	C(6)-C(13)	1.510(3)
C(3)-C(4)	1.365(4)	C(7)-C(14)	1.513(3)
C(4)-C(5)	1.463(3)	S(1)-C(1)	1.746(3)
C(5)-C(6)	1.370(3)	S(1)-C(4)	1.716(2)
C(6)-C(7)	1.440(3)	S(2)-C(5)	1.728(2)
C(7)-C(8)	1.379(3)	S(2)-C(8)	1.734(2)
C(8)-C(9)	1.464(3)	S(3)-C(9)	1.736(2)
C(9)-C(10)	1.366(3)	S(3)-C(12)	1.731(2)
C(10)-C(11)	1.423(3)		
Bond angles (º)			
C(1)-S(1)-C(4)	92.04(12)	S(2)-C(5)-C(4)	119.86(17)
C(5)-S(2)-C(8)	91.90(11)	S(2)-C(8)-C(9)	117.71(17)
C(9)-S(3)-C(12)	92.63(11)	S(3)-C(9)-C(8)	120.88(17)
S(1)-C(4)-C(5)	122.86(16)		

Table 3.8. Selected bond lengths (Å) and angles (º) for **2**[206]

Bond distances (Å)			
C(1)-C(2)	1.3154(1)	C(11)-C(12)	1.3528(2)
C(2)-C(3)	1.3878(2)	C(6)-C(13)	1.5007(2)
C(3)-C(4)	1.3784(2)	C(7)-C(14)	1.4820(2)
C(4)-C(5)	1.4435(2)	S(1)-C(1)	1.7123(2)
C(5)-C(6)	1.3781(2)	S(1)-C(4)	1.7370(2)
C(6)-C(7)	1.4231(2)	S(2)-C(5)	1.7415(2)
C(7)-C(8)	1.4022(2)	S(2)-C(8)	1.7327(3)
C(8)-C(9)	1.4420(2)	S(3)-C(9)	1.7349(3)
C(9)-C(10)	1.3556(2)	S(3)-C(12)	1.7292(2)
C(10)-C(11)	1.4267(2)		
Bond angles (º)			
C(1)-S(1)-C(4)	91.08	S(2)-C(5)-C(4)	114.54
C(5)-S(2)-C(8)	92.88	S(2)-C(8)-C(9)	117.18
C(9)-S(3)-C(12)	92.66	S(3)-C(9)-C(8)	123.05
S(1)-C(4)-C(5)	118.62		

Table 3.9. Crystal data and structure refinement for **3**

Formula	$C_{48}\ H_{62}\ S_6$
FW	831.34
T (K)	100(2)
Crystal system	Monoclinic
Space group	$P2_1/c$
a (Å)	11.948(7)
b (Å)	5.368(3)
c (Å)	35.404(19)
α (deg)	90.000
β (deg)	99.002(9)
γ (deg)	90.000
V ($Å^3$)	2243(2)
Z	2
ρ (g/cm^3)	1.231
μ (mm^{-1})	0.337
F(000)	892
Crystal size (mm)	.215 x .050 x .058
θ (deg)	1.93 to 25.00
Index ranges	$-14 \le h \le 14$
	$-6 \le k \le 6$
	$-42 \le l \le 42$
Absorption correction	Multi-scan
Max. and min. transmission	1.000 and 0.555
GOF on F^2	1.485
$R1$, w$R2$ [$I > 2\sigma(I)$]	0.1605, 0.2547
$R1$, w$R2$ (all data)	0.1711, 0.2592
Largest diff. peak and hole ($e.Å^{-3}$)	0.423 and -0.408

Table 3.10. Selected bond lengths (Å) and angles (º) for **3**

Bond distances (Å)			
C(1)-C(2)	1.357(13)	C(11)-C(12)	1.366(11)
C(2)-C(3)	1.420(12)	C(6)-C(13)	1.525(11)
C(3)-C(4)	1.386(12)	C(7)-C(14)	1.513(12)
C(4)-C(5)	1.477(11)	S(1)-C(1)	1.713(9)
C(5)-C(6)	1.389(12)	S(1)-C(4)	1.748(9)
C(6)-C(7)	1.445(11)	S(2)-C(5)	1.731(8)
C(7)-C(8)	1.386(12)	S(2)-C(8)	1.739(9)
C(8)-C(9)	1.470(11)	S(3)-C(9)	1.738(8)
C(9)-C(10)	1.373(12)	S(3)-C(12)	1.735(8)
C(10)-C(11)	1.414(11)		
Bond angles (º)			
C(1)-S(1)-C(4)	91.1(4)	S(2)-C(5)-C(4)	117.0(6)
C(5)-S(2)-C(8)	92.1(4)	S(2)-C(8)-C(9)	116.7(7)
C(9)-S(3)-C(12)	92.5(4)	S(3)-C(9)-C(8)	121.8(7)
S(1)-C(4)-C(5)	122.1(6)		

Table 3.11. Crystal data and structure refinement for **4**

Formula	$C_{56}\ H_{78}\ S_6$
FW	943.54
T (K)	153(2)
Crystal system	Monoclinic
Space group	$P2_1/n$
a (Å)	19.430(4)
b (Å)	7.0877(14)
c (Å)	20.538(4)
α (deg)	90
β (deg)	104.78(3)
γ (deg)	90
V ($Å^3$)	2734.6(9)
Z	2
ρ (g/cm^3)	1.146
μ (mm^{-1})	0.284
F(000)	1020
θ (deg)	2.99 to 27.50
Index ranges	$-25 \le h \le 25$
	$-9 \le k \le 9$
	$-26 \le l \le 26$
Absorption correction	Multi-scan
GOF on F^2	1.032
$R1$, w$R2$ [$I > 2\sigma(I)$]	0.0510, 0.1350
$R1$, w$R2$ (all data)	0.0754, 0.1495
Largest diff. peak and hole ($e.Å^{-3}$)	0.687 and -0.435

Table 3.12. Selected bond lengths (Å) and angles (º) for **4**

Bond distances (Å)			
C(1)-C(2)	1.342(4)	C(11)-C(12)	1.371(3)
C(2)-C(3)	1.425(3)	C(6)-C(13)	1.509(3)
C(3)-C(4)	1.455(3)	C(7)-C(14)	1.503(3)
C(4)-C(5)	1.458(3)	S(1)-C(1)	1.690(3)
C(5)-C(6)	1.381(3)	S(1)-C(4)	1.712(2)
C(6)-C(7)	1.441(3)	S(2)-C(5)	1.731(2)
C(7)-C(8)	1.385(3)	S(2)-C(8)	1.733(2)
C(8)-C(9)	1.457(3)	S(3)-C(9)	1.737(2)
C(9)-C(10)	1.378(3)	S(3)-C(12)	1.732(2)
C(10)-C(11)	1.404(3)		
Bond angles (º)			
C(1)-S(1)-C(4)	92.86(12)	S(2)-C(5)-C(4)	116.94(16)
C(5)-S(2)-C(8)	92.30(10)	S(2)-C(8)-C(9)	116.75(16)
C(9)-S(3)-C(12)	92.43(10)	S(3)-C(9)-C(8)	123.67(16)
S(1)-C(4)-C(5)	123.66(17)		

Table 3.13. Crystal data and structure refinement for **5**

Formula	C_{64} H_{94} S_6
FW	1055.75
T (K)	100(2)
Crystal system	Triclinic
Space group	[illegible]
a (Å)	5.344(2)
b (Å)	20.401(10)
c (Å)	26.935(13)
α (deg)	87.750(11)
β (deg)	87.628(17)
γ (deg)	87.093(19)
V ($Å^3$)	2928(2)
Z	2
ρ (g/cm^3)	1.198
μ (mm^{-1})	0.272
F(000)	1148
Crystal size (mm)	.466 x .087 x .049
θ (deg)	1.78 to 25.00
Index ranges	$-6 \le h \le 6$
	$-24 \le k \le 24$
	$-32 \le l \le 32$
Absorption correction	Multi-scan
Max. and min. transmission	1.0000 and .8107
GOF on F^2	1.357
$R1$, w$R2$ [$I > 2\sigma(I)$]	.1171, .2084
$R1$, w$R2$ (all data)	.1402, .2202
Largest diff. peak and hole ($e.Å^{-3}$)	.599 and -.380

Table 3.14. Selected bond lengths (Å) and angles (º) for **5**

Bond distances (Å)			
C(1)-C(2)	1.352(8)	C(11)-C(12)	1.373(7)
C(2)-C(3)	1.404(7)	C(6)-C(13)	1.495(7)
C(3)-C(4)	1.368(7)	C(7)-C(14)	1.512(7)
C(4)-C(5)	1.460(7)	S(1)-C(1)	1.716(6)
C(5)-C(6)	1.403(7)	S(1)-C(4)	1.737(5)
C(6)-C(7)	1.427(7)	S(2)-C(5)	1.729(5)
C(7)-C(8)	1.385(7)	S(2)-C(8)	1.741(5)
C(8)-C(9)	1.455(7)	S(3)-C(9)	1.731(5)
C(9)-C(10)	1.373(7)	S(3)-C(12)	1.731(5)
C(10)-C(11)	1.414(7)		
Bond angles (º)			
C(1)-S(1)-C(4)	92.5(3)	S(2)-C(5)-C(4)	117.8(4)
C(5)-S(2)-C(8)	92.8(2)	S(2)-C(8)-C(9)	118.0(4)
C(9)-S(3)-C(12)	92.8(3)	S(3)-C(9)-C(8)	123.7(4)
S(1)-C(4)-C(5)	122.7(4)		

Table 3.15. Crystal data and structure refinement for **6**

Formula	$C_{48}\ H_{50}\ F_{12}\ S_6$
FW	1047.24
T (K)	100(2)
Crystal system	Triclinic
Space group	[illegible]
a (Å)	4.6690(7)
b (Å)	12.3352(18)
c (Å)	21.126(3)
α (deg)	82.202(4)
β (deg)	85.826(5)
γ (deg)	82.343(6)
V ($Å^3$)	1192.9(3)
Z	1
ρ (g/cm^3)	1.458
μ (mm^{-1})	0.368
F(000)	542.0
Crystal size (mm)	.183 x .055 x .052
θ (deg)	3.00 to 25.00
Index ranges	$-5 \le h \le 5$
	$-14 \le k \le 14$
	$-25 \le l \le 25$
Absorption correction	Multi-scan
Max. and min. transmission	1.000 and 0.410
GOF on F^2	1.111
$R1$, w$R2$ [$I > 2\sigma(I)$]	0.1263, 0.2587
$R1$, w$R2$ (all data)	0.1906, 0.2977
Largest diff. peak and hole ($e.Å^{-3}$)	0.718 and -0.509

Table 3.16. Selected bond lengths (Å) and angles (º) for **6**

Bond distances (Å)			
C(1)-C(2)	1.307(15)	C(11)-C(12)	1.396(18)
C(2)-C(3)	1.542(16)	C(6)-C(13)	1.511(10)
C(3)-C(4)	1.440(14)	C(7)-C(14)	1.506(10)
C(4)-C(5)	1.452(11)	S(1)-C(1)	1.623(13)
C(5)-C(6)	1.393(10)	S(1)-C(4)	1.767(8)
C(6)-C(7)	1.427(11)	S(2)-C(5)	1.744(8)
C(7)-C(8)	1.387(10)	S(2)-C(8)	1.730(8)
C(8)-C(9)	1.496(11)	S(3)-C(9)	1.734(10)
C(9)-C(10)	1.398(17)	S(3)-C(12)	1.733(9)
C(10)-C(11)	1.41(2)		
Bond angles (º)			
C(1)-S(1)-C(4)	91.6(6)	S(2)-C(5)-C(4)	110.5(6)
C(5)-S(2)-C(8)	92.5(4)	S(2)-C(8)-C(9)	117.1(5)
C(9)-S(3)-C(12)	93.1(4)	S(3)-C(9)-C(8)	124.6(6)
S(1)-C(4)-C(5)	122.7(5)		

Chapter 4. Visible Light Emission from Lanthanide(III) Complexes Containing Ethylenedioxythiophene-Derivatized Bis(pyrazolyl)pyridine and Acetylacetonate Ligands as Efficient Sensitizers

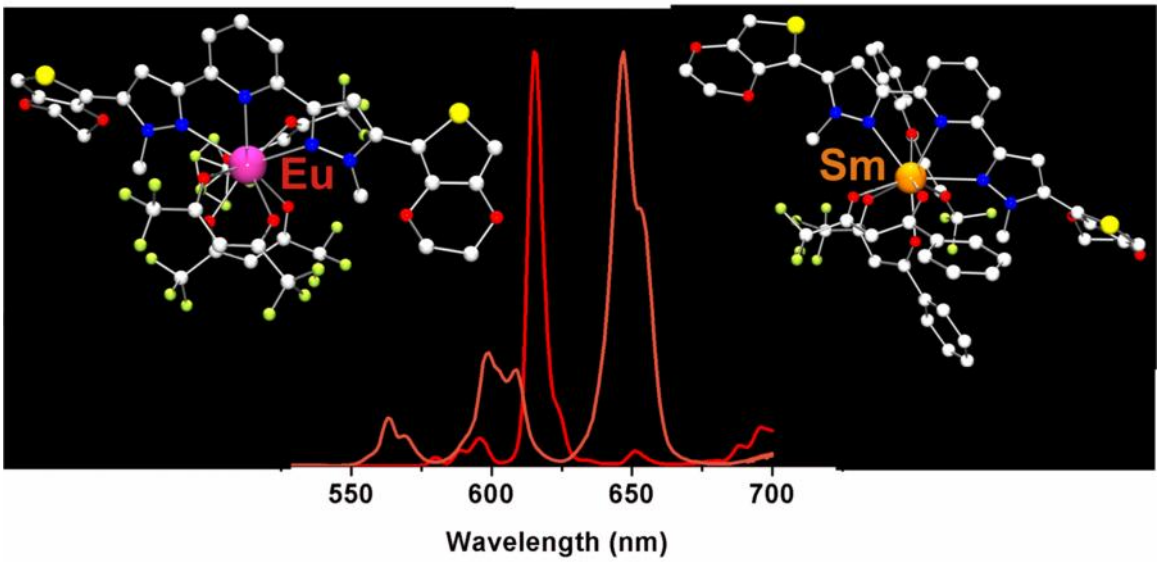

4.1. INTRODUCTION

Organometallic complexes containing lanthanide metal centers have been intensely researched due to interesting photophysical properties and potential applications in a variety of luminescent systems. Extremely sharp emission peaks and characteristic emission color specific to each Ln^{III} ion make these compounds attractive candidates for applications in which highly emissive, optically color-pure lumiphores are necessary.[27] For this reason, lanthanide complexes have been utilized in fluoroimmunoassays, light-emitting diodes (LEDs), liquid crystals, biomedical imaging and sensing applications.[27,54,234-236] Lanthanide-centered emission arises from *f-f* transitions within the atomic core of the Ln^{III} ion. These *f* electrons within the core shell of the Ln^{III} ion are effectively shielded by the $5s^2$ and $5p^6$ orbitals, such that the emission of the lanthanide ion is independent of coordinated ligands. For this reason, each Ln^{III} emits a characteristic color with very sharp (< 10 nm width at half maximum) emission peaks. However, *f-f* transitions are both parity- and spin-forbidden so direct excitation of the lanthanide ion is not possible. Thus, sensitization by another chromophore, or antenna molecule, is necessary for lanthanide emission.[27,234,237]

Use of an antenna molecule for sensitization, or indirect excitation of a lanthanide ion, is also known as the antenna effect. In the antenna effect, the singlet state of the coordinated ligand or chromophore is populated by direct excitation. Through intersystem crossing, the excited electron undergoes a spin flip and is transferred to the triplet state of the coordinated ligand. From the triplet excited state of the ligand, energy is transferred to the emissive *f** excited state of the lanthanide by way of a Förster-type dipole-dipole exchange mechanism. Relaxation from this excited *f** state gives luminescent emission that is characteristic of the particular lanthanide ion.[27,237] Coordinated antenna molecules are typically aromatic, multidentate chromophores such

as bipyridine, terpyridine, triphenylene, quinolone, or benzoic acid derivatives.[27,155,179,237-240] Because an energy cascade must occur from the excited state of the antenna ligand to the excited state of the lanthanide, energy matching between the antenna ligand and the lanthanide must be carefully considered. For the most efficient energy transfer, an energy difference between the triplet excited state of the ligand and the $^5D_0$ state of Eu^{III} has been suggested to be between 2000-3500 cm^{-1}.[27] Likewise, for Tb^{III}, the energy difference between the antenna molecule triplet state and $^5D_4$ excited state should range from 2000-4000 cm^{-1} for maximum sensitization.[27,155,237,238] In addition to these energy differences, the antenna molecule-lanthanide system must be thermodynamically and kinetically stable with a saturated coordination sphere to eliminate non-radiative energy loss.[235]

We have designed and synthesized a series of lanthanide(III) complexes sensitized with *β*-diketonates and a 3,4-ethylenedioxythiophene (EDOT)-functionalized 2,6-bis(pyrazol-3-yl)pyridine (**BPP**) ligand (**$EDOT_2$-BPP**), a tridentate nitrogen-donor ligand. The **BPP** ligand is functionalized with EDOT moieties to increase the population of the triplet excited state of the ligand and thus, increase the photoluminescent quantum yield of the lanthanide complex. The heavy sulfur atoms of the EDOT group induce spin-orbit coupling allowing for increased population of the triplet state of the ligand and more efficient energy transfer to the lanthanide center. Additionally, the extended conjugation provided by the appended EDOTs lowers the triplet state energy of the sensitizing BPP ligand, optimizing the energy difference between the antenna ligand and the lanthanide. Work by de Bettencourt-Días *et al.* in 2006 demonstrated this tuning of the ligand triplet state; derivatization of isophthalic acid with thiophene lowered the triplet state of the ligand by nearly 5000 cm^{-1}.[158] Herein, we report the synthesis, characterization, and photophysical properties of a series of tris(*β*-diketonate) trivalent, nine-coordinate lanthanide complexes containing Eu^{III}, Sm^{III}, and Tb^{III}: $Eu(btfac)_3(EDOT_2\text{-}BPP)$ (**1a**),

$Eu(hfac)_3(EDOT_2\text{-}BPP)$ (**1b**), $Eu(tta)_3(EDOT_2\text{-}BPP)$ (**1c**), $Sm(btfac)_3(EDOT_2\text{-}BPP)$ (**2a**), $Sm(hfac)_3(EDOT_2\text{-}BPP)$ (**2b**), $Sm(tta)_3(EDOT_2\text{-}BPP)$ (**2c**), $Tb(btfac)_3(EDOT_2\text{-}BPP)$ (**3a**), $Tb(hfac)_3(EDOT_2\text{-}BPP)$ (**3b**), and $Tb(tta)_3(EDOT_2\text{-}BPP)$ (**3c**). The anionic *β*-diketonates, btfac (btfac = 4,4,4-trifluoro-1-phenyl-1,3-butanedionate), hfac (hfac = 1,1,1,5,5,5-hexafluoro-2,4-pentanedionate), and tta (tta = 2-thenoyltrifluoroacetonate) offset the trivalent charge of the lanthanide ion. Additionally, the *β*-diketonates create a rigid environment around the lanthanide ion filling the coordination sphere to nine and excluding the incorporation of solvent or water that can quench luminescence.[159]

4.2. EXPERIMENTAL

4.2.1. Instrumentation

4.2.1.1. General Methods

Air- and moisture-sensitive reactions were carried out in flame-dried glassware using standard Schlenk techniques under an inert nitrogen atmosphere. All chemicals were purchased from commercial sources and used as received. Dry solvents were dried using an Innovative Technology, Pure Solv solvent purifier with a double purifying column. Low-resolution and high-resolution mass spectrometry was carried out by a Thermo Finngan TSQ 700 and Waters Autospec Ultima, respectively. Melting points were recorded with an OptiMelt Automated Melting Point System with digital image processing technology from Stanford Research System (SRS, Sunnyvale, CA). Elemental analysis was performed by QTI, Whitehouse, NJ (www.qtionline.com).

4.2.1.2. Crystal Structure Determination

The single–crystal diffraction data were collected on a Rigaku AFC12 diffractometer with a Saturn 724+ CCD using a graphite monochromator with MoKα radiation (λ = 0.71073 Å). Absorption corrections were applied using the multi-scan

technique using Abscor[160]. Data reduction were performed using the Rigaku Americas Corporation's Crystal Clear version 1.40.[165] The structures were solved by direct methods and refined anisotropically using full-matrix least-squares methods with the SHELX 97 program package.[241-243] The coordinates of the non-hydrogen atoms were refined anisotropically, while hydrogen atoms were included in the calculation isotropically but not refined. Neutral atom scattering factors and values used to calculate the linear absorption coefficient are from the International Tables for X-ray Crystallography (1992).[179] Crystal data collection and refinement details for **1b**, **2a**, and **3b** are given in Tables 4.1, 4.3, and 4.5, respectively. Selected bond lengths are given for **1b**, **2a**, and **3b** are in Tables 4.2, 4.4, and 4.6, respectively.

4.2.1.3. Spectroscopy

All spectroscopic data were obtained in methylene chloride solutions unless otherwise noted. Quartz fluorometer cells with a pathlength of 10 mm. Luminescence measurements were recorded on a Photon Technology International QM 4 spectrophotometer equipped with a 6-inch diameter K Sphere-B integrating sphere for quantum yield measurements. The quantum yield was calculated by dividing the area under the emission peak of the complex by the difference between the area under the excitation peak of the sample from that of a blank solution ($A_{em,\ sample}$ / ($A_{ex,\ blank}$ - $A_{ex,\ sample}$), where A = area under peak).[179] Measurements at 77 K were recorded using an optical liquid nitrogen Dewar sample holder. Low-temperature samples were made in 2-methyltetrahydrofuran (2-MeTHF) in quartz 4 mm outer diameter EPR tubes. Ligand triplet state energies were calculated by using the wavelength corresponding to the onset of ligand phosphorescence and converting to cm^{-1}.

4.2.2. Synthesis

The $EDOT_2$-BPP ligand, 2,6-bis[1-methyl-5-(3,4-ethylenedioxythien-2-yl)pyrazol-3-yl]pyridine, was prepared according to a procedure described in Chapter 2. $Ln(tta)_3 \cdot 2H_2O$ (tta = 2-thenoyltrifluoroacetonate), $Ln(btfac)_3 \cdot 2H_2O$ (btfac = 4,4,4-trifluoro-1-phenyl-1,3-butanedionate), and $Ln(hfac)_3 \cdot 2H_2O$ (hfac = 1,1,1,5,5,5-hexafluoro-2,4-pentanedionate) (Ln = Eu^{III}, Sm^{III}, and Tb^{III}) were prepared according to literature procedures.[179,244-247] The Ln(*β*-diketonate)$_3$($EDOT_2$-BPP) (Ln = Eu^{III}, Sm^{III}, and Tb^{III}) complexes (**1a-c**, **2a-c**, and **3a-c**) were prepared according to a general procedure described by Stanley *et al*.[248]

Eu(btfac)$_3$($EDOT_2$-BPP) (1a). Yield: 89%. mp: 177 °C; UV-Vis (CH_2Cl_2, nm): λ_{max} 265 (ε, 5.82 x 10^4 M^{-1} cm^{-1}); HRMS (CI+) calcd. for $[C_{45}H_{33}N_5O_8S_2F_6Eu]^+$ ($[Eu(btfac)_2(EDOT_2\text{-BPP})]^+$): 1102.0887. Found 1102.0897; Anal. calcd. for $C_{55}H_{39}N_5O_{10}S_2F_9Eu \cdot C_6H_5CH_3$: C, 52.85; H, 3.36; N, 4.97. Found: C, 52.97; H, 3.81; N, 4.39.

Eu(hfac)$_3$($EDOT_2$-BPP) (1b). Yield: 88%. mp: 200 °C; UV-Vis (CH_2Cl_2, nm): λ_{max} 307 (ε, 6.00 x 10^4 M^{-1} cm^{-1}); HRMS (CI+) calcd. for $[C_{35}H_{23}N_5O_8S_2F_{12}Eu]^+$ ($[Eu(hfac)_2(EDOT_2\text{-BPP})]^+$): 1086.0009. Found 1086.0011; Anal. calcd. for $C_{40}H_{24}N_5O_{10}S_2F_{18}Eu$: C, 37.16; H, 1.87; N, 5.42. Found: C, 37.81; H, 1.56; N, 5.35.

Eu(tta)$_3$($EDOT_2$-BPP) (1c). Yield: 83%. mp: 252 °C; UV-Vis (CH_2Cl_2, nm): λ_{max} 269 (ε, 6.78 x 10^4 M^{-1} cm^{-1}); HRMS (CI+) calcd. for $[C_{41}H_{29}N_5O_8S_4F_6Eu]^+$ ($[Eu(tta)_2(EDOT_2\text{-BPP})]^+$): 1114.00. Found 1114.0003; Anal. calcd. for $C_{49}H_{33}N_5O_{10}S_5F_9Eu \cdot CH_2Cl_2$: C, 42.29; H, 2.48; N, 5.08. Found: C, 42.11; H, 2.58; N, 5.18.

Sm(btfac)$_3$($EDOT_2$-BPP) (2a). Yield: 75%. mp: 202 °C; UV-Vis (CH_2Cl_2, nm): λ_{max} 265 (ε, 7.14 x 10^4 M^{-1} cm^{-1}); HRMS (CI+) calcd. for $[C_{45}H_{33}N_5O_8S_2F_6Sm]^+$

([Sm(btfac)$_2$(EDOT$_2$-BPP)]$^+$): 1101.0872. Found 1101.0868; Anal. calcd. for $C_{55}H_{39}N_5O_{10}S_2F_9Sm$: C, 50.22; H, 2.99; N, 5.32. Found: C, 50.54; H, 3.09; N, 5.19.

Sm(hfac)$_3$(EDOT$_2$-BPP) (2b). Yield: 99%. mp: 196 °C; UV-Vis (CH_2Cl_2, nm): λ_{max} 307 (ε, 6.63 x 10^4 M^{-1} cm^{-1}); HRMS (CI+) calcd. for $[C_{35}H_{23}N_5O_8S_2F_{12}Sm]^+$ ([Sm(hfac)$_2$(EDOT$_2$-BPP)]$^+$): 1084.9994. Found 1084.9998; Anal. calcd. for $C_{40}H_{24}N_5O_{10}S_2F_{18}Sm$: C, 37.21; H, 1.87; N, 5.42. Found: C, 37.38; H, 1.19; N, 5.29.

Sm(tta)$_3$(EDOT$_2$-BPP) (2c). Yield: 98%. Decomp. at 236 °C; UV-Vis (CH_2Cl_2, nm): λ_{max} 270 (ε, 6.68 x 10^4 M^{-1} cm^{-1}); HRMS (CI+) calcd. for $[C_{41}H_{29}N_5O_8S_4F_6Sm]^+$ ([Sm(tta)$_2$(EDOT$_2$-BPP)]$^+$): 1113.0001. Found 1113.0012; Anal. calcd. for $C_{49}H_{33}N_5O_{10}S_5F_9Sm$: C, 44.13; H, 2.49; N, 5.25. Found: C, 44.64; H, 2.23; N, 5.24.

Tb(btfac)$_3$(EDOT$_2$-BPP) (3a). Yield: 86%. mp: 216 °C; UV-Vis (CH_2Cl_2, nm): λ_{max} 265 (ε, 6.51 x 10^4 M^{-1} cm^{-1}); HRMS (CI+) calcd. for $[C_{45}H_{33}N_5O_8S_2F_6Tb]^+$ ([Tb(btfac)$_2$(EDOT$_2$-BPP)]$^+$): 1108.0928. Found 1108.0939; Anal. calcd. for $C_{55}H_{39}N_5O_{10}S_2F_9Tb$: C, 49.89; H, 2.97; N, 5.29. Found: C, 49.88; H, 2.64; N, 5.11.

Tb(hfac)$_3$(EDOT$_2$-BPP) (3b). Yield: 94%. mp: 195 °C; UV-Vis (CH_2Cl_2, nm): λ_{max} 307 (ε, 5.41 x 10^4 M^{-1} cm^{-1}); HRMS (CI+) calcd. for $[C_{35}H_{23}N_5O_8S_2F_{12}Tb]^+$ ([Tb(hfac)$_2$(EDOT$_2$-BPP)]$^+$): 1092.0050. Found 1092.0057; Anal. calcd. for $C_{40}H_{24}N_5O_{10}S_2F_{18}Tb \cdot C_6H_5CH_3 \cdot H_2O$: C, 40.04; H, 2.43; N, 4.97. Found: C, 39.14; H, 2.14; N, 5.10.

Tb(tta)$_3$(EDOT$_2$-BPP) (3c). Yield: 98%. Decomp. at 245 °C; UV-Vis (CH_2Cl_2, nm): λ_{max} 270 (ε, 8.17 x 10^4 M^{-1} cm^{-1}); HRMS (CI+) calcd. for $[C_{41}H_{29}N_5O_8S_4F_6Tb]^+$ ([Tb(tta)$_2$(EDOT$_2$-BPP)]$^+$): 1120.0057. Found 1120.0050; Anal. calcd. for $C_{49}H_{33}N_5O_{10}S_5F_9Tb$: C, 43.85; H, 2.48; N, 5.22. Found: C, 44.11; H, 2.65; N, 5.16.

Gd(tta)$_3$(EDOT$_2$-BPP) (4). Yield: 99%. Decomp. at 181 °C; UV-Vis (CH_2Cl_2, nm): λ_{max} 270 (ε, 6.39 x 10^4 M^{-1} cm^{-1}); HRMS (CI+) calcd. for $[C_{41}H_{29}N_5O_8S_4F_6Gd]^+$

([Gd(tta)$_2$(EDOT$_2$-BPP)]$^+$): 1119.0044. Found 1119.0060; Anal. calcd. for $C_{49}H_{33}N_5O_{10}S_5F_9Gd$: C, 43.19; H, 2.48; N, 5.22. Found: C, 43.54; H, 2.34; N, 5.05.

4.3. Results and Discussion

4.3.1. Synthesis of Ln(*β*-diketonate)$_3$(EDOT$_2$-BPP)

The EDOT-functionalized 2,6-bis(pyrazol-3-yl)pyridine ligand, **EDOT$_2$-BPP**, was prepared according to a previously reported procedure in Chapter 2. Complexes **1a-c**, **2a-c**, and **3a-c** were synthesized by heating the **EDOT$_2$-BPP** ligand with the appropriate Ln^{III} tris *β*-diketonate dihydrate in toluene, as shown in Scheme 4.1.[155,249] Proposed structures for compounds **1a-c**, **2a-c**, and **3a-c** were confirmed by melting point, high-resolution mass spectrometry, combustion analysis, and single crystal X-ray diffraction (*vide infra*).

Scheme 4.1. Synthesis of Ln(III) complexes **1a-c**, **2a-c**, **3a-c**

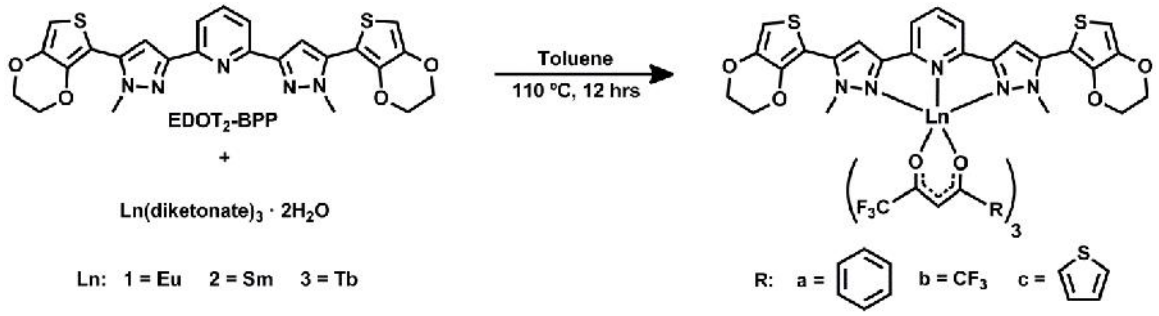

4.3.2. X-Ray Crystal Structures of Lanthanide Complexes

4.3.2.1. X-Ray Crystallography of Europium(III) Complexes

Crystals suitable for single crystal X-ray diffraction were grown from slow diffusion of hexanes into a saturated solution of **1b** in methylene chloride. The single crystal structure of **1b** is shown in Figure 4.1 and is a representative example of the solid-state structure of the entire Eu(*β*-diketonate)$_3$(EDOT$_2$-BPP) series. As depicted in Figure

4.1A, the Eu^{III} metal center is bound to three nitrogens of the tridentate $EDOT_2$-BPP ligand and six oxygens of the three bound β-dikentonate ligands. Additionally, as shown in Figure 4.1B, this nine-coordinate Eu^{III} metal center is in a slightly distorted tri-capped trigonal prism environment. The Eu^{III}-N and Eu^{III}-O average bond lengths of 2.599 Å and 2.434 Å, respectively, agree closely to that of analogous Eu^{III} complexes.[179] Selected bond distances and angles for **1b** are listed in Table 4.2.

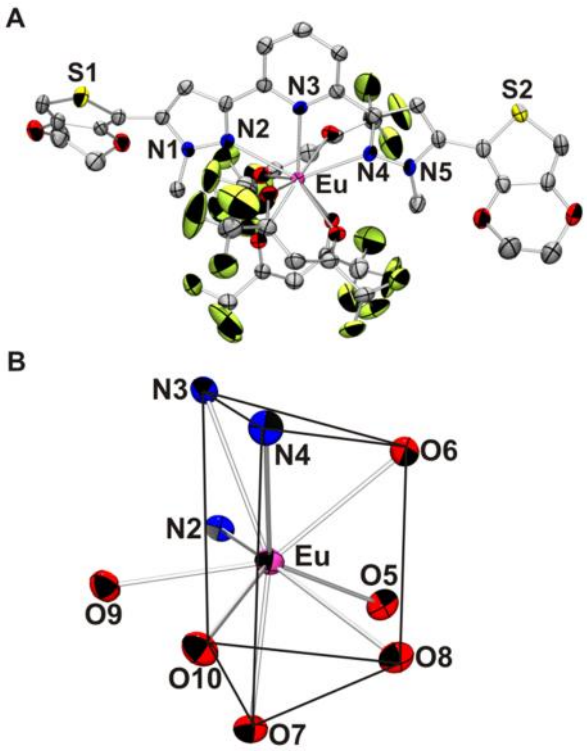

Figure 4.1. (A) ORTEP diagram of **1b**, showing the labeling scheme of selected atoms. Thermal ellipsoids are drawn at the 50% probability level. Hydrogen atoms have been omitted for clarity. (B) Coordination environment around Eu^{III} in **1b**.

Table 4.1. Crystal data and structure refinement for **1b**

Formula	$C_{40}\ H_{24}\ Eu\ F_{18}\ N_5\ O_{10}\ S_2$
FW	1292.72
T (K)	100(2)
Crystal system	Monoclinic
Space group	$P2_1/n$
a (Å)	15.286(2)
b (Å)	17.131(2)
c (Å)	19.662(3)
α (deg)	90.000
β (deg)	110.729(3)
γ (deg)	90.000
V ($Å^3$)	1309.6(5)
Z	4
ρ (g/cm^3)	1.738
μ (mm^{-1})	1.519
F(000)	2544
Crystal size (mm)	0.15 × 0.04 × 0.04
θ (deg)	3.00 to 27.50
Index ranges	$-19 \le h \le 19$
	$-22 \le k \le 22$
	$-25 \le l \le 25$
Absorption correction	Multi-scan
Max. and min. transmission	1.000 and .6587
GOF on F^2	1.113
$R1$, w$R2$ [$I > 2\sigma(I)$]	0.0483, 0.1021
$R1$, w$R2$ (all data)	0.0726, 0.1105
Largest diff. peak and hole ($e.Å^{-3}$)	1.003 and -0.782

Table 4.2. Selected bond lengths (Å) and angles (°) for **1b**

Bond distances (Å)			
Eu(1)-N(2)	2.609(3)	Eu(1)-O(7)	2.405(3)
Eu(1)-N(3)	2.599(3)	Eu(1)-O(8)	2.407(3)
Eu(1)-N(4)	2.589(4)	Eu(1)-O(9)	2.429(3)
Eu(1)-O(5)	2.484(3)	Eu(1)-O(10)	2.437(3)
Eu(1)-O(6)	2.444(3)		
Bond angles (°)			
N(2)-Eu(1)-N(4)	126.56(11)	N(3)-Eu(1)-O(10)	113.63(10)
N(2)-Eu(1)-N(3)	63.37(11)	N(3)-Eu(1)-O(7)	143.54(10)
N(3)-Eu(1)-N(4)	63.19(11)	N(3)-Eu(1)-O(6)	75.30(10)
N(2)-Eu(1)-O(5)	70.02(11)	N(4)-Eu(1)-O(9)	97.56(11)
N(2)-Eu(1)-O(8)	139.88(11)	N(4)-Eu(1)-O(8)	87.86(11)
N(2)-Eu(1)-O(9)	69.30(10)	N(4)-Eu(1)-O(5)	133.09(11)

4.3.2.2. X-Ray Crystallography of Samarium(III) Complexes

The solid-state structure of **2a**, as determined by single crystal X-ray diffraction, is shown in Figure 4.2A as a representative example of the entire Sm^{III} $EDOT_2$-BPP *β*-diketonate series. X-ray quality crystals were grown from slow diffusion of hexanes into a saturated solution of **2a** in methylene chloride. The nine-coordinate Sm^{III} complex is defined by six oxygens from the three *β*-diketonate ligands and three nitrogens from the tridentate $EDOT_2$-BPP ligand. Complex **2a** crystallized in the triclinic space group $P\bar{1}$ and contained two molecules in the unit cell. The geometry about the trivalent samarium metal center is a distorted tri-capped trigonal prism, as depicted in Figure 4.2B. The average bond lengths of 2.654 Å and 2.413 Å for Sm^{III}-N and Sm^{III}-O, respectively, differ greatly from Sm^{III}-N (2.373 Å) and Sm^{III}-O (2.661 Å) bond distances reported for a $Sm(DBM)_3(Phen)$ complex.[239] This difference in bond lengths between $Sm(DBM)_3(Phen)$ and Sm(*β*-diketonate)$_3$($EDOT_2$-BPP) is likely caused by differences in

the bound multidentate ligand, as phenanthroline (Phen) serves as a bidentate chelate and the $EDOT_2$-BPP ligand binds as a tridentate chelate. Additional bond lengths and angles for **2a** can be found in the Table 4.4.

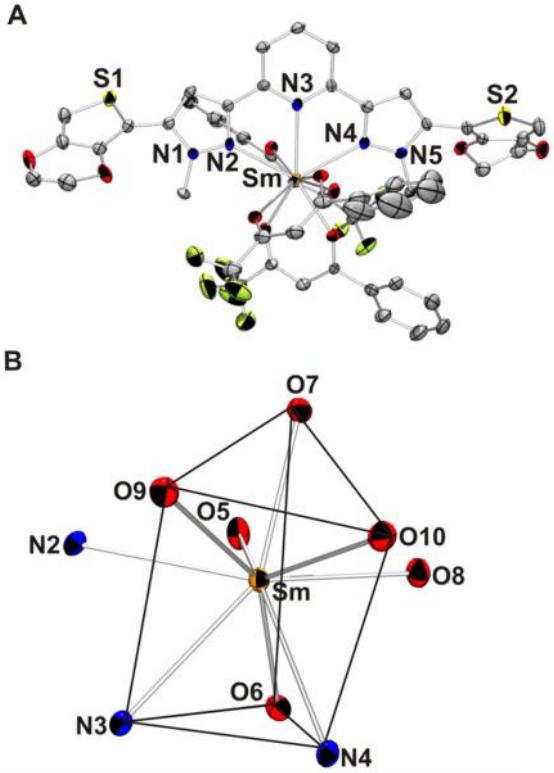

Figure 4.2. (A) ORTEP diagram of **2a**, showing the labeling scheme of selected atoms. Thermal ellipsoids are drawn at the 50% probability level. Hydrogen atoms have been omitted for clarity. (B) Coordination environment around Sm^{III} in **2a**.

Table 4.3. Crystal data and structure refinement for **2a**

Formula	C_{55} H_{33} F_9 N_5 O_{10} S_2 Sm
FW	1309.33
T (K)	100(2)
Crystal system	Triclinic
Space group	[illegible]
a (Å)	9.8755(7)
b (Å)	16.1927(12)
c (Å)	18.9065(13)
α (deg)	104.950(7)
β (deg)	104.183(7)
γ (deg)	92.161(7)°
V ($Å^3$)	2815.5(3)
Z	2
ρ (g/cm^3)	1.544
μ (mm^{-1})	1.208
F(000)	1306
Crystal size (mm)	0.12 × 0.07 × 0.04
θ (deg)	1.47 to 27.41
Index ranges	$-11 \le h \le 11$
	$-19 \le k \le 18$
	$0 \le l \le 22$
Absorption correction	Multi-scan
Max. and min. transmission	1.000 and .734
GOF on F^2	1.048
$R1$, w$R2$ [$I > 2\sigma(I)$]	0.0530, 0.1189
$R1$, w$R2$ (all data)	0.0683, 0.1253
Largest diff. peak and hole ($e.Å^{-3}$)	0.934 and -0.989

Table 4.4. Selected bond lengths (Å) and angles (°) for **2a**

Bond distances (Å)			
Sm(1)-N(2)	2.617(5)	Sm(1)-O(7)	2.395(4)
Sm(1)-N(3)	2.670(5)	Sm(1)-O(8)	2.383(3)
Sm(1)-N(4)	2.676(5)	Sm(1)-O(9)	2.441(4)
Sm(1)-O(5)	2.439(3)	Sm(1)-O(10)	2.408(4)
Sm(1)-O(6)	2.409(4)		
Bond angles (°)			
N(2)-Sm(1)-N(4)	123.5(2)	N(3)-Sm(1)-O(6)	72.2(1)
N(2)-Sm(1)-N(3)	62.1(2)	N(3)-Sm(1)-O(9)	78.5(1)
N(3)-Sm(1)-N(4)	61.6(2)	N(3)-Sm(1)-O(8)	138.0(1)
N(2)-Sm(1)-O(5)	69.8(1)	N(4)-Sm(1)-O(5)	136.4(1)
N(2)-Sm(1)-O(10)	133.9(1)	N(4)-Sm(1)-O(10)	68.0(1)
N(2)-Sm(1)-O(7)	90.9(1)	N(4)-Sm(1)-O(7)	140.6(1)

4.3.2.3. X-Ray Crystallography of Terbium(III) Complexes

The solid-state structure of the Tb(β-diketonate)$_3$(EDOT$_2$-BPP) complexes was confirmed by single-crystal X-ray diffraction. Crystals suitable for X-ray diffraction were grown from the slow evaporation of hexanes into a concentrated solution of **3b** in methylene chloride. The crystal structure of **3b** in Figure 4.3A is shown as a representative example of the solid-state structures of **3a-c**. The coordination environment of the Tb^{III} ion, along with the atom labeling scheme, is shown in Figure 4.3B. Complex **3b** crystallized in the monoclinic $P2_1/c$ space group and contained four molecules in the unit cell. Like the previously described Eu^{III} and Sm^{III} complexes **1b** and **2a**, the coordination environment of the Tb^{III} complex is defined by the six oxygen atoms from the three β-diketonates and three nitrogens from the EDOT$_2$-BPP ligand. As depicted in Figure 4.3B, the Tb^{III} metal center is in a slightly distorted tri-capped trigonal prism geometry. The average bond distances of 2.574 Å and 2.407 Å for Tb^{III}-N and

Tb^{III}-O, respectively, are similar to bond lengths reported for similar Tb^{III} complexes.[239] Additional bond lengths and angles for **3b** are listed in Table 4.6. A trend is observed between the ionic radii of Sm^{III}, Eu^{III}, and Tb^{III} and the average Ln^{III}-N bond distance reported in **1b**, **2a**, and **3b**. As the ionic radii of the lanthanide decreases ($Sm^{III} > Eu^{III} > Tb^{III}$) the average Ln^{III}-N bond distance also decreases: Sm^{III}-N: 2.65 ±0.03 Å; Eu^{III}-N: 2.60 ±0.01 Å; Tb^{III}-N: 2.574 ±0.009 Å.

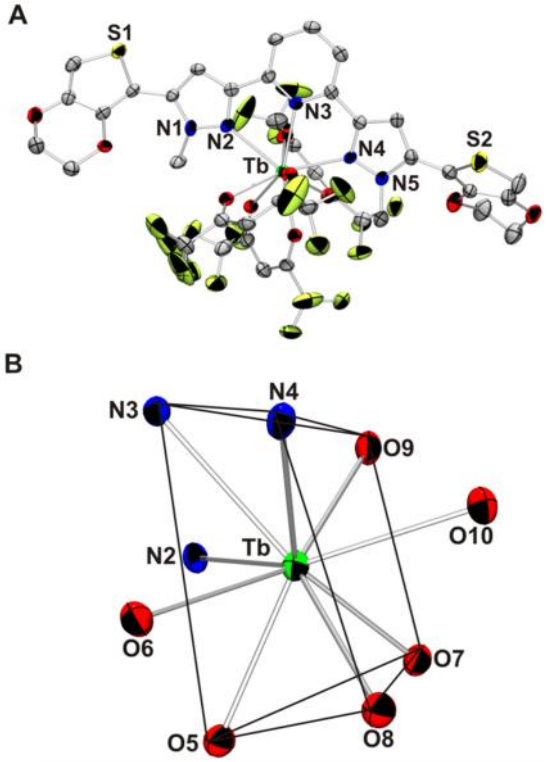

Figure 4.3. (A) ORTEP diagram of **3b**, showing the labeling scheme of selected atoms. Thermal ellipsoids are drawn at the 50% probability level. Hydrogen atoms have been omitted for clarity. (B) Coordination environment around Tb^{III} in **3b**.

Table 4.5. Crystal data and structure refinement for **3b**

Formula	$C_{40}\ H_{24}\ F_{18}\ N_5\ O_{10}\ S_2\ Tb$
FW	1299.68
T (K)	100(2)
Crystal system	Monoclinic
Space group	$P2_1/c$
a (Å)	15.236(5)
b (Å)	16.967(5)
c (Å)	20.103(4)
α (deg)	90.000
β (deg)	114.393(17)
γ (deg)	90.000
V ($Å^3$)	4733(2)
Z	4
ρ (g/cm^3)	1.824
μ (mm^{-1})	1.715
F(000)	2552
Crystal size (mm)	0.20 × 0.13 × 0.08
θ (deg)	1.47 to 27.41
Index ranges	$-19 \le h \le 19$
	$-21 \le k \le 21$
	$-26 \le l \le 25$
Absorption correction	Multi-scan
Max. and min. transmission	1.000 and .681
GOF on F^2	1.305
$R1$, w$R2$ [$I > 2\sigma(I)$]	0.0493, 0.1183
$R1$, w$R2$ (all data)	0.0585, 0.1405
Largest diff. peak and hole ($e.Å^{-3}$)	1.612 and -1.357

Table 4.6. Selected bond lengths (Å) and angles (°) for **3b**

Bond distances (Å)			
Tb(1)-N(2)	2.583(5)	Tb(1)-O(7)	2.371(4)
Tb(1)-N(3)	2.566(3)	Tb(1)-O(8)	2.377(3)
Tb(1)-N(4)	2.574(3)	Tb(1)-O(9)	2.405(4)
Tb(1)-O(5)	2.458(4)	Tb(1)-O(10)	2.410(3)
Tb(1)-O(6)	2.423(4)		
Bond angles (°)			
N(2)-Tb(1)-N(4)	127.7(1)	N(3)-Tb(1)-O(6)	74.7(1)
N(2)-Tb(1)-N(3)	63.9(1)	N(3)-Tb(1)-O(10)	113.8(1)
N(3)-Tb(1)-N(4)	63.8(1)	N(3)-Tb(1)-O(8)	143.6(1)
N(2)-Tb(1)-O(5)	69.8(1)	N(4)-Tb(1)O(5)	133.3(1)
N(2)-Tb(1)-O(9)	69.0(1)	N(4)-Tb(1)-O(7)	140.8(1)
N(2)-Tb(1)-O(7)	86.2(1)	N(4)-Tb(1)-O(9)	97.9(1)

4.3.3. Photophysics of Ligand and Lanthanide(III) Complexes

4.3.3.1. Determination of Triplet Excited State Energy of EDOT$_2$-BPP.

The Gd(tta)$_3$(EDOT$_2$-BPP) (**4**) complex was prepared according to a general complexation procedure described by Stanley and coworkers.[250] The **EDOT$_2$-BPP** ligand was complexed with Gd^{III} to enhance spin-orbit coupling and thus, ligand phosphorescence, due to the presence of the heavy atom, Gd. Additionally, only pure ligand-centered emission should be observed as the emissive excited state of Gd^{III} (f^* = 32,066 cm^{-1})[250] is too high for sensitized luminescent lanthanide emission. The triplet state energy of the **EDOT$_2$-BPP** ligand was determined as proposed by Crosby *et al.* at 77 K from solutions of the Gd^{III} complex in 2-MeTHF.[179] The ligand triplet state energy of the **EDOT$_2$-BPP** ligand was calculated by using the wavelength corresponding to the onset of ligand phosphorescence at 77 K and converting to cm^{-1} (see spectrum in Figure

4.4). Ligand phosphorescence is observed from 450 to 600 nm, and the energy of the ligand triplet state, when bound to Gd^{III} in a tridentate mode, is 21,300 cm^{-1}.

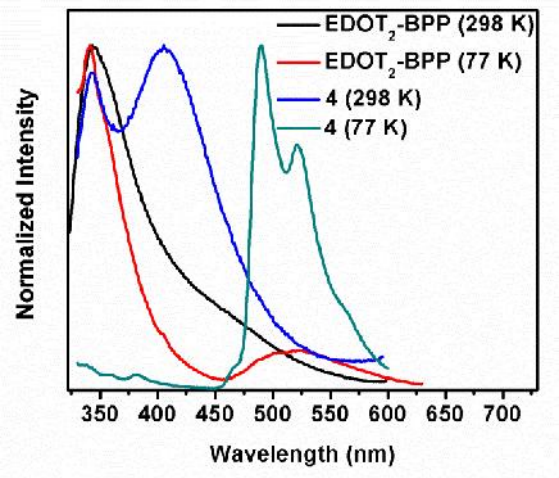

Figure 4.4. Emission spectra of **$EDOT_2$-BPP** and **4** at 298 K in CH_2Cl_2 and 77 K in 2-MeTHF.

4.3.3.2. Spectroscopy of Europium(III) Complexes

The photophysical properties for Eu^{III} complexes **1a-c** are shown in Figure 4.5 and are summarized in Table 4.7. The absorption and excitation spectra for **1a-c** are shown in Figure 4.5A; a λ_{abs} of 269-271 nm is observed for each of the three Eu^{III} complexes, which is attributed to the $\pi \rightarrow \pi^*$ transition of the $EDOT_2$-BPP ligand. An additional shoulder is observed in each of the absorption profiles (312-332 nm) which is attributed to absorbance from the bound β-diketonate ligands. While monitoring the characteristic emission of Eu^{III} at 615 nm, an excitation profile is obtained that matches the absorption shoulder corresponding to contribution from the β-diketonate ligands (Figure 4.5A). This indicates that photoluminescent europium emission occurs predominantly from energy transfer from the β-diketonate ligands to the Eu^{III} ion. Shown in Figure 4.5B are the emission profiles of complexes **1a-c**. The spectra of all three complexes are dominated by the characteristic sharp peak of Eu^{III} photoluminescent

emission at 615 nm with additional peaks belonging to $^5D_0 \rightarrow {}^7F_{0\text{-}4}$ transitions occurring between 575-725 nm. Notably, no residual fluorescence (343 nm) or phosphorescence (490 nm, see Figure 4.4) from the $EDOT_2$-BPP ligand is observed, indicating that energy transfer from the $EDOT_2$-BPP antenna ligand to the Eu^{III} ion is an efficient process. The emission spectra is dominated by the hypersensitive $^5D_0 \rightarrow {}^7F_2$ transition of the Eu^{III} ion at 615 nm, indicating that the symmetry of the coordination environment around the Eu^{III} metal center is low in solution.[155] This low symmetry of complexes **1a-c** is supported by the low symmetry observed in the solid-state X-ray crystal structure (see Figure 4.5B). Additionally, no splitting is observed in the $^5D_0 \rightarrow {}^7F_0$ transition peak, indicating that there is only one chemical environment around the Eu^{III} ion and only one emissive species is present in solution.[243,251] Absolute quantum yields were obtained in triplicate using an integrating sphere and range between 15 to 34% in solution. These quantum yields agree closely with the values obtained by Stanley and coworkers (16 to 28%) in which the photoluminescence of Eu^{III} complexes sensitized with a structural isomer of the $EDOT_2$-BPP ligand was studied.[252-256] The solution-state lifetimes of complexes **1a-c** range from 217 to 380 μs and closely agree with the lifetimes determined for Eu^{III} complexes containing thiophene-derivatized antenna ligands (248 to 338 μs) reported by de Bettencourt-Días.[252-261] Upon cooling to 77 K, the emission profile appears very similar to that obtained at room temperature, with the spectra dominated by the sharp, characteristic emission peak at 615 nm (Figure 4.5C), with little to no ligand fluorescence or phosphorescence present. However, the peaks located from 575 to 700 nm become sharper and more intense due to the deactivation of non-radiative pathways in a rigid media at 77 K. Additionally, at room temperature, solid-state photoluminescent emission is observed, as shown in Figure 4.5D. No residual ligand fluorescence or phosphorescence remains in the emission spectra, suggesting that in the solid-state, the

energy transfer between the antenna ligand and the Eu^{III} ion is extremely efficient. Solid-state quantum yields range from 6 to 25%, demonstrating that these Eu^{III} complexes could have potential applications in solid-state light-emitting devices.

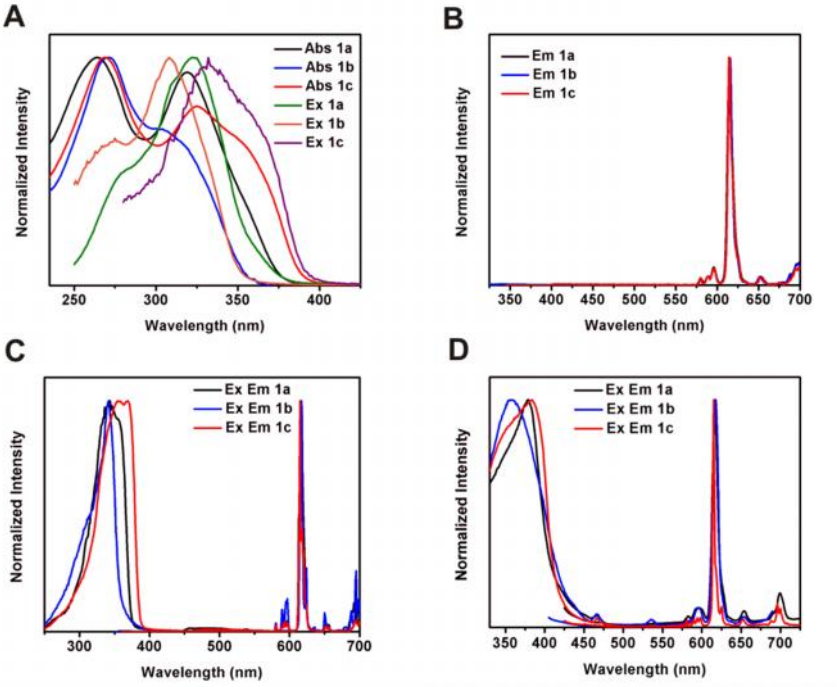

Figure 4.5. (A) Absorption and excitation spectra of **1a-c** at room temperature in CH_2Cl_2. (B) Emission spectra of **1a-c** at room temperature in CH_2Cl_2. (C) Excitation and emission spectra of **1a-c** at 77 K in 2-MeTHF. (D) Excitation and emission spectra of **1a-c** at room temperature in the solid state.

Table 4.7. Photophysical properties of complexes **1a-c**, **2a-c**, and **3a-c**

Complex	Medium	λ_{Abs} (nm)	λ_{Ex} (nm)	λ_{Em} (nm)	Φ_{Em} (%)	τ_0 (μs)
1a	CH_2Cl_2	269	322	615	15 ±2	380 ±2
	2-MeTHF	a	344	614	a	313 ±1
	Solid	a	380	616	13 ±5	389 ±13
1b	CH_2Cl_2	271	316	615	34 ±4	340 ±9
	2-MeTHF	a	342	615	a	941 ±6
	Solid	a	359	618	6 ±3	766 ±16
1c	CH_2Cl_2	271	335	614	26 ±9	217 ±2
	2-MeTHF	a	354	615	a	352 ±3
	Solid	a	384	615	25 ±5	512 ±4
2a	CH_2Cl_2	265	343	647	6.0 ±0.4	118.3 ±0.4
	2-MeTHF	a	370	647	a	74.7 ±0.4
	Solid	a	374	652	3 ±1	98.5 ±0.5
2b	CH_2Cl_2	307	323	647	14 ±2	147.2 ±0.5
	2-MeTHF	a	350	646	a	89.2 ±0.3
	Solid	a	355	647	5 ±1	118.1 ±0.4
2c	CH_2Cl_2	270	358	647	3.4 ±0.5	113.7 ±0.4
	2-MeTHF	a	376	648	a	82.4 ±0.9
	Solid	a	387	652	6 ±1	95.57 ±0.02
3a	CH_2Cl_2	265	341	547	0.5 ±0.3	16 ±1
	2-MeTHF	a	359	545	a	484 ±2
	Solid	a	b	b	b	b
3b	CH_2Cl_2	307	326	546	0.07 ±0.02	15.2 ±0.4
	2-MeTHF	a	337	546	a	860 ±3
	Solid	a	b	b	b	b
3c	CH_2Cl_2	270	368	616	0.52 ±0.12	305 ±5
	2-MeTHF	a	372	545	a	411 ±2
	Solid	a	b	b	b	b

a: Not measured
b: Not measured due to minimal or no Ln^{III} emission
*Measurements taken in CH_2Cl_2 and in the solid state were performed at 298 K. Measurements taken in 2-MeTHF were performed at 77 K.

4.3.3.3. Spectroscopy of Samarium(III) Complexes

The photoluminescent properties of complexes **2a-c** were studied in solution at room temperature and 77K and in the solid-state at room temperature. The photophysical properties of **2a-c** are displayed in Figure 4.6 and summarized in Table 4.7. The

absorption spectra of complexes **2a-c** (Figure 4.6A) are comprised of two components: high energy bands (265-270 nm) typical of $\pi \rightarrow \pi^*$ transitions within the $EDOT_2$-BPP ligand and lower energy bands (307-327 nm) due to the bound *β*-diketonate ligands. Monitoring the characteristic Sm^{III} emission at 647 nm gives an excitation profile that is slightly red-shifted of the λ_{max} of the UV-Vis spectra, corresponding to *β*-diketonate absorption. This indicates that Sm^{III} emission is due to population of the lowest singlet excited state of the *β*-diketonate ligands, similar to what is observed with the aforementioned Eu^{III} complexes. The solution (Figure 4.6B) and solid-state (Figure 4.6D) emission spectra show the characteristic $^4G_{5/2} \rightarrow {}^6H_{5/2\text{-}13/2}$ transitions of the trivalent Sm^{III} ion from 550 to 700 nm with the intense, hypersensitive $^4G_{5/2} \rightarrow {}^6H_{9/2}$ transition dominating the spectra at 647 nm. The photoluminescent lifetimes of **2a-c** were measured while monitoring the dominant $^4G_{5/2} \rightarrow {}^6H_{9/2}$ transition and range from 114 to 147 μs in solution and 96 to 118 μs in the solid-state. In both the solution and solid-state, the energy gap (ΔE) between the *β*-diketonate and the $^4G_{5/2}$ excited state of the Sm^{III} ion dictates the lifetime of the excited state; the larger energy gap (ΔE (x 10^3 cm^{-1}): **2a** = 3.4; **2b** = 4.0; **2c** = 2.4) results in the longer excited-state lifetime (τ_{Sm} (solution, solid-state): **2a** = 118 μs, 99 μs; **2b** = 147 μs, 118 μs; **2c** = 114 μs, 96 μs), as has been previously observed.[252-256] Upon cooling to 77 K, Stark splitting is observed in the emission spectra from 550 to 700 nm, as observed in Figure 4.6C. This Stark splitting arises from the degeneracies of the $^6H_{5/2\text{-}11/2}$ levels of the ground state manifold at lowered temperatures. The absolute quantum yields were measured in triplicate using an integrating sphere and were found to be 6.0 ±0.4%, 14 ±2%, 3.4 ±0.5% for solution-state complexes, **2a**, **2b**, and **2c**, respectively. The average quantum efficiency (~8%) of **2a-c** is 40 times greater than the average solution-state quantum yield (~0.2%) for analogous Sm^{III} complexes.[262] In fact, **2b** displays the largest quantum yield reported to date for trivalent samarium

complexes. Additionally, the average solid-state quantum yield of **2a-c** (5 ±2%) is 25 times greater than the previously mentioned average value for Sm^{III} luminescence. These remarkably high quantum yields are speculated to arise from the absence of coordinated water or solvent molecules, lack of non-radiative *intra*molecular energy transfer from the $EDOT_2$-BPP ligand to the β-diketonates, and the absence of residual ligand fluorescence or phosphorescence. These factors lead to increased population of the β-diketonate triplet state and thus, efficient energy transfer to the Sm^{III} metal center.

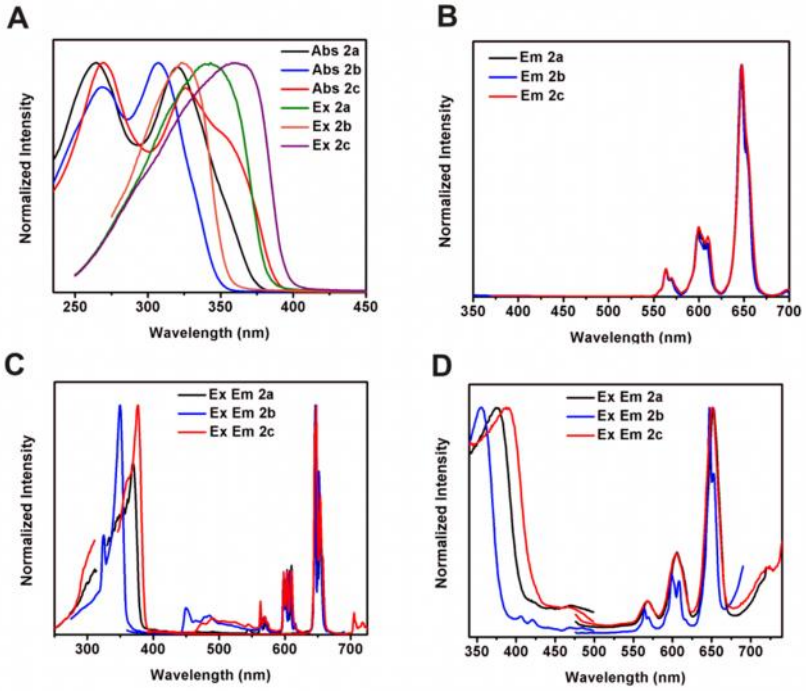

Figure 4.6. (A) Absorption and excitation spectra of **2a-c** at room temperature in CH_2Cl_2. (B) Emission spectra of **2a-c** at room temperature in CH_2Cl_2. (C) Excitation and emission spectra of **2a-c** at 77 K in 2-MeTHF. (D) Excitation and emission spectra of **2a-c** at room temperature in the solid state.

4.3.3.4. Spectroscopy of Terbium(III) Complexes

The photoluminescent properties of complexes **3a-c** have been thoroughly studied and are shown in Figure 4.7 and summarized in Table 4.7. As previously observed for

complexes **1a-c** and **2a-c**, the absorption profiles for complexes **3a-c** (Figure 4.7A) contain higher energy components (265-307 nm) attributed to $EDOT_2$-BPP $\pi \rightarrow \pi^*$ transitions and lower energy absorption bands (307-326 nm) corresponding to *β*-diketonate singlet absorption. Monitoring emission at either 545 nm or 615 nm, with varied excitation wavelength, produced excitation profiles (Figure 4.7A) that suggest maximum emission from the Tb^{III} ion arises from direct excitation of the *β*-diketonate ligands, as previously discussed with the analogous Eu^{III} and Sm^{III} complexes, **1a-c** and **2a-c**. Figure 4.7B shows the emission spectra for complexes **3a-c** and the characteristic $^5D_4 \rightarrow {}^7F_{6\text{-}2}$ transitions from 475 to 700 nm. However, differences in the emission spectra arise from the origin of the most intense transition. For complexes **3a** and **3c**, the most intense emission occurs at 617 nm, corresponding to the $^5D_4 \rightarrow {}^7F_3$ transition. Conversely, the emission spectrum of **3b** is dominated by emission at 546 nm from the $^5D_4 \rightarrow {}^7F_5$ transition. Notably, for all three Tb^{III} complexes, ligand-centered emission from $EDOT_2$-BPP is present in the spectra (~350-450 nm), indicating that energy transfer to Tb^{III} is not completely efficient. This inefficient energy transfer is supported by the extremely low solution-state absolute quantum yields of 0.5 ±0.3%, 0.07 ±0.02%, and 0.52 ±0.12% for **3a**, **3b**, and **3c**, respectively. Less than optimal energy gaps between the triplet excited state of the *β*-diketonate and the Tb^{III} emissive excited state ($^5D_4$) are responsible for the inefficient sensitization of the Tb^{III} ion and the low observed solution-state photoluminescent quantum yields. The small energy gaps (ΔE) between the *β*-diketonate and Tb^{III} excited states (ΔE: **3a** = 900 cm^{-1}; **3b** = 1500 cm^{-1}; **3c** = 100 cm^{-1}) increase the likelihood that back energy transfer will occur from the Ln^{III} ion to the sensitizing ligand, leading to increased ligand-centered emission. Upon cooling to 77 K, the emission spectra for all of the Tb^{III} complexes are dominated by the $^5D_4 \rightarrow {}^7F_5$ transition at 545 nm, as shown in Figure 4.7C. Additionally, at 77 K, no ligand-centered

fluorescence or phosphorescence is observed in the emission spectra. Stark splitting is also observed at 77 K due to the degeneracies of the $^7F_{6-2}$ levels of the ground state manifold. Longer radiative lifetimes were found at 77 K than at room temperature for complexes **3a-c** due to the deactivation of non-radiative pathways at lowered temperatures. In the solid-state, no detectable emission was observed for complexes **3a-c**.

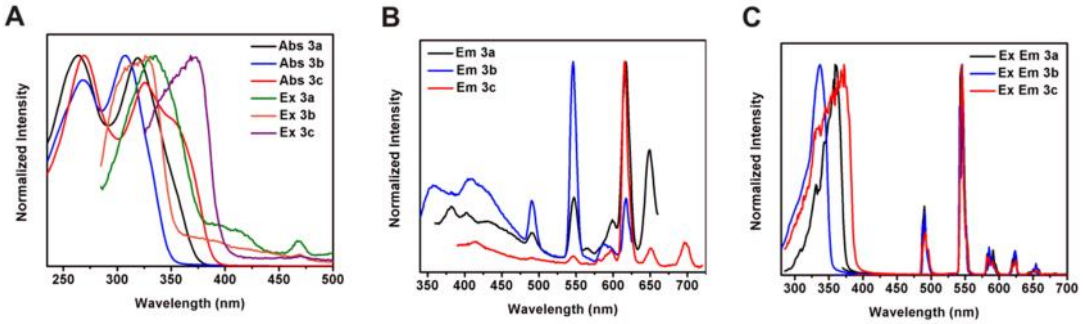

Figure 4.7. (A) Absorption and excitation spectra of **3a-c** at room temperature in CH_2Cl_2. (B) Emission spectra of **3a-c** at room temperature in CH_2Cl_2. (C) Excitation and emission spectra of **3a-c** at 77 K in 2-MeTHF.

4.4. CONCLUSIONS

In summary, a series of trivalent lanthanide complexes containing tris(*β*-diketonates) and a 3,4-ethylenedioxythiophene-derivatized BPP ligand have been synthesized and characterized by single-crystal X-ray crystallography and photophysical studies. Intense luminescent emission is observed from the Eu^{III} and Sm^{III} metal centers due to sensitization and efficient energy transfer from the bound $EDOT_2$-BPP and *β*-diketonate ligands. The lack of residual fluorescence and phosphorescence from the *β*-diketonates and $EDOT_2$-BPP ligands indicates that lanthanide emission is favored, as made evident by the high luminescent quantum yields and long microsecond radiative lifetimes. Incorporation of thiophene and thiophene derivatives into the architecture of the sensitizing ligands increases population of the triplet state of the ligand and enhances energy transfer to the emissive state of the trivalent lanthanide ion. Conversely, weak

luminescence was observed from the Tb^{III} complexes due to inefficient energy transfer and less-than-optimal energy gaps between the antenna ligand and the *f** excited state of the Tb^{III} metal center. Since electropolymerization of complexes **1a-c**, **2a-c**, and **3a-c** was unsuccessful, future efforts will be focused on synthesizing EDOT-functionalized lanthanide complexes that can be successfully electropolymerized into luminescent conducting metallopolymers.

References

(1) Gustafsson, G.; Cao, Y.; Treasy, G. M.; Klavetter, F.; Colaneri, N.; Heeger, A. J. *Nature* **1992**, *357*, 477.

(2) Forrest, S. R. *Nature* **2004**, *428*, 911.

(3) Wolf, M. O. *Inorg. Organomet. Polym.* **2006**, *16*, 189.

(4) Wolf, M. O. *Adv. Mater.* **2001**, *13*, 545.

(5) Holliday, B. J.; Swager, T. M. *Chem. Commun.* **2005**, 23.

(6) Manners, I. *Synthetic Metal-Containing Polymers*; Wiley-VCH: Weinheim, Germany, 2004.

(7) Manners, I. *Science* **2001**, *294*, 1664.

(8) Whittel, G. R.; Manners, I. *Adv. Mater.* **2007**, *19*, 3439.

(9) Eloi, J.; Chabanne, L.; Whittel, G. R.; Manners, I. *Mater. Today* **2008**, *11*, 28.

(10) Bignozzi, C. A.; Ferri, V.; Scoponi, M. *Macromol. Chem. Phys.* **2003**, *204*, 1851.

(11) Huynh, L.; Wang, Z.; Yang, J.; Stoeva, V.; Lough, A.; Manners, I.; Winnik, M. A. *Chem. Mater.* **2005**, *17*, 4765.

(12) Pang, Z.; Gu, X.; Yekta, A.; Masoumi, Z.; Coll, J. B.; Winnik, M. A.; Manners, I. *Adv. Mater.* **1996**, *8*, 768.

(13) Che, C.-M.; Zhang, J.-L.; Lin, L.-R. *Chem. Commun.* **2002**, 2556.

(14) Saatchi, K.; Haefeli, U. O. *Dalton Trans.* **2007**, 4439.

(15) Wang, C.; Gong, Y.; Fan, N.; Liu, S.; Luo, S.; Yu, J.; Huang, J. *Colloids Surf. B* **2009**, *70*, 84.

(16) Abd-El-Aziz, A. S.; Carraher Jr., C. E.; Pittman Jr., C. U.; Zeldin, M. *Macromolecules Containing Metals and Metal-Like Elements*; Wiley: Hoboken, NJ, 2004; Vol. 3.

(17) Madhavan, N.; Jones, C. W.; Weck, M. *Acc. Chem. Res.* **2008**, *41*, 1153.

(18) Leadbeater, N. E.; Marco, M. *Chem. Rev.* **2002**, *102*, 3217.

(19) Wrighton, M. S.; Morse, D. L. *J. Am. Chem. Soc.* **1974**, *96*, 998.

(20) Geoffroy, G. L.; Wrighton, M. S. *Organometallic Photochemistry*; Academic Press: New York, NY, 1979.

(21) Henly, T. J. *Coord. Chem. Rev.* **1989**, *93*, 269.

(22) Giordano, P. J.; Wrighton, M. S. *J. Am. Chem. Soc.* **1979**, *101*, 2888.

(23) Sullivan, B. P. *J. Phys. Chem.* **1989**, *93*, 24.

(24) Kalyanasundaram, K. *Photochemistry of Polypyridine and Porphyrin Complexes*; Academic Press: London, England, 1992.

(25) Lees, A. J. *J. Coord. Chem. Rev.* **1998**, *177*, 127.

(26) Stufkens, D. J.; Vlcek, A. *Coord. Chem. Rev.* **1998**, *177*, 179.

(27) de Bettencourt-Dias, A. *Curr. Org. Chem.* **2007**, *11*, 1460.

(28) Baldo, M. A.; O'Brian, D. F.; You, Y.; Shoustikov, A.; Sibley, S.; Thompson, M. E.; Forrest, S. R. *Nature* **1998**, *395*, 151.

(29) Ostrowski, J. C.; Robinson, M. R.; Heeger, A. J.; Bazan, G. C. *Chem. Commun.* **2002**, 784.

(30) Ma, Y.; Zhang, H.; Shen, J.; Che, C.-M. *Synth. Met.* **1998**, *94*, 245.

(31) Kwong, R. C.; Sibley, S.; Dubovoy, T.; Baldo, M. A.; Forrest, S. R.; Thompson, M. E. *Chem. Mater.* **1999**, *11*, 3709.

(32) Amoroso, A. J.; Coogan, M. P.; Dunne, J. E.; Fernandez-Moreira, V.; Hess, J. B.; Hayes, A. J.; Lloyd, D.; Millet, C.; Pope, S. J. A.; Williams, C. *Chem. Commun.* **2007**, 3066.

(33) Lo, K. K.-W.; Lee, T. K.-M.; Lo, J. S.-Y.; Poon, W.-L.; Cheng, S.-H. *Inorg. Chem.* **2008**, *47*, 200.

(34) Lo, K. K.-W.; Tsang, K. H.-K.; Zhu, N. *Organometallics* **2006**, *25*, 3220.

(35) Hawecker, J.; Lehn, J. M.; Ziessel, R. J. *J. Chem. Soc., Chem. Commun.* **1983**, 536.

(36) Hawecker, J.; Lehn, J. M.; Ziessel, R. J. *J. Chem. Soc., Chem. Commun.* **1984**, 328.

(37) Kutal, C.; Weber, M. A.; Ferraudi, G.; Geiger, D. *Organometallics* **1985**, *4*, 2161.

(38) Kutal, C.; Corbin, A. J.; Ferraudi, G. *Organometallics* **1987**, *6*, 553.

(39) Juris, A.; Campagna, S.; Bidd, I.; Lehn, J. M.; Ziessel, R. J. *Inorg. Chem.* **1988**, *27*, 4007.

(40) Yam, V. W.-W.; Lau, V. C.-Y.; Cheung, K.-K. *Organometallics* **1995**, *14*, 2749.

(41) O'Toole, T. R.; Margerum, L. D.; Westmoreland, T. D.; Vining, W. J.; Murray, R. W.; Meyer, T. J. *J. Chem. Soc., Chem. Commun.* **1985**, *20*, 1416.

(42) Ranjan, S.; Lin, S.-Y.; Hwang, K.-C.; Ching, W.-L.; Liu, C.-S. *Inorg. Chem.* **2003**, *42*, 1248.

(43) Coogan, M. P.; Fernandez-Moreira, V.; Hess, J. B.; Pope, S. J. A.; Williams, C. *New J. Chem.* **2009**, *33*, 1094.

(44) Louie, M.-W.; Liu, H.-W.; Lam, M. H.-C.; Lau, T.-C.; Lo, K. K.-W. *Organometallics* **2009**, *28*, 4297.

(45) Hawecker, J.; Lehn, J. M.; Ziessel, R. J. *Helv. Chim. Acta* **1986**, *69*, 1990.

(46) Smieja, J. M.; Kubiak, C. P. *Inorg. Chem.* **2010**, *49*, 9283.

(47) Sullivan, B. P.; Bolinger, C. M.; Conrad, D.; Vining, W. J.; Meyer, T. J. *J. Chem. Soc., Chem. Commun.* **1985**, 1414.

(48) Baldo, M. A.; Lamansky, S.; Burrows, P. E.; Thompson, M. E.; Forrest, S. R. *Appl. Phys. Lett.* **1999**, *75*, 4.

(49) Adachi, M. A.; Baldo, S. R.; Forrest, S. R.; Thompson, M. E. *Appl. Phys. Lett.* **2000**, *77*, 904.

(50) Bernhard, S.; Gao, X.; Malliaras, G. G.; Abruna, H. D. *Adv. Mater.* **2002**, *14*, 433.

(51) Jiang, X.; Jen, A. K.-Y.; Carlson, B.; Dalton, L. R. *Appl. Phys. Lett.* **2002**, *80*, 713.

(52) Chan, S. C.; Chan, M. C. W.; Wang, Y.; Che, C.-M.; Cheung, K. K.; Zhu, N. *Chem. Eur. J.* **2001**, *7*, 4108.

(53) Lu, W.; Mi, B.-X.; Chan, C. W.; Hui, Z.; Zhu, N.; Lee, S.-T.; Che, C.-M. *Chem. Commun.* **2002**, 206.

(54) de Bettencourt-Dias, A. *Dalton Trans.* **2007**, 2229.

(55) Grimsdale, A. C.; Chan, K. L.; Martin, R. E.; Jokisz, P. G.; Holmes, A. B. *Chem. Rev.* **2009**, *109*, 897.

(56) Lei, Z. Q.; Wang, Y. P. *J. Appl. Polym. Sci.* **1997**, *64*, 1575.

(57) Chan, W. K.; Gong, X.; Ng, W. Y. *Appl. Phys. Lett.* **1997**, *71*, 2919.

(58) Yu, S. C.; Hou, S. J.; Chan, W. K. *Macromolecules* **1999**, *32*, 5251.

(59) Wong, W.-Y.; Wang, X. Z.; He, Z.; Chan, K.-K.; Djurisic, A. B.; Cheung, K.-Y.; Yip, C. T.; Ng, A. M.-C.; Xi, Y. Y.; Mak, C. S. K.; Chan, W.-K. *J. Am. Chem. Soc.* **2007**, *129*, 14372.

(60) Liu, L.; Ho, C.-L.; Wong, W.-Y.; Cheung, K.-Y.; Fung, M.-K.; Lam, W.-T.; Djurisic, A. B.; Chan, W. K. *Adv. Funct. Mater.* **2008**, *18*, 2824.

(61) Wu, P.-T.; Bull, T.; Kim, F. S.; Luscombe, C. K.; Jenekhe, S. A. *Macromolecules* **2009**, *42*, 671.

(62) Mei, J.; Ogawa, K.; Kim, Y.-G.; Heston, N. C.; Arenas, D. J.; Nasrollahi, Z.; McCarley, T. D.; Tanner, D. B.; Reynolds, J. R.; Schanze, K. S. *ACS Appl. Mater. Interfaces* **2009**, *1*, 150.

(63) Baek, N. S.; Hau, S. K.; Yip, H.-L.; Acton, O.; Chen, K.-S.; Jen, A. K.-Y. *Chem. Mater.* **2008**, *20*, 5734.

(64) Man, K. Y. K.; Wong, H. L.; Chan, W. K.; Djurisic, A. B.; Beach, E.; Rozeveld, S. *Langmuir* **2006**, *22*, 3368.

(65) Man, K. Y. K.; Wong, H. L.; Chan, C. W.; Kwong, C. Y.; Djurisic, A. B. *Chem. Mater.* **2004**, *16*, 365.

(66) Cheng, K. W.; Mak, C. S. K.; Chan, W. K.; Ng, A. M.-C.; Djurisic, A. B. *J. Polym. Sci., Part A: Polym. Chem.* **2008**, *46*, 1305.

(67) Chan, C. W.; Ng, P. K.; Gong, X.; Hou, S. J. *J. Mater. Chem.* **1999**, *9*, 2103.

(68) Tse, C. W.; Lam, L. S. M.; Man, K. Y. K.; Wong, W. T.; Chan, W. K. *J. Polym. Sci., Part A: Polym. Chem.* **2005**, *43*, 1292.

(69) Li, L.; Ho, C.-L.; Wong, W.-Y. *J. Organomet. Chem.* **2012**, *703*, 43.

(70) Wong, W.-Y.; Wong, W.-K.; Raithby, P. R. *J. Chem. Soc., Dalton Trans,* **1998**, 2761.

(71) Stanley, J. M.; Holliday, B. J. *Coord. Chem. Rev.* **2012**, *256*, 1520.

(72) Williams, K. A.; Boydston, A. J.; Bielawski, C. W. *Chem. Soc. Rev.* **2007**, *36*, 729.

(73) Nguyen, P.; Gomez-Elipe, P.; Manners, I. *Chem. Rev.* **1999**, *99*, 1515.

(74) Schubert, U. S.; Eschbaumer, C. *Angew. Chem. Int. Ed.* **2002**, *41*, 2892.

(75) Kingsborough, R. P.; Swager, T. M. *Prog. Inorg. Chem.* **1999**, *48*, 123.

(76) Mak, C. S. K.; Leung, Q. Y.; Li, C. H.; Chan, W. K. *J. Polym. Sci., Part A: Polym. Chem.* **2010**, *48*, 2311.

(77) Mak, C. S. K.; Cheung, W. K.; Leung, Q. Y.; Chan, W. K. *Macromol. Rapid Commun.* **2010**, *31*, 875.

(78) Hubner, E.; Turkoglu, G.; Wolf, M.; Zenneck, U.; Burzlaff, N. *Eur. J. Inorg. Chem.* **2008**, 1226.

(79) Xu, Z.; Feng, G.; Bai, Z.; Ma, Y.; Chang, W.; Li, J. *Sci. China, Ser. B* **2006**, *49*, 430.

(80) Ainscough, E. W.; Allcock, H. R.; Brodie, A. M.; Gordon, K. C.; Hindenlang, M. D.; Horvath, R.; Otter, C. A. *Eur. J. Inorg. Chem.* **2011**, 3691.

(81) Wolf, M. O.; Wrighton, M. S. *Chem. Mater.* **1994**, *6*, 1526.

(82) Bracco, L. L. B.; Einschlag, F. S. G.; Wolcan, E.; Ferraudi, G. J. *J. Photochem. Photobiol., A* **2009**, *208*, 50.

(83) Feliz, M. R.; Ferraudi, G. J. *Inorg. Chem.* **2004**, *43*, 1551.

(84) Xu, P.; Ji, X.; Abetz, V.; Jiang, S.; Shen, J. *J. Polym. Sci., Part B: Polym. Phys.* **2008**, 2047.

(85) Lee, P.-I.; Hsu, S. L.-C. *J. Polym. Sci., Part A: Polym. Chem.* **2006**, 1492.

(86) Ley, K. D.; Whittle, C. E.; Bartberger, M. D.; Schanze, K. S. *J. Am. Chem. Soc.* **1997**, *119*, 3423.

(87) Ley, K. D.; Li, Y.; Johnson, J. V.; Powell, D. H.; Schanze, K. S. *Chem. Commun.* **1999**, 1749.

(88) Walters, K. A.; Ley, K. D.; Cacalaheiro, C. S. P.; Miller, S. C.; Gosztola, D.; Wasielewski, M. R.; Bussandri, A. P.; van Willigen, H.; Schanze, K. S. *J. Am. Chem. Soc.* **2001**, *123*, 8329.

(89) Liu, Y.; Li, Y.; Schanze, K. S. *J. Photochem. Photobiol., C* **2002**, *3*, 1.

(90) Ley, K. D.; Schanze, K. S. *Coord. Chem. Rev.* **1998**, *171*, 287.

(91) Li, Y.; Whittle, C. E.; Walters, K. A.; Ley, K. D.; Schanze, K. S. *Pure Appl. Chem.* **2000**, *73*, 497.

(92) Tse, C. W.; Cheng, K. W.; Chan, W. K.; Djurisic, A. B. *Macromol. Rapid Commun.* **2004**, *25*, 1335.

(93) Yamamoto, Y.; Sawa, S.; Funada, Y.; Morimoto, T.; Falkenstrom, M.; Miyasaka, H.; Shishido, S.; Ozeki, T.; Koike, K.; Ishitani, O. *J. Am. Chem. Soc.* **2008**, *130*, 14659.

(94) Xue, W.-M.; Kuhn, F. E.; Herdtweck, E. *Polyhedron* **2001**, *20*, 791.

(95) Dequeant, M. Q.; Ren, T. *J. Cluster Sci.* **2010**, *21*, 291.

(96) Tarasenko, M. S.; Naumov, N. G.; Naumov, D. Y.; Kim, S.-J.; Fedorov, V. E. *Polyhedron* **2008**, 2357.

(97) Efremova, O. A.; Mironov, Y. V.; Kuratieva, N. V.; Fedorov, V. E. *Polyhedron* **2011**, *30*, 1404.

(98) Jeitschko, W.; Block, G.; Kahnert, G. E.; Behrens, R. K. *J. Solid State Chem.* **1990**, *89*, 191.

(99) Cotton, F. A.; Norman, J. G. *J. Coord. Chem.* **1971**, *1*, 161.

(100) Morison, B.; Hughes, R. C.; Soos, Z. G. *Acta Crystallogr., Sect. B* **1975**, *31*, 762.

(101) Cotton, F. A.; Feithouse, T. R. *Inorg. Chem.* **1980**, *19*, 328.

(102) Cotton, F. A.; Feithouse, T. R. *Inorg. Chem.* **1981**, *20*, 600.

(103) Handa, M.; Kasamatsu, K.; Kasuge, K.; Mikuriya, M.; Fujii, T. *Chem. Lett.* **1990**, 1753.

(104) Kerby, M. C.; Eichhorn, B. W.; Creighton, J. A.; Vollhardt, K. P. C. *Inorg. Chem.* **1990**, *29*, 1319.

(105) Ouyang, X.; Campana, C.; Dunbar, K. R. *Inorg. Chem.* **1996**, *35*, 7188.

(106) Wesemann, J. L.; Chisholm, M. H. *Inorg. Chem.* **1997**, *36*, 3258.

(107) Handa, M.; Matsumoto, H.; Yashioka, D.; Nukada, R.; Mikuriya, M.; Hiromltsu, I.; Kasuge, K. *Bull. Chem. Soc. Jpn.* **1998**, *71*, 1811.

(108) Xue, W.-M.; Kuhn, F. E.; Herdtweck, E.; Li, Q. *Eur. J. Inorg. Chem.* **2001**, 213.

(109) Dequeant, M. Q.; McGuire Jr., R.; McMillin, D. R.; Ren, T. *Inorg. Chem.* **2005**, *44*, 6521.

(110) *Multiple Bonds Between Metal Atoms*; 3rd ed.; Springer Science and Business Media, Inc.: New York, NY, 2005.

(111) Cotton, F. A.; Lin, C.; Murillo, C. A. *Acc. Chem. Res.* **2001**, *34*, 759.

(112) Cotton, F. A.; Lin, C.; Murillo, C. A. *Proc. Natl. Acad. Sci. USA* **2002**, *99*, 4810.

(113) Cayton, R. H.; Chisholm, M. H.; Huffman, J. C.; Lobkovsky, E. B. *J. Am. Chem. Soc.* **1991**, *113*, 8709.

(114) Cayton, R. H.; Chisholm, M. H.; Huffman, J. C.; Lobkovsky, E. B. *Angew. Chem. Int. Ed.* **1991**, *30*, 862.

(115) Suen, M.-C.; Tseng, G.-W.; Chen, J.-D.; Keng, T.-C.; Wang, J.-C. *Chem. Commun.* **1999**, 1185.

(116) Chisholm, M. H. *Dalton Trans.* **2003**, 3821.

(117) Kuang, S.-M.; Fanwick, P. E.; Walton, R. A. *Inorg. Chem.* **2000**, *39*, 2968.

(118) Barral, M. C.; Gallo, T.; Herrero, S.; Jimenez-Aparicio, R.; Torres, M. R.; Urbanos, F. A. *Inorg. Chem.* **2006**, *45*, 3639.

(119) Chen, W.-Z.; Ren, T. *Inorg. Chem.* **2006**, *45*, 9175.

(120) Ren, T. *Chem. Rev.* **2008**, *108*, 4185.

(121) Burroughs, J. H.; Bradley, D. D. C.; Brown, A. R.; Marks, R. N.; MacKay, K.; Friend, R. H.; Burn, P. L.; Holmes, A. B. *Nature* **1990**, *347*, 539.

(122) Zhang, Y.; Huang, Z.; Zeng, W.; Cao, Y. *Polymer* **2008**, 1211.

(123) Ng, P. K.; Gong, X.; Chan, S. H.; Lam, L. S. M.; Chan, W. K. *Chem. Eur. J.* **2001**, *7*, 4358.

(124) Zhang, M.; Lu, P.; Wang, X.; He, L.; Xia, H.; Zhang, W.; Yang, B.; Liu, L.; Yang, L.; Yang, M.; Ma, Y.; Feng, J.; Wang, D.; Tamai, N. *J. Phys. Chem. B* **2004**, *108*, 13185.

(125) Chan, W. K.; Hui, C. S.; Man, K. Y. K.; Cheng, K. W.; Wong, H. L.; Zhu, N.; Djurisic, A. B. *Coord. Chem. Rev.* **2005**, *249*, 1351.

(126) Tse, C. W.; Cheng, K. W.; Chan, W. K. *J. Inorg. Organomet. Polym.* **2008**, *18*, 59.

(127) Johnson, F. P. A.; George, M. W.; Hartl, F.; Turner, J. J. *Organometallics* **1996**, *15*, 3374.

(128) Collin, J. P.; Sauvage, J. P. *Coord. Chem. Rev.* **1989**, *93*, 245.

(129) Stor, G. J.; Hartl, F.; Van Outerstep, J. W. M.; Stufkens, D. J. *Organometallics* **1995**, *14*, 1115.

(130) O'Toole, T. R.; Sullivan, B. P.; Bruce, M. R.-M.; Margerum, L. D.; Murray, R. W.; Meyer, T. J. *J. Electroanal. Chem.* **1989**, *259*, 217.

(131) Breikss, A. I.; Abruna, H. D. *J. Electroanal. Chem.* **1986**, *201*, 347.

(132) Christensen, P.; Hamnett, A.; Muir, A. V. G.; Timney, J. A. *J. Chem. Soc., Dalton Trans.* **1992**, 1455.

(133) Calzaferri, G.; Hadener, K.; Li, J. *J. Photochem. Photobiol. A.* **1992**, *64*, 259.

(134) Ishitani, O.; George, M. W.; Ibusuki, T.; Johnson, F. P. A.; Koike, K.; Pac, C.; Turner, J. J.; Westwell, J. R. *Inorg. Chem.* **1994**, *33*, 4712.

(135) Cabrera, C. R.; Abruna, H. D. *J. Electroanal. Chem.* **1986**, *209*, 101.

(136) Cheung, K.-C.; Guo, P.; So, M.-H.; Lee, L. Y. S.; Ho, K.-P.; Wong, W.-L.; Lee, K.-H.; Wong, W.-T.; Zhou, Z.-Y.; Wong, K.-Y. *J. Organomet. Chem.* **2009**, *694*, 2842.

(137) Cosnier, S.; Deronzier, A.; Moutet, J. C. *J. Mol. Catal.* **1988**, *45*, 381.

(138) Halman, M. M.; Steinberg, M. *Greenhouse Gas Carbon Dioxide Mitigation: Science and Technology*; CRC Press LLC: Boca Raton, FL, 1999.

(139) Sullivan, B. P.; Krist, K.; Guard, H. E. *Electrochemical and Electrocatalytic Reaction of Carbon Dioxide*; Elsevier: New York, NY, 1993.

(140) Underwood, A. J. V. *Ind. Eng. Chem.* **1940**, *32*, 449.

(141) Benson, E. E.; Kubiak, C. P.; Sathrum, A. J.; Smieja, J. M. *Chem. Soc. Rev.* **2009**, *38*, 89.

(142) Saatchi, K.; Hafeli, U. O. *Dalton Trans.* **2007**, 4439.

(143) Kunz, P. C.; Bruckmann, N. E.; Spingler, B. *Eur. J. Inorg. Chem.* **2007**, 394.

(144) Wallace, C.; Woods, C.; Rillema, D. P. *J. Am. Chem. Soc.* **1995**, *34*, 2875.

(145) Worl, L. A.; Duesing, R.; Chen, P.; Ciana, L. D.; Meyer, T. J. *J. Chem. Soc., Dalton Trans.* **1991**, 849.

(146) Luong, J. C.; Nadjo, L.; Wrighton, M. S. *J. Am. Chem. Soc.* **1978**, *100*, 5790.

(147) Giordano, P. J.; Fredericks, S. M.; Wrighton, M. S.; Morse, D. L. *J. Am. Chem. Soc.* **1978**, *100*, 2257.

(148) Lees, A. J. *Chem. Rev.* **1987**, *87*, 711.

(149) Guerrero, J.; Piro, O. E.; Wolcan, E.; Feliz, M. R.; Ferraudi, G.; Moya, S. A. *Organometallics* **2001**, *20*, 2842.

(150) Roundhill, D. M. *Photochemistry and Photophysics of Metal Complexes*; Plenum Press: New York, 1994.

(151) O'Toole, T. R.; Margerum, L. D.; Westmoreland, T. D.; Vining, W. J.; Murray, R. W.; Meyer, T. J. *J. Chem. Soc., Chem. Commun.* **1985**, *20*, 1414.

(152) Koga, Y.; Yoshida, N.; Matsubara, K. *J. Polym. Sci., Part A: Polym. Chem.* **2009**, *47*, 4366.

(153) Zhu, S. S.; Swager, T. M. *J. Am. Chem. Soc.* **1997**, *119*, 12568.

(154) Chen, X.-Y.; Yang, X.; Holliday, B. J. *J. Am. Chem. Soc.* **2008**, *130*, 1546.

(155) Viswanathan, S.; de Bettencourt-Dias, A. *Inorg. Chem.* **2006**, *45*, 10138.

(156) Abscor. T. Higashi; The Rigaku Corportation: Tokyo, Japan, 2001.

(157) Otwinoski, Z.; Minor, W. In *Macromolecular Crystallography, Part A*; Carter Jr., C. W., Sweets, R. M., Eds.; Academic Press: 1997, p 307-326.

(158) *CrystalClear, 1.40*; Rigaku Americas Corporation: The Woodlands, Texas, USA, 2008.

(159) Sheldrick, G. M. *SHELX 97. A software package for the solution and refinement of X-ray data*; University of Gottingen: Gottingen, Germany, 1997.

(160) Cromer, D. T.; Waber, J. T. In *International Tables for X-ray Crystallography*; Kynoch Press: Birmingham, England, 1974; Vol. 4.

(161) Fujita, E.; Szalda, D. J.; Creutz, C.; Sutin, N. *J. Am. Chem. Soc.* **1988**, *110*, 4870.

(162) Gennaro, A.; Isse, A. A.; Vianello, E. J. *J. Electroanal. Chem.* **1990**, *289*, 203.

(163) Bard, A. J.; Faulkner, L. R. *Electrochemical Methods: Fundamentals and Applications*; 2nd ed.; John Wiley & Sons: New York, NY, 2001.

(164) Laoire, C. O.; Mukerjee, S.; Abraham, K. M. *J. Phys. Chem. C* **2009**, *113*, 20127.

(165) Aebischer, A.; Gumy, F.; Bunzli, J.-C. G. *Phys. Chem. Chem. Phys.* **2009**, *11*, 1346.

(166) Becke, A. D. *J. Chem. Phys.* **1993**, *98*, 5648.

(167) Frisch, M. J.; Trucks, G. W.; Schlegel, H. B.; Scuseria, G. E.; Robb, M. A.; Cheeseman, J. R.; Montgomery Jr., J. A.; Vreven, T.; Kudin, K. N.; Burant, J. C.; Millam, J. M.; Iyengar, S. S.; Tomasi, J.; Barone, V.; Mennucci, B.; Cossi, M.; Scalmani, G.; Rega, N.; Petersson, G. A.; Nakatsuji, H.; Hada, M.; Ehara, M.; Toyota, K.; Fukuda, R.; Hasegawa, J.; Ishida, M.; Nakajima, T.; Honda, Y.; Kitao, O.; Nakai, H.; Klene, M.; Li, X.; Knox, J. E.; Hratchian, H. P.; Cross, J. B.; Bakken, V.; Adamo, C.; Jaramillo, J.; Gomperts, R.; Stratmann, R. E.; Yazyev, O.; Austin, A. J.; Cammi, R.; Pomelli, C.; Ochterski, J.; Ayala, P. Y.; Morokuma, K.; Voth, G. A.; Salvador, P.; Dannenberg, J. J.; Zakrzewski, V. G.; Dapprich, S.; Daniels, A. D.; Strain, M. C.; Farkas, O.; Malick, D. K.; Rabuck, A. D.; Raghavachari, K.; Foresman, J. B.; Ortiz, J. V.; Cui, Q.; Baboul, A. G.; Clifford, S.; Cioslowski, J.; Stefanov, B. B.; Liu, G.; Liashenko, A.; Piskorz, P.; Komaromi, I.; Martin, R. L.; Fox, D. J.; Keith, T.; Al-Laham, M. A.; Peng, C. Y.; Nanayakkara, A.; Challecombe, M.; Gill, P. M. W.; Johnson, B. G.; Chen, W.; Wong, M. W.; Gonzalez, C.; Pople, J. A.; Gaussian, Inc.: Wallingford, CT, 2004.

(168) Fuentealba, P.; Preuss, H.; Stoll, H.; Szentpaly, L. V. *Chem. Phys.* **1982**, *89*, 418.

(169) Foresman, J. B.; Frisch, A. *Exploring Chemistry with Electronic Structure Methods*; 2nd ed.; Gaussian, Inc.: Pittsburgh, PA, 1996.

(170) Zhao, L.; Wong, K. M.-C.; Li, B.; Li, W.; Zhu, N.; Wu, L.; Yam, V. W.-W. *Chem. Eur. J.* **2010**, *16*, 6797.

(171) Mohanakrishnan, A. K.; Hucke, A.; Lyon, M. A.; Lakshmikantham, M. V.; Cava, M. P. *Tetrahedron* **1999**, *55*, 11745.

(172) Alberto, R.; Egli, A.; Abram, U.; Hegetschweiler, K.; Gramlich, V.; Schubiger, P. A. *Dalton Trans.* **1994**, 2815.

(173) Turbiez, M.; Frere, P.; Roncali, J. *J. Org. Chem.* **2003**, *68*, 5357.

(174) Vitali, D.; Calderazzo, F. *Gazz. Chim. Ital.* **1972**, *102*, 587.

(175) Si, Z.; Li, X.; Li, X.; Zhang, H. *J. Organomet. Chem.* **2009**, *694*, 3742.

(176) Fenton, D. E.; Tate, J. R.; Casellato, U.; Tamburini, S.; Vigato, P. A.; Vidali, M. *Inorg. Chim. Acta* **1984**, *83*, 23.

(177) Lytwak, L. A.; Stanley, J. M.; Mejia, M. L.; Holliday, B. J. *J. Chem. Soc., Dalton Trans.* **2010**, *39*, 7692.

(178) Sacksteder, L.; Lee, M.; Demas, J. N.; DeGraff, B. A. *J. Am. Chem. Soc.* **1993**, *115*, 8230.

(179) Stanley, J. M.; Zhu, X.; Yang, X.; Holliday, B. J. *Inorg. Chem.* **2010**, *49*, 2035.

(180) Cotton, F. A. *Chemical Applications of Group Theory*; 3rd ed.; Wiley: New York, NY, 1990.

(181) Dong, J.-Y.; You, T.-P. *Acta Crystallogr., Sect. E: Structure Rep. Online* **2008**, *64*, o820.

(182) Zabel, D.; Schubert, A.; Wolmershauser, G.; Jones, R. L.; Thiel, W. R. *Eur. J. Inorg. Chem.* **2008**, 3648.

(183) Zhou, Y.; Chen, W.; Wang, D. *Dalton Trans.* **2008**, 1444.

(184) Ge, Q.; Corkery, T. C.; Humphrey, M. G.; Samoc, M.; Hor, T. S. A. *J. Chem. Soc., Dalton Trans.* **2009**, 6192.

(185) Heard, P. J.; Jones, C. *J. Chem. Soc., Dalton Trans.* **1997**, 1083.

(186) Machura, B.; Penczek, R.; Kruszynski, R. *Polyhedron* **2007**, *26*, 2470.

(187) Heard, P. J.; King, P. M.; Bain, A. D.; Hazendonk, P.; Tocher, D. A. *J. Chem. Soc., Dalton Trans.* **1999**, 4495.

(188) Gelling, A.; Orrell, K. G.; Osborne, A. G.; Sik, V. *J. Chem. Soc., Dalton Trans.* **1998**, 937.

(189) Abel, E. W.; Hylands, K. A.; Olsen, M. D.; Orrell, K. G.; Osborne, A. G.; Sik, V.; Ward, G. N. *J. Chem. Soc., Dalton Trans.* **1994**, 1079.

(190) Luong, J. C.; Faltynek, R. A.; Wrighton, M. S. *J. Am. Chem. Soc.* **1980**, *102*, 7892.

(191) Yam, V. W.-W.; Lau, V. C.-Y.; Wu, L.-X. *J. Chem. Soc., Dalton Trans.* **1998**, 1461.

(192) Katrib, A.; Yousef, R. M.; Fitzpatrick, N. J. *Inorg. Chem.* **1982**, *21*, 1523.

(193) Lam, S.-T.; Zhu, N.; Yam, V. W.-W. *Inorg. Chem.* **2009**, *48*, 9664.

(194) Stoeffler, H. D.; Thornton, N. B.; Temkin, S. L.; Schanze, K. S. *J. Am. Chem. Soc.* **1995**, *117*, 7119.

(195) Henry, M. S.; Hoffman, M. Z. *J. Phys. Chem.* **1979**, *83*, 618.

(196) Kalyanasundaram, K. *J. Chem. Soc., Faraday Trans. 2* **1986**, 2401.

(197) Kaim, W.; Kramer, H. E. A.; Volger, C.; Reiker, J. *J. Organomet. Chem.* **1989**, *367*, 107.

(198) Haines, R. J.; Wittrig, R. E.; Kubiak, C. P. *Inorg. Chem.* **1994**, *33*, 4723.

(199) Bredas, J. L.; Street, G. B. *Acc. Chem. Rev.* **1985**, *18*, 309.

(200) *Conjugated Polymers: Theory, Synthesis, Properties, and Characterization*; 3rd ed.; CRC Press: Boca Raton, FL, 2007; Vol. 1.

(201) *Handbook of Oligo- and Polythiophenes*; Wiley-VCH: Weinheim, Germany, 1999.

(202) Ukai, S.; Ito, H.; Marumoto, K.; Kuroda, S. *J. Phys. Soc. Jpn.* **2005**, *74*, 3314.

(203) Bredas, J. L.; Themans, B.; Fripiat, J. G.; Andre, J. M. *Phys. Rev. B: Solid State* **1984**, *29*, 6761.

(204) Leclerc, M.; Diaz, F. M.; Wegner, G. *Makromol. Chem.* **1989**, *190*, 3105.

(205) Chen, S. A.; Tsai, C. C. *Macromolecules* **1993**, *26*, 2234.

(206) Liao, J.-H.; Benz, M.; LeGoff, E.; Kanatzidis, M. G. *Adv. Mater.* **1994**, *6*, 135.

(207) Barbarella, G.; Zambianchi, M.; Bongini, A.; Antolini, L. *Adv. Mater.* **1993**, *5*, 834.

(208) Torsi, L.; Dodableapur, A.; Katz, H. E. *Polym. Mater. Sci. Eng.* **1995**, *72*, 569.

(209) Horowitz, G.; Fichou, D.; Peng, X. Z.; Garnier, F. *Synth. Met.* **1991**, *41*, 1127.

(210) Burroughes, J. H.; Bradley, D. C. C.; Brown, A. R.; Marks, R. N.; Mackay, K.; Friend, R. H.; Burns, P. L.; Holmes, A. B. *Nature* **1990**, *347*, 539.

(211) Garnier, F.; Hajlaoui, R.; Yassar, A.; Srivasyava, P. *Science* **1994**, *265*, 1684.

(212) Geiger, F.; Stoldt, M.; Schweizer, H.; Bauerle, P.; Umbach, E. *Adv. Mater.* **1993**, *5*, 922.

(213) Grem, C.; Leditzky, G.; Ulrich, B.; Leising, G. *Adv. Mater.* **1992**, *4*, 36.

(214) Garnier, F.; Horowitz, G.; Peng, X. Z.; Fichou, D. *Adv. Mater.* **1990**, *2*, 592.

(215) Servet, B.; Horowitz, G.; Ries, S.; Lagorsse, O.; Alnot, P.; Yassar, A.; Deloffre, F.; Srivastava, P.; Hajlaoui, R.; Lang, P.; Garnier, F. *Chem. Mater.* **1994**, *6*, 1809.

(216) Connelly, N. G.; Geiger, W. E. *Chem. Rev.* **1996**, *96*, 877.

(217) Bard, A. J.; Faulkner, L. R. *Electrochemical Methods: Fundamentals and Applications*; 1st ed.; John Wiley & Sons: New York, 1980.

(218) Tsierkezos, N. G. *J. Solution Chem.* **2007**, *36*, 289.

(219) Zoski, C. G. *Handbook of Electrochemistry*; Elsevier: Amsterdam, The Netherlands, 2007.

(220) Denuault, G.; Mirkin, M. V.; Bard, A. J. *J. Electroanal. Chem. Interfacial Electrochem.* **1991**, *308*, 27.

(221) Wurthner, F.; Yao, S.; Debaerdemaeker, T.; Worthmann, R. *J. Am. Chem. Soc.* **2002**, *124*, 9431.

(222) Guo, K.; Hao, J.; Zhang, T.; Zu, F.; Zhai, J.; Qiu, L.; Zhen, Z.; Liu, X.; Shen, Y. *Dyes Pigm.* **2008**, *77*, 657.

(223) Araki, K.; Endo, H.; Masuda, G.; Ogawa, T. *Chem. Eur. J.* **2004**, *10*, 3331.

(224) Pappenfus, T. M.; Mann, K. R. *Inorg. Chem.* **2001**, *40*, 6301.

(225) Li, Y.; Xue, L.; Li, H.; Li, Z.; Xu, B.; Wen, S.; Tian, W. *Macromolecules* **2009**, *42*, 4491.

(226) Diaz-Quijada, G. A.; Weinberg, N.; Holdcroft, S.; Pinto, B. M. *J. Phys. Chem. A.* **2002**, *106*, 1266.

(227) Liu, B.; Yu, W.-L.; Lai, Y.-H.; Huang, W. *Macromolecules* **2000**, *33*, 8945.

(228) Ie, Y.; Hirose, T.; Aso, Y. *J. Mater. Chem.* **2009**, *19*, 8169.

(229) Horowitz, G.; Bachet, B.; Yassar, A.; Lang, P.; Demanze, F.; Fave, J.-L.; Garnier, F. *Chem. Mater.* **1995**, *7*, 1337.

(230) Colditz, R.; Grebner, D.; Helbig, M.; Rentsch, S. *Chem. Phys.* **1995**, *201*, 309.

(231) Ostrowski, D. P.; Lytwak, L. A.; Mejia, M. L.; Stevenson, K. J.; Holliday, B. J. *ACS Nano* **2012**, *6*, 5507.

(232) Spano, F. C. *Acc. Chem. Rev.* **2010**, *43*, 429.

(233) Spano, F. C.; Clark, J.; Silva, C.; Friend, R. H. *J. Chem. Phys.* **2009**, *130*, 074904.

(234) *Lanthanide Probes in Life, Chemical, and Earth Sciences- Theory and Practice*; Elsevier: Amsterdam, The Netherlands, 1989.

(235) Faulkner, S.; Natrajan, L. S.; Perry, W. S.; Sykes, D. *Dalton Trans.* **2009**, 3890.

(236) Bunzli, J.-C. G. *Chem. Lett.* **2009**, *38*, 104.

(237) Bunzli, J.-C. G.; Piguet, C. *Chem. Soc. Rev.* **2005**, *34*, 1048.

(238) Latva, M.; Takalo, H.; Mukkala, V.-M.; Matachescu, C.; Rodriguez-Ubis, J. C.; Kankare, J. *J. Lumin.* **1997**, *75*, 149.

(239) Crosby, G. A.; Whan, R. E.; Alire, R. M. *J. Chem. Phys.* **1961**, *34*, 743.

(240) *Electronic Materials: The Oligomer Approach*; Wiley-VCH: Weinheim, Germany, 1998.

(241) Jian, Y.; Xian-Qi, H.; Zhang-Yuan, Z.; Li, L. *J. Struct. Chem* **1989**, *8*, 187.

(242) De Silva, C. R.; Maeyer, J. R.; Wang, R.; Nichol, G. S.; Zheng, A. *Inorg. Chim. Acta* **2007**, *360*, 3543.

(243) Lenaerts, P.; Driesen, K.; Van Deun, R.; Binnemans, K. *Chem. Mater.* **2005**, *17*, 2148.

(244) Holz, R. C.; Thompson, L. C. *Inorg. Chem.* **1988**, *27*, 4640.

(245) De Silva, C. R.; Wang, R.; Zheng, Z. *Polyhedron* **2006**, *25*, 3449.

(246) Li, X.-L.; Dai, F.-R.; Zhang, L.-Y.; Zhu, Y.-M.; Peng, Q.; Chen, Z.-N. *Organometallics* **2007**, *26*, 4483.

(247) Ziessel, R.; Diring, S.; Kadjane, P.; Charbonniere, L.; Retailleau, P.; Philouze, C. *Chem. Asian J.* **2007**, *2*, 975.

(248) Stanley, J. M.; Chan, C. K.; Yang, X.; Jones, R. A.; Holliday, B. J. *Polyhedron* **2010**, *29*, 2511.

(249) de Bettencourt-Dias, A. *Inorg. Chem.* **2005**, *44*, 2734.

(250) Carlos, L. D.; Videira, A. L. L. *Phys. Rev. B.* **1994**, *49*, 11721.

(251) Klink, S. I.; Hebbink, G. A.; Grave, L.; Oude Alink, P. G. B.; Van Veggel, F. C. J. M.; Werts, M. H. V. *J. Phys. Chem. A* **2002**, *106*, 3681.

(252) Petoud, S.; Cohen, S. M.; Bunzli, J.-C. G.; Raymond, K. N. *J. Am. Chem. Soc.* **2003**, *125*, 13324.

(253) Lunstroot, K.; Nockemann, P.; Van Heck, K.; Van Meervelt, L.; Gorller-Walrand, C.; Binnemans, K.; Driesen, K. *Inorg. Chem.* **2009**, *48*, 3018.

(254) Goncalves e Silva, F. R.; Malta, O. L.; Reinhard, C.; Gudel, H.-U.; Piguet, C.; Moser, J. E.; Bunzli, J.-C. G. *J. Phys. Chem. A* **2002**, *106*, 1670.

(255) Hakala, H.; Liitti, P.; Peuralahti, J.; Karvinen, J.; Mukkala, V.-M.; Hovinen, J. *J. Lumin.* **2005**, *113*, 17.

(256) Hakala, H.; Liitti, P.; Puukka, J. P.; Peuralahti, J.; Loman, K.; Karvinen, J.; Ollikka, P.; Ylikoski, A.; Mukkala, V.-M.; Hovinen, J. *Inorg. Chem. Commun.* **2002**, *5*, 1059.

(257) Kawai, H.; Zhao, C.; Tsuruoka, S.-I.; Yoshida, T.; Hasegawa, Y.; Kawai, T. *J. Alloys Cmpd.* **2009**, *488*, 612.

(258) Kang, D.; Yoo, H. S.; Jung, S. H.; Kim, H.; Jeon, D. Y. *J. Phys. Chem. C* **2011**, *115*, 24334.

(259) Attia, M. S.; Mahmoud, W. H.; Ramsis, M. N.; Khalil, L. H.; Othman, A. M.; Hashem, S. G.; Mostafa, M. S. *J. Fluoresc.* **2011**, *21*, 1739.

(260) Voloshin, A. I.; Shavaleev, N. M.; Kazakov, V. P. *J. Photochem. Photobio., A* **2000**, *136*, 203.

(261) Wang, X. Y.; Li, C. M.; Li, X. J.; Tanabe, S.; Yu, J. Y. *Spectrochimica Acta Part A* **2007**, *67*, 1417.

(262) Bunzli, J.-C. G. *Chem. Rev.* **2010**, 2729.